UNIVERSITY OF OKLAHOMA

GRADUATE COLLEGE

MODELING NANOFLUID UTILIZATION TO CONTROL FINES MIGRATION

A DISSERTATION

SUBMITTED TO THE GRADUATE FACULTY

in partial fulfillment of the requirements for the

Degree of

DOCTOR OF PHILOSOPHY

By

BIN YUAN
Norman, Oklahoma
2017

Downloaded from SHAREOK. Persistent Handle URL: https://hdl.handle.net/11244/50898

MODELING NANOFLUID UTLIZATION TO CONTROL FINES MIGRATION

A DISSERTATION APPROVED FOR THE
MEWBOURNE SCHOOL OF PETROLEUM AND GEOLOGICAL ENGINEERING

BY

_____
Dr. Rouzbeh Ghanbarnezhad Moghanloo, Chair

_____
Dr. Jeffrey H. Harwell

_____
Dr. Chandra S. Rai

_____
Dr. Xingru Wu

_____
Dr. Bor-Jier (Ben) Shiau

_____
Dr. Pavel Bedrikovetski

© Copyright by BIN YUAN 2017
All Rights Reserved.

Dedicated to my mom, my dad and my elder sisters who gave me countless love and support.

Acknowledgements

I would like to express my wholehearted gratitude to my advisor, Dr. Rouzbeh Ghanbarnezhad Moghanloo. His generous support and patient guidance, and encouragement of independent thinking made it possible the success of conducting this topic that was of great interest to me. Without his continuous guidance, my learning and research experience would never have been the same.

I am also in debt to the committee members, Dr. Jeffrey H. Harwell, Dr. Chandra S. Rai, Dr. Xingru Wu, Dr. Dr. Bor-Jier (Ben) Shiau and Dr. Pavel Bedrikovetski for their guidance and support of my research. Special thanks to Dr. Pavel Bedrikovetski, Professor of Petroleum Engineering at the University of Adelaide, who always provides great advice on my research work. His intelligence navigates my entire degree program.

My genuine thanks go to my closest confidantes, Da Zheng, Kai Wang, Wendong Wang, and Zhe Liu for their continuous concern and selfless support. The countless efforts we together dedicate in so many aspects will be the unforgettable memory. It is all of you that let me know the enormous power of friendship and teamwork. Coven will win!

I would like to acknowledge Dr. David Wood, Editor-in-Chief in Journal of Natural Gas Science and Engineering, who leads me to a new world of academy as an Executive Editor. I also express my appreciation to my friends, Yao Wang, Purachet Pattamasingh, and other teammates for their help and contributions on my publications. I am grateful to all the international colleagues for their experimental findings and theoretical works to make this research work rich, e.g., Dr. Shidong Li, Dr. Ole Torseter and Dr. Tim Huang etc. I also want to express great thanks to my mentors Dr. Wells Michael and Dr. Sumit

Mukhopadhyay during my intern at GE Oil & Gas Technology Center. They helped me know the needs from the industrial aspects.

I owe my deepest appreciation to my parents, Mr. Yixin Yuan and Ms. Jinrong Liu, my elder sisters, Ms. Juan Gao (Yang Yuan) and Ms. Yuan Yuan, for their unconditional love and support. I am everything I am, because you love me. Love you, my family!

I want to express my gratitude to the Mewbourne School of Petroleum and Geological Engineering for their support. Thanks to all the friends in Oklahoma Chinese Petroleum Association for our joyful time we spend together in Norman, OK.

Please allow me to say thanks here to the absence of my future wife, who contributed to my dissertation in ways she never knew. Your being late allows me plenty of time and energy devoting to my career, even I always look forward your early arrival.

Finally, thanks to all the people appear in my life. It is all of you inspire me to be a better man.

Table of Contents

Acknowledgements iv

List of Figures xi

Abstract xix

Chapter 1: Introduction 1

1.1 Introduction to Fines Migration Problems 1

1.2 Introduction to Nanofluids Application in Petroleum Industry 5

1.3 Objective and Outline 8

Chapter 2: Nanoparticles Adsorption, Straining and Detachment Behavior: Mechanistic Modeling and Experimental Work 13

2.1 Nanoparticles and Experimental Methods 14

2.2 Mechanistic Nanoparticles Transport and Adsorption Model 15

2.2.1 Particle Equilibrium and Maximum Retention Concentration 16

2.2.2 Nanoparticles Transport Model with Adsorption and Straining 21

2.2.3 Method of Characteristic (MOC) Solutions 23

2.3 Characterization on Nanoparticles Adsorption, Straining and Detachment 31

2.4 Conclusions and Summary 39

2.5 Nomenclature 39

Chapter 3: Nanoparticles Utilization to Mitigate Fines Migration in Porous Media 42

3.1 Problem Statement and Assumption 42

3.1.1 Scenario I: Co-injection of Nanoparticles and Fine particles 44

3.1.2 Scenario II: Nanoparticles Pre-flush prior to Fines Invasion 45

3.2 Mathematical Model and Descriptions 46

3.2.1 Mutual Reactions among Nanoparticles, Fines and Rock Grains 46
3.2.2 Nanoparticles and Fines Co-injection with Mutual Reactions 55
3.2.3 Modeling Nanoparticles Pre-flush to Control Fines Migration 57
3.2.4 Modeling Nanoparticles Pre-flush to Maintain Well Injectivity 58
3.3 Analytical Solutions and Validations 62
3.3.1 Scenario I: Co-injection of Nanoparticles and Fine particles 62
3.3.2 Scenario II: Nanoparticles Pre-flush Prior to Fines Invasion 69
3.3.3 Nanoparticles Pre-flush to Maintain Well Injectivity 73
3.4 Evaluation and Optimization of Nanoparticles Utilization 93
3.4.1 Nanoparticles Utilization to Control Fines Migration 94
3.4.2 Nanoparticles Utilization to Improve Well Injectivity 99
3.5 Conclusions and Summary 103
3.6 Nomenclature 104
Chapter 4: Control Two-Phase Fines Migration using Nanoparticles 107
4.1 Problem Statement and Assumptions 107
4.2 Nanofluid Co-Injection to Reduce Two-Phase Fines Migration 109
4.2.1 Model Description and Methodology 109
4.2.2 Analytical Solutions and Derivations 112
4.2.3 Results Discussion and Verification 118
4.3 Nanofluid Pre-Flush to Control Fines Migration in Two-Phase Radial Flow .. 139
4.3.1 Model Description and Governing System 139
4.3.2 Analytical Solutions and Derivations 144
4.3.3 Results and Discussions 166

4.4 Conclusions and Summary 182
4.5 Nomenclature 184
Chapter 5: Combined Nanofluids with Low-Salinity Waterflooding 186
5.1 Problem Statement and Assumption 186
5.2 Nanofluid Improve Performance of Low-Salinity Waterflooding 190
5.2.1 Maximum Retention Concentration in Two-phase Flow 190
5.2.2 Fractional Flow Function Considering Particles Straining 194
5.2.3 Mechanistic Assumption of Nanoparticles to Control Fines Migration.. 196
5.2.4 Governing Equations and Semi-Analytical Solutions 197
5.2.5 Effects of Nanofluids Treatment on Low-Salinity Waterflooding..... 202
5.3 Combine Nanofluid with Low-Salinity Waterflooding in Layered Reservoirs 212
5.3.1 Description of Layered Radial Flow System..... 212
5.3.2 Fines Migration-Assisted Mobility Control in Layered System 214
5.3.3 Combine Nanofluid with Low-Salinity Waterflooding..... 219
5.4 Conclusions and Summary 223
Chapter 6: Contributions and Recommendations..... 224
6.1 Major Contributions 224
6.2 Recommendation for Future Work..... 226
References 227
Appendix A 243
Appendix B..... 249

List of Table

Table 2-1 Properties of Nano-Structure Particles, Li et al. (2015 a, b) 14

Table 2-2 The summary of suspended, attached and strained nanoparticles concentration along 1-D permeable medium within the different zones in distance-time diagram 30

Table 2-3 Summary of nanoparticles adsorption, straining & detachment behavior for the cases with different injected nanoparticles concentrations 34

Table 2-4 Permeability reduction of core plugs after NSP nanofluid injection 35

Table 3-1 Values of parameters in MOC solutions of all scenarios 72

Table 3-2 The summary of suspended, attached and strained fines concentration for different cases along 1-D permeable medium 81

Table 3-3 Values of parameters to characterize fines migration behavior with the effects of nanoparticles from the analytical solutions 91

Table 4-1 Values of parameters used the examples in section 4.2 138

Table 4-2 The summary of suspended fines concentration in different flow zones in the plane of (φ, x_D) for the scenario A in Figure 4.20 158

Table 4-3 The summary of attached fines concentration in different flow zones in the plane of (φ, x_D) for the scenario A in Figure 4.20 159

Table 4-4 The summary of strained fines concentration in different flow zones in the plane of (φ, x_D) for the scenario A in Figure 4.20 160

Table 4-5 The summary of suspended fines concentration in different flow zones in the plane of (φ, x_D) for the scenario B in Figure 4.20 161

Table 4-6 The summary of attached fines concentration in different flow zones in the plane of (φ, x_D) for the scenario B in Figure 4.20 162

Table 4-7 The summary of strained fines concentration in different flow zones in the plane of (φ, x_D) for the scenario B in Figure 4.20 163

Table A-1 Summary of assumptions of nanoparticles, fine particles, water, and oil behaviors in different cases of nanofluid application to control fines migration, maintain well injectivity and improve oil recovery..... 248

List of Figures

Figure 1.1. The formation damage mechanisms related to fines migration 3

Figure 2.1 Forces and momentum vectors exerted on a single particle 17

Figure 2.2 The maximum (critical) retention concentration of fine particles on rock grains decreases with the increase of flow velocity. 21

Figure 2.3 Distance–time diagram or motion of nanoparticles concentration fronts in the plane of x_D-t_D 29

Figure 2.4 Comparison between nanoparticles effluent history obtained from analytical models with experimental results 33

Figure 2.5 Comparison between pressure drop obtained from analytical models and lab experimental results 33

Figure 2.6 Workflow to quantify nanoparticles adsorption, straining and detachment using models and experimental results 36

Figure 2.7 Effects of injected nanoparticles concentration on maximum adsorption concentration, irreversible adsorption, and reversible adsorption of nanoparticles 37

Figure 2.8 Effects of injected nanoparticles concentration on nanoparticles adsorption and straining rates 38

Figure 2.9 Effects of injected nanoparticles concentration on formation damage effects attributed to nanoparticles adsorption and straining 38

Figure 3.1 Mutual interactions among nanoparticles, fines and rock grains indicating various physical mechanisms by which nanoparticles control fines migration 53

Figure 3.2 Enhanced fines attachment by nanoparticles coated on rock grains 54

Figure 3.3 Composition path diagram of fine particles and nanoparticles concentration along fast and slow path 65

Figure 3.4 Scenario I: composition path from the injection point J to initial point I (J：C_{NP}=0.00033， C_{FP}=0.02；constant point Q：C_{NP}=2.57E-6， C_{FP}=0；initial point I：C_{NP}=0， C_{FP}=0.02)..... 65

Figure 3.5 Scenario I: Distance–time diagram with characteristic lines and nanoparticles & fines concentration profile along 1-D medium at t_D= 0.7 67

Figure 3.6 Scenario I: Comparison of fine particle concentration profile at t_D=0.7 obtained from numerical simulation (solid line) and MOC solution (dashed line)..... 68

Figure 3.7 Scenario I: Comparison between fine particles cumulative production obtained from numerical simulation (solid line) and MOC solution (dashed line)..... 68

Figure 3.8 Scenario II: Suspended fines concentration profile along 1-D permeable medium at different dimensionless times (t_D=0.3, 0.5, 5.0 and 12.0) 70

Figure 3.9 Scenario II: Retained fines concentration on rock grains along the permeable medium at different dimensionless times (t_D=0.3, 0.62, 5.0 and 12.0) 70

Figure 3.10 Comparison of fines effluent concentration obtained from analytical models (solid line) and experimental results (Huang, 2008a) (discrete points)..... 71

Figure 3.11 Distance–time diagram or motion of particles concentration fronts in the plane of x_D-t_D..... 82

Figure 3.12 Suspended fine particles concentration profile along the 1-D permeable medium at different time for three different scenarios..... 84

Figure 3.13 Attached fines concentration profile along 1-D permeable medium at different moments for three different cases..... 87

Figure 3.14 Strained fines concentration profile along 1-D permeable medium at different moments for three different cases 89
Figure 3.15 Effluent history of fine particles concentration 89
Figure 3.16 Flowchart to explain the experimental results with analytical solutions and characterize the behavior of fines migration with nanoparticles utilizations 92
Figure 3.17 Comparison of fine particles effluent concentration history obtained from analytical models (solid line) and lab experimental results (discrete points) for different cases with types of nanoparticles utilizations approaches 93
Figure 3.18 Effluent history of fine particles concentration at the outlet for different scenarios of nanoparticles utilization 97
Figure 3.19 Cumulative fine particles production volume for different scenarios of nanoparticle utilization 98
Figure 3.20 Pressure drop along 1-D permeable medium at different time for three different cases 101
Figure 3.21 Decline of injection index with the increase of injected pore volume for three different cases 102
Figure 3.22 Comparison of permeability changes obtained from analytical models (solid line) and lab experimental results (discrete points) for both cases (case with nanoparticles effects; and reference case without nanoparticles) 103
Figure 4.1 Composition diagram of suspended nanoparticles and fines concentration along the slow path and fast path in coordinate of stream-function and distance 115
Figure 4.2 Flowchart to derive the propagation of water saturation, nanoparticles, and fines concentration in the plane of stream-function and distance 118

Figure 4.3 Composition path from the injection to initial condition in the example ... 120
Figure 4.4 Stream-function/distance diagram with the propagation of different nanoparticles-fines condition for two-fluid phase flow ... 121
Figure 4.5 Stream-function and distance diagram with the propagation of water-saturation wave and different nanoparticles-fines concentration wave ... 122
Figure 4.6 Graphical solution of nanoparticles and fines concentration in oil-water flow along 1-D porous media ... 124
Figure 4.7 Distance-time diagram of nanoparticles-fines transport in oil-water flow in the coordinate of (x_D, t_D) ... 125
Figure 4.8 Profile of water saturation, suspended nanoparticles, suspended fines and attached fines concentration in oil-water flow along 1-D porous medium ... 127
Figure 4.9 Suspended fines concentration profile in oil-water flow along 1-D porous medium (Dash line: without nanoparticles injection; Solid line: with nanoparticles injection. The difference between two lines represents the reduction number of mobile fines attributed to nanoparticles effects) ... 129
Figure 4.10 Profile of water saturation in oil-water flow along 1-D porous medium .. 129
Figure 4.11 Water-cut history accounting for effects of fines migration and nanoparticles utilization ... 130
Figure 4.12 Stream-function/distance diagram with the propagation of different nanoparticles-fines condition in water and two-phase flow in coordinate of (x_D, t_D) .. 133
Figure 4.13 Comparison of suspended nanoparticles concentration profile in water flow and in oil-water flow along 1-D porous medium ... 133

Figure 4.14 Comparison of suspended fines concentration profile in water flow and in oil-water flow along 1-D porous medium 135
Figure 4.15 Comparison of water saturation profile in oil-water flow along 1-D porous medium at the same moment (injected-pore-volume=0.2)..... 136
Figure 4.16 Comparison of suspended nanoparticles profile in oil-water flow along 1-D porous medium with injected-pore-volume as 0.2 137
Figure 4.17 Comparison of suspended fines profile in oil-water flow along 1-D porous medium with injected-pore-volume as 0.2)..... 137
Figure 4.18 Maximum retention concentration of fines at different radial locations, and scheme of different nanoparticles pre-treatment radius 142
Figure 4.19 The initial suspended fines concentration and maximum fines retention with 0.01nanofluid treatment range..... 144
Figure 4.20 Stream-function and distance diagram with the structure of analytical solutions within different flow zones for both scenario A and scenario B 157
Figure 4.21 Time-distance diagram indicates the propagation of different water saturation waves (no fines migration effects)..... 166
Figure 4.22 Stream-function and distance diagram indicates the propagation of water saturation waves (with fines migration in two-phase flow) 167
Figure 4.23 Time-distance diagram indicating the propagation of different water saturation waves in coordinate of dimensionless distance and time (with fines migration in two-phase flow)..... 168
Figure 4.24 The variation of water saturation, suspended fines, attached fines and strained fines concentration along the characteristic lines 171

Figure 4.25 Comparison of water saturation profile between the scenario with fines migration and that with no fines migration in two-phase radial flow system 172
Figure 4.26 Stream-function and distance diagram indicating the propagation of water saturation waves (with nanofluids in two-phase radial flow)..... 174
Figure 4.27 Time-distance diagram indicating the propagation of different water saturation waves (with nanofluids in two-phase flow)..... 174
Figure 4.28 The variation of water saturation, suspended fines, attached fines and strained fines concentration along different characteristic lines 176
Figure 4.29 Distributions of water saturation in the radial flow system at different time for both cases with and without nanofluid treatment 177
Figure 4.30 Distributions of suspended fines concentration in the radial flow system at different time for both cases with and without nanofluid treatment 179
Figure 4.31 Distributions of attached fines concentration in the radial flow system at different time for both cases with and without nanofluid treatment 180
Figure 4.32 Distributions of strained fines concentration in the radial flow system at different time for both cases with and without nanofluid treatment 181
Figure 4.33 Comparison of injection pressure drop changes for two scenarios with and without nanofluid to control fines migration in two-phase radial flow..... 181
Figure 5.1 Forces and momentum vectors exerted on fines in water-oil flow 191
Figure 5.2 Relationship between fluid salinity and particles separation distance..... 193
Figure 5.3 The effects of low-salinity water saturation on the maximum retention concentration of fine particles onto rock grains 194

Figure 5.4 Comparisons of fractional flow curves at different distances from injection wells considering the effects of fines straining 196
Figure 5.5 Schematic profile of nanofluid pretreatment, pressure drop, phase saturation, and maximum retention concentration of fines in radial flow 197
Figure 5.6 Comparison of analytical solutions (Distance-time diagram and composition variation along characteristic lines) between low-salinity waterflooding and conventional waterflooding cases considering fines migration..... 200
Figure 5.7 Comparison of water saturation profile at the same injected pore-volume (0.2) of conventional waterflooding cases and low-salinity waterflooding cases considering fines migration effects 202
Figure 5.8 Variation of maximum retention concentration of fine particles with the changes of distance from well (in radial coordinate) 203
Figure 5.9 Comparison of analytical solutions (distance-time diagram and composition variation along characteristic lines) of low-salinity waterflooding with different nanofluid treatment ranges (0.05; 0.10; 0.25) 207
Figure 5.10 Comparison of water saturation profile for cases with different nanofluid treatment ranges (0.05; 0.10; 0.25) prior to low-salinity waterflooding 208
Figure 5.11 Comparison of water-cut history of low-salinity waterflooding with different nanofluid treatment ranges (0.05; 0.10; 0.25)..... 208
Figure 5.12 Comparison of injection pressure drop for low-salinity waterflooding with different nanofluid treatment range 210
Figure 5.13 Comparison of recovery factor for low-salinity waterflooding with different nanofluid treatment ranges 212

Figure 5.14 Schematic profile of nanofluid pretreatment, pressure drop, phase saturation, and retention concentration of fines particles during low-salinity waterflooding in two-layered heterogenous reservoirs. 214
Figure 5.15 Workflow of analytical solutions for two-layered heterogeneous system with fines migration-assisted mobility control during low-salinity waterflooding 217
Figure 5.16 Water saturation profiles along each layer at different times 218
Figure 5.17 Changes of injected fluid fraction entering each layer at different times . 218
Figure 5.18 The maximum retention concentration of fine particles changing with distances away from the injection well 220
Figure 5.19 The propagation of water saturation profile along each layer at different time for case with nanofluid treatment prior to waterflooding..... 221
Figure 5.20 The comparison of injection pressure drop for cases with and without nanofluid pre-treatment cases..... 221
Figure 5.21 The comparison of location ratio of front movement along each layer for cases with and without nanofluid pre-treatment cases 222

Abstract

This dissertation presents analytical solutions to address several unresolved issues on modeling of nanofluid utilization to control fines migration in porous media. Despite numerical simulations, analytical solutions derived in this dissertation yield explicit expressions in terms of controlling parameters.

The main objectives of this dissertation are as follows: 1) provide a profound insight into the mechanisms of fines migration in both single-phase (water) and two-phase (oil & water) flow; 2) evaluate the pros and cons of fines migration impact on improving performance of low-salinity waterflooding in terms of both well injectivity and oil recovery; 3) evaluate impacts of nanofluid on formation damage; 4) develop a theoretical structure to evaluate the success of nanoparticles to control fines migration in both linear and radial flow system. 5) compare the performance of two different schemes of nanoparticles utilization to control fines migration; 6) develop the mathematical foundations and investigate the feasibility of combining nanofluid with low-salinity water to improve production performance in layered reservoirs.

To accomplish the above objectives, the following tasks are pursued in this dissertation:

- Adsorption/detachment and straining behavior of nanoparticles and their effects on permeability are studied using analytical solutions. The analytical solutions are verified by experimental results.
- An application of method of characteristics (MOC) is examined to evaluate the effectiveness of nanoparticles to mitigate fines migration in single-phase flow for two different scenarios of nanoparticles utilization to control fines migration: (1) co-injection

of nanoparticles with fines suspension into one-dimensional permeable medium and (2) pre-coating of porous medium with nanoparticles before injection. The analytical solutions are verified by both numerical simulations and experimental results.

- Nanofluid utilization to mitigate fines migration in two-phase (oil and water) flow is examined. The corresponding analytical solution is derived via implementing splitting method to transfer 3×3 system of governing equations into a combination of 2×2 auxiliary system containing only particles components (nanoparticles & fines) and one lifting equation with phase saturation. The analytical solutions are verified by numerical simulations.

- In two-phase flow, the integrated effects of fines migration and nanoparticles utilization are evaluated for two different schemes of nanoparticles utilization to control fines migration, including 1) co-injection of nanoparticle-fine particles mixture into 1-D permeable medium that initially oversaturated with fine particles and 2) pre-coating /pre-treatment with nanoparticles prior to fines injection in radial flow system.

- An axisymmetric radial flow model through single-layer homogenous/ multi-layer heterogeneous reservoirs systems is used to evaluate the mobility control obtained owing to fines migration. The same solution is used to optimize nanofluid treatment and to maintain well injectivity during low- salinity waterflooding.

Chapter 1: Introduction

1.1 Introduction to Fines Migration Problems

Particulates flow in porous media occurs in numerous processes of petroleum industry (Civan 2007), e.g., injection of seawater for water flooding (Bear et al. 1999), filtrate invasion into reservoirs during well drilling, cold water injection into geothermal reservoirs (Rosenbrand et al. 2014; You et al. 2015), microbial enhanced oil recovery (MEOR), alkaline flooding (AF), low salinity waterflooding (LSWF), and other secondary and tertiary recovery cases (Yuan et al. 2016a and b). Formation fines are defined as loose/unconsolidated clay or non-clay, charged or non-charged particles in the pore spaces with typical size of few tens of microns, and thus they are usually small enough to pass through 400 U.S mesh screens or pore-throats (Muecke, 1979; Penberthy, 1992).

Fines migration within reservoirs has been regarded as a significant cause to decrease reservoir permeability and impair well production/injection performance (Yuan et al. 2016e; Sarkar, 1990; Civan 2007). The formation damage mechanisms related to fines migration (Nguyen, 2007) include surface deposition or attachment, pore-throat bridging or straining, internal cake formation and infiltration sedimentation etc., as shown in Figure 1.1. Various factors have been experimentally recognized to affect fines migration within reservoirs, including fluid salinity, flow rates, pH, temperature, rock, and fluid polarity (Ezeukwu, 1998; Sarkar, 1990; Bedrikovetsky et al. 2011 and 2014; Civan 2007, 2010a and b). Civan (2007) and Bedrikovetsky (2011) have explained the mechanical equilibrium of torque balance among the detaching drag force, lifting force, and the attaching electrostatic forces exerting on fine particles. Generally, high flowing velocity

can increase the detachment forces, however, the decrease of fluid salinity and temperature, and increase of pH would weaken the attaching electrostatic force. All those changes cause fines detachment and migration in porous media. In deepwater reservoirs, during the deposition process of turbidite reservoirs, sands and clays are accumulated to form turbidite currents due to the slope instability, and then these currents formulated deepwater oil reservoirs at hundreds of kilometers away from their initial locations. As results, those types of reservoirs are usually poorly consolidated with high pressure, temperature, porosity, and permeability. All those reservoir properties dramatically enhance the probability of troublesome fines migration during deepwater oil production. (Ezeudoh, 2014; Ofurhie, 2002; Yuan et al., 2015b and 2016b).

Two-phase fines migration in under-saturated reservoirs occurs in types of waterflooding and enhanced oil recovery processes. Despite the diverse positive effects of EOR techniques have been extensively reported, however, the changes of chemical environment (pH, fluid salinity, and temperature etc.) induced by injected EOR fluids may simultaneously lead to the debating problem of fines migration. In one hand, fines migration may improve displacement efficiency by carrying small amounts of residual oil detached from rock grains (Bernard, 1967). In addition, the reduction of water-phase effective permeability in EOR fluid swept-area provides a simple mobility-control method and enhance the sweep efficiency by blocking high permeability layers to (Lemon, 2011; Zeinijahromi, 2011, 2012, 2013). In other hands, however, fines migration and size exclusion effects can also result in severe damage of reservoir permeability, especially near vertical wells with higher flow velocity, and then impair well injectivity (productivity in cases of production well), which leads to the traditional understanding of

avoiding fines migration. Therefore, in view of those debates upon the pros and cons of fines migration, it is desirable to control fines migration by taking advantages of its mobility-control effects far from the wellbore and minimizing its weaknesses of formation damage near wellbores. An effective design to control fines migration near wellbore needs the foundation of mathematical modeling works considering the various mechanisms of fines migration. Analytical solutions with explicitly quantitative relationship among physical parameters are desirable to explain the core-flood findings and field tests to improve our understanding on the effects of fines migration in multi-scale porous medium. In addition, the incorporation of analytical models with numerical simulations can be used for stream-line analysis and front-track (Holden et al., 2013). One of the objectives of this dissertation is to deliver analytical solutions for problems of fines migration and its control using nanofluids in different scenarios.

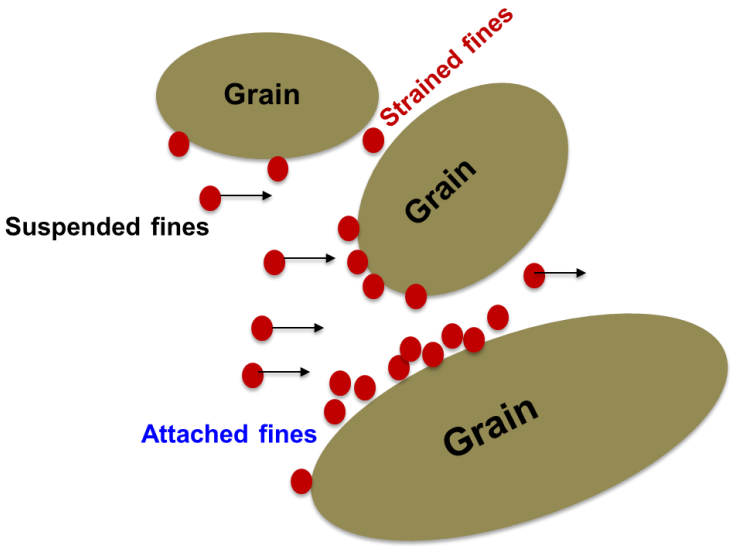


Figure 1.1. The formation damage mechanisms related to fines migration

Fines migration is usually modeled by kinetic equations that assumes the detachment/attachment rates proportional to the difference between the current and

critical detaching factors, such as velocity, salinity, and temperature. Diverse mathematical modeling works of particulates flow in porous media and associated permeability damage have been widely studied (Tufenkji, 2007; Civan, 2010; Bedrikovetsky, 2011). Those models mainly include, classical advective-diffusive model combined with kinetics of particles detachment (Logan, 2001) using average particle and pore sizes, population balance models (Santos, 2006; Shapiro, 2008) with probabilistic distributions of particles and pores size, and random walk models (Yuan, 2011), trajectory analysis (Chatterjee et al., 2011), and stochastic mean-field model (Lin, 2009).

The classical advective-diffusive model combined with kinetics of particles detachment provides an asymptotical stabilized fines retention concentration when flowing time is sufficiently large (Logan, 2001; Tufenkji, 2007). However, this method cannot reflect the instant fines release due to an abrupt changes of pressure gradient or fluid salinity (Ochi, 1998; Saripalli, 2000). Another shortcoming is its deficiency to incorporate effects of mechanical behaviors on fines migration. In fact, it has been long recognized that detachment of particles is controlled by the mechanical equilibrium (Civan, 2007; Bedrikovetsky, 2011). Hence, to put away those shortcuts of classical particles-capture kinetics model, the concept of maximum retention concentration determined by the torque equilibrium on particles has been developed as an alternative approach to describe the problem of fines migration (Al-Abduwani, 2005; Bedrikovetsky et al., 2011; Zeinijahromi, 2012; Yuan, 2015b). By introducing the maximum retention model of fine particles, Bedrikovetsky (2014) presented the exact solution of axisymmetric flow during single-phase water injection with fines detachment, migration, re-attachment, and straining effects. Borazjani et al (2016a) also developed the analytical

models of oil-water flow accounting for salinity-induced fines migration during low salinity waterflooding. Borazjani et al (2016b) applied the splitting technique to obtain the analytical models for two-phase flow with fines migration and multiple particles capture mechanisms (e.g., particles straining and attachment).

One of the objectives of this study is to extend the splitting methods to solve the oil-water flow with fines migration in radial flow system where the initial conditions of fines concentrations along the porous medium is non-uniform. In addition, flow modeling of low-salinity waterflooding in radial flow system in both single-layered homogeneous and two-layered heterogeneous reservoirs will also be discussed. Followed by, as reference scenarios, the analytical solutions of fines migration in both single-phase and two-phase flow are extended to cases with the effects of nanoparticles utilization.

1.2 Introduction to Nanofluids Application in Petroleum Industry

Recently, nanotechnology has been widely reported in diverse potential applications in the oil and gas industry, including formation damage mitigation, assisted surfactant/alkaline/low salinity/gas flooding, functional nanoparticles used as tracers or sensors to detect certain reservoir rock and fluid properties, and fracturing fluid additives in unconventional reservoirs etc. The types of nanoparticles mainly include Al_2O_3, MgO, ZrO_2, CeO_2, TiO_2, ZnO and Fe_2O_3. Nanofluids can exhibit unique electrical, magnetic, and chemical properties. Achinta et al (2016) reviewed the applications of nanoparticles and nano-dispersion in the upstream of oil industry, including oilfield exploration, reservoir characterization, drilling and completion, and enhanced oil recovery etc.

Song et al (2007) proposed hyperpolarized silicon nanoparticles to be applied to take images of hydrocarbon reserves. Nano-sensor and nano-identification techniques have

been proposed to identify the physical and chemical properties, fluid flow type, rock mechanical characteristics (Kapusta et al. 2011; Abousleiman et al. 2009; Berlin et al. 2011; Jahagirdar et al. 2008). The designed nanoparticles can also have been used in drilling or completion fluids for clay stabilization (McDonald et al. 2012), fluid loss control (Contreras et al. 2014), viscosity alternation (Gurluk et al. 2013), wellbore stability (Zhang et al. 2015), drag and torque friction (Sharma et al. 2012), cementation additives (Santra et al. 2012; Pang et al. 2014; Van et al. 2010) and fracturing fluid purposes (Huang et al. 2008b). In addition, nanotechnology has been extensively applied into enhanced oil recovery related to wettability alteration (Li et al. 2013 and 2014; Crews et al. 2012; Bera et al. 2015), IFT reduction (Moghadam et al. 2014), enhanced adsorption of injected chemicals (Esmaeilzadeh et al. 2011), enhanced stability of emulsion and foam stability (Yu et al. 2012; Aminzadeh et al. 2012; Adkins et al. 2007; Gonzenbach et al. 2007; Prigiobbe et al. 2016), channels plugging and emulsification (Ju et al. 2006 and 2009; Ogolo et al. 2012; El-Diasty et al. 2015).

In past decades, the mechanisms of nanofluid or nano-dispersion stability, transport, adsorption, and desorption have been studied by means of limited numbers of lab experiments. The inherent higher adsorption tendency, and finely tuned structures of nanofluids make them excellent candidate for specific purposes. However, under certain conditions, aggregations of nanoparticles could be also adsorbed and plugged into pore-throats, resulting in permeability impairment (Kartic et al., 1999; Zhang et al. 2013; Yuan et al. 2017; Li et al. 2015a). Numbers of laboratory experiments have demonstrated that the equilibrium adsorption of silica nanoparticles on sandstone, limestone, and dolomite are different (Yu et al. 2012; Huang et al. 2015). The higher concentration of injected

nanofluids would block the pore-throats and result in permeability impairment and wettability alteration (Wang et al. 2016; Li et al., 2015a, b). One of the objectives of this study is to better understand nanofluid transport phenomenon and their effects on permeability impairment using both existing lab experiments and mathematical modelling works.

The application of nanoparticles to control fines migration has been previously investigated (Ahmadi et al. 2011; Assef et al. 2014; Yuan et al. 2016c). Nanoparticles with extremely high surface areas of approximately 200m^3/g are suitable to help fixating mobile fines by altering the surface potential of fines particles or rock grains. As results, the double-layer repulsive forces between fine particles and rock can be reduced effectively (Huang et al. 2008a; Ju et al. 2006). Both mathematical modellings and lab experiments have demonstrated that only a very small concentration of nanoparticles coated with fracture proppants can greatly help prevent fines migration and subsequent formation damage (Huang et al. 2010; Yuan et al. 2015a, b and 2016b). The successful applications of silica nanoparticles to mitigate fines migration in sand packs saturated with nC60 have been reported under the high-salinity conditions (Cheng et al. 2005; Ju et al. 2009; Yu et al. 2012). When it comes to the interaction model between nanoparticles and fine particles, Yuan (2015b, 2016b) presented analytical nanoparticle/fines particles flow modeling in residual-oil condition and confirmed the positive effects of nanoparticles treatment (pre-flush or co-injection) on controlling fines migration control. In addition, during low-salinity waterflooding, the mitigation of fines migration by using nanoparticles to both maintain well injectivity and enhance oil recovery has also been reported by Yuan et al. (2016c). Yuan et al. (2016a and d) also evaluated the mobility-

control performance of LSW taking fines migration into consideration through modifying the fractional flow function, and optimized the nanofluid-slug size to improve well injectivity during low-salinity waterflooding.

As described above, many laboratory experiments and phenomenon observations have been provided serving as proof of concept for nanofluid application to control fines migration, however, the evaluation of nanoparticles adsorption and detachment have yet to be addressed. Therefore, this study will introduce a comprehensive study of nanoparticles adsorption/detachment behaviors, which can provide an essential foundation for the numerous benefits of nanoparticles. Another objective of this study is to develop analytical solutions characterizing the effects of nanoparticles utilizations on fines migration control and performance of enhanced oil recovery.

1.3 Objective and Outline

The aims of this dissertation include, 1) deepen the understandings on the problems of fines migration in both single-phase and oil-water two-phase flow; 2) evaluate the pros and cons of fines migration on the performance of low-salinity waterflooding in terms of both well injectivity and oil recovery; 3) quantify the various behaviors of nanoparticles transport in porous medium and their impacts on formation damage; 4) develop a theoretical structure to evaluate the success of nanoparticles to control fines migration along both 1-D permeable medium and radial flow system; 5) extend the mathematical foundation toward confirm the improved performance (both EOR and well injectivity by combining nanofluid with low-salinity waterflood in single-layered and multi-layered heterogeneous reservoirs.

In Chapter 2, the mechanical equilibrium of particles and maximum retention concentration model will be extended to study nanoparticles transport. This chapter will present an integrated approach to study the permeability alteration resulting from nanofluids flow through porous media. Hydrophilic Nano-structure particles (NSP) are dispersed in the injected brine stream into oil-wet Berea sandstones at 0.05, 0.2 and 0.5wt% concentrations. Both the pressure drops across the whole cores and the effluent nanoparticles concentrations are monitored. To quantify the nanoparticles adsorption/detachment and straining behavior and their associated effects on formation permeability, mechanistic models are delivered to interpret lab experiments. The interplay between nanoparticles and rocks is described by the classical particles filtration theory coupled with the maximum nanoparticles adsorption concentration model. Series of parameters to describe the transport and capture of nanoparticles are characterized, including the maximum nanoparticles adsorption concentrations, reversible or detachment adsorption concentrations, nanoparticles adsorption rates and straining rates, and the corresponding formation damage coefficients.

In Chapter 3, an application of method of characteristics (MOC) is used to evaluate the effectiveness of nanoparticles to mitigate fines migration in porous media. The positive contribution of nanoparticles to mitigate fines migration is characterized by the increase of maximum retention concentration of fine particles on rock grains through two chemical reactions: (1) adsorption of nanoparticles onto the fines/grain surface to alter surface potential; and (2) increased retention of fines attachment onto the pore surfaces via reducing the surface potential between grains and fines.

Semi-analytical MOC solutions are developed for two different scenarios of nanoparticles utilization to control fines migration: (1) co-injection of nanoparticles with fines suspension into one-dimensional permeable medium and (2) pre-coating porous medium with nanoparticles prior to fines injection to evaluate the enhanced capability of porous medium to capture unsettled fines. Mitigation index (MI) is introduced as a new parameter to evaluate the success of nanoparticles to control fines migration. In addition, this chapter also optimizes nanoparticles treatment (nanoparticles concentration and the required amounts of nanoparticles) to control fines migration. Through quantitative comparison of effluent concentration history and pressure drop, the accuracy of analytical solution is verified by both numerical simulations and experimental results for different scenarios of nanoparticles application.

In Chapter 4, as an extension of modeling works of co-injection nanoparticle and fine particles in single-phase water flow, this chapter will derive analytical solutions of nanoparticles-fine particles transport in two-phase (oil and water) flow accounting for the mutual reactions among fines, nanoparticles, and rock grains. Both the performance of formation damage mitigation and enhanced oil recovery caused by fines migration and nanoparticles effects are evaluated. Two different scenarios of nanoparticles utilization to control fines migration in radial flow are discussed, including 1) co-injection of nanoparticle-fine particles mixture into 1-D permeable medium that initially oversaturated with fine particles and 2) pre-coating nanoparticles in radial flow system with nanoparticles prior to fines injection. The splitting method is implemented to separate the 3×3 system into a combination of 2×2 auxiliary system containing only particles components (nanoparticles & fines) and one lifting equation with phase

saturation, in the transformed plane of distance and stream-function. After the analytical solutions of auxiliary system and lifting equation are obtained, an inverse transformation will be applied to obtain the solutions of nanoparticles-fines transport in oil & water two -phase flow.

The different performance of nanoparticles to reduce fines migration in two-phase flow is compared with that in single-phase water flow. The profiles of phase saturation, suspended nanoparticles, and fines, attached fines and nanoparticles adsorption along 1-D porous medium are also compared for the cases of low-salinity waterflooding with and without nanoparticles utilization. The series of analytical solutions are verified by finite-difference numerical solutions. In radial flow system, in view of the differences of released fines concentration caused by different flowing velocity at different locations, an analytical solution in two-phase flow is derived for nanoparticles utilization to control fines migration. The optimal radius of nanofluid pre-treatment is obtained to maximize the efficiency of nanoparticles treatment.

In Chapter 5, in radial flow through single-layer homogenous system, analytical solution is derived to confirm the feasibility of nanoparticle application to reduce fines migration, and quantify the improvement of the displacement performance of low-salinity waterflooding with nanoparticles nanofluid-slug pre-flush application. The maximum retention concentration of fine particles is extended in two-phase flow. The interplay among nanoparticles, fines, and rocks is described by a physical-chemical reaction model. A new formulation for fraction flow function considering fines migration in water-phase is introduced. The semi-analytical solutions of low-salinity waterflooding without/with

fines migration and nanofluid pre-treatment are compared. The analytical solutions are verified by numerical simulations.

In addition, in multi-layer heterogeneous reservoirs, an application of nanofluid-slug pre-flush is also introduced to maintain well injectivity and improve the sweep efficiency by fines migration-assisted mobility control during low-salinity waterflooding. An axisymmetric radial flow model and fraction flow analysis are applied to interpret the performance of both nanofluid-slug and low-salinity waterflooding in a multi-layered heterogeneous flow system. The improvement of mobility control is characterized as the ratio of displacement fronts' advancing velocity along each layer. The improved well injectivity by nanofluid pre-flush is characterized as an explicit formulation of well injectivity index. A graphic workflow is also presented to optimize nanofluid treatment and injected water salinity for combining nanofluid with low-salinity water under arbitrary initial and injection conditions. The analytical solution is verified by numerical simulations.

Finally, Chapter 6 provides a summary of this dissertation's findings and conclusions.

Chapter 2: Nanoparticles Adsorption, Straining and Detachment Behavior: Mechanistic Modeling and Experimental Work

A comprehensive study on nanoparticles adsorption/detachment behavior is essential to provide a foundation to illustrate the numerous benefits of nanoparticles applications. In view that hydrophilic nanoparticles are widely preferable for the alteration of rock wettability from oil-wet toward water-wet and enhanced oil recovery, it is of great interest to study the hydrophilic nanofluid transport phenomenon with dynamic particles adsorption/detachment behaviors, and its negative effects on the permeability of oil-wet cores during waterflooding. Li et al. (2015a) carried the experimental works of hydrophilic silica nanoparticles and studied their effects on core permeability. The hydrophilic silica Nano-structure Particles (NSP) (particles sized in nanoscale) are chosen because they consist of more than 90% silicon oxide, which is the main constituent of sandstone reservoirs; hence, they refrain from negatively effecting the environment (Hendraningrat et al. 2012 and 2015). NSP has average particles sizes of 7 nm, and specific area of $300 m^2/g$, but they can aggregate to form particles which might be bigger than 100nm under certain conditions. In this chapter, the effluent nanoparticles concentrations and pressure drop across the cores recorded for the core flooding works of Li et al. (2015a) are used to estimate nanoparticles adsorption and retention behavior, as well as nanoparticles detachment behaviors during brine post-flush.

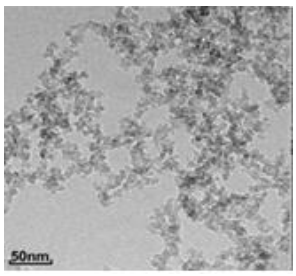
The aim of this chapter is to better understand nanofluid effects on permeability impairment using both lab experiments and mathematical modeling works. To quantify hydrophilic nanoparticles adsorption, straining and detachment behaviors, and associated formation damage effects, analytical solutions are derived using method of characteristics (MOC). This chapter also provides great insight on the importance of optimal

nanoparticles treatment design (e.g., different injection concentration of nanoparticles) by considering both the excessive loss of nanofluids and their induced formation damage.

2.1 Nanoparticles and Experimental Methods

This section first reviews the experimental works carried by Li et al. (2015a, b). In this experimental work, the materials used to conduct the experiments include, Nano-structure Particles (NSP), Berea sandstone, and NaCl diluted with 3wt% to the desired concentration. The Berea sandstone, with 8cm in length and 3.83cm in diameter, is used as core samples. The core permeability before and after nanofluid injection is evaluated by the records of pressure drop along 1-D core using Darcy-flow model, respectively, hydrophilic silica Nano-Structure Particles (NSP) are dispersed in different concentrations. The diameters of these nanoparticles are in order of nanometers. The Transmission Electron Microscope (TEM) images of NSP are shown in Table 2.1.

Table 2-1 Properties of Nano-Structure Particles, Li et al. (2015 a, b)

Type of Nanoparticles	Particle Size, nm	Surface areas, m^2/g	TEM images	Nanofluid
Nano-Structure Particles (NSP)	7	300		

	Density, g/cm^3	Viscosity, cP
NaCl Brine, 3 wt. %	1.022	1.0026
NSP fluid 0.05 wt. %	1.021	1.0858
NSP fluid 0.2 wt. %	1.022	1.1550
NSP fluid 0.5 wt. %	1.022	1.5627

Prior to core flooding experiments, the core plugs are saturated with 3wt% NaCl brine using a vacuum pump to ensure no trapped air left inside the cores. The hydrophilic silica Nano-Structure Particles (NSP) dispersion is diluted as three different concentrations (0.05 wt. %, 0.2 wt. % and 0.5 wt. %) into 3wt% NaCl solutions. The density and viscosity of nanofluids at different concentrations are also measured, as shown in Table 2.1. The experimental process is started with the core plug being exposed to sets of experiments conducted under confining pressures, up to 20 bars. The flow rates in series of experiments are kept constant as 2 ml/min. At the beginning, 1 PV (about 16ml) of brine is injected to establish a base permeability under initial condition. Then, a slug of 4 PV Nanofluid (NSP nanoparticles) is injected into the core plug. After, a continuous 20 PV injection of brine is used as post-flush to ensure the desorption of nanoparticles occurs. The differential pressure across the core plug is continuously recorded by a data gathering system. The effluent history of nanoparticles concentrations is measured in use of UV Spectrophometer, after collecting the effluent fluid sample every 1/4 PV. The detailed schematic of flooding setup has been described by Li et al. (2015a, b).

2.2 Mechanistic Nanoparticles Transport and Adsorption Model

During the nanoparticles flow in porous medium, nanoparticles would be adsorbed and strained at the stagnant points on the pore-throat surfaces, which can be identified by the reduction of effluent nanoparticles concentration from the injection conditions (Zhang et al. 2013; Li et al. 2015). Nanoparticles with lower surface zeta potential can be adsorbed on the surfaces of fine particles/rock grains including both reversible and irreversible adsorption (Yuan et al. 2017; Zhang et al. 2013). Meanwhile, particles collisions also occur when nanofluids flow through the pore-throats. Consequently,

nanoparticles can be blocked or plugged into the entrances of pore-throats. In this chapter, the various behaviors of nanoparticles are coupled into analytical solutions, including nanoparticles adsorption, straining, and detachment. Some commonly used assumptions are listed as follows: (1) The porous medium (core plug or sand pack) is one-dimensional (1D), uniform and homogeneous by ignoring heterogeneity, and the local thermodynamic equilibrium assumption applies; (2) Two-components exist (water, nanoparticles) and two-phase (one flowing and one stagnant) isothermal flow takes place; (3) Adsorption of nanoparticles are described using both the classic particles filtration theory and the maximum adsorption concentration model; (4) Flow velocity sufficiently large to neglect the particles dispersion effects.

2.2.1 Particle Equilibrium and Maximum Retention Concentration

Firstly, the concept of maximum retention concentration of particles is introduced for nanoparticles or fine particles flow inside bundles of capillary tubes. The forces acting on a single particle located on rock grain surfaces (pore walls) consist of: the drag force F_d from viscous water flow, the electrostatic force F_e, the lifting force F_l, and the buoyancy F_g, (Figure 2.1). In cases of tertiary flooding (no mobile oil phase), water saturation is equal to one minus residual oil saturation, 1-S_{or}; hence, this problem of single-phase flow can be modeled by changing permeability $k_{intrinsic}$ to ($k_{intrinsic}\, k_{rwor}$) and porosity ϕ to [ϕ(1-S_{or})].

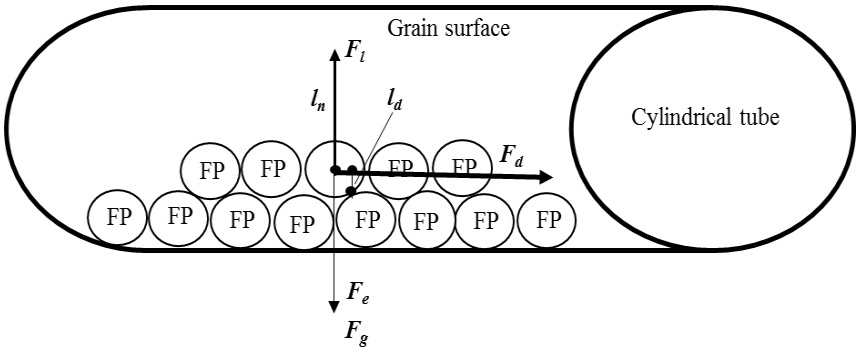


Figure 2.1 Forces and momentum vectors exerted on a single particle

The forces can be expressed as:

Drag force: $F_d = \dfrac{\omega\pi\mu r_{Particle}{}^2 U}{2\phi(1-S_{or})(r_P - r_C)}$ ……..…..……..... (2.1)

Electrostatic force: $F_e = -\dfrac{\partial V_{FP}}{\partial h}$ ……..…….……. (2.2)

Lifting force: $F_l = \chi r_{Particle}{}^3 \sqrt{\dfrac{\rho\mu U^3}{8[\phi(1-S_{or})]^3 (r_P - r_C)^3}}$ ……..…….....…….... (2.3)

Buoyancy force: $F_g = 4/3\pi r_{Particle}{}^3 \Delta\rho$ ……..……..……..... (2.4)

Here, ω *is* dimensionless drag force coefficient varying in the range of 10~60; μ *is* fluid viscosity, Pa.s; $r_{Particle}$ is the radius of the fine particle or nanoparticles, m; r_c is the thickness of the deposit cake, m; r_p is the pore radius, m; U is the fluid flow velocity, m/s; χ is the lifting force coefficient; ρ *is* fluid density, kg/m^3; $\Delta\rho$ is the difference between the density of particles and fluid, kg/m^3.

Then, in terms of electrostatic force, the total energy, V_{FP}, between particles and the grain surface is the sum of London–van-der-Waals V_{LVA}, double electric layer repulsive energy V_{DLR} and Born energy V_{BR}, described by the DLVO (Derjagin–Landau–Verwey–Overbeek) theory (Israelachvili, 2011).

$$V_{FP} = V_{LVA} + V_{DLR} + V_{BR} \quad \text{(2.5)}$$

$$V_{LVA} = -\frac{A_{123} r_{Particle}}{6h}[1 - \frac{5.32h}{l}\ln(1 + \frac{l}{5.32h})] \quad \text{(2.6)}$$

$$V_{DLR} = \frac{128\pi r_{Particle} n_{\infty} k_B T}{\kappa^2} \varsigma_{Particle} \varsigma_{GS} e^{-\kappa h} \quad \text{(2.7)}$$

$$V_{BR} = \frac{A_{123} d^6}{7560}[\frac{8r_{Particle} + h}{(2r_{Particle} + h)^7} + \frac{6r_{Particle} - h}{h^7}] \quad \text{(2.8)}$$

where A_{132} is the Hamaker constant; h is the surface-to-surface separation length, m, h<<r_{FP}; l is the characteristic wave length of interaction, 100 nm; n_{∞} is the bulk number density of ions, 6.022×10^{25} number/m^3; k_B *is* the Boltzmann's constant, 1.381×10^{-21} J/K; T is the absolute temperature of the reservoir, K; $\varsigma_{Particle}, \varsigma_{GS}$ are the Zeta potentials for the fine particle surface, nanoparticle surface, and grain surface, mV; d is the atomic collision diameter in Lennard-Jones potential of 0.5 nm;

The one-dimensional porous medium is considered as bundles of parallel cylindrical tubes/pores. Porosity and permeability can be expressed using pore size, $2r_p$, and the number of pores per unit area, n (Dullien, 2012).

$$\phi = n\pi r_P^2 \quad \text{(2.9)}$$

$$k_0 = n\frac{\pi r_P^4}{8} \quad \text{(2.10)}$$

The drag force and lifting force make the particles prone to dislodge from pore surfaces, however, the electrostatic force and buoyancy force bring positive contributions on particles attachment. The particle mechanical equilibrium is achieved by equating torques for attachment forces (electrostatic force and buoyance force) and detachment forces (drag force and lifting force):

$$\overbrace{F_e l_n + F_g l_n}^{Attachment} = \overbrace{F_d l_d + F_l l_n}^{Detachment} = \sqrt{3} l_n F_d + F_l l_n \quad \text{(2.11)}$$

$$F_n = F_e + \frac{4\pi r_{FP}^{\ 3}}{3}\Delta\rho g - \chi r_{FP}^{\ 3}\sqrt{\frac{\rho\mu U^3}{8[\phi(1-S_{or})]^3(r_P - r_C)^3}} = \sqrt{3}F_d = \sqrt{3}\frac{\omega\pi\mu r_{Particle}^{\ 2} U}{2\phi(1-S_{or})(r_P - r_c)} \quad \text{(2.12)}$$

Therefore, defining the ratio between the drag (representing effects of flow velocity) and electrostatic force (representing the surface properties of particles) as:

$$y = \frac{\omega\pi\mu r_{Particle}^{\ 2} U}{2\phi(1-S_{or})(r_P - r_C)F_e} \quad \text{(2.13)}$$

where y is the ratio between drag and electrostatic force. Furthermore, the ratio between cake thickness and pore size could be expressed as:

$$r_C / r_P = 1 - \frac{\mu r_{Particle}^{\ 2} U}{2\phi(1-S_{or})r_P F_e y} \quad \text{(2.14)}$$

Substituting Eq. 2.13 into Eq. 2.12:

$$1 + \frac{4\pi r_{Particle}^{\ 3}}{3F_e}\Delta\rho g - \frac{\chi}{\mu}\sqrt{\frac{\rho F_e}{\omega^3\pi^3}}y^{3/2} - \sqrt{3}y = 0 \quad \text{(2.15)}$$

This equation can be solved numerically to obtain y, independent on flow velocity.

$$y = f\left(\frac{\chi}{\mu}\sqrt{\frac{\rho F_e}{\omega^3\pi^3}},\ \frac{4\pi r_{Particle}^{\ 3}}{3F_e}\Delta\rho g\right) \quad \text{(2.16)}$$

For individual cylindrical shaped pores, the maximum retention concentration of fines on rock grains is expressed as the internal retention cake thickness, r_c:

$$\sigma_{cr}(U) = \left[r_P^{\ 2} - (r_P - r_C)^2\right](1-\phi_c)n \quad \text{(2.17)}$$

$$\sigma_{cr}(U) = \left[1 - \left(\frac{\mu r_{Particle}^{\ 2} U}{2\phi(1-S_{or})r_P F_e y}\right)^2\right]\phi(1-\phi_c)(1-S_{or}) \quad \text{(2.18)}$$

where, σ_{cr} is the maximum retention concentration of fine particles; ϕ_c is the percentage of internal cake thickness (package of fine particles), about 0.10.

The relationship between the capacity of rock grains retaining particles and flow velocity is shown in Figure 2.2. The higher is the flow velocity, the higher are the lifting force and drag force, and consequently, the lower is the maximum (critical) retention concentration of fines. As noted by Bedrikovetsky (2011), the relationship between the maximum retention concentration of particles and flow velocity corresponds to the power law. The results of Eq. 2.18 also indicate the same conclusion. In addition, Gruebeck and Collins (1982) performed suspension injection with particles with 5~10μm in diameters into a packed column of unconsolidated sands with grain varying 250-297μm in diameter (Gruesbeck, 1982). In Figure 2.2, the two points are the experimental results with different flow velocities in Gruebeck and Collins's experiments. There is acceptable agreement between the results of Eq. 2.18 and previous experimental results; thus, which confirms the accuracy of the maximum retention concentration model of particles.

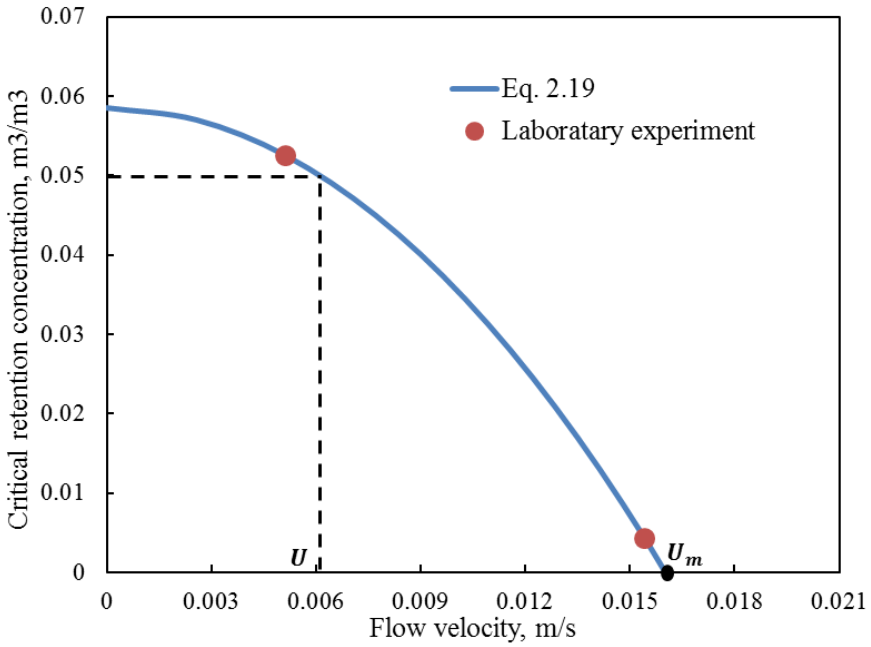


Figure 2.2 The maximum (critical) retention concentration of fine particles on rock grains decreases with the increase of flow velocity.

2.2.2 Nanoparticles Transport Model with Adsorption and Straining

Here, introducing dimensionless length and time:

$$x_D = \frac{x}{L}, \quad t_D = \frac{q_{inj} t}{\phi A L} \qquad \text{(2.19)}$$

where x_D is the dimensionless distance; t_D is the dimensionless time; L is the length of 1-D porous media.

The mass-balance equation of nanoparticles flowing through the permeable medium, considering their deposition and straining on rock grains can be written as,

$$\frac{\partial C_{NP}}{\partial x_D} + \frac{\partial C_{NP}}{\partial t_D} + \frac{1}{\phi}\frac{\partial \sigma_{NP}}{\partial t_D} + \frac{1}{\phi}\frac{\partial S_{NP}}{\partial t_D} = 0 \qquad \text{(2.20)}$$

Nanoparticles straining and adsorption rates can be expressed by the particles filtrat ion kinetics (Guedes et al. 2006; Massoudieh et al. 2010),

$$\frac{\partial S_{NP}}{\partial t_D} = \lambda_s C_{NP} \phi L, \quad \frac{\partial \sigma_{NP}}{\partial t_D} = \lambda_{\text{ad}} C_{NP} \phi L \quad \text{..... (2.21)}$$

$$\text{when, } \sigma_{NP} < \sigma_{NP,\max}, \sigma_{NP,\max 1} = \left[1 - (\frac{\mu r_{NP}^2 U}{2\phi r_P F_{e,\max} y})^2 \right] \phi (1 - S_{or}).$$

Before that nanoparticles adsorption reaches the maximum limits, the classic particles capture kinetics are applied to quantify the attachment rates of nanoparticles (Vafai 2005). λ_{ad} and λ_s are filtration coefficients for nanoparticles adsorption and straining, respectively. Usually, they are assumed as constants.

Initially, there are no nanoparticles suspended in pores, and the injected nanoparticles concentrations are kept as constant, hence, the initial and boundary conditions are described as below:

$$\begin{cases} C_{NP}(x_D, 0) = 0 \\ \sigma_{NP}(x_D, 0) = 0 \\ S_{NP}(x_D, 0) = 0 \\ C_{NP}(0, t_D) = C_{NP,inject} = C_0 \\ \sigma_{NP}(0,\ t_D) = \lambda_{ad} \phi L C_0 t_D \\ S_{NP}(0,\ t_D) = \lambda_s \phi L C_0 t_D \end{cases} \quad \text{..... (2.22)}$$

During the post-flush of brine, the previously absorbed nanoparticles might detach from the pore surfaces due to the changes of flowing fluid properties. Inferred from the maximum retention concentration of nanoparticles, it is assumed that the changes of drag-electrostatic force ratio lead to detachment of absorbed nanoparticles, as follows:

$$\sigma_{NP,\max}(U) = \left[1 - (\frac{\mu r_{NP}^2 U}{2\phi r_P F_e y})^2 \right] \phi \quad \text{..... (2.23)}$$

$$y = f(\frac{\chi \sqrt{\rho F_e}}{\mu},\ \frac{4\pi r_{NP}^{\ 3}}{3F_e} \Delta \rho g) \quad \text{..... (2.24)}$$

In the experimental work, there are no changes on the injected fluid salinity, it can be derived that the changes of drag-electrostatic force ratio (Eq. 2.24) are not be attributed to the alteration of salinity, but only to the decrease of average fluid density caused by changes of nanofluid concentration. The average fluid density is expressed as a weighted average between nanoparticles and carrier water density:

$$\rho = \rho_w \left(1 - C_{NP}\right) + \rho_{NP} C_{NP} = \rho_w + C_{NP}\left(\rho_{NP} - \rho_w\right) \text{..... (2.25)}$$

Hence, the maximum retention concentration of nanoparticles becomes a function of injected nanoparticles concentration. The detachment of nanoparticles occurs instantly along with the abrupt changes of flowing nanoparticles concentration. Thus, the mass-balance equation of nanoparticles during the post-flush of brine could be expressed, as follows:

$$\frac{\partial C_{NP}}{\partial x_D} + \left(1 + \frac{1}{\phi}\frac{\sigma_{NP,\max 1} - \sigma_{NP,\max 2}}{C_{NP}}\right)\frac{\partial C_{NP}}{\partial t_D} = 0 \text{..... (2.26)}$$

Before the post-flush of brine, there are already amounts of absorbed nanoparticles on surfaces of pores, and hence, the initial conditions for the post-flush process are:

$$C_{NP}(0, t_D) = 0; \quad \sigma_{NP}\left(0,\ t_D\right) = \sigma_{NP,\max 2} \text{..... (2.27)}$$

Where, $\sigma_{NP,\max 1}$ is the maximum retention concentration of nanoparticles at the phase of nanoparticles injection, and $\sigma_{NP,\max 2}$ is the maximum retention concentration of nanoparticles at the phase of post-flush.

2.2.3 Method of Characteristic (MOC) Solutions

The MOC (Courant, 1962) is a robust analytical approach to address first-order, strictly hyperbolic PDEs. The goal of MOC is to convert the original PDEs into a set of ODEs along the characteristics. The MOC solution is presented as the form of waves

along which specific values of dependent variables (concentration, in this paper) carried through a time/distance domain (Moghanloo, 2010, 2012b, 2014 and 2015).

Substituting the particles capture kinetics equation Eq. 2.21 into mass-balance equation Eq. 2.20, yields:

Suspended Nanoparticles: $\frac{\partial C_{NP}}{\partial x_D}+\frac{\partial C_{NP}}{\partial t_D}+\left(\lambda_{\text{ad}}+\lambda_{\text{s}}\right)C_{NP}L=0$ …..... (2.28)

Nanoparticles Adsorption: $\frac{\partial \sigma_{NP}}{\partial x_D}+\frac{\partial \sigma_{NP}}{\partial t_D}+\left(\lambda_{\text{ad}}+\lambda_{\text{s}}\right)\sigma_{NP}L=0$ ……..... (2.29)

Nanoparticles Straining: $\frac{\partial S_{NP}}{\partial x_D}+\frac{\partial S_{NP}}{\partial t_D}+\left(\lambda_{ad}+\lambda_{s}\right)S_{NP}L=0$ …..... (2.30)

Appling the approach of MOC, the following ordinary differential equations can be obtained, along characteristic line $\frac{dx_D}{dt_D}=1$:

$$\frac{dC_{NP}}{dt_D}=-\left(\lambda_{\text{ad}}+\lambda_{\text{s}}\right)C_{NP}L,\quad \frac{d\sigma_{NP}}{dt_D}=-\left(\lambda_{\text{ad}}+\lambda_{\text{s}}\right)L\sigma_{NP},\quad \frac{dS_{NP}}{dt_D}=-\left(\lambda_{\text{ad}}+\lambda_{\text{s}}\right)LS_{NP} \quad \text{.. (2.31)}$$

Figure 2.3 shows the distance-time diagram in which different lines represent the propagation path of different nanofluid concentration waves along the 1-D porous media.

The features of nanoparticles transport in different flow zones are summarized as,

Zone I: Initial conditions without nanoparticles ahead of concentration front;

Zone II: flow of nanoparticles at the presence of particles attachment and straining;

Zone III: Ahead of erosion front, flow with nanoparticles straining and attachment;

Zone IV: Behind of erosion front, flow with only nanoparticle straining in over-saturated of nanoparticles attachment zone.

Zone V: The detachment of reversible nanoparticles adsorption during the post-flush of brine without nanoparticles.

Combining with the boundary conditions, Eq. 2.22, the solutions of suspended nanoparticles and retained nanoparticles concentration are determined in Zone I and Zone II, when $0 < t_D < t_{Dc}$. Time t_{Dc} is the moment when the retained nanoparticles concentration onto rock grains at the inlet reaches the maximum value, $\sigma_{NP,\max 1}$:

$$t_{Dc} = \frac{\sigma_{NP,\max 1}}{\lambda_{ad}\phi L(1-S_{or})C_0} \quad \text{..... (2.32)}$$

$$(x_D > t_D),\ \text{Zone I:}\ \begin{cases} C_{NP}(x_D,t_D) = 0 \\ \sigma_{NP}(x_D,t_D) = 0 \\ S_{NP}(x_D,t_D) = 0 \end{cases} \quad \text{..... (2.33)}$$

$$(x_D < t_D),\ \text{Zone II:}\ \begin{cases} C_{NP}(x_D,t_D) = C_0 \exp\left(-\left(\lambda_{\text{ad}} + \lambda_s\right) L x_D\right) \\ \sigma_{NP}(x_D,t_D) = \left[\lambda_{\text{ad}}\phi L C_0 \left(t_D - x_D\right)\right] \exp\left(-\left(\lambda_{\text{ad}} + \lambda_s\right) L x_D\right) \\ S_{NP}(x_D,t_D) = \left[\lambda_s \phi L C_0 \left(t_D - x_D\right)\right] \exp\left(-\left(\lambda_{\text{ad}} + \lambda_s\right) L x_D\right) \end{cases} \quad \text{..... (2.34)}$$

As the distance-time diagram, or motion of particles concentration fronts in the plane of x_D-t_D shown in Figure 2.3, there is an "attached front". Ahead of this front, flow of nanoparticles with attachment and straining occurs, and behind of this front, there is no further room for retained nanoparticles.

At $t_D = t_{Dc}$, the suspended, attached and strained fines concentration are:

$$C_{NP}(x_D,t_D) = C_0 \exp\left(-\left(\lambda_{\text{ad}} + \lambda_s\right) L x_D\right) \quad \text{..... (2.35a)}$$

$$\sigma_{NP}(x_D,t_D) = \sigma_{NP,\max 1} \exp\left(-\left(\lambda_{\text{ad}} + \lambda_s\right) L x_D\right) \quad \text{..... (2.35b)}$$

$$S_{NP}(x_D,t_D) = \frac{\lambda_s}{\lambda_{\text{ad}}} \sigma_{NP,\max 1} \exp\left(-\left(\lambda_{\text{ad}} + \lambda_s\right) L x_D\right) \quad \text{..... (2.35c)}$$

Based on the continuity condition around the "attached front," $C^+ = C^- = C_0$, the following differential equations can be derived:

$$\frac{\partial \sigma_{NP}}{\partial x_D} + \frac{\partial \sigma_{NP}}{\partial t_D} + \left(\lambda_{\text{ad}} + \lambda_s\right)\sigma_{NP,\max_1} L = 0 \quad \text{..... (2.36)}$$

Substituting nanoparticles attachment kinetics Eq. 2.21 into Eq. 2.36 yields in,

$$\frac{\partial \sigma_{NP}}{\partial x_D} = -\lambda_{ad}\phi L C_0 - L\left(\lambda_{ad} + \lambda_s\right)\sigma_{\text{NP,max1}} \quad \text{..... (2.37)}$$

Along the nanoparticles attachment front, the attached nanoparticle concentration is equal to the maximum retention value. Taking the ordinary derivative in x_D leads to,

$$\frac{dt_D}{dx_{cr}}\frac{\partial \sigma_{NP}}{\partial t_D} + \frac{\partial \sigma_{NP}}{\partial x_D} = \frac{\partial \sigma_{\max}}{\partial x_D} \quad \text{..... (2.38)}$$

Substituting Eq. 2.37 and Eq. 2.21 into Eq. 2.38 yields in,

$$\frac{dx_{cr}}{dt_D} = \frac{\lambda_{ad}\phi L C_0}{\lambda_{ad}\phi L C_0 + L\left(\lambda_{ad} + \lambda_s\right)\sigma_{\text{NP,max1}}} = const. \quad \text{..... (2.39)}$$

The moving trajectory of nanoparticles "attached front" can be represented by:

$$x_{cr} = \frac{\lambda_{ad}\phi L C_0}{\lambda_{ad}\phi L C_0 + L\left(\lambda_{ad} + \lambda_s\right)\sigma_{NP,\max 1}}\left(t_D - \frac{\sigma_{NP,\max 1}}{\lambda_{ad}\phi L C_0}\right) \quad \text{..... (2.40a)}$$

$$t_{cr} = \frac{\lambda_{ad}\phi L C_0 + L\left(\lambda_{ad} + \lambda_s\right)\sigma_{NP,\max 1}}{\lambda_{ad}\phi L C_0} x_{cr} + \frac{\sigma_{NP,\max 1}}{\lambda_{ad}\phi L C_0} \quad \text{..... (2.40b)}$$

Because the slopes of characteristic lines in Zone III are in unity, the lines which start from any intersection points at the "attachment front" can be obtained by:

$$\text{Line III: } x_D - x_{cr} = t_D - t_{cr} \quad \text{..... (2.41)}$$

According to Eq. 2.40 and Eq. 2.41, the start points on the "attachment front" at Zone III is given by,

$$x_{cr0} = \left(t_D - x_D\right)\frac{\lambda_{ad}\phi C_0}{\left(\lambda_{ad}+\lambda_s\right)\sigma_{NP,\max 1}} - \frac{1}{\left(\lambda_{ad}+\lambda_s\right)L} \quad \text{..... (2.42)}$$

$$t_{cr0} = \left(t_D - x_D\right)\left(\frac{\lambda_{ad}\phi C_0 + \left(\lambda_{ad}+\lambda_s\right)\sigma_{NP,\max 1}}{\left(\lambda_{ad}+\lambda_s\right)\sigma_{NP,\max 1}}\right) - \frac{1}{\left(\lambda_{ad}+\lambda_s\right)L} \quad \text{..... (2.43)}$$

The retained and suspended nanoparticles concentration at Zone III and Zone IV are given as:

$$\sigma_{NP} = \sigma_{NP,\max 1}\exp\left(-\left(\lambda_{ad}+\lambda_s\right)L\left(x_D - \left(t_D - x_D\right)\frac{\lambda_{ad}\phi C_0}{\left(\lambda_{ad}+\lambda_s\right)\sigma_{NP,\max 1}} + \frac{1}{\left(\lambda_{ad}+\lambda_s\right)L}\right)\right). \quad \text{(2.44a)}$$

$$C_{NP} = C_0\exp\left(-\left(\lambda_{ad}+\lambda_s\right)L\left(x_D - \left(t_D - x_D\right)\frac{\lambda_{ad}\phi C_0}{\left(\lambda_{ad}+\lambda_s\right)\sigma_{NP,\max 1}} + \frac{1}{\left(\lambda_{ad}+\lambda_s\right)L}\right)\right) \quad \text{...(2.44b)}$$

$$S_{NP} = \lambda_s C_0\phi L\left(t_D - x_D\right)\exp\left(-\left(\lambda_{ad}+\lambda_s\right)Lx_D\right) \quad \text{..... (2.44c)}$$

In zone IV, the retained nanoparticles become steady-state, $\sigma_{NP,\max 1}$. Since then, the suspended nanoparticles become constant. After $t_D = t_{cr}(x_D = 1)$, any pores along the permeable medium have reached the state of maximum retention concentration of fine particles:

$$\text{Zone IV:} \quad \begin{cases} \sigma_{NP}(x_D, t_D) = \sigma_{NP,\max 1} & \text{(a)} \\ C_{NP}(x_D, t_D) = C_0\exp\left(-\lambda_s Lx_D\right) & \text{(b)} \\ S_{NP} = \lambda_s C_0\phi L\left(t_D - x_D\right)\exp\left(-\lambda_s Lx_D\right) & \text{(c)} \end{cases} \quad \text{..... (2.45)}$$

$$t_{cr}(x_D = 1) = \frac{\phi C_0 + \sigma_{NP,\max 1}}{\phi C_0}x_D\Big|_{x_D=1} + \frac{\sigma_{NP,\max 1}}{\lambda_{ad}\phi LC_0} \quad \text{..... (2.46)}$$

At t_{D_1} , when the post-flush of brine starts, the initial conditions of post-flush are described as follows:

$$\begin{cases} C_{NP}(x_D, t_{D1}) = C_0 \exp(-\lambda_s L x_D) \\ \sigma_{NP}(x_D, t_{D1}) = \sigma_{NP,\max 1} \\ S_{NP}(x_D, t_{D1}) = \lambda_s C_0 \phi L (t_{D1} - x_D) \exp(-\lambda_s L x_D) \end{cases} \quad \text{……..……..…. (2.47)}$$

Applying the approach of MOC for the mass-balance equation (Eq. 2.27), the following ordinary differential equations are obtained along the characteristic lines,

$$\frac{dt_D}{dx_D} = 1 + \frac{1}{\phi} \frac{\sigma_{NP,\max 1} - \sigma_{NP,\max 2}}{C_{NP}} \quad \text{…… (2.48)}$$

Analytical solutions for suspended nanoparticles and absorbed nanoparticles in zone V can be determined:

$$\begin{cases} 0 < x_D < 1 \\ t_D > \left(1 + \frac{1}{\phi} \frac{\sigma_{NP,\max 1} - \sigma_{NP,\max 2}}{C_{NP}}\right) x_D + t_{D1} \end{cases}, \text{ZoneV: } \begin{cases} C_{NP}(x_D, t_D) = 0 \\ \sigma_{NP}(x_D, t_D) = \sigma_{NP,\max 2} \end{cases} \quad \text{…….. (2.49)}$$

The irreversible (maximum detached) retention concentration of nanoparticles during brine post-flush, $\sigma_{NP,\max 2}$, can be determined by identifying the time with constant nanoparticles effluent concentrations equal to the cumulative amounts, Δt_{D2}.

$$\sigma_{NP,\max 2} = \sigma_{NP,\max 1} - \left(\frac{1}{\Delta t_{D1}} - 1\right) \phi C_{NP} \quad \text{…… (2.50)}$$

Table 2.2 summarizes the analytical solutions of nanoparticles adsorption, straining and detachment for different flow zones in distance-time diagram, Figure 2.3. As for the case with constant injection rates and constant injected nanoparticles concentration, the pressure drop along 1-D permeable medium increases with the accumulation of nanoparticles attachment and straining. The damage of permeability has been proposed as empirical formulas coupled the effects of particulates adsorption and straining by

Sharma et al. (1987). The modified Darcy's flow equation considering the damage of core permeability is written as,

$$U = \frac{k_0}{L\mu\left(1+\beta_a\sigma_{NP}+\beta_s S_{NP}\right)}\frac{dp}{dx_D} \quad \text{..... (2.51)}$$

The pressure drop can be obtained by integrating Eq. 2.51 along the 1-D core.

$$\Delta p\left(t_D\right) = \int_0^1 \frac{UL\mu\left(1+\beta_a\sigma_{NP}+\beta_s S_{NP}\right)}{k_0} dx_D \quad \text{..... (2.52)}$$

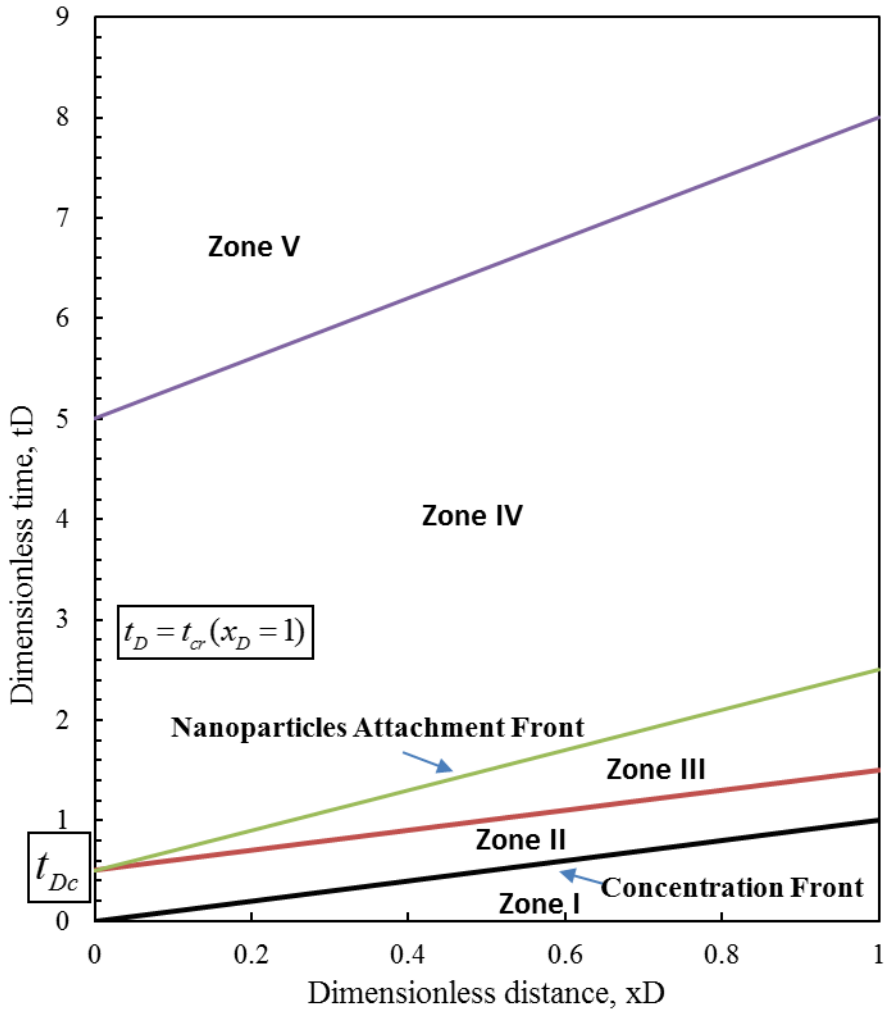


Figure 2.3 Distance–time diagram or motion of nanoparticles concentration fronts in the plane of x_D-t_D

Table 2-2 The summary of suspended, attached and strained nanoparticles concentration along 1-D permeable medium within the different zones in distance-time diagram

Zone	Suspended concentration C_{NP}	Attached concentration σ_{NP}	Strained concentration S_{NP}
I	0	0	0
II	$C_0 \exp\left(-\left(\lambda_{ad}+\lambda_s\right)Lx_D\right)$	$\lambda_a C_0 \phi L\left(t_D - x_D\right)\exp\left(-\left(\lambda_{ad}+\lambda_s\right)Lx_D\right)$	$\lambda_s C_0 \phi L\left(t_D - x_D\right)\exp\left(-\left(\lambda_{ad}+\lambda_s\right)Lx_D\right)$
III	$C_0 \exp\left(-\left(\lambda_{ad}+\lambda_s\right)L\left(\begin{array}{l} x_D-\left(t_D-x_D\right) \\ \times\dfrac{\lambda_{ad}\phi C_0}{\left(\lambda_{ad}+\lambda_s\right)\sigma_{NP,\max 1}} \\ +\dfrac{1}{\left(\lambda_{ad}+\lambda_s\right)L}\end{array}\right)\right)\sigma_{NP,\max 1}\exp\left(-\left(\lambda_{ad}+\lambda_s\right)L\left(\begin{array}{l} x_D-\left(t_D-x_D\right) \\ \times\dfrac{\lambda_{ad}\phi C_0}{\left(\lambda_{ad}+\lambda_s\right)\sigma_{NP,\max 1}} \\ +\dfrac{1}{\left(\lambda_{ad}+\lambda_s\right)L}\end{array}\right)\right)$	$\lambda_s C_0 \phi L\left(t_D - x_D\right)\exp\left(-\left(\lambda_{ad}+\lambda_s\right)Lx_D\right)$
IV	$C_0 \exp\left(-\lambda_s Lx_D\right)$	$\sigma_{NP,\max 1}$	$\lambda_s C_0 \phi L\left(t_D - x_D\right)\exp\left(-\lambda_s Lx_D\right)$
V	0	$\sigma_{NP,\max 2}$	$\lambda_s C_0 \phi L\left(t_{D1} - x_D\right)\exp\left(-\lambda_s Lx_D\right)$

2.3 Characterization on Nanoparticles Adsorption, Straining and Detachment

The trends of discreet points in Figure 2.4 show the effluent history of dimensionless NSP nanoparticles concentrations (Li et al. 2015b) with different injected concentrations, which is defined as the ratio of effluent nanoparticles concentration to the injected concentration. First, the case with 0.05 wt.% NSP has the earliest breakthrough of injected nanofluids, at which nanofluid effluent reaches the steady state. The 0.05 wt. % case has the least amounts of NSP loss caused by the adsorption and straining effects of nanoparticles. Indicated by the different levels of effluent concentration at the steady-state plateau, as the injected nanoparticles concentration increases, there are more nanoparticles to be retained by rock grains, as results, the breakthrough of nanofluid is also delayed. A "tail" of nanofluid effluent curve during post-flush of brine indicates the detachment of absorbed nanoparticles, which is also referred as reversible nanoparticles adsorption. Moreover, the non-symmetric features of nanofluid effluent history between the early injection phase and the latter post-flush phase indicates that there are only limited amounts of absorbed nanoparticles to detach during brine post-flush.

The recorded pressure drops during nanofluid injection (Li et al. 2015b) is presented in Figure 2.5. The results of NSP with different injected concentrations have different tendencies. Caused by the adsorption and straining of nanoparticles, the pressure drop increases rapidly after the start of nanofluid injection. This may be attributed to the multilayer adsorption of nanoparticles and straining effects, which leads to the reduction of pore-throat sizes and the escalation of pressure drop. The higher the injected nanoparticles concentration is, the more rapid and significant the pressure drop increases. During the post-flush of brine, the pressure drop decreases gradually. It may be attributed

to the enlargement of porosity caused by detachment of those previously adsorbed nanoparticles. After several PVs of brine post-flush, the pressure drop reaches steady-state. Since then, no more detachment and straining of nanoparticles occur. To quantify the nanoparticles adsorption behavior, a workflow described in Figure 2.6 is followed.

Indicated by the nanoparticles effluent history (Figure 2.4), the values of λ_s are obtained by using the peak values of effluent nanoparticles concentration (Eq. 2.47). Combining Eq. 2.40b into Eq. 2.44b could leave only one unknown parameter t_{cr} in Eq. 2.53. In the experimental results, the values of t_{cr} can also easily be determined by finding the infection points from the effluent history. To obtain the unknown, λ_{ad}, a trial and error algorithm is applied by calculating Eq. 2.53 to best fit with the effluent history.

$$\frac{C_{NP,eff}}{C_{NP,inj}} = \exp\left(-(\lambda_{ad}+\lambda_s)L\left(x_D-(t_D-x_D)\frac{L(\lambda_{ad}+\lambda_s)+1}{L(\lambda_{ad}+\lambda_s)(t_{cr}-1)}+\frac{1}{(\lambda_{ad}+\lambda_s)L}\right)\right) \quad \text{..... (2.53)}$$

Followed by, the total retention amounts of nanoparticles $\sigma_{\max_2}$ including both reversible and irreversible adsorption can be quantified by substituting both λ_{ad} and λ_s into Eq. 2.44b. The irreversible (detached) adsorption of nanoparticles $\sigma_{\max_2}$ during post-flush is determined using Eq. 2.50 by substituting the breakthrough time of post-flush brine, Δt_2. In addition, after $t_D = t_{cr}(x_D = 1)$, no nanoparticles adsorption can occur any more, hence, in the range of time, Δt_2, the increase of pressure drop can only be attributed to the nanoparticles straining effects. Substituting Eq. 2.47 into Eq. 2.52, the increase of pressure drop for the range of Δt_1 is formulated, as shown in Eq. 2.54. Using Eq. 2.54, the formation damage coefficient β_s is determined to match the recorded

pressure drop in the range of time, Δt_1. Followed by, β_a is found out by matching Eq. 2.52 with the pressure drop curves for time ranges during nanofluid injection.

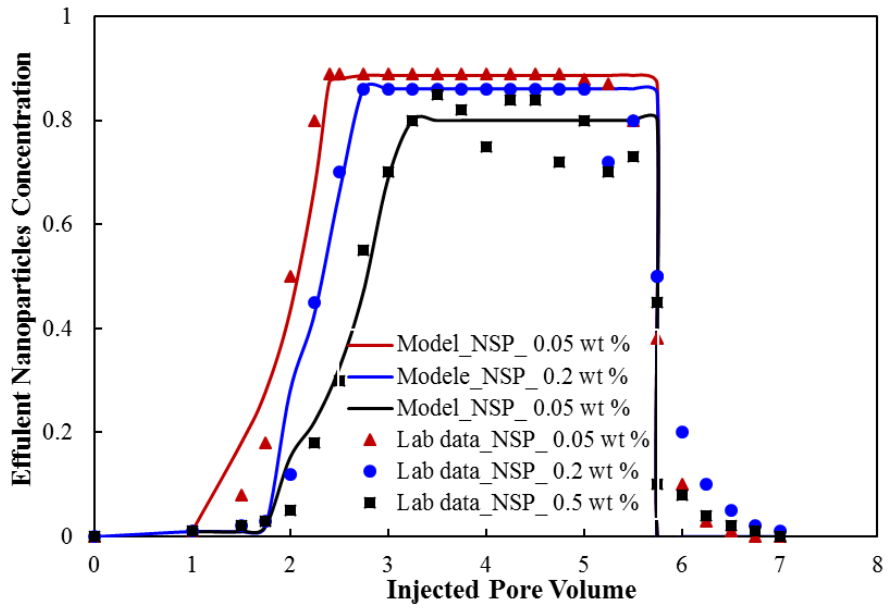


Figure 2.4 Comparison between nanoparticles effluent history obtained from analytical models with experimental results

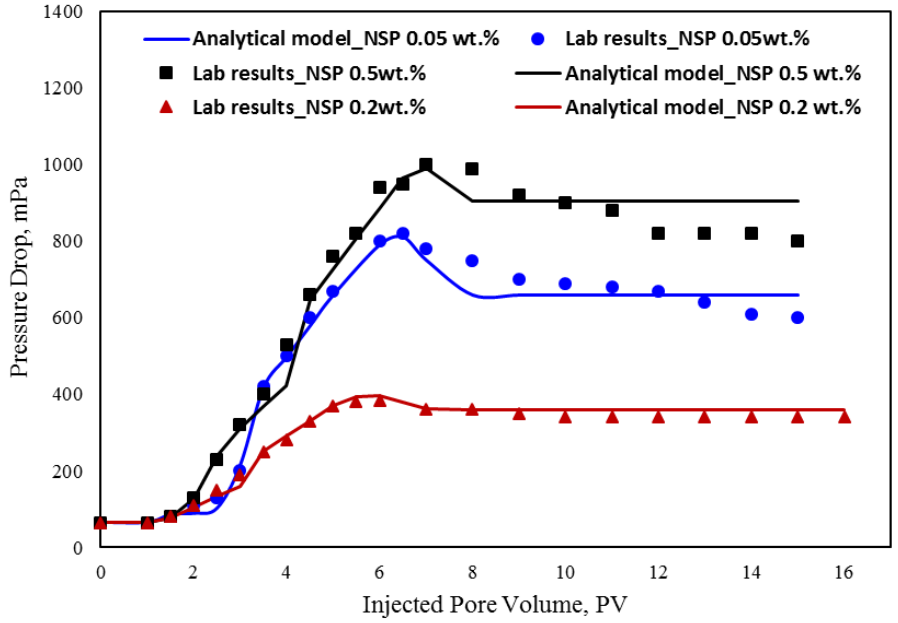


Figure 2.5 Comparison between pressure drop obtained from analytical models and lab experimental results

Figure 2.4 and Figure 2.5 compare the results of nanoparticles effluent concentration and pressure drop calculated from both analytical models and record history in lab experiment results, respectively. The excellent agreement with lab experimental results help quantifying series of parameters which describe nanoparticles adsorption, straining and detachment behavior, including the maximum nanoparticles adsorption, reversible adsorption, nanoparticles adsorption and straining rates, formation damage coefficients β_a and β_s, as summarized in Table 2.3.

$$\Delta p_1 = \int_0^1 \frac{UL\mu\beta_s\lambda_s C_0\phi L\Delta t_D \exp\left(-\lambda_s L\right)}{\left(k_{intrinsic}k_{rw}\right)_0} dx_D \quad \text{..... (2.54)}$$

Table 2-3 Summary of nanoparticles adsorption, straining & detachment behavior for the cases with different injected nanoparticles concentrations

	NSP 0.05 wt. %	NSP 0.2 wt. %	NSP 0.5 wt. %
$\sigma_{NP,\max 1}$	4.5×10^{-3}	2.1×10^{-2}	7.7×10^{-2}
$\sigma_{NP,\max 2}$	2.9×10^{-3}	1.4×10^{-3}	5.8×10^{-2}
σ_{detach}	1.6×10^{-3}	0.7×10^{-2}	1.9×10^{-2}
Reversible adsorption ratio	0.34	0.33	0.26
λ_{ad}	15~20	20~25	25~30
λ_s	1.3	1.9	2.8
β_a	100	20	20
β_s	2500	900	250

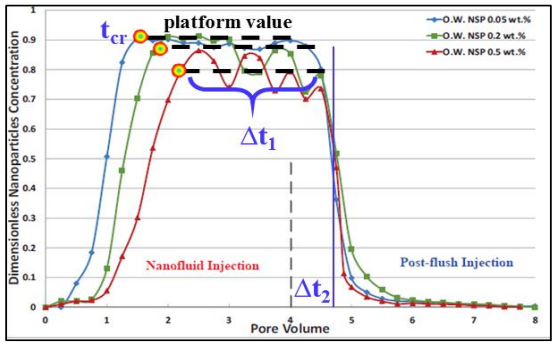
Indicated by Table 2.3, as the injected nanoparticles concentration increases, the maximum nanoparticles adsorption amounts are enhanced (the solid line in Figure 2.7). The detachment of reversible adsorbed nanoparticles occurs during the post-flush of brine. The amount of reversible adsorption also increases along with the increase of the injected nanoparticles injection concentration (the dash line in Figure 2.7). In addition,

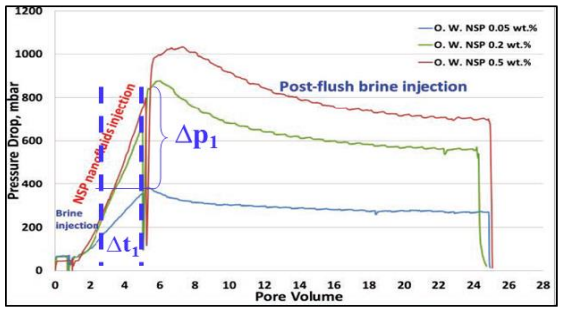
the average percentage of reversible adsorption is approximately 30% of the total amounts of nanoparticles adsorption. In other words, there are only 70% of absorbed nanoparticles to be retained in total. As shown in Figure 2.8, moreover, the nanoparticles adsorption and straining rates are also functions of injected nanoparticles concentrations. The higher the injected nanoparticles concentration is, the larger the nanoparticles adsorption and straining rates will be. In general, the rates of nanoparticles adsorption are larger than nanoparticles straining rates.

The inversed values of core permeability from pressure drops are compared for both before nanofluid injection and after brine post-flush in Table 2.4. The damage of permeability is characterized by a ratio between those two values for different cases. As the injected nanoparticles concentration increases, the damage of core permeability is exaggerated, as indicated by the data in the right second column. The last column in Table 2.4 lists the damage of permeability using analytical solutions. The comparisons between the last two columns indicates the accuracy of the analytical solutions.

Table 2-4 Permeability reduction of core plugs after NSP nanofluid injection

Concentration, wt.%	Lab experimental results (Li et al, 2015)			Analytical model
	Pre-injection K_1, mD	After post-flush, K_2, mD	K_2/K_1	K_2/K_1
0.05	327	86	0.263	0.212
0.2	362	42	0.116	0.010
0.5	526	33	0.063	0.068





Step 1: From the experimental nanoparticles effluent concentration history (left figure), find out the breakthrough of steady-state condition, t_{cr}

⇩

Step 2: Read out the highest platform value, and based on **Eq. 2.47**. We can determine the number of λ_s

⇩

Step 3: Apply trial and error algorithm to determine λ_{ad} by the match of the effluent concentration at different time using equations in **Table.2.2**, with the experimental results.

⇩

Step 4: Substitute λ_a **and** λ_s into Eq. 2.44b to determine the maximum adsorption of nanoparticles, σ_{max1}

⇩

Step 5: Identify the breakthrough time of post-flush Δt_2, and using **Eq.2.50** to determine the irreversible maximum adsorption of nanoparticles, σ_{max2}

⇩

Step 6: Identify the range time of Δt_1, and using Eq. 2.52 to determine the formation damage coefficient β_s, and then, identify β_a by matching the pressure drop calculated from Eq.33 with the experimental results.

Figure 2.6 Workflow to quantify nanoparticles adsorption, straining and detachment using models and experimental results

Figure 2.9 summarizes the formation damage coefficients caused by both nanoparticles adsorption and straining. It explains the reasons why pressure drop increases during nanofluid injection. As the injected nanoparticles concentration increases, the formation damage effects from both two behaviors decreases, correspondingly. In opposite to the relationship between nanoparticles adsorption and straining rates, the formation damage coefficients of nanoparticles straining are much larger than that of nanoparticles adsorption. That is to say, the formation damage caused by nanoparticles straining dominates the increase of pressure drop.

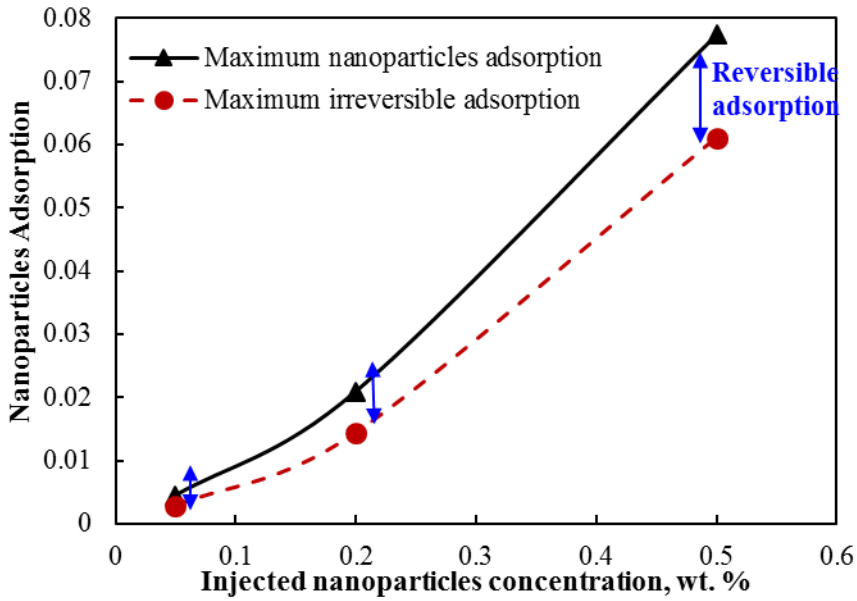


Figure 2.7 Effects of injected nanoparticles concentration on maximum adsorption concentration, irreversible adsorption, and reversible adsorption of nanoparticles

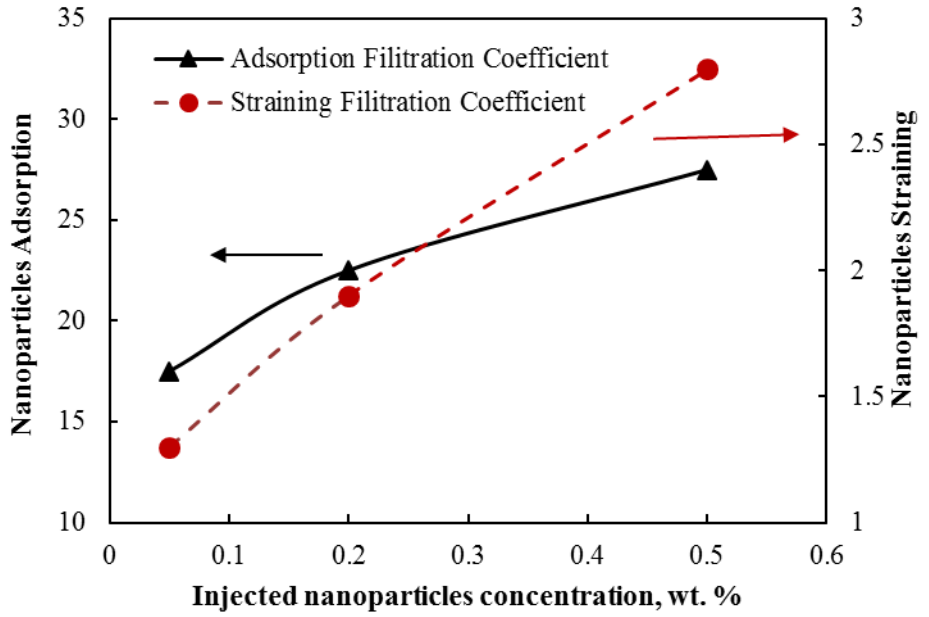


Figure 2.8 Effects of injected nanoparticles concentration on nanoparticles adsorption and straining rates

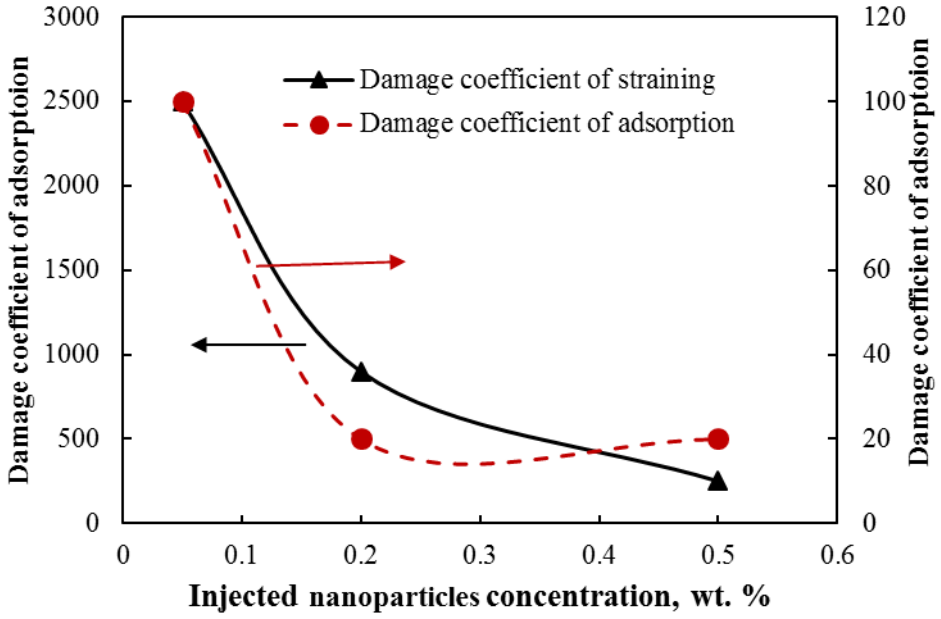


Figure 2.9 Effects of injected nanoparticles concentration on formation damage effects attributed to nanoparticles adsorption and straining

2.4 Conclusions and Summary

This chapter provides analytical solutions to explain the experimental studies and quantify the reversible/irreversible adsorption and straining behaviors of NSP and their effects on the permeability of oil-wet cores. The main outcomes of this chapter include:

- Analytical solutions coupled the classical filtration theory with the maximum retention concentration model is derived to characterize nanoparticles adsorption, detachment, and straining phenomenon.
- As the injected nanoparticles concentration increases, the breakthrough of NSP can be delayed, and the maximum adsorption capacity of nanoparticles are enhanced.
- There are positive trends between the rates of nanoparticles adsorption & straining and the injected nanoparticles concentrations. In general, the nanoparticles adsorption rates are larger than straining rates.
- The formation damage caused by nanoparticles straining are usually larger than that of nanoparticles adsorption, and hence, the damage of formation permeability is dominated by nanoparticles straining leading to the increase of pressure drop.

2.5 Nomenclature

A_{132} = Hamaker constant

C_{NP} = Volumetric concentration of adsorbed nanoparticles with respect to pore volume, m^3/m^3

$C_{NP,inject}$ = Volumetric concentration of injected nanoparticles with respect to pore volume, m^3/m^3

S_{NP} = Volumetric concentration of Straining nanoparticles with respect to pore volume, m^3/m^3

λ_s = Straining filtration coefficient

λ_{ad} = Adsorption filtration coefficient

ϕ = Porosity of core plug

ϕ_c = Percentage of internal cake thickness in pore space

L = Length of core plug

A = Cross-section area of core plug

σ_{NP} = Volumetric concentration of retained nanoparticles with respect to bulk volume, m^3/m^3

$\sigma_{NP,\max 1}$ = Maximum retention concentration of nanoparticles during nanoparticles injection, m^3/m^3

$\sigma_{NP,\max 2}$ = Maximum retention concentration of nanoparticles during the phase of post-flush, m^3/m^3

x_D = Dimensionless distance

t_D = Dimensionless time or injected pore volume

t_{Dc} = Injected pore-volume while maximum nanoparticles adsorption is reached

t_{D1} = Injected pore volume at the start of brine post-flush without nanoparticles

r_{NP} = Radius of nanoparticles, m

μ = Fluid viscosity, Pa.s

q_{inj} = Fluid injection rate, ml/min

r_c = Internal cake thickness due to retention of particles type *k*, m

r_{NP} = Radius of nanoparticles, m

$r_{Particle}$ = Radium of particles, e.g., nanoparticles or fine particles, m

r_p = Pore radius, m

d = Atomic collision diameter in Lennard-Jones potential, 0.5 nm

F_d = Drag force, N

F_e = Electrostatic forces, N

F_l = Lifting force, N

F_n = Normal force, N

h = Surface-to-surface separation length, m, $h << r_{fp}$

k_B = The Boltzmann's constant, 1.381×10^{-21} J/K

l = Characteristic wave length of interaction, l=100 nm

n = Pore concentration, number/m^3

y = Ratio between drag and electrostatic force

χ = Lifting force coefficient

ρ = Fluid density, kg/m^3

$\Delta\rho$ = Density difference between particles and fluid, kg/m^3

ρ_w = Water fluid density, kg/m^3

ρ_{NP} = Nanoparticles fluid density, kg/m^3

Δt_{D1} = Range of time for steady-state effluent nanoparticles concentration

k_0 = Permeability of core plug, mD

$k_{1,2}$ = Intrinsic permeability of core plug before and after core-flood, mD

β_a = Formation damage coefficient related to nanoparticles adsorption

β_s = Formation damage coefficient related to nanoparticles straining

Δp = Pressure drop, MPa

T = Absolute temperature of reservoir, K

U = Fluid velocity, m/s

V_{FP} = Total energy, J

V_{LVA} = London–van-der-Waals adsorption energy, J

V_{DLR} = Double electric layer repulsion energy, J

V_{BR} = Born potentials, J

ω = Dimensionless drag force coefficient varying in the range 10~60

n_∞ = Bulk number density of ions, 6.022×10^{25} number/m^3

κ = Inverse Debye length, m^{-1}

x_D = Dimensionless distance

t_D = Dimensionless time or injected pore volume

Chapter 3: Nanoparticles Utilization to Mitigate Fines Migration in Porous Media

3.1 Problem Statement and Assumption

Fines migration within reservoirs has been regarded as a significant cause of reservoir permeability damage and decline of well productivity/injectivity. The best strategy to avoid fines migration is to keep them stagnant at their original location/sources through either limiting flow rate (less than the critical rates) or somehow settling them. Nanoparticles with extremely high surface areas of approximately $200m^3/g$ are suitable to help settling mobile formation fines by altering the surface potential of fines particles or grain surfaces. Nanoparticles that are used to control fines migration are usually in order of tens of nanometers. Because of their relatively small sizes compared to pore-throat sizes (in order of μm), nanofluid flow has negligible effects on the damage of pore-throat structures and reservoir permeability. It has been justified that nanoparticles can effectively reduce the double layer repulsive forces between fine particles and rock grains through changing the surface zeta potentials of adsorbents (fines or rock grains). The reduction of repulsive forces among loose particles maintains the integrity of rock textures without any fines detachment (Huang, 2008b; Ju, 2006). Whether suspensions/colloidal fluids are co-injected with small amounts of nanoparticles (Scenario I), or flow through the nanoparticles pre-treated permeable medium (Scenario II), the modified physical-chemical forces (including London-van-der-Waals, Double electric layer and Born repulsive force) help retaining more amounts of fine particles. Laboratory experiments have demonstrated that only a very small concentration of nanoparticles to be coated on fracture proppants can greatly help preventing fines migration and subsequent formation damage (Huang, 2008b). Several studies have also

reported successful applications of silica nanoparticles to mitigate fines migration in sand packs saturated with nC60 under high salinity conditions (Cheng, 2005; Ju, 2009; Yu, 2010). However, to the best of our knowledge, our understanding about the effectiveness of nanoparticles is only limited to few laboratory experiments, serving only as proof of the concept. The theoretical evaluation approach by which nanoparticles control fines migration has yet to be addressed.

This chapter will examine an application of method of characteristics (MOC) to evaluate the effectiveness of nanoparticles to mitigate fines migration in porous media. The positive contributions of nanoparticle to mitigate fines migration are characterized by the enhancement of maximum retention concentration of fines particles onto rock grains through two reactions: (1) adsorption of nanoparticles onto the fines/grain surfaces and (2) increased concentration of fines attachment onto pore surfaces via reducing the surface potential between grains and fines.

By applying method of characteristics, analytic solutions are developed for two different scenarios of nanoparticles utilization to evaluate the enhanced capability of porous medium to capture unsettled fines: (1) co-injection of nanoparticles with fines suspension into one-dimensional permeable medium and (2) pre-coating porous medium with nanoparticles prior to fines injection.

In this chapter, to quantify the positive contributions of nanoparticles pre-coating to maintain well injectivity for Scenario II discussed in section 3.2.4 and section 3.2.3, analytical solutions of two reference scenarios are compared to nanoparticles pre-coat case: (1) Case I: nanoparticles are pre-treated into porous medium, and hence, the retaining capacity of rock grains toward the flowing fines becomes under-saturated. (2)

Reference case II: For reservoirs with small content of clay minerals, the initial attached fines concentration is less than or just close to the maximum capacity of rock grains capturing fine particles. It does mean that there are no suspended particles in flowing fluid prior to the invasion of newly fine particles. (3) Reference case III: For the reservoirs with high content of clay minerals, the initial fines concentration (including both freely suspended and attached fines) have been already more than the maximum capacity of rock grains. This scenario can be confirmed by the decline of formation water (no changes of chemical environment in porous media) injection rates without any new particulates invasion into reservoirs. Therefore, to demonstrate the effects of clay fines contents on the performance of nanofluid utilization, the analytical solutions for both case II and III are compared with the case with nanofluid pre-coating.

In addition, the significance of analytical solutions presented in this chapter is not only restricted to characterize nanoparticle application to mitigate fines migration. As recognized by Dominguez (1977), there are strong similarities among polymer mechanical entrapment, deep filtration of emulsions, and solid suspensions. Hence, any theoretical works or methodologies developed to address particulates flow, at least in principle, can be applicable to the wider variety of applications, such as nanoparticles utilization to stable oil-water emulsions, synergistic effects of nanoparticles, and polymers as drilling or fracturing fluid additives.

3.1.1 Scenario I: Co-injection of Nanoparticles and Fine particles

In this scenario, initially, there are more fine particles than the maximum retention capacity of fines. That is, the initial concentration of unattached fine particles is non-zero. As noted in the previous published papers (Ahmadi, 2011; Bedrikovetsky, 2011; Habibi,

2011; Zeinijahromi, 2012), the surface potential of fine particles is usually less than that of rock grains, which results in stronger attractive forces between nanoparticles and fine particles than that of nanoparticles and rock grains. Therefore, while nanoparticles as an additive are continuously injected into the injection stream with new fines invasion, nanoparticles are preferentially adsorbed on the surfaces of fines rather than pore surfaces. The attachment of fine particles onto pore surfaces and adsorption of nanoparticles on fines occur simultaneously but at different rates. In addition, the adsorption of nanoparticles onto the surfaces of fines could alter the surface potential of fine particles, which consequently lowers the repulsive force between fine particles and rock grains. As a result, the co-injection of nanoparticles helps increase the maximum (critical) retention concentration of fine particles on rock grains.

3.1.2 Scenario II: Nanoparticles Pre-flush prior to Fines Invasion

In many unconsolidated reservoirs, fines migration usually occurs near wellbore and leads to pore blockage and plugging of flow paths. To prevent this problem, pre-treating porous medium (e.g., fracture proppant for gravel pack) with nanofluid may lead to an effective remediation to fixate the injected or mobile fines near their original location and from moving downstream.

Our assumptions are listed for this scenario, as follows (Yuan, 2015b and 2016b):

- The sand pack is one-dimensional (1D), uniform and homogeneous medium, and local thermodynamic equilibrium assumption applies. In addition, the system is water wet and only the aqueous phase flows.
- Three-components exist (water, nanoparticles, and fine particles) and two-phase (one flowing and one stagnant) isothermal flow takes place.

- Adsorption of nanoparticles can be described by Langmuir isotherm, which provides an asymptotical maximum adsorption capacity when time tends to infinite. Beyond that, there are unsettled nanoparticles left in the carrier fluid.
- Flow velocity is sufficiently large to neglect the dispersion flow effects; therefore, hyperbolic conservation equations are obtained.
- No nanoparticle-nanoparticle aggregation occurs, and no bridging happens to cause bigger colloids that may eventually plug the pore-throats. Fines particles and nanoparticles are small enough compared to the sizes of pore-throats (size ratio less than 0.08 (Herzig, 1970); therefore, the changes of porosity and permeability caused by the attachment of fines and nanoparticles are neglected (Dábrowski, 1988).
- For scenario II, after being coated by nanoparticles, the permeable medium becomes "under-saturated", which means there is potential for rock grains to retain unsettled fines.
- For both scenarios I and II, the adsorbed nanoparticles can only enhance the maximum attachment concentration of fine particles onto the rock, but not affects the attachment rates of fines particles.

3.2 Mathematical Model and Descriptions

3.2.1 Mutual Reactions among Nanoparticles, Fines and Rock Grains

Assuming that nanoparticles are small enough in relation to the sizes of adsorbents (fine particles or rock grains), Langmuir adsorption isotherm can be applied to describe the amount of nanoparticles adsorbed on surfaces of fine particles (O'Brien, 2014).

$$\text{Scenario I: } \hat{C}_{NP} = \frac{\hat{C}_{NP,\max} K_{NP} C_{NP}}{1 + K_{NP} C_{NP}} = \left[A \frac{4\phi(1 - S_{or}) C_{FP} r_{NP}}{r_{FP}} \right] \frac{K_{NP} C_{NP}}{1 + K_{NP} C_{NP}}$$

$$\text{Scenario II: } \hat{C}_{NP} = \frac{\hat{C}_{NP,\max} K_{NP} C_{NP}}{1 + K_{NP} C_{NP}} = \left[A \frac{8\phi(1 - S_{or}) L r_{NP}}{3 r_P} \right] \frac{K_{NP} C_{NP}}{1 + K_{NP} C_{NP}} \quad \text{……..……} \quad (3.1)$$

where $\hat{C}_{NP}$ is volumetric concentration of adsorbed nanoparticles with respect to bulk volume; $\hat{C}_{NP,\max}$ is the maximum Langmuir adsorption amount; C_{FP}, C_{NP} are the volumetric concentrations of fine particles and nanoparticles with respect to pore volume; K_{NP} is nanoparticles Langmuir adsorption constant.

Senger et al (1992) investigated the maximum adsorption limit as jamming-limit coverage (54.6% for monolayer adsorption) for the attachment of hard spheres onto a planar surface. In practice, the maximum limit of nanoparticle adsorption is usually less than this jamming-limit value because of the repulsive force among nanoparticles and surface heterogeneity. However, in this paper, to simplify the complex mechanisms of nanoparticle adsorption, we choose the jamming-limit coverage as the maximum nanoparticles adsorption concentration (A=0.546 in Eq.3.1); under this condition of maximum monolayer adsorption, the surface potential of rock grains can be modified as that of coated nanoparticles on their surfaces.

Consistent with the existing experimental work, the mechanisms of nanoparticles to control fines migration are assumed for two scenarios of nanoparticles utilization to control fines migration (Figure 3.1): (1) Scenario I: simultaneous injection of nanoparticles and fine particles and (2) Scenario II: nanoparticle pre-treated porous media before the invasion of new fines.

Scenario I: Co-injection of Nanoparticles and Fines into Porous Media

In this scenario, the surface potential of fines is assumed usually less than that of rock grains, which results in stronger attractive forces between nanoparticles and fine particles than that of nanoparticles and rock grains. Therefore, nanoparticles are preferentially adsorbed on the surfaces of fines rather than the surfaces of rock grains during the co-injection of nanoparticles and fines. The adsorption of nanoparticles on the surfaces of fines will alter the surface potential of fine particles, which consequently lowers the repulsive force between fine particles and rock grains.

As inferred from Eq. 2.8, the double layer repulsive force between fine particles and rock grains becomes a function of nanoparticles adsorption concentration on fines. Here, the electrostatic force is the derivative of total energy, V_{FP}, with respect to surface-to-surface separation length, h. Hence, we directly express the derivative of double layer repulsive energy, V_{DLR}, with respect to h, as shown in Eq. 3.1.

Without nanoparticles utilization:

$$\frac{\partial V_{DLR}}{\partial h} = -\frac{128\pi r_{FP} n_{\infty} k_B T}{\kappa} \varsigma_{FP}\varsigma_{GS} e^{-\kappa h} \quad \text{..... (3.1a)}$$

With varying nanoparticles adsorption on fine particles as the co-injection continues:

$$\frac{\partial V_{DLR}}{\partial h} = -\frac{128\pi r_{FP} n_{\infty} k_B T}{\kappa} e^{-\kappa h} (\varsigma_{FP} - \frac{\hat{C}_{NP}}{\hat{C}_{NP,cr}} (\varsigma_{FP} - \varsigma_{NP}))\varsigma_{GS} \text{..... (3.1b)}$$

With the maximum nanoparticles adsorption on fines particles finally:

$$\frac{\partial V_{DLR}}{\partial h} = -\frac{128\pi r_{FP} n_{\infty} k_B T}{\kappa} e^{-\kappa h} \varsigma_{NP}\varsigma_{GS} \text{..... (3.1c)}$$

In Figure.3.1a, the mutual interactions among nanoparticles, fine particles, and rock grains can be described as follows:

Initially, the attached concentration of fine particles on rock grains has reached the maximum retention concentration of fines, $\sigma_{cr,initial}$ (Eq. 2.19 and Eq. 3.2a), which is determined by the surface charges of fine particles and rock grains. However, there are still some unattached fines left in the porous medium. When the injected nanoparticles arrive, the already attached fine particles on rock grains would not be the immediate targets for the arriving nanoparticle; instead, the remaining unattached fines left in the suspension can immediately host the injected nanoparticles. The more nanoparticle adsorption occurs, the larger the surface potential of fines particles covered by nanoparticles would drop; thus, the attractive electrostatic forces between unattached fines and rock grains could be enhanced (noted from Eq. 2.2, Eq. 2.6-2.9, and Eq. 3.1). Meanwhile, the excessive attachment of unattached fine particles on the pore surface simultaneously occurs with the adsorption of nanoparticles on their surfaces. Therefore, the nanoparticle-fines complex would attach to the rock grain surfaces continuously until the attachment concentration of fine particles on rock grains reaches a new maximum value, $\sigma_{cr,i+1}$. This new maximum concentration (Eq. 3.2b) is controlled by the amount of nanoparticle adsorption on fines at that moment, which can be derived by replacing the new double layer repulsive energy with nanoparticle adsorption (Eq. 3.1b) into the term of the electrostatic force in Eq. 2.19.

The step-wise reaction process of nanoparticles adsorption and subsequent nanoparticles-fines complex attachment described above would continuously repeat, and thus more unattached fines can be retained on rock grains with an increase of nanoparticle adsorption on their surfaces. However, the adsorption capacity/affinity of fine particles with respect to nanoparticles is limited, which means beyond some levels of nanoparticle

adsorption (function of salinity, pH, temperature) on fine particles, the surface potential of fine particles does not change anymore. At that moment, we assume that the surface potential of fines has already become identical with that of adsorbed nanoparticles. The maximum retention concentration of fine particles on rock grains also reaches the ultimate attachment concentration value, $\sigma_{cr,\max}$, determined by the surface charges of nanoparticles and rock grains as shown in Eq. 3.2c.

Therefore, there is an optimal nanoparticle concentration sufficient for nanoparticle adsorption to reach the ultimate concentration and modify the surface charges of fines to that of injected nanoparticles. When nanoparticle concentration is less than the optimal value, there would be still unattached fines left in the flowing fluid (carrier). Conversely, if nanoparticle concentration is larger than that optimal value, there are excessive nanoparticles unused in the system:

Without nanoparticles utilization:

$$\sigma_{cr,\text{initial}} = \left[1-\left(\frac{\mu r_{FP}^2 U}{2\phi(1-S_{or})r_P F_{ei} y}\right)^2\right]\phi(1-S_{or}) \quad \text{..... (3.2a)}$$

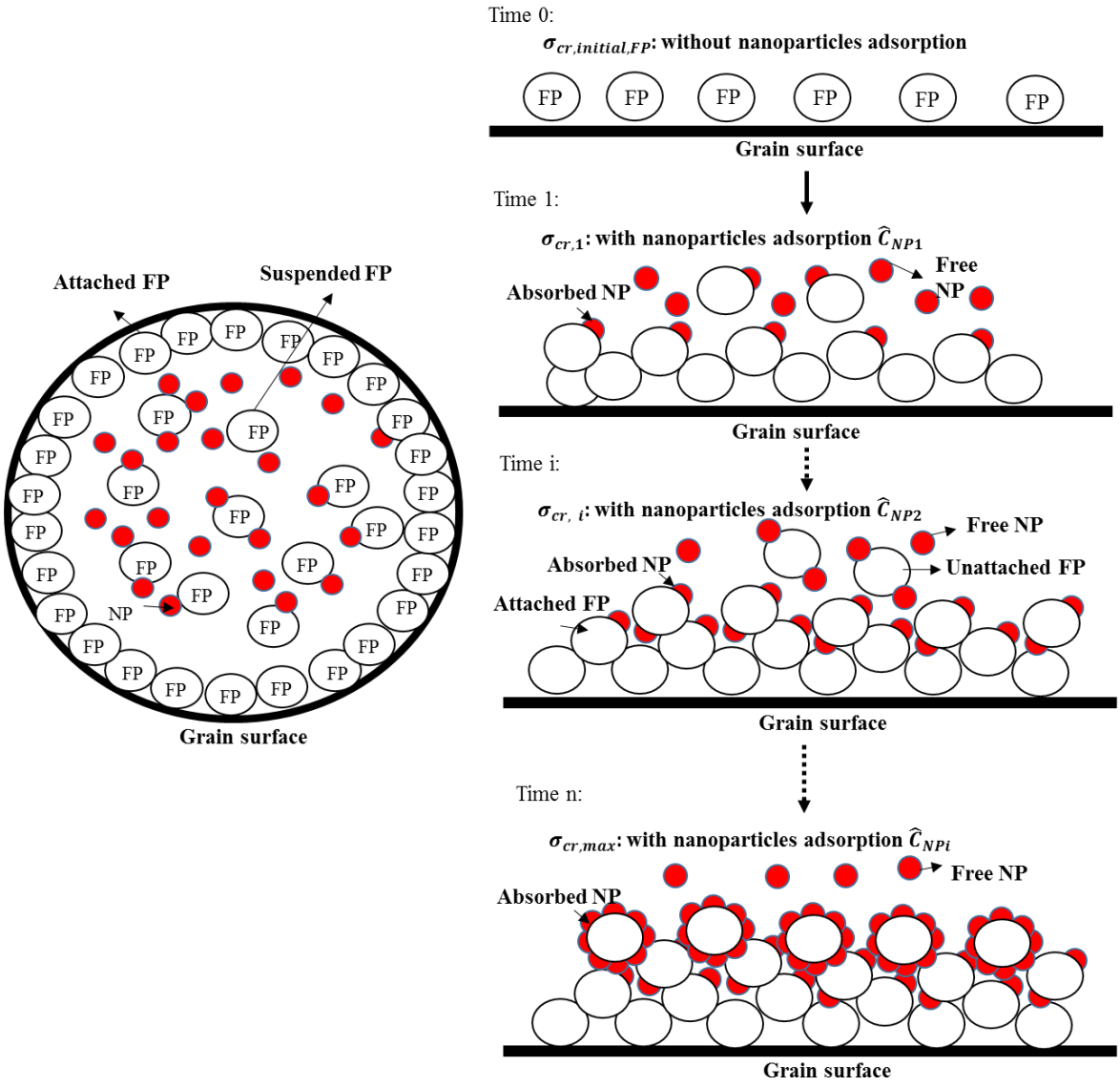
With varying nanoparticles adsorption on fine particles as the co-injection continues:

$$\sigma_{cr,i} = \left[1-\left(\frac{\mu r_{FP}^2 U}{2\phi(1-S_{or})r_P y\left(F_{ei} + \frac{128\pi r_{FP} n_\infty k_B T}{\kappa} e^{-\kappa h}\left[\frac{K_{NP}C_{NP}}{1+K_{NP}C_{NP}}(\varsigma_{FP}-\varsigma_{NP})\varsigma_{GS}\right]\right)}\right)^2\right]\phi(1-S_{or}) \quad \text{(3.2b)}$$

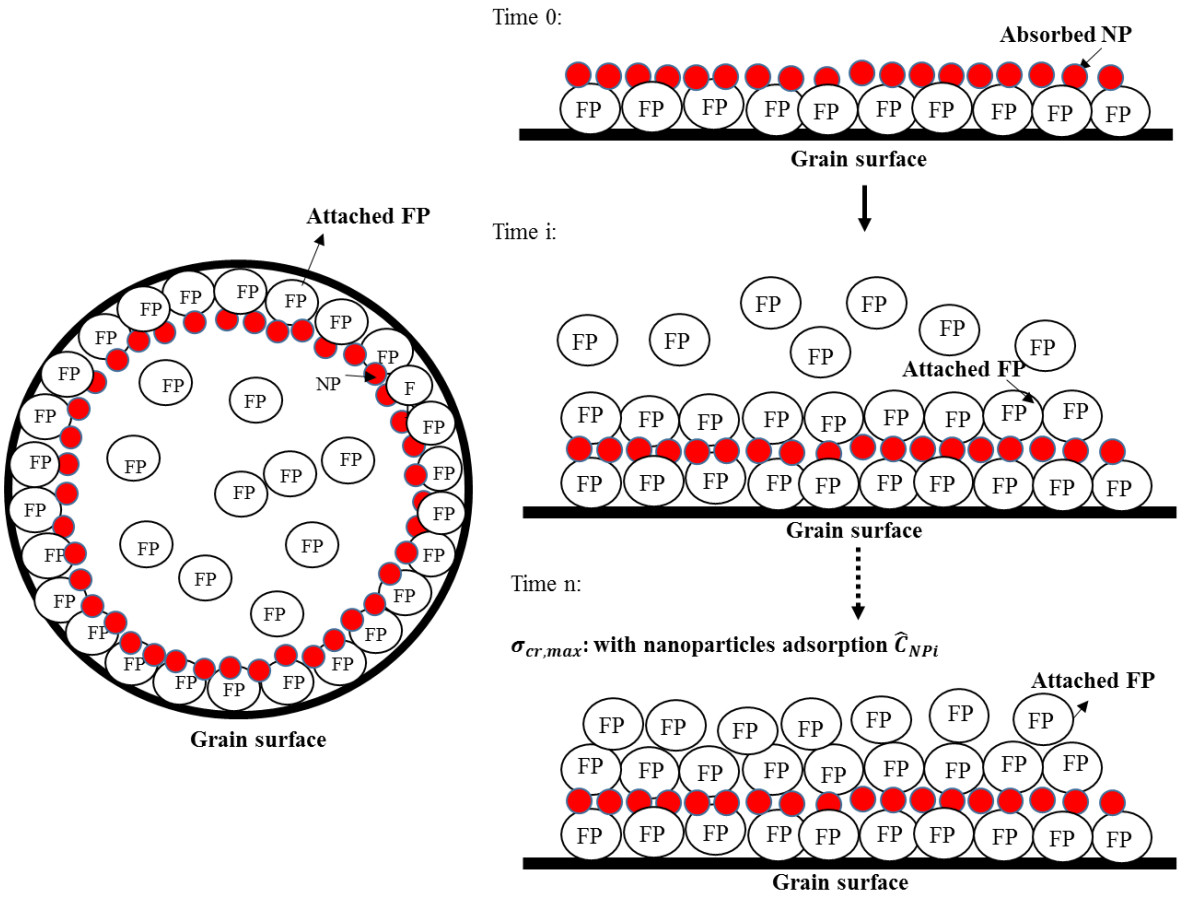
With the maximum nanoparticles adsorption on fine particles finally:

$$\sigma_{cr,\max} = \left[1 - \left(\frac{\mu r_{FP}^2 U}{2\phi(1-S_{or}) r_P y(F_{ei} + \frac{128\pi r_{FP} n_\infty k_B T}{\kappa} e^{-\kappa h}(\varsigma_{FP} - \varsigma_{NP})\varsigma_{GS}} \right)^2 \right] \phi(1 - S_{or}) \quad (3.2c)$$

where, $\sigma_{cr,initial}$ is the initial maximum retention concentration of fine particles (with zero nanoparticles injection into system); $\sigma_{cr,i}$ is the maximum retention concentration of fine particles at time i (when the adsorbed concentration of nanoparticles is still less than the ultimate maximum adsorption on fines); $\sigma_{cr,\max}$ is the ultimate maximum retention concentration of fine particles with the aid of nanoparticle adsorption.



a. Scenario I: Co-injection of nanoparticle with fines suspension



b. Scenario II: Nanoparticle treated porous prior to fines injection

Figure 3.1 Mutual interactions among nanoparticles, fines and rock grains indicating various physical mechanisms by which nanoparticles control fines migration

Scenario II: Pre-coat Porous Media with Nanofluids prior to Suspension Invasion

In this scenario, as indicated in Figure 3.1b, prior to introduction of fines particles into porous medium, nanofluid slug containing nanoparticles has been injected to modify the surface potential of rock grains. Thus, the repulsive forces between mobile fines and rock grains as (Eq. 3.3) decrease, which can be derived similarly with Eq. 3.1. The only difference between Eq. 3.3 and Eq. 3.1 lies on the changes on surface potentials of

absorbent carriers, from mobile fines to stationery rock grains. Thus, in scenario II, the pre-injected nanoparticles can be adsorbed onto rock grains for retaining more fine particles, as shown in Figure 3.2. Combined Eq. 2.19 and Eq. 3.3, the new maximum retention concentration of fines on rock grains can be obtained by considering the effects of pre-coated nanoparticles onto rock grains, as shown in Eq. 3.4.

Without nanoparticles pre-treatment:

$$\frac{\partial V_{DLR}}{\partial h} = -\frac{128\pi r_{FP} n_{\infty} k_B T}{\kappa} \varsigma_{FP} \varsigma_{GS} e^{-\kappa h} \quad \text{..... (3.3a)}$$

With small numbers of nanoparticles usage to coat rock grains:

$$\frac{\partial V_{DLR}}{\partial h} = -\frac{128\pi r_{FP} n_{\infty} k_B T}{\kappa} e^{-\kappa h} (\varsigma_{GS} - \frac{\hat{C}_{NP}}{\hat{C}_{NP,cr}} (\varsigma_{GS} - \varsigma_{NP})) \varsigma_{FP} \text{ ..... (3.3b)}$$

With enough amounts of to cover rock grains totally:

$$\frac{\partial V_{DLR}}{\partial h} = -\frac{128\pi r_{FP} n_{\infty} k_B T}{\kappa} e^{-\kappa h} \varsigma_{NP} \varsigma_{FP} \text{ ..... (3.3c)}$$

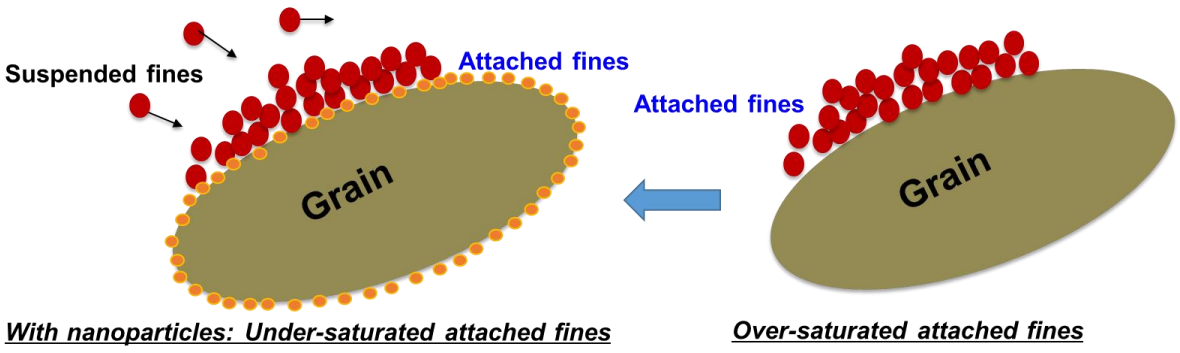


Figure 3.2 Enhanced fines attachment by nanoparticles coated on rock grains

Without nanoparticles pre-treatment:

$$\sigma_{cr,\text{initial}} = \left[1-\left(\frac{\mu r_{FP}^2 U}{2\phi(1-S_{or})r_P F_{ei} y}\right)^2\right]\phi(1-S_{or}) \quad \text{……...……..... (3.4a)}$$

With small numbers of nanoparticles usage to coat rock grains:

$$\sigma_{cr,\text{j}} = \left[1-\left(\frac{\mu r_{FP}^2 U}{2\phi(1-S_{or})r_P y(F_{ei} + \frac{128\pi r_{FP} n_\infty k_B T}{\kappa} e^{-\kappa h}\left[\frac{K_{NP}C_{NP}}{1+K_{NP}C_{NP}}(\varsigma_{GS}-\varsigma_{NP})\varsigma_{FP}\right])}\right)^2\right]\phi(1-S_{or}) \quad \text{(3.4b)}$$

With amounts of nanoparticles to cover the whole surfaces of rock grains totally:

$$\sigma_{cr,\max} = \left[1-\left(\frac{\mu r_{FP}^2 U}{2\phi(1-S_{or})r_P y(F_{ei} + \frac{128\pi r_{FP} n_\infty k_B T}{\kappa} e^{-\kappa h}(\varsigma_{GS}-\varsigma_{NP})\varsigma_{FP}}\right)^2\right]\phi(1-S_{or}) \text{ . (3.4c)}$$

where, $\sigma_{cr,initial}$ is the initial maximum retention concentration of fines (with zero coated nanoparticles adsorption in non-treated system); $\sigma_{cr,\text{j}}$ is the maximum retention concentration of fine particles when the usage of nanoparticles is less than the maximum nanoparticles adsorption capacity pre-coated on rock grains; $\sigma_{cr,\max}$ is the maximum retention concentration of fine particles with the maximum pre-coated nanoparticle adsorption on rock grains.

3.2.2 Nanoparticles and Fines Co-injection with Mutual Reactions

In scenario I, the mass-balance equation of nanoparticles flowing through 1-D permeable medium considering their adsorption onto mobile fines can be written as:

$$\begin{cases} U\dfrac{\partial C_{NP}}{\partial x}+\dfrac{\partial[\phi(1-S_{or})C_{NP}+\hat{C}_{NP}]}{\partial t}=0 \\ \hat{C}_{NP}=\begin{cases}\dfrac{\hat{C}_{NP,cr}K_{NP}C_{NP}}{1+K_{NP}C_{NP}} & \hat{C}_{NP}<\hat{C}_{NP,cr} \\ \hat{C}_{NP,cr}\end{cases} \\ \hat{C}_{NP,cr}=\dfrac{4\phi(1-S_{or})C_{FP}r_{NP}}{r_{FP}} \end{cases} \quad \text{..... (3.5)}$$

Introducing dimensionless length and time:

$$x_D=\frac{x}{L};\qquad t_D=\frac{Ut}{\phi(1-S_{or})L},$$

where, x_D is dimensionless distance; t_D is dimensionless time or injected pore-volume;

Then, Eq. 3.5 can be expressed as the dimensionless form:

$$\begin{cases} \dfrac{\partial C_{NP}}{\partial x_D}+\dfrac{\partial C_{NP}}{\partial t_D}+\dfrac{1}{\phi(1-S_{or})}\dfrac{\partial \hat{C}_{NP}}{\partial t_D}=0 \\ \hat{C}_{NP}=\begin{cases}\dfrac{\hat{C}_{NP,cr}K_{NP}C_{NP}}{1+K_{NP}C_{NP}} & \hat{C}_{NP}<\hat{C}_{NP,cr} \\ \hat{C}_{NP,cr}\end{cases} \\ \hat{C}_{NP,cr}=\dfrac{4\phi(1-S_{or})C_{FP}r_{NP}}{r_{FP}} \end{cases} \quad \text{..... (3.6)}$$

The initial and boundary conditions are:

$$C_{NP}(x_D,0)=0;\quad C_{NP}(0,t_D)=C_{NP,injected};\quad \hat{C}_{NP}(x_D,0)=0; \text{..... (3.7)}$$

Meanwhile, the mass-balance equation of fine particles while considering nanoparticle adsorption on their surfaces can be written as below:

$$\begin{cases} \dfrac{\partial C_{FP}}{\partial x_D}+\dfrac{\partial C_{FP}}{\partial t_D}+\dfrac{1}{\phi(1-S_{or})}\dfrac{\partial \sigma_{cr}}{\partial t_D}=0, & \sigma_{cr,\text{initial}}<\sigma_{cr}<\sigma_{cr,\max} \\ \sigma_{cr}=\left[1-(\dfrac{\mu r_{FP}^2 U}{2\phi(1-S_{or})r_P F_e y})^2\right]\phi(1-S_{or}) & \end{cases} \quad \text{..... (3.8)}$$

After nanoparticle adsorption on fines reaches the maximum capacity, the surface potential of fine particles ς_{FP} would eventually become same as that of adsorbed nanoparticle ς_{NP}. At that time, the ultimate maximum retention concentration of fine particles becomes constant as $\sigma_{cr,\max}$, as shown in Eq. 3.2c.

$$\begin{cases} \dfrac{\partial C_{FP}}{\partial x_D}+\dfrac{\partial C_{FP}}{\partial t_D}=0, & \sigma_{cr}=\sigma_{cr,\max} \\ \sigma_{cr,\max}=\left[1-(\dfrac{\mu r_{FP}^2 U}{2\phi(1-S_{or})r_P F_{e,\max} y})^2\right]\phi(1-S_{or}) & \end{cases} \quad \text{.....} \quad (3.9)$$

As assumed above, the initial concentration of fine particles is non-zero. In addition, in this scenario, the injected fines concentration is designed as same with the initial condition. Thus, both the initial and boundary conditions are described as:

$$C_{FP}(x_D,0)=C_{FP}(0,t_D)=C_{FP,\text{initial}};\quad \sigma_{NP}(x_D,0)=\sigma_{cr,initial} \quad \text{.....} \quad (3.10)$$

3.2.3 Modeling Nanoparticles Pre-flush to Control Fines Migration

As described in section 3.2.1, along with the positive effects of nanoparticles to pre-coat porous media, there are no free d fine particles initially in permeable mediums; in other words, the attachment capacity of rock grains (with respect to fines) becomes "under-saturated". The mass-balance equation of fine particles flowing through the permeable medium with consideration of their deposition onto rock grains are written as:

$$\begin{cases} \dfrac{\partial C_{FP}}{\partial x_D}+\dfrac{\partial C_{FP}}{\partial t_D}+\dfrac{1}{\phi(1-S_{or})}\dfrac{\partial \sigma_{FP}}{\partial t_D}=0 \\ \dfrac{\partial \sigma_{FP}}{\partial t_D}=\lambda C_{FP}\phi L(1-S_{or}) \qquad \sigma_{cr,\text{initial}}<\sigma_{FP}<\sigma_{cr,\max} \\ \sigma_{cr,\max}=\left[1-(\dfrac{\mu r_{FP}^2 U}{2\phi(1-S_{or})r_P F_{e,\max} y})^2\right]\phi(1-S_{or}) \end{cases} \quad \text{..... (3.11)}$$

where, before the moment when the retention concentration of fines on rock grains reaches maximum values, the classic particles capture kinetics are applied to quantify the attachment rates of fines (Vafai, 2005); λ is filtration coefficient, which depends on particle sizes, particle interactions, and flow velocity, usually assumed as constant (Bedrikovetsky, 2011).

The initial and boundary conditions of this scenario are as follows:

$$\begin{aligned} &C_{FP}(x_D,0)=0; && \sigma_{FP}(x_D,0)=\sigma_{cr,initial}; \\ &C_{FP}(0,t_D)=C_0=C_{FP,initial}; && \sigma_{FP}(0,\ t_D)=\lambda\phi L(1-S_{or})C_0 t_D+\sigma_{cr,initial}; \end{aligned} \quad \text{..... (3.12)}$$

3.2.4 Modeling Nanoparticles Pre-flush to Maintain Well Injectivity

In this section, the analytical modeling work will not only consider fines adsorption onto rock grains, but also incorporate fines straining into pore-throats, and the induced formation damage by those two phenomena. The outcomes of this section are to evaluate nanoparticle pre-flush to maintain well injectivity by mitigating fines migration near the wellbore during oil &gas production, or wastes disposal processes. Nanoparticles pre-flush to coat rock grains in 1-D porous medium is one of the most common application approaches to prevent the movement of fine particles in reservoirs. The positive contributions of nanoparticles to reduce fines migration are hypothesized to the increase of the maximum particles retention capacity of host rock grains. By applying method of

characteristics, series of analytic solutions of suspension flow considering particles adsorption/desorption, and particles straining effects are developed for the case of nanoparticles pre-coat and other two reference scenarios. The formulas of permeability impairment, injection index and pressure drop are also derived to evaluate the performance of nanofluid pre-flush to mitigate formation damage caused by fines migration. Analytical solutions are also validated with several existing lab experiments. Meanwhile, this paper provides detailed workflow to explain the lab experimental findings using our analytical models.

Hence, the mass-balance equation of fine particles flowing through the permeable medium, which considers their deposit onto rock grains and their straining or plugging into throats, can be written as:

$$\frac{\partial C_{FP}}{\partial x_D}+\frac{\partial C_{FP}}{\partial t_D}+\frac{1}{\phi(1-S_{or})}\frac{\partial \sigma_{FP}}{\partial t_D}+\frac{1}{\phi(1-S_{or})}\frac{\partial S_{FP}}{\partial t_D}=0 \quad \text{(3.13a)}$$

$$\frac{\partial \sigma_{FP}}{\partial t_D}=\begin{cases}\lambda_a C_{FP}\phi L(1-S_{or}) & \sigma_{cr,0}<\sigma_{FP}<\sigma_{cr,\max} \\ \left[1-\left(\dfrac{\mu r_{FP}^2 U}{2\phi(1-S_{or})r_P\left(F_{ei}+\dfrac{128\pi r_{FP} n_\infty k_B T}{\kappa}e^{-\kappa h}(\varsigma_{GS}-\varsigma_{NP})\varsigma_{FP}\right)y}\right)^2\right]\phi(1-S_{or}) & \sigma_{FP}=\sigma_{cr,\max}\end{cases} \quad \text{(3.13b)}$$

$$\frac{\partial S_{FP}}{\partial t_D}=\lambda_s C_{FP}\phi L(1-S_{or}) \quad \text{(3.13c)}$$

Where, σ_{FP} is the adsorption or attached concentration of fines particles onto rock grains; S_{FP} is the straining or plugging concentration of fines particles; x_D is the dimensionless distance; t_D is the dimensionless time or injected pore volume; In addition, before the retention concentration of fines on rock grains reaches the maximum limit, we apply the particles capture kinetics to quantify the attachment and straining rates of fines; λ_a, λ_s are the filtration coefficient for both particles attachment and straining, respectively.

After nanoparticles are pre-coated onto rock grains prior to fines suspension injection, at the beginning of injection, there are no unattached fines flowing in permeable medium. In other words, nanoparticles have made the retaining capacity of rock grains (with respect to fines) "under-saturated". The initial conditions can be expressed as below for the case of nanoparticles pre-treatment.

Case I: Initial conditions and boundary conditions are listed as,

$$C_{FP}(x_D,0)=0; \quad \sigma_{FP}(x_D,0)=\sigma_{cr,initial}; \quad S_{FP}(x_D,0)=0; \ldots\ldots\ldots\ldots\ldots\ldots\ldots\ldots \quad (3.14)$$

$$C_{FP}(0,t_D)=C_0; \sigma_{FP}=\lambda_a C_0 \phi L(1-S_{or})t_D+\sigma_{cr,initial}; \; S_{FP}=\lambda_s C_0 \phi L(1-S_{or})t_D \ldots\ldots\ldots \quad (3.15)$$

In this study, to quantify the effects of clay content on nanoparticles treatment to maintain well injectivity, reference case II is introduced, that is, without nanoparticles pre-flush, and in which the initial attached fines concentration has just reached or less than the maximum value $\sigma_{cr,initial}$ as shown in Eq. 3.4a. To be simpler, in this reference case, the initial fines concentration is assumed to just equal to the maximum limit. Without nanoparticle effects, the newly injected fines cannot be absorbed any more. Hence, the initial and boundary conditions become as:

Reference case II: Initial conditions and boundary conditions are listed as,

$$C_{FP}(x_D,0)=0;\ \sigma_{FP}(x_D,0)=\sigma_{cr,initial};\ S_{FP}(x_D,0)=0;\ \ldots\ldots\ldots\ldots\ldots\ldots\ldots\ldots\ldots\ldots\ (3.16)$$

$$C_{FP}(0,t_D)=C_{FP,injection};\ \sigma_{FP}=\sigma_{cr,initial};\ S_{FP}=\lambda_s C_0\phi L(1-S_{or})t_D\ \ldots\ldots\ldots\ldots\ldots\ldots\ldots\ldots\ (3.17)$$

However, in fact, because of high content of clay minerals, even initially, the already attached fines in reservoirs has exceeded the retaining capacity of rock grains, which can be confirmed by the decline of even formation water injectivity without any particulates invasion in oilfields. Therefore, to demonstrate the effects of higher clay fines concentration on the performance of pre-coated, this chapter also discusses another reference case II, where even without nanoparticles injection, there are unattached free fine particles, which means the initial fines concentration (including both suspended and attached fines) are larger than the maximum value $\sigma_{cr,initial}$ (Eq.3.4a). There are initial fines ($C_{FP,initial}=\left(\sigma_{FP}(x_D,0)-\sigma_{cr,initial}\right)/\phi\left(1-S_{or}\right)$) freely suspended in porous medium before the invasion of newly injected fines. As for this scenario, different from reference scenario I, the initial condition with unattached fines would bring more negative effects on fluid flow, because that the straining of initially suspended fine particles occurs from the beginning (Eq.6-c).

Reference case III: The initial and boundary conditions become:

$$C_{FP}(x_D,0)=\frac{\sigma_{FP}(x_D,0)-\sigma_{cr,initial}}{\phi\left(1-S_{or}\right)};\ \sigma_{FP}(x_D,0)=\sigma_{cr,initial};\ S_{FP}(x_D,0)=0;\ \ldots\ldots\ (3.18)$$

$$C_{FP}(0,t_D)=C_{FP,injection};\ \sigma_{FP}=\sigma_{cr,initial};\ S_{FP}=\lambda_s C_0\phi L(1-S_{or})t_D;\ \ldots\ldots\ldots\ldots\ldots\ (3.19)$$

3.3 Analytical Solutions and Validations

3.3.1 Scenario I: Co-injection of Nanoparticles and Fine particles

3.3.1.1 MOC Analytical Solutions

The general analytical solutions for multi-phase multi-component transport system are derived using Method of Characteristic, as shown in Appendix A. The problem discussed in this scenario is a typical Riemann problem with uniform initial conditions and step-wise changes at the boundary. The detailed MOC derivations of solutions of scenario I are presented as below.

The combination of Eq. 3.6-Eq. 3.10 forms a system of quasilinear first-order partial differential equations with two independent variables, C_{NP} (x_D, t_D) and C_{FP} (x_D, t_D):

$$L_1 = \frac{\partial C_{NP}}{\partial x_D} + (1 + \frac{1}{\phi(1-S_{or})} \frac{\partial \hat{C}_{NP}}{\partial C_{NP}}) \frac{\partial C_{NP}}{\partial t_D} + \frac{1}{\phi(1-S_{or})} \frac{\partial \hat{C}_{NP}}{\partial C_{FP}} \frac{\partial C_{FP}}{\partial t_D} = 0$$
$$L_2 = \frac{1}{\phi(1-S_{or})} \frac{\partial \sigma_{cr}}{\partial C_{NP}} \frac{\partial C_{NP}}{\partial t_D} + \frac{\partial C_{FP}}{\partial x_D} + \frac{\partial C_{FP}}{\partial t_D} = 0 \quad \text{…….. (3.20)}$$

To ensure the characteristic lines of both variables C_{NP} (x_D, t_D) and C_{FP} (x_D, t_D) along the same direction, we define a linear combination of the above differential equations, as $\lambda_1 L_1 + \lambda_2 L_2$ to yield:

$$\lambda_1 \frac{\partial C_{NP}}{\partial x_D} + \left[\lambda_1 (1 + \frac{1}{\phi(1-S_{or})} \hat{C}_{NP,\,NP}) + \lambda_2 \frac{1}{\phi(1-S_{or})} \sigma_{cr,\,NP} \right] \frac{\partial C_{NP}}{\partial t_D}$$
$$+ \lambda_2 \frac{\partial C_{FP}}{\partial x_D} + \left[\lambda_2 + \lambda_1 \frac{1}{\phi(1-S_{or})} \hat{C}_{NP,\,FP} \right] \frac{\partial C_{FP}}{\partial t_D} = 0 \quad \text{……...……. (3.21)}$$

where L_1 and L_2 are the functions of derivatives of two variables; λ_1, λ_2 are the linear combination coefficients.

Inferred from Eq. A.5 in Appendix A, the two characteristic directions can be obtained as:

$$\sigma^{\pm}=\frac{1}{2}\left[\left(2+\frac{1}{\phi(1-S_{or})}\hat{C}_{NP,\,NP}\right)\pm\sqrt{\left[\frac{1}{\phi(1-S_{or})}\hat{C}_{NP,\,NP}\right]^2+4\left[\frac{1}{\phi(1-S_{or})}\right]^2\hat{C}_{NP,\,FP}\,\sigma_{cr,\,NP}}\right] \tag{3.22}$$

Followed by, the composition diagram is determined along the fast path and slow path, respectively, as shown in Figure 3.3.

$$\begin{cases} t_D=\sigma^{+}x_D \\ \dfrac{dC_{NP}}{dC_{FP}}=\dfrac{\dfrac{1}{\phi(1-S_{or})}\hat{C}_{NP,\,NP}-\sigma^{+}+1}{\dfrac{1}{\phi(1-S_{or})}\sigma_{cr,\,NP}} \end{cases} \quad \text{..... (3.23)}$$

$$\begin{cases} t_D=\sigma^{-}x_D \\ \dfrac{dC_{NP}}{dC_{FP}}=\dfrac{\dfrac{1}{\phi(1-S_{or})}\hat{C}_{NP,\,NP}-\sigma^{-}+1}{\dfrac{1}{\phi(1-S_{or})}\sigma_{cr,\,NP}} \end{cases} \quad \text{..... (3.24)}$$

To clarify the application of this MOC solution, this chapter presents an application example, as shown in Figure 3.4, where the injected and initial conditions are presented as injected point J ($C_{FP,\text{injected}}=0.02\ \text{m}^3/\text{m}^3$; $C_{NP,\text{injected}}=0.00033\ \text{m}^3/\text{m}^3$) and initial point I ($C_{FP,\text{initial}}=0.02\ \text{m}^3/\text{m}^3$; $C_{NP,\text{injected}}=0$). The values of other parameters designed in analytical solutions are defined in Table 3.1. Along the slow path from point J to Q, the slopes of characteristic lines show a downward trend from 2.695 to 2.214, which implies that the slow path from the state J to Q fans clockwise, as shown in Fig.6-a. We have a spreading wave from point J to Q. However, along the fast path from point Q to point I, the slopes of characteristic lines increase from 0.164 to 1.00, which fans

counterclockwise; thus, there is a shock from point Q to point I. To determine this shock point, we apply the compatibility condition (Hankins, 2004; Lake, 1989), the left side of shock front (upstream) is a constant-state region and the right side of shock front (downstream) is the initial-condition region where the fines concentration wave velocity is in unity.

In view of the above analysis, for the particles concentration profiles along the one-dimensional permeable medium, there are generally four different-state regions from the injected point to the initial point, which include: (1) injection-condition region ($C_{FP,\text{injected}} = 0.02\ \text{m}^3/\text{m}^3;\ \ C_{NP,\text{injected}} = 0.00033\ \text{m}^3/\text{m}^3$); (2) spreading-wave region; (3) constant-state region ($C_{FP} = 0;\ \ C_{NP} = 2.57\times10^{-6}\ \text{m}^3/\text{m}^3$) and (4) initial-condition region ($C_{FP,\text{initial}} = 0.02\ \text{m}^3/\text{m}^3;\ \ C_{NP,\text{injected}} = 0$). Meanwhile, a genuine shock occurs to maintain the physical integrity of analytical solutions that can be determined by Eq. 3.25-3.26 (Moghanloo 2012a, b; Noh et al. 2004). In this scenario, this shock front represents the "nanoparticle absorption front" that connects the constant-state region and the initial-condition region, as shown in Fig. 3.5b.

$$\sigma^{-} = \tilde{\sigma}_{NP} = \tilde{\sigma}_{FP} \quad \text{..... (3.25)}$$

$$\left(\frac{dt_D}{dx_D}\right)^{-} = \frac{\left[C_{FP}^{\ initial} + \dfrac{\sigma_{cr2}^{\ initial}}{\phi(1-S_{or})}\right] - \left[C_{FP}^{\ const} + \dfrac{\sigma_{cr2}^{\ const}}{\phi(1-S_{or})}\right]}{\left[C_{FP}^{\ initial} - C_{FP}^{\ const}\right]} = \frac{\left[C_{NP}^{\ initial} + \dfrac{\hat{C}_{NP}^{\ initial}}{\phi(1-S_{or})}\right] - \left[C_{NP}^{\ const} + \dfrac{\hat{C}_{NP}^{\ const}}{\phi(1-S_{or})}\right]}{\left[C_{NP}^{\ initial} - C_{NP}^{\ const}\right]} \quad \text{(3.26)}$$

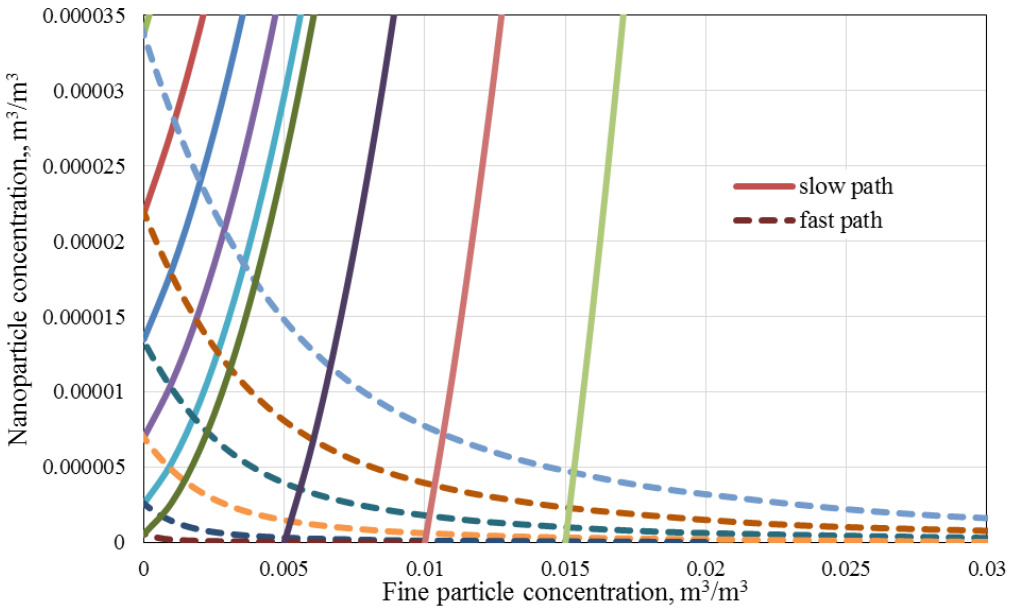


Figure 3.3 Composition path diagram of fine particles and nanoparticles concentration along fast and slow path

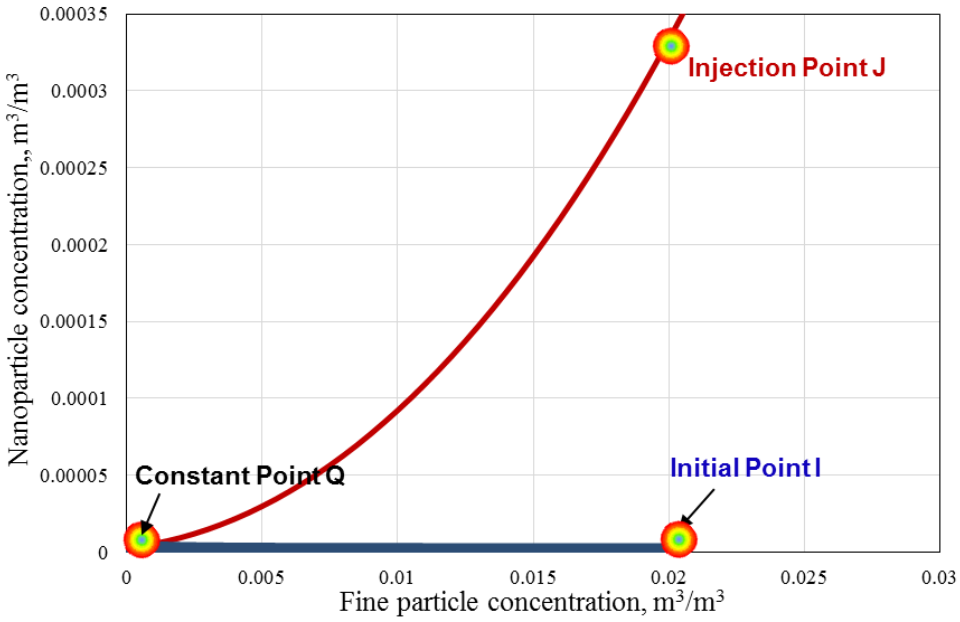


Figure 3.4 Scenario I: composition path from the injection point J to initial point I (J：C_{NP}=0.00033， C_{FP}=0.02；constant point Q：C_{NP}=2.57E-6， C_{FP}=0；initial point I：C_{NP}=0， C_{FP}=0.02)

3.3.1.2 Verification with Numerical Simulations

To verify the above MOC solutions, numerical simulations are applied using STARS, the CMG's three-phase multi-component simulator. Motivated by the similar treatments to expand conventional simulator's capabilities to address shale gas problems (Moghanloo, et al. 2015), this chapter defines the mutual relationships among nanoparticles, fines particles, and the complex of nano-fine particles as two fictitious chemical reactions. Those two reactions consist of a fictitious chemical reaction between nanoparticles and fine particles (Eq. 3.27) and the attachment reaction of the complex of fines-nanoparticles on the rock grains (Eq. 3.28). The sequence of those two defined fictitious reactions is that, firstly, fine particles C_1 and nanoparticles C_2 reacted together to generate the complex of nano-fine particles in the fluid phase, C_{12}, and then C_{12} deposits as solid phase on the rock grains. Obviously, the fictitious chemical reactions can mime the physical processes that has been described in Figure. 3.1a, including nanoparticles' preferential adsorption on fine particles and the subsequent attachment of fine particles on rock grains. Therefore, the two fictitious chemical reactions defined in CMG simulation could be applied to verify our analytical solutions of scenario I.

$$\textit{Chemical reaction I in fluid phase}: \quad C_1 + C_2 \rightarrow C_{12} \quad \text{..... (3.27)}$$

$$\textit{Chemical reaction II in solid phase}: \quad C_{12} \xrightarrow{deposit} C_{12,\text{att}} \quad \text{..... (3.28)}$$

where C_1 is the nanoparticles in fluid phase defined in fictitious chemical reaction; C_2 is the fine particles in fluid phase defined in fictitious chemical reaction; C_{12} is the nanoparticles -fine complex defined in fictitious chemical reaction; $C_{12,attachment}$ is the nanoparticle-fines complex attached on rock grains from fluid phase to solid phase.

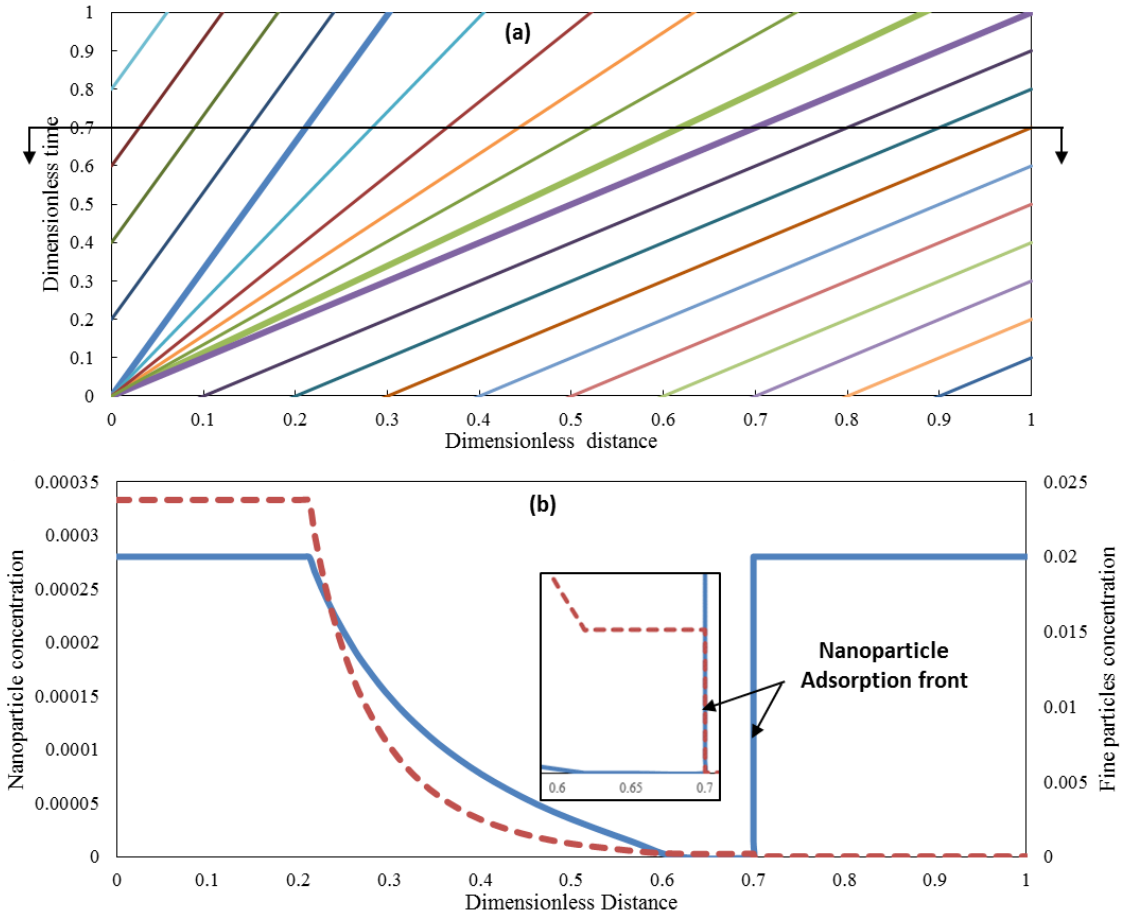


Figure 3.5 Scenario I: Distance–time diagram with characteristic lines and nanoparticles & fines concentration profile along 1-D medium at t_D= 0.7 (a: Distance-time diagram; b: Fine particles concentration (solid line) and nanoparticles concentration (dash line))

Figure 3.6 shows the comparison of fine particles concentration profile obtained from both analytical model and numerical simulation at the same injected pore-volume 0.7. Except for small inevitable numerical dispersion effects in finite-difference simulations, where the shape of shock front spreads, the results calculated from both approaches are consistent. Figure 3.7 compares the increase of cumulative fines production with time. As indicated from those matching plots, the MOC solutions of scenario I have been confirmed with excellent accuracy.

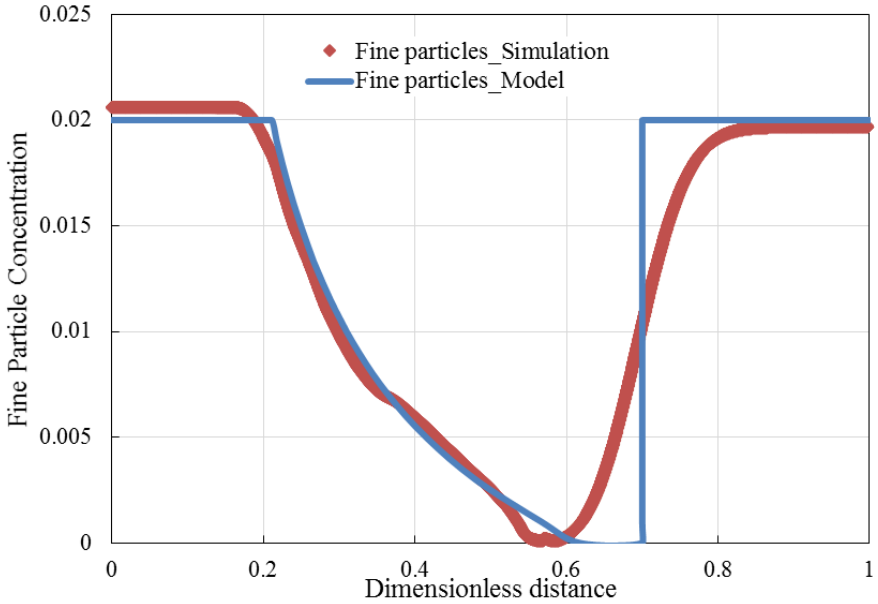


Figure 3.6 Scenario I: Comparison of fine particle concentration profile at t_D=0.7 obtained from numerical simulation (solid line) and MOC solution (dashed line)

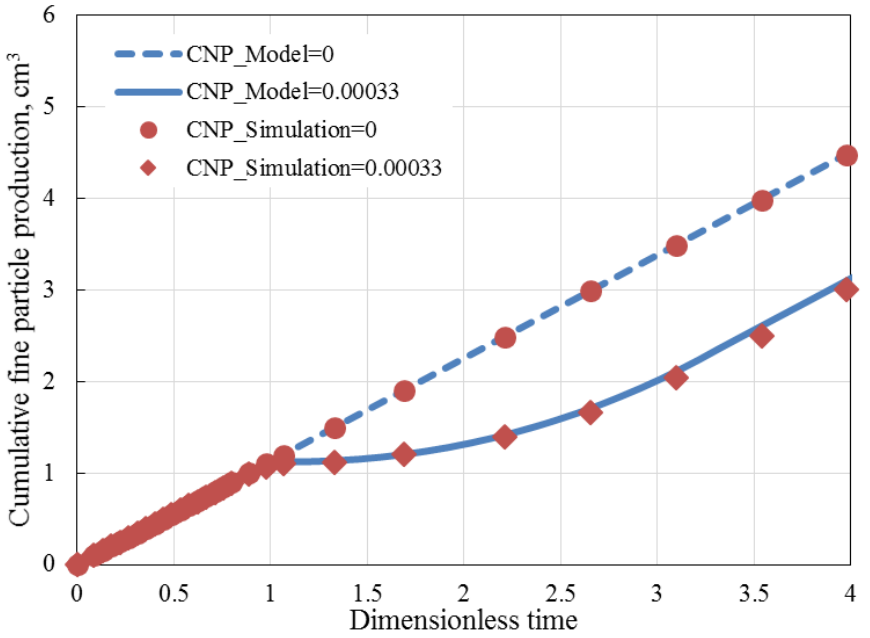


Figure 3.7 Scenario I: Comparison between fine particles cumulative production obtained from numerical simulation (solid line) and MOC solution (dashed line)

3.3.2 Scenario II: Nanoparticles Pre-flush Prior to Fines Invasion

3.3.2.1 MOC Analytical Solutions

For the system of Eq. 3.11 and Eq. 3.12, analogous to the workflow of the MOC solution in scenario I, the detailed derivation of the MOC solution is presented in Appendix B. The values of parameters that appear in analytical solutions are defined in Table 3.1. In Figure B-1, there are four zones to describe the propagation of suspended fines concentration front and attached fines concentration front in the plane of "distance-time diagram". As described above, because of the pre-coated nanoparticles on surfaces of rock grains prior to fines suspension injection, the attachment capacity of rock grains (with respect to fines) becomes "under-saturated." which means the rock grains can still capture more injected fines until the maximum retention concentration of fines is reached. For the suspended fine particles concentration profiles shown in Figure 3.8 and retained particles concentration profile shown in Figure 3.9, there does appear a "suspended fines concentration front" where divides the initial condition from the injected condition, downstream of which in zone I, the suspended fines and attached fines concentration are at the initial condition. Upstream of this front in zone II, the suspended fines concentration profile is in steady state, and the retained fines concentration increases proportionally with time (Eq. B.4). At t_{Dc}, the retained fines concentration at the inlet reaches maximum, since then there does appear an "attached front", no fines could be captured upstream of this front in zone IV, and downstream of this front in zone III, the capture of fines onto rock grains still takes place.

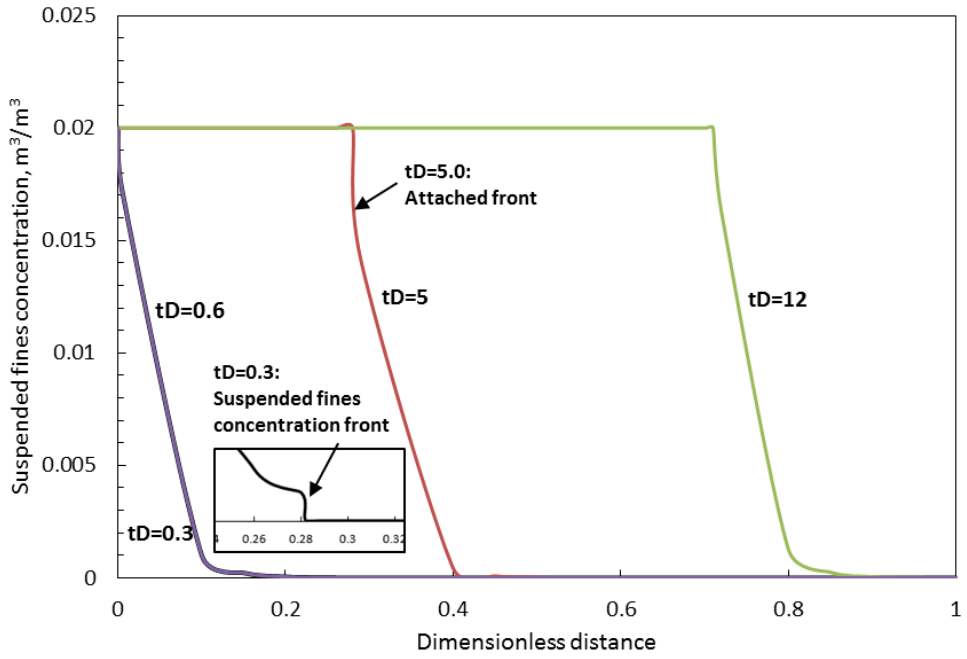


Figure 3.8 Scenario II: Suspended fines concentration profile along 1-D permeable medium at different dimensionless times (t_D=0.3, 0.5, 5.0 and 12.0)

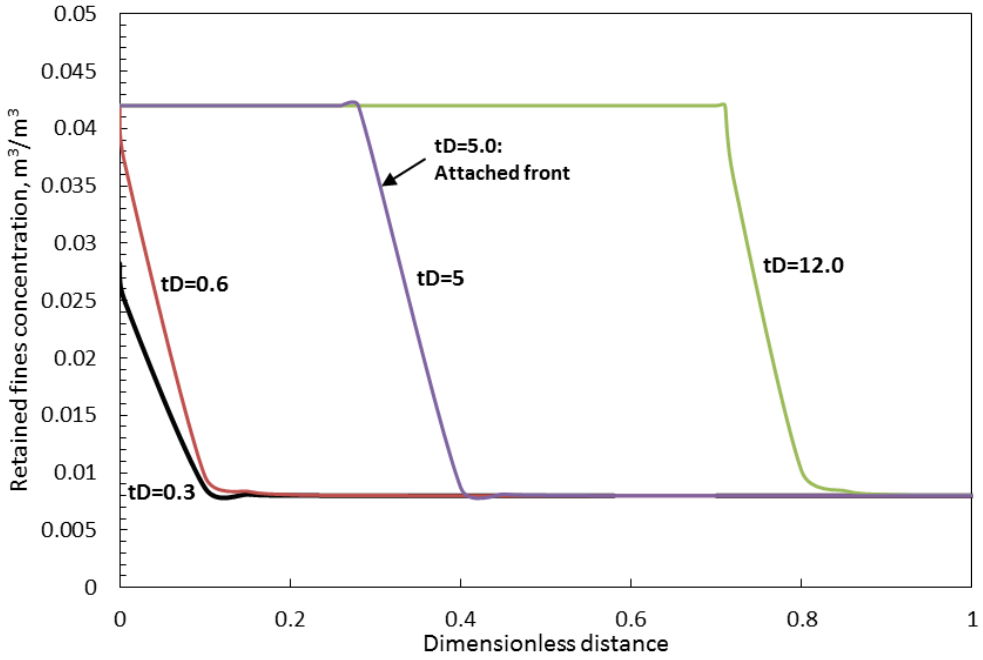


Figure 3.9 Scenario II: Retained fines concentration on rock grains along the permeable medium at different dimensionless times (t_D=0.3, 0.62, 5.0 and 12.0)

3.3.2.2 Validation with Experimental Results

To validate the analytical solutions of scenario II, analytical solutions are used to match the existing lab experimental results (Huang, 2008a). Inferred from their lab experiments, some experimental parameters are concluded as follows, i.e., flow velocity 1.7×10^{-4}m/s, length of permeable medium 0.33m, the injected fines concentration 5.2×10^{-5}m^3/m^3, and nanoparticle concentration 3.0×10^{-6}m^3/m^3. Meanwhile, inferred from lab results, the moment t_{Dc} is about 5.0, in other words, the term $\frac{\sigma_{cr,\max}-\sigma_{cr,initial}}{\lambda\phi L(1-S_{or})C_0}=5.0$ in Eq. B-11. The filtration coefficient is assumed as 15m^{-1}. Substituting all the values of parameters into Eq. B.11 to obtain the effluent history of fines concentration. As shown in Figure 3.10, the analytical solutions of scenario II can explain the laboratory experiments results very well.

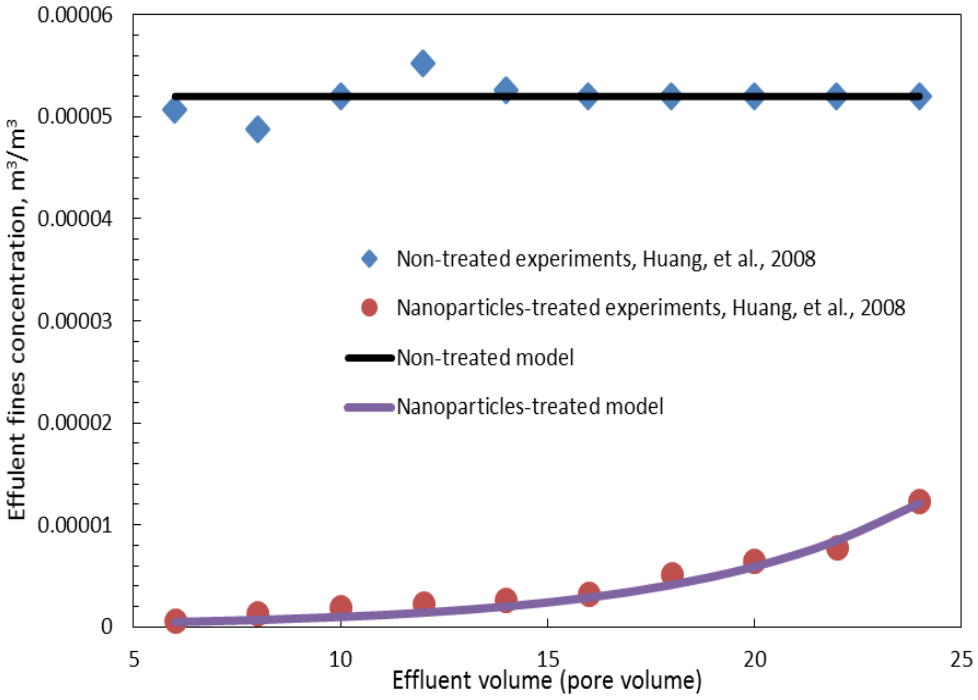


Figure 3.10 Comparison of fines effluent concentration obtained from analytical models (solid line) and experimental results (Huang, 2008a) (discrete points)

Table 3-1 Values of parameters in MOC solutions of all scenarios

Nanoparticle Langmuir adsorption constant K, m^3/m^3	100	Fine particle density, ρ_{FP}, kg/m^3	2000
Bulk number density of ions, n_∞, number/m^3	6.022×10^{25}	Viscosity, μ, mPa.s	1
Force lever of drag force and normal force, l_d, l_n,, m	l_d / l_n=1.73	Nanoparticle radius, r_{NP}, nm	20
Boltzmann's constant, k_B, J/K	1.381×10^{-21}	Fine particle radius, r_{FP}, μm	1.0
Hamaker constant, A_{132}, J	7.73×10^{-21}	Pore size radius, r_p, μm	10.0
Inverse Debye length, κ, m^{-1} (Elimelech, 1995)	1.05×10^{8}	Flow velocity, U, m/s	0.006
Surface-to-surface separation length, h, m	0.15	Porosity, ϕ, decimal	$h<<r_s$
Residual oil saturation, S_{or}, decimal	0.25	Dimensionless drag empirical coefficient	5
Atomic collision diameter in Lennard-Jones potential, nm	-0.001	Nanoparticle surface charge, ς_{NP}, mV	0.5
Fine particle surface Zeta potential, ς_{FP}, mV	-0.015	Absolute temperature of reservoir, T, K,	398
Grain surface Zeta potential, ς_{GS}, mV	-0.017	Lifting force coefficient, χ	640
Liquid density, ρ_l, kg/m^3	1000	Cross-sectional area of sand pack, A, m^2	0.001
Characteristic wave length of interaction, l, nm	100	Length of 1-D sand pack, L, m	0.5
Formation damage coefficient for straining, β_s	1000	Filtration coefficient for straining, λ_s, m^{-1}	2
Formation damage coefficient for straining, β_a	5	Filtration coefficient for attachment, λ_a, m^{-1}	60

3.3.3 Nanoparticles Pre-flush to Maintain Well Injectivity

3.3.3.1 Case I: Pre-treatment with Nanoparticles to Maintain Well Injectivity

In this case of nanoparticle pre-treatment porous medium, as described in Eq.3.13, the retaining capacity of rock grains toward the flowing fines has been under-saturated. The boundary and initial conditions are described in Eq. 3.14 and Eq.3.15.

The problem in this scenario is a Riemann problem with uniform initial conditions and step-wise changes of boundary conditions. Analytical solutions for "under-saturated" porous medium, $\sigma_{cr,\text{initial}} < \sigma < \sigma_{cr,\max}$, can be obtained by methods of characteristics. Firstly, substituting the particles capture kinetics equation into mass- balance equation Eq.3.13a yields,

$$\text{Suspended fines: } \frac{\partial C_{FP}}{\partial x_D} + \frac{\partial C_{FP}}{\partial t_D} + \left(\lambda_a + \lambda_s\right) C_{FP} L = 0 \quad \text{..... (3.29)}$$

Applying the concept of MOC, the following ordinary differential equations are obtained:

$$\frac{dC_{FP}}{dt_D} = -\left(\lambda_a + \lambda_s\right) C_{FP} L \text{, along } \frac{dx_D}{dt_D} = 1 \text{..... (3.30)}$$

Combined with the boundary conditions, Eq.3.30, leads to the solution of suspended fines concentration in zone I and zone II, as shown in Figure 3.11:

$$0 < t_D < t_{Dc}$$

$$\begin{cases} \text{Zone I } (x_D > t_D): & C_{FP} = 0; \quad \sigma_{FP} = \sigma_{cr,\text{initial}}, \\ \text{Zone II } (x_D < t_D): & C_{FP} = C_0 \exp\left(-\left(\lambda_a + \lambda_s\right) L x_D\right) \end{cases} \quad \text{..... (3.31)}$$

Let us express the suspended fines concentration and strained fines concentration by attached fines:

$$C_{FP} = \frac{1}{\lambda_a \phi L(1-S_{or})} \frac{\partial \sigma_{FP}}{\partial t_D} \quad \text{..... (3.32a)}$$

$$\frac{\partial S_{FP}}{\partial t_D} = \frac{\lambda_s}{\lambda_a} \frac{\partial \sigma_{FP}}{\partial t_D} \quad \text{..... (3.32b)}$$

Substituting Eq. 3.32 into the mass-balance equation Eq. 3.13,

$$\frac{\partial}{\partial t_D}\left(\frac{1}{\lambda_a L}\frac{\partial \sigma_{FP}}{\partial x_D}\right) + \frac{\partial}{\partial t_D}\left(\frac{1}{\lambda_a L}\frac{\partial \sigma_{FP}}{\partial t_D}\right) + \left(1+\frac{\lambda_s}{\lambda_a}\right)\frac{\partial \sigma_{FP}}{\partial t_D} = 0 \quad \text{..... (3.33)}$$

Then, integrating in t_D concerning the initial condition to obtain,

$$\frac{\partial \sigma_{FP}}{\partial x_D} + \frac{\partial \sigma_{FP}}{\partial t_D} + L\left(\lambda_a+\lambda_s\right)\left(\sigma_{FP} - \sigma_{cr,initial}\right) = 0 \quad \text{..... (3.34)}$$

The characteristic forms of differential equation Eq.3.34 are:

$$\frac{d\sigma_{FP}}{dt_D} = -L\left(\lambda_a+\lambda_s\right)\left(\sigma_{FP} - \sigma_{cr,initial}\right) \text{ , along } \frac{dx_D}{dt_D} = 1 \quad \text{..... (3.35)}$$

Combined with the boundary conditions leads to the solution of attached fines concentration in zone II,

$$\sigma_{FP} = \lambda_a C_0 \phi L(1-S_{or})\left(t_D - x_D\right)\exp\left(-\left(\lambda_a+\lambda_s\right)Lx_D\right) + \sigma_{cr,initial} \quad \text{..... (3.36)}$$

Similarly, for the strained fines concentration, the characteristic forms of differential equations can be obtained using strained fines. Combined with the boundary conditions leads to the solution of straining fines concentration in zone II,

$$\frac{dS_{FP}}{dt_D} = -L\left(\lambda_a+\lambda_s\right)S_{FP} \text{ , along } \frac{dx_D}{dt_D} = 1 \quad \text{..... (3.37)}$$

$$S_{FP} = \lambda_s C_0 \phi L(1-S_{or})\left(t_D - x_D\right)\exp\left(-\left(\lambda_a+\lambda_s\right)Lx_D\right) \quad \text{..... (3.38)}$$

In addition, the strained fines concentration in zone II can also be directly obtained by integrating Eq.3.13c in t_D from the initial condition at t_D=0 as shown in Eq.3.39. Since

the suspended fines are zero in zone I, which results in the strained fines concentration in zone I to be zero. Therefore, in zone II, the strained fines concentration becomes an integration of Eq.3.13c from the suspended fines front (will be introduced later) $t_D = x_D$.

$$S_{FP} = \lambda_s \phi L(1-S_{or}) \int_0^{t_D} C_{FP} dt_D = \lambda_s \phi L(1-S_{or}) \int_{x_D}^{t_D} C_{FP} dt_D \quad \text{..... (3.39)}$$

At the moment of t_{DC}, as shown in Eq. 3.41, the retained fines concentration on rock grains at the inlet reaches the maximum value $\sigma_{cr,\max}$ (Eq. 3.4c). It does mean that there would be no more fines to be attached on rock grains, and the injected condition will spread through the porous medium.

$$t_{Dc} = \frac{\sigma_{cr,\max} - \sigma_{cr,initial}}{\lambda_a \phi L(1-S_{or}) C_0} \quad \text{..... (3.40)}$$

At this moment, the retained and suspended fines concentration along the characteristic line starting from the point of $(0, t_{Dc})$ in Figure 3.11 can be obtained by substituting Eq. 3.40 into Eq. 3.36 and Eq. 3.38, respectively. It is worth mentioning that there does appear an "erosion front" after the maximum retention concentration of fines is reached.

Retained fines concentration:

$$\sigma_{FP} = \left(\sigma_{cr,\max} - \sigma_{cr,\text{initial}}\right) \exp\left(-\left(\lambda_a + \lambda_s\right) L x_D\right) + \sigma_{cr,\text{initial}} \text{.....} \quad \text{(3.41a)}$$

Suspended fines concentration:

$$C_{FP} = C_0 \exp\left(-\left(\lambda_a + \lambda_s\right) L x_D\right) \text{.....} \quad \text{(3.41b)}$$

Strained fines concentration:

$$S_{FP} = \frac{\lambda_s}{\lambda_a}\left(\sigma_{cr,\max} - \sigma_{cr,initial}\right)\exp\left(-\left(\lambda_a + \lambda_s\right)Lx_D\right) \text{..... (3.41c)}$$

Based on the continuity condition derived by (Bedrikovetsky, 2011), around the "erosion front", $C^+ = C^- = C_0$, and thus the time-derivative of the attached fines concentrations along this erosion front can be expressed from Eq. 3.13b:

$$\frac{\partial \sigma_{FP}}{\partial t_D} = \lambda_a \phi L(1 - S_{or})C_0 \text{ .....(3.42)}$$

By substituting Eq. 3.42 into Eq.3.34, the distance-derivative of the attached fines concentration is presented along this erosion front,

$$\frac{\partial \sigma_{FP}}{\partial x_D} = -\lambda_a \phi L(1 - S_{or})C_0 - L\left(\lambda_a + \lambda_s\right)\left(\sigma_{cr,\max} - \sigma_{cr,initial}\right) \text{..... (3.43)}$$

In addition, the total derivative of the maximum attached fines concentration along the erosion front can be written as:

$$\sigma_{cr,\max} = \sigma_{FP}\left(x_{cr}\left(t_D\right), t_D\right) \Rightarrow \frac{\partial \sigma_{FP}}{\partial t_D} + \frac{dx_{cr}}{dt_D}\frac{\partial \sigma_{FP}}{\partial x_D} = 0 \text{ ..... (3.44)}$$

By substituting Eq. 3.42 and Eq. 3.43 into Eq.3.44, the moving velocity of erosion front is expressed as,

$$\frac{dx_{cr}}{dt_D} = \frac{\lambda_a \phi L(1 - S_{or})C_0}{\lambda_a \phi L(1 - S_{or})C_0 + L\left(\lambda_a + \lambda_s\right)\left(\sigma_{cr,\max} - \sigma_{cr,initial}\right)} = const. \text{ ..... (3.45)}$$

Therefore, the moving trajectory of particles erosion front can be represented by integrating Eq.3.45:

$$x_{cr} = \frac{\lambda_a \phi L(1 - S_{or})C_0}{\lambda_a \phi L(1 - S_{or})C_0 + L\left(\lambda_a + \lambda_s\right)\left(\sigma_{cr,\max} - \sigma_{cr,initial}\right)}\left(t_{cr} - \frac{\sigma_{cr,\max} - \sigma_{cr,initial}}{\lambda_a \phi L(1 - S_{or})C_0}\right) \text{..... (3.46a)}$$

$$t_{cr} = \frac{\lambda_a \phi L(1 - S_{or})C_0 + L\left(\lambda_a + \lambda_s\right)\left(\sigma_{cr,\max} - \sigma_{cr,initial}\right)}{\lambda_a \phi L(1 - S_{or})C_0}x_{cr} + \frac{\sigma_{cr,\max} - \sigma_{cr,initial}}{\lambda_a \phi L(1 - S_{or})C_0} \text{..... (3.46b)}$$

Inferred from Eq. 3.34, the slopes of characteristic lines in zone III are in unity, therefore, the characteristic lines starting from any intersection points along the erosion front paths can be represented as:

$$\text{Line III: } x_D - x_{cr} = t_D - t_{cr} \quad \text{..... (3.47)}$$

By combining Eq. 3.46 and Eq. 3.47, the starting point along the erosion front at zone III can be obtained, as shown in Figure 3.11.

$$x_{cr0} = \left(t_D - x_D\right)\frac{\lambda_a \phi (1-S_{or})C_0}{\left(\lambda_a + \lambda_s\right)\left(\sigma_{cr,\max} - \sigma_{cr,initial}\right)} - \frac{1}{\left(\lambda_a + \lambda_s\right)L} \quad \text{..... (3.48a)}$$

$$t_{cr0} = \left(t_D - x_D\right)\frac{\lambda_a \phi (1-S_{or})C_0 + \left(\lambda_a + \lambda_s\right)\left(\sigma_{cr,\max} - \sigma_{cr,initial}\right)}{\left(\lambda_a + \lambda_s\right)\left(\sigma_{cr,\max} - \sigma_{cr,initial}\right)} - \frac{1}{\left(\lambda_a + \lambda_s\right)L} \quad \text{..... (3.48b)}$$

At the starting point $\left(x_{cr0}, t_{cr0}\right)$, the retained fines concentration is the maximum value determined by Eq. 3.4c. The suspended and strained fines concentrations are the same with the injected conditions, and thus, by combining the characteristic equations of Eq. 3.30, Eq.3.35 and Eq.3.37 with the boundary condition at this starting point, the retained, suspended and straining fines concentration in zone III are obtained, respectively.

$$\sigma_{FP} = \left(\sigma_{cr,\max} - \sigma_{cr,initial}\right)\exp\left(-\left(\lambda_a + \lambda_s\right)L\left(x_D - \left(t_D - x_D\right)\frac{\lambda_a \phi (1-S_{or})C_0}{\left(\lambda_a + \lambda_s\right)\left(\sigma_{cr,\max} - \sigma_{cr,initial}\right)} + \frac{1}{\left(\lambda_a + \lambda_s\right)L}\right)\right) + \sigma_{cr,initial} \quad \text{(3.49a)}$$

$$C_{FP} = C_0 \exp\left(-\left(\lambda_a + \lambda_s\right)L\left(x_D - \left(t_D - x_D\right)\frac{\lambda_a \phi (1-S_{or})C_0}{\left(\lambda_a + \lambda_s\right)\left(\sigma_{cr,\max} - \sigma_{cr,initial}\right)} + \frac{1}{\left(\lambda_a + \lambda_s\right)L}\right)\right) \quad \text{(3.49b)}$$

$$S_{FP} = \lambda_s C_0 \phi L (1-S_{or})\left(t_D - x_D\right)\exp\left(-\left(\lambda_a + \lambda_s\right)L x_D\right) \quad \text{..... (3.49c)}$$

At $t = t_{cr1}(x_D = 1)$, the erosion front reaches the outlet of 1-D permeable medium, and the whole 1-D permeable medium has reached the state with the maximum retention concentration of fine particles, and thus, in Zone IV, the retained fines concentration would become constant, $\sigma_{cr,\max}$.

$$t_{cr}(x_D = 1) = \frac{\phi(1-S_{or})C_0 + \sigma_{cr,\max}}{\phi(1-S_{or})C_0} x_D\Big|_{x_D=1} + \frac{\sigma_{cr,\max}}{\lambda\phi L(1-S_{or})C_0} \quad \text{..... (3.50)}$$

$$\text{Zone IV: } \begin{cases} \sigma_{FP} = \sigma_{cr,\max}, & \text{(a)} \\ C_{FP} = C_0 \exp\left(-\lambda_s L x_D\right) & \text{(b)} \\ S_{FP} = \lambda_s C_0 \phi L(1-S_{or})\left(t_D - x_D\right)\exp\left(-\lambda_s L x_D\right) & \text{(c)} \end{cases} \quad \text{..... (3.51)}$$

So far, the suspended, attached and straining fine concentration coupled with the effects of pre-coated nanoparticles on rock grains along the 1-D permeable medium at any time have been obtained, as shown in Table 3.2.

3.3.3.2 Case II: No Nanoparticles in Porous Medium with Low Clay Content

Substituting particles straining kinetics into mass-balance equation Eq.3.13a yields,

$$\text{Suspended fines: } \frac{\partial C_{FP}}{\partial x_D} + \frac{\partial C_{FP}}{\partial t_D} + \lambda_s C_{FP} L = 0 \quad \text{..... (3.52)}$$

Similar to case I, suspended fines concentration is expressed by strained fines concentration:

$$C_{FP} = \frac{1}{\lambda_s \phi L(1-S_{or})} \frac{\partial S_{FP}}{\partial t_D} \quad \text{..... (3.53)}$$

Substituting Eq. 3.53 into the mass-balance model Eq. 3.52, and integrating in t_D concerning the initial condition to obtain,

Strained fines: $\frac{\partial S_{FP}}{\partial x_D}+\frac{\partial S_{FP}}{\partial t_D}+L\lambda_s S_{FP}=0$ ……. (3.54)

The characteristic forms of differential equation Eq.3.52 and Eq.5.54 are presented:

$\frac{dC_{FP}}{dt_D}=-\lambda_s C_{FP}L$, and $\frac{dS_{FP}}{dt_D}=-\lambda_s S_{FP}L$, along $\frac{dx_D}{dt_D}=1$……..…….. (3.55)

Combining Eq. .55 with the boundary conditions Eq. 3.17 leads to the solutions of suspended, strained and attached fines concentration in zone II in Figure 3.11,

$$\begin{cases} C_{FP}=C_0\exp\left(-\lambda_s L x_D\right), & \text{(a)} \\ \sigma_{FP}=\sigma_{cr,initial} & \text{(b)} \\ S_{FP}=\lambda_s C_0\phi L(1-S_{or})\left(t_D-x_D\right)\exp\left(-\lambda_s L x_D\right), & \text{(c)} \end{cases} \text{……..... (3.56)}$$

In zone I, the suspended, strained and attached fines concentration are always equal to the initial conditions:

$$\begin{cases} C_{FP}=0, & \text{(a)} \\ S_{FP}=0, & \text{(b)} \\ \sigma_{FP}=\sigma_{cr,initial} & \text{(c)} \end{cases} \text{…… (3.57)}$$

3.3.3.3 Case III: No Nanoparticles in Porous Medium with High Clay Content

Analogues to case II, the characteristic forms of differential equation of suspended and strained fines concentrations are:

$\frac{dC_{FP}}{dt_D}=-\lambda_s C_{FP}L$, along $\frac{dx_D}{dt_D}=1$ ……..... (3.58)

In zone I, in Figure 3.11, by combining with the initial condition along the porous medium, the suspended fines concentration can be obtained as:

$C_{FP}=\frac{\sigma_{FP}(x_D,0)-\sigma_{cr,initial}}{\phi\left(1-S_{or}\right)}\exp\left(-\lambda_s L t_D\right)$ ……..…. (3.59)

The fines straining concentration can be also derived by integrating the suspended fines concentration in Eq.3.13c from the initial conditions:

$$S_{FP} = \left(\sigma_{FP}(x_D, 0) - \sigma_{cr,initial}\right)\left(1 - \exp\left(-\lambda_s L t_D\right)\right) \quad \text{..... (3.60)}$$

Combining with the boundary conditions Eq.3.19 leads to the solutions of suspended and attached fines concentration in zone II. The strained fines concentration is obtained by integrating suspended fines concentration in zone II from $t_D = 0$.

$$\begin{cases} C_{FP} = C_0 \exp\left(-\lambda_s L x_D\right), & \text{(a)} \\ \sigma_{FP} = \sigma_{cr,initial} & \text{(b)} \\ S_{FP} = \lambda_s C_0 \phi L (1 - S_{or})\left(t_D - x_D\right)\exp\left(-\lambda_s L x_D\right) + \left(\sigma_{FP}(x_D, 0) - \sigma_{cr,initial}\right)\left(1 - \exp\left(-\lambda_s L x_D\right)\right) & \text{(c)} \end{cases} \quad (3.61)$$

Table 3.2 summarizes the analytical solutions of fines for all three cases. By combining Table 3.2 with Figure 3.11, the various behaviors of fines can be easily obtained, including suspended fines, strained fines, and attached fines concentration profile at different moments. To clarify the positive effects of nanofluid pre-flush on maintaining well injectivity, analytical solutions for three different cases are compared as shown in Figure. 3.12-16, where the boundary and initial conditions are presented as ($C_{FP,\ injection}$=0.02 for all three cases) and initial-condition (C_{NP}=0 for case I & II, $\sigma_{FP}(x_D, 0) = 0.01$ and $C_{FP}(x_D, 0) = 0.02$ for case III). All necessary data are summarized in Table 3.1.

In Figure 3.11, for case I, there are four different zones describing the propagation paths of suspended fines concentration front and attached front in the plane of "distance-time diagram".

Table 3-2 The summary of suspended, attached and strained fines concentration for different cases along 1-D permeable medium

	Suspended fines concentration	Attached fines concentration σ_{FP}	Strained fines concentration s_{FP}
I	0	$\sigma_{cr,\text{initial}}$	0
II	$C_0 \exp\left(-\left(\lambda_a+\lambda_s\right)Lx_D\right)$	$\lambda_a C_0 \phi L(1-S_{or})\left(t_D-x_D\right)\exp\left(-\left(\lambda_a+\lambda_s\right)Lx_D\right)+\sigma_{cr,initial}$	$\lambda_s C_0 \phi L(1-S_{or})\left(t_D-x_D\right)\exp\left(-\left(\lambda_a+\lambda_s\right)Lx_D\right)$
III	$C_0 \exp\left(\begin{array}{l}-\left(\lambda_a+\lambda_s\right)L\times \\ \left(\begin{array}{l}x_D-\left(t_D-x_D\right) \\ \times\dfrac{\lambda_a\phi(1-S_{or})C_0}{\left(\lambda_a+\lambda_s\right)\left(\sigma_{cr,\max}-\sigma_{cr,initial}\right)} \\ +\dfrac{1}{\left(\lambda_a+\lambda_s\right)L}\end{array}\right)\end{array}\right)$	$\left(\sigma_{cr,\max}-\sigma_{cr,initial}\right)\times$ $\exp\left(-\left(\lambda_a+\lambda_s\right)L\left(\begin{array}{l}x_D-\left(t_D-x_D\right) \\ \times\dfrac{\lambda_a\phi(1-S_{or})C_0}{\left(\lambda_a+\lambda_s\right)\left(\sigma_{cr,\max}-\sigma_{cr,initial}\right)} \\ +\dfrac{1}{\left(\lambda_a+\lambda_s\right)L}\end{array}\right)\right)+\sigma_{cr,initial}$	$\lambda_s C_0 \phi L(1-S_{or})\left(t_D-x_D\right)\exp\left(-\left(\lambda_a+\lambda_s\right)Lx_D\right)$
IV	$C_0 \exp\left(-\lambda_s Lx_D\right)$	$\sigma_{cr,\max}$	$\lambda_s C_0 \phi L(1-S_{or})\left(t_D-x_D\right)\exp\left(-\lambda_s Lx_D\right)$
Case II: No nanoparticles, and $\sigma_{FP}(x_D,0)\le\sigma_{cr,initial}$			
I	0	$\sigma_{cr,\text{initial}}$	0
II	$C_0 \exp\left(-\lambda_s Lx_D\right)$	$\sigma_{cr,initial}$	$\lambda_s C_0 \phi L(1-S_{or})\left(t_D-x_D\right)\exp\left(-\lambda_s Lx_D\right)$
Case III: No nanoparticles, and $\sigma_{FP}(x_D,0)>\sigma_{cr,initial}$			
I	$\dfrac{\sigma_{FP}(x_D,0)-\sigma_{cr,initial}}{\phi\left(1-S_{or}\right)}\exp\left(-\lambda_s Lt_D\right)$	$\sigma_{cr,\text{initial}}$	$\left(\sigma_{FP}(x_D,0)-\sigma_{cr,initial}\right)\left(1-\exp\left(-\lambda_s Lt_D\right)\right)$
II	$C_0 \exp\left(-\lambda_s Lx_D\right)$	$\sigma_{cr,initial}$	$\lambda_s C_0 \phi L(1-S_{or})\left(t_D-x_D\right)\exp\left(-\lambda_s Lx_D\right)$ $+\left(\sigma_{FP}(x_D,0)-\sigma_{cr,initial}\right)\left(1-\exp\left(-\lambda_s Lx_D\right)\right)$

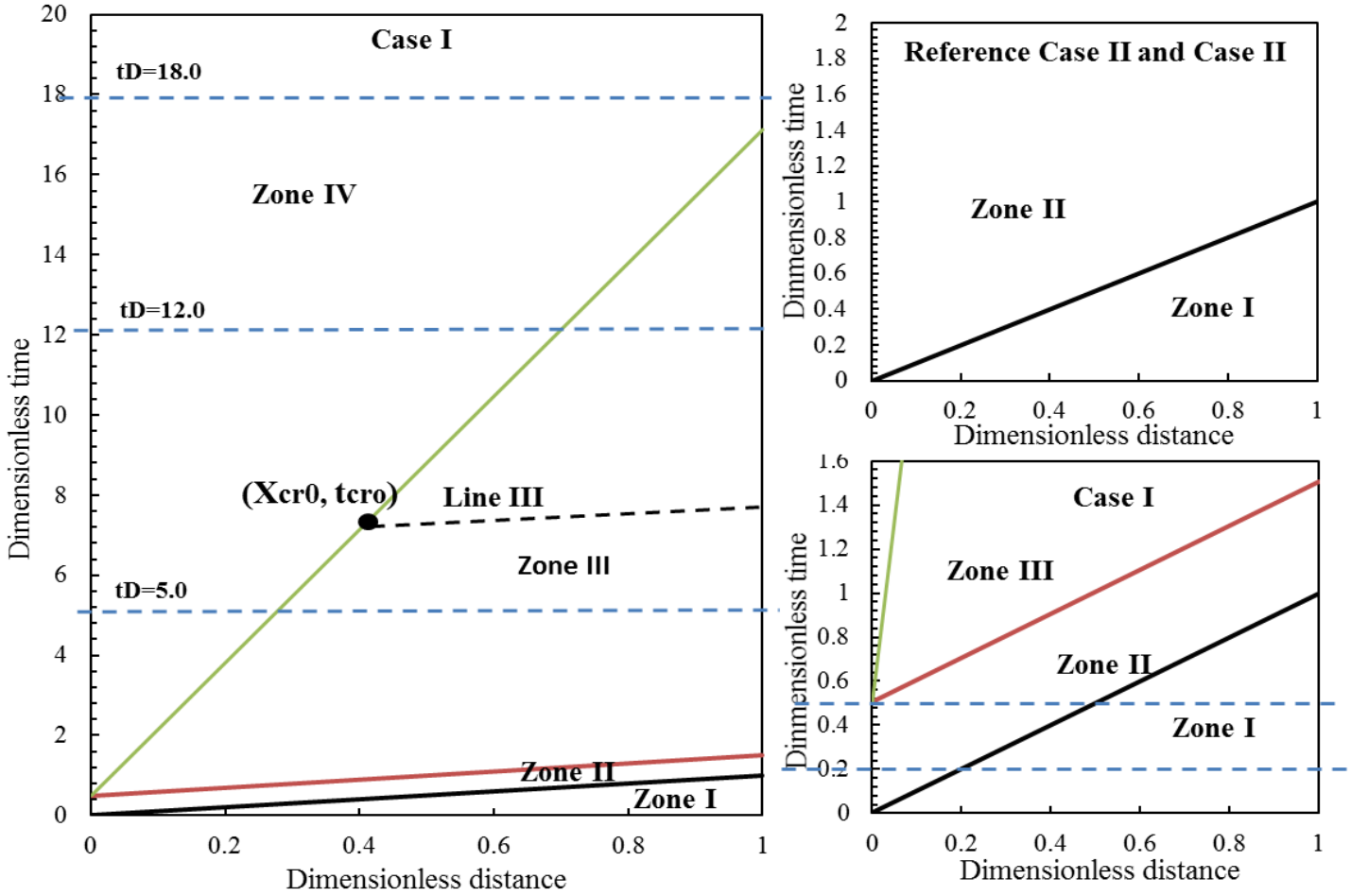
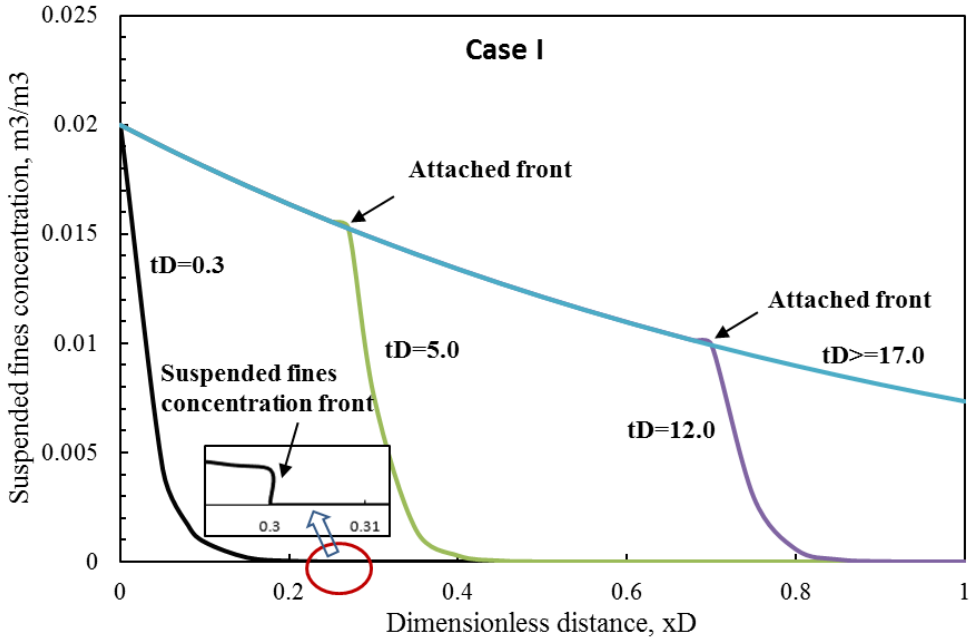
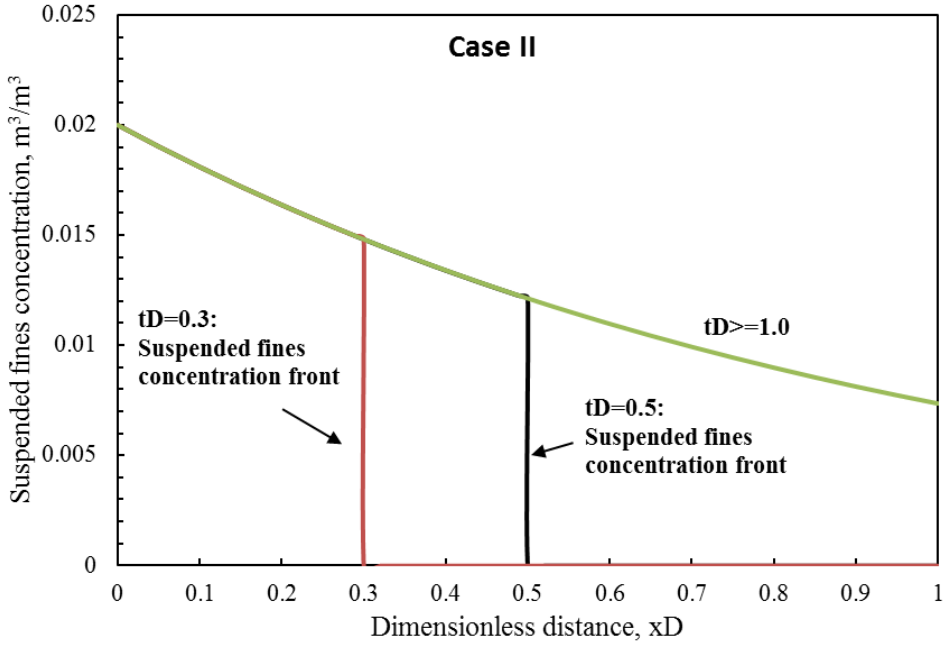


Figure 3.11 Distance–time diagram or motion of particles concentration fronts in the plane of x_D-t_D

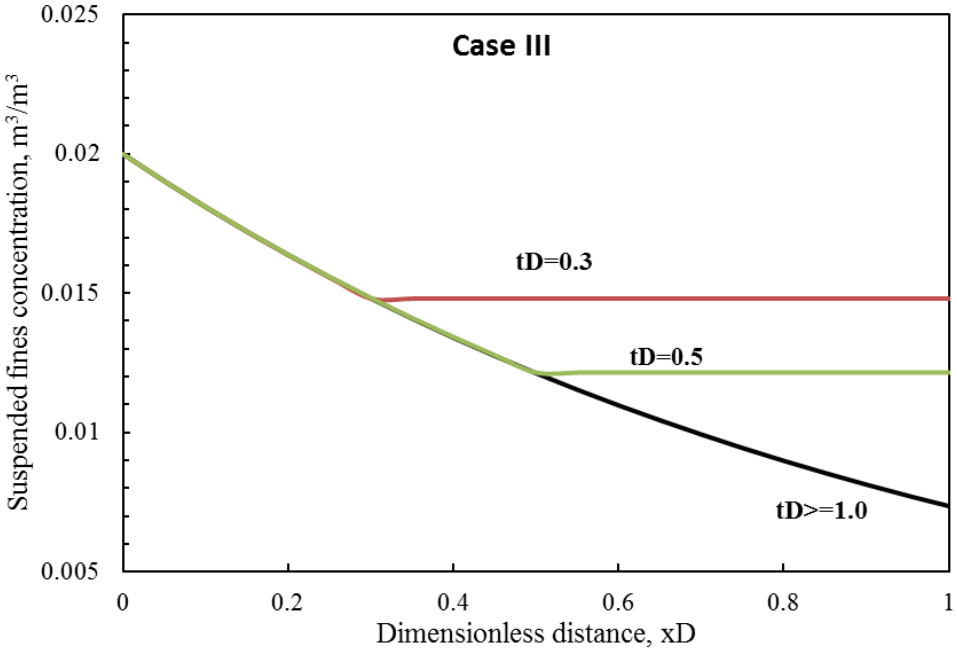
In Figure 3.12, the suspended fines concentration profiles along 1-D permeable medium, there does appear a "suspended fines concentration front", where separates the initial condition from the injected conditions, ahead of which, the suspended fines are kept as the initial condition. In zone II behind this front, the suspended fines concentration profile is kept as steady state, and thus the retained fines concentration can increase proportionally with time. At the moment of $t_{DC} = 0.5$, the attached fines concentration at the inlet reaches the maximum limit, there does appear an "attached front", no more fines could be captured in zone IV. However, in zone III, fines capture on rock grains still takes place. Followed by, at $t_D = 1.0$, the breakthrough of injected fines starts, and the effluent fines concentration starts to increase.



a. Case I: Nanoparticles pre-coat to enhance well injectivity



b. **Case II: No nanoparticles pre-coat, and** $\sigma_{FP}(x_D, 0) = \sigma_{cr,initial}$



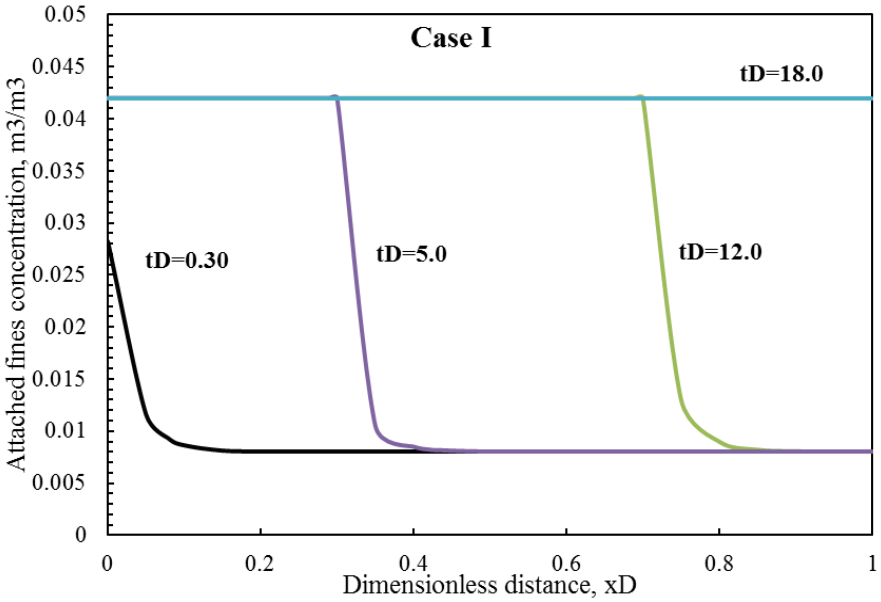
c. Case III: No nanoparticles pre-coat, and $\sigma_{FP}(x_D, 0) > \sigma_{cr,initial}$

Figure 3.12 Suspended fine particles concentration profile along the 1-D permeable medium at different time for three different scenarios

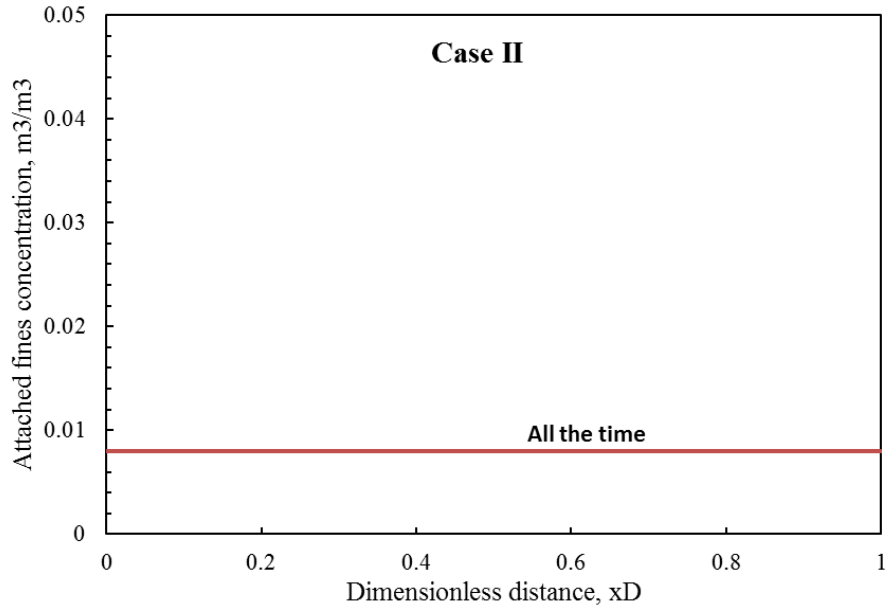
As for the comparison of suspended fines concentration profiles of three different scenarios in Figure.3.12, the existence of nanofluid pre-flush makes the suspended fines concentration decrease dramatically. Without nanoparticles effects, the injected condition of fines particles would arrive the outlet at $t_D = 1.0$, and since then, the suspended fines concentration is kept as steady state, as shown in Figure 3.12b and c. When it comes to case I, as shown in Figure 3.12a, the positive contribution of nanoparticles elongates the duration of transient flow of fines suspension. As results, until $t_D = 17.0$, the injected condition of fines can arrive to the outlet.

In Figure 3.13 and Figure 3.14, the differences of attached and strained fines concentration profile among three different cases are compared. Because in case II and case III, the initial fines concentration has already become larger than the maximum retention limit of fine particles, the attached fines concentration along the 1-D permeable medium would not increase any more, and always keep same with the initial conditions. As results, as fines suspension injection continues, even without any more fines to be attached onto rock grains, all the newly injected fines would be continuously strained, or pass through the porous medium. Therefore, the strained fines concentration in both case II and case III are larger than that of case I ahead of the suspended particles concentration front. When compared case II to case III, due to the existence of unattached fines at the initial condition in case III, ahead of the suspended front, there are heavier fine particles straining effects. Obviously, in case III, fines migration would bring more severe damage on the flowing capacity of 1-D permeable medium.

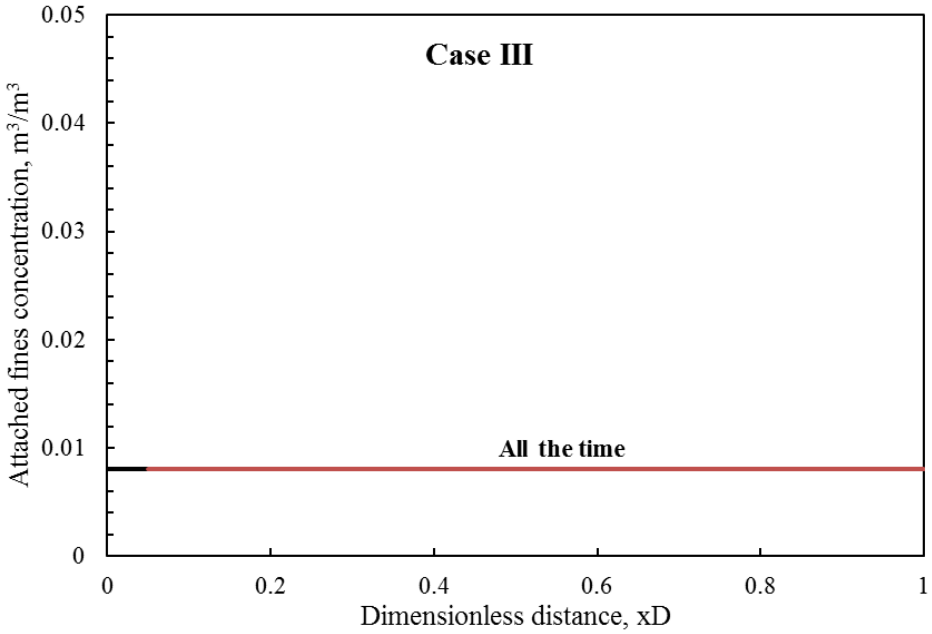
In Figure 3.15, the comparison of effluent history of fines concentration can also demonstrate the awesome positive performance of nanoparticles to control fines migration. For case I, even at $t_D = 1.0$, the injected fines reach the outlet, however, the effluent concentration keeps lower in order of about 10^{-16}~10^{-7}, nearly zero for long time. Until $t_D = 15.0$, the effluent fines concentration starts to increase dramatically and reaches the steady-state condition of about 0.007 m^3/m^3 at $t_D = 17.0$.



a. Case I: Nanoparticles pre-coat to enhance well injectivity

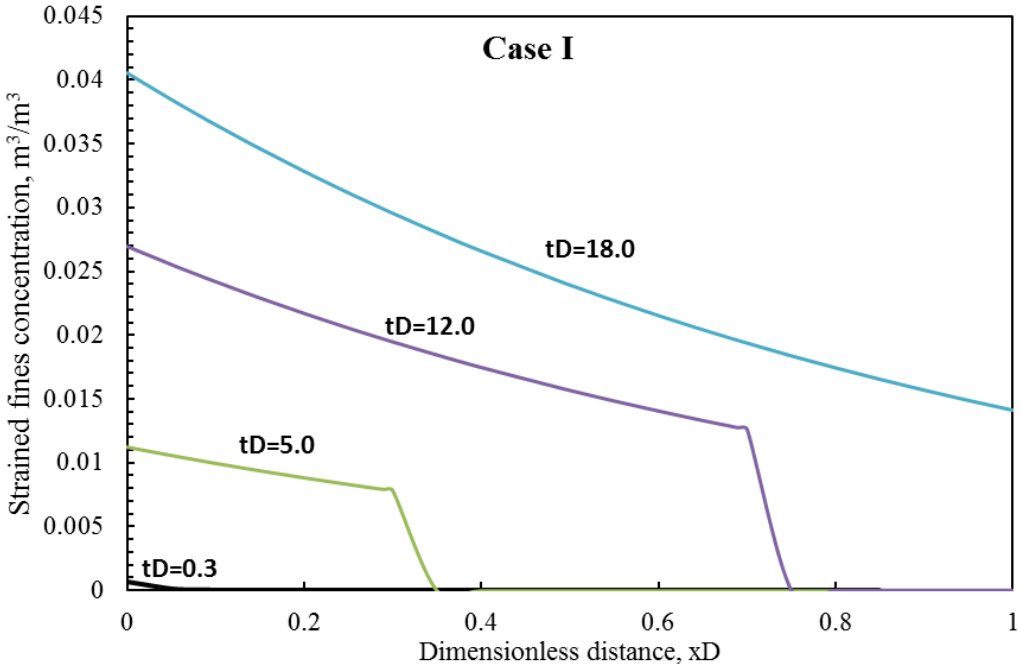


b. **Case II: No nanoparticles pre-coat, and** $\sigma_{FP}(x_D, 0) = \sigma_{cr,initial}$

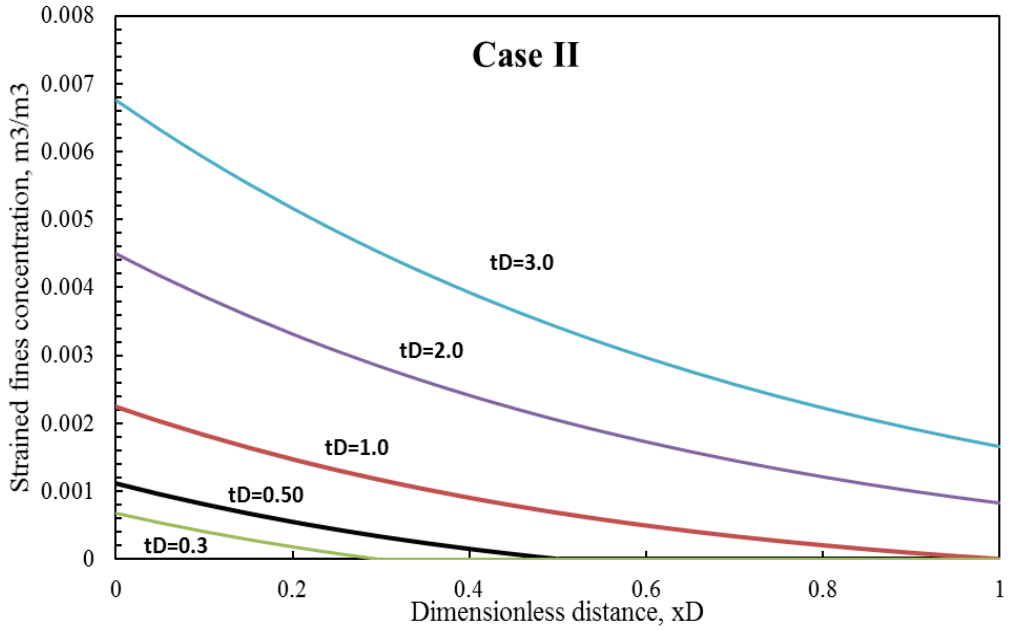


c. Case III: No nanoparticles pre-coat, and $\sigma_{FP}(x_D, 0) > \sigma_{cr,initial}$

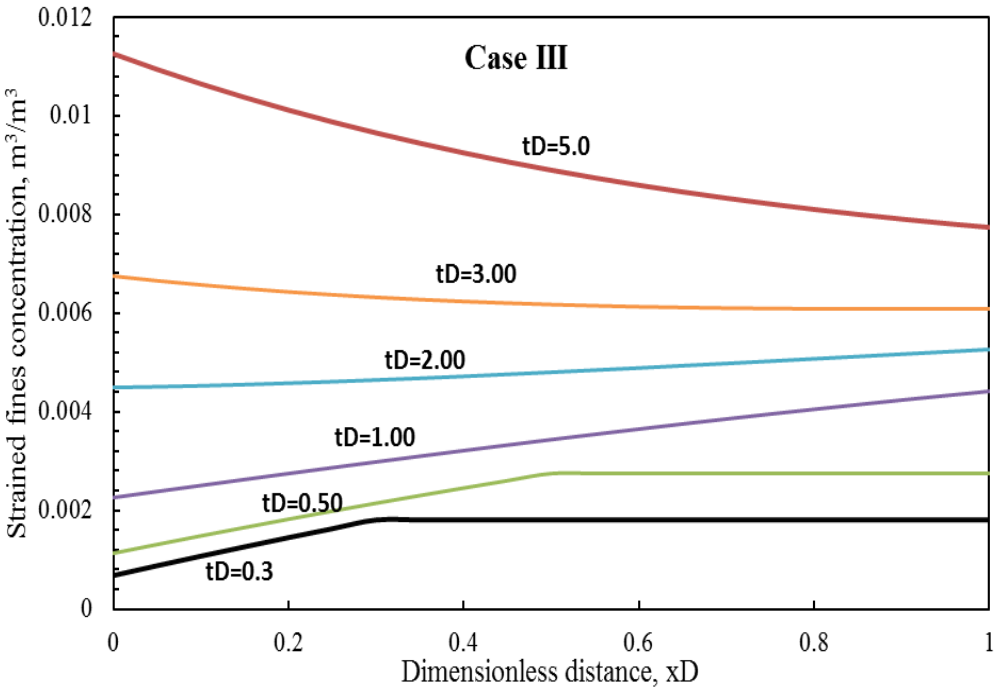
Figure 3.13 Attached fines concentration profile along 1-D permeable medium at different moments for three different cases



a. Case I: Nanoparticles pre-coat to enhance well injectivity



b. **Case II: No nanoparticles pre-coat, and** $\sigma_{FP}(x_D, 0) = \sigma_{cr,initial}$



c. Case III: No nanoparticles pre-coat, and $\sigma_{FP}(x_D,0) > \sigma_{cr,initial}$

Figure 3.14 Strained fines concentration profile along 1-D permeable medium at different moments for three different cases

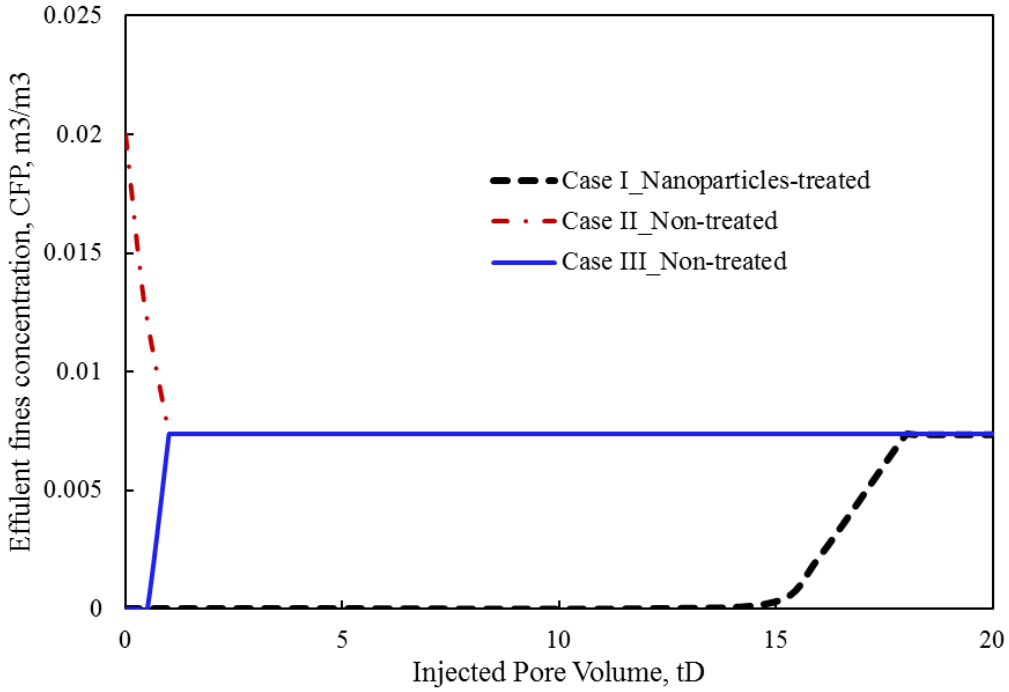


Figure 3.15 Effluent history of fine particles concentration

(Case I: black dashed line-with nanoparticle pre-coat; Case II: blue solid line-without nanoparticles pre-coat, and $\sigma_{FP}(x_D,0)=\sigma_{cr,initial}$; and Case III: red dotted line- without nanoparticles pre-coat, and $\sigma_{FP}(x_D,0)>\sigma_{cr,initial}$)

3.3.3.4 Validation with Lab Experimental Results

To validate the accuracy of the analytical solutions and hypothesized nanoparticles-rocks interaction model, our analytical solutions are applied to match the existing lab experimental results from Arab et al. (2013). Inferred from their lab experiments, some experimental parameters are concluded, i.e., flow velocity 1.7×10^{-4}m/s, length of permeable medium 0.33m, the injected fines concentration $5.2\times10^{-5}m^3/m^3$, and nanoparticle concentration $3.0\times10^{-6}m^3/m^3$. Other unknowns are referred to Table 3.1.

To simplify the matching procedure, combine Eq. 3.46b into Eq. 3.49b to replace the combination of many unknown parameters $\left(\sigma_{cr,\max}-\sigma_{cr,initial}\right)/\lambda_a\phi L(1-S_{or})C_0$ by only one unknown parameters t_{cr} in Eq. 3.63. The t_{cr} can also easily be found from the effluent history in Figure 3.16.

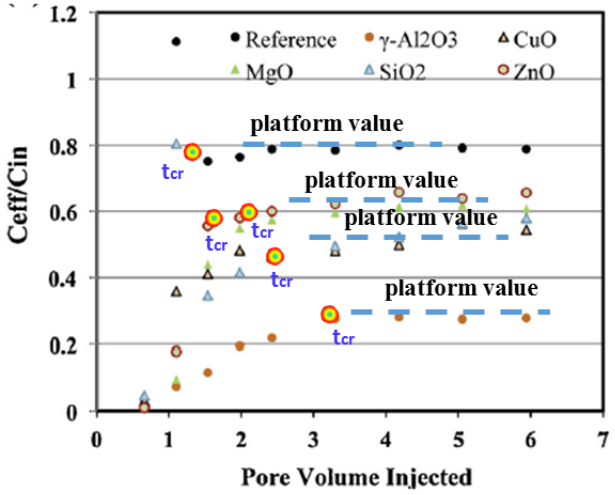
$$\frac{C_{FP,eff}}{C_{FP,inj}}=\exp\left(-\left(\lambda_a+\lambda_s\right)L\left(x_D-\left(t_D-x_D\right)\frac{L\left(\lambda_a+\lambda_s\right)+1}{L\left(\lambda_a+\lambda_s\right)\left(t_{cr}-1\right)}+\frac{1}{\left(\lambda_a+\lambda_s\right)L}\right)\right)\ldots\ldots\ldots\ldots \quad (3.63)$$

Figure 3.17 presents the comparison of effluent history of fine particles concentration between analytical solutions and the existing lab results. They indicate that the analytical solutions can explain the laboratory experiments results very well. In addition, through matching with lab experiments, this paper quantifies the characterization parameters of different types of nanoparticles, including fine particles attachment coefficients and fine particles straining coefficients, which reflect the attachment and straining rates of fines

particles, with the effects of types of nanoparticles coated onto rock grain surfaces. Table 3.3 summarizes the values of characterization parameters on fines migration behavior obtained by trial and error algorithm. As indicated from Table 3.3, for the case with the effects of Al_2O_3-based nanoparticles, it has the largest particles attachment and straining coefficient, which means that the attachment and straining rates of fines particles are enhanced the most significantly by Al_2O_3-based nanoparticles. All those characterization results confirm that Al_2O_3-based nanoparticles is the optimal type of nanoparticles to reduce fines migration from Arab's lab experimental results.

Table 3-3 Values of parameters to characterize fines migration behavior with the effects of nanoparticles from the analytical solutions

Parameters	reference	Al_2O_3	SiO_2	ZnO	CuO	MgO
λs	2	10	5	4	6	4.5
λa	7	11	10	8	2	14.5
t_{cr}	1	3	2.5	2.3	1.5	1.5



Ref., Fig.2b in Arab & Pourafshary, 2013

Step 1: From the experimental fines effluent concentration history (left figure), find out the breakthrough of steady-state condition, t_{cr} , which is the inflection point from slanted line to the final platform line.

⇩

Step 2: From the experimental fines effluent concentration history (left figure), read out the highest platform value, and based on **Eq. 3.52b**. We can determine the number of λ_s

⇩

Step 3: The only unknown parameter is λ_a, we need to apply trial and error algorithm determine the number of λ_a by calculating the effluent fines concentration **Eq.3.42b and Eq. 3.64**. until the results calculated by our model can match the lab experiments enough well.

Figure 3.16 Flowchart to explain the experimental results with analytical solutions and characterize the behavior of fines migration with nanoparticles utilizations

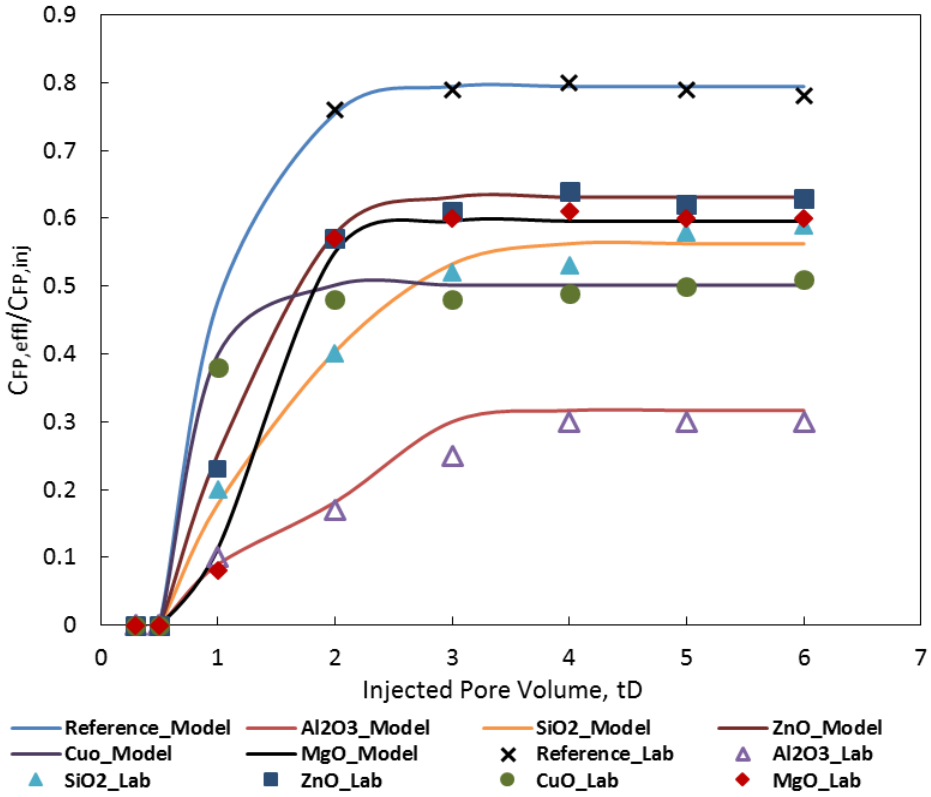


Figure 3.17 Comparison of fine particles effluent concentration history obtained from analytical models (solid line) and lab experimental results (discrete points) for different cases with types of nanoparticles utilizations approaches

3.4 Evaluation and Optimization of Nanoparticles Utilization

In above sections, the analytical solutions for different cases of nanoparticles utilization have been obtained.

In section 3.3.1 and 3.3.2, with the ignorance of fine particles straining effects, the two scenarios of nanoparticles utilization are compared to control fines migration, including scenario I:co-injection of nanoparticles and fines; and scenario II: nanoparticle pre-treatment prior to the invasion of fines. Analytical solutions of those two scenarios are applicable to the reservoirs with lower clay contents or smaller sized particles flowing through porous media.

In section 3.3.3, the effects of fine particles straining are incorporated into the analytical solutions. In comparison with particles adsorption phenomenon, the straining of fine particles into pore-throats can bring more significant formation damage, that is, the severe impairment of formation permeability.

In this section, a comprehensive analysis on positive contributions of nanoparticles are evaluated by comparing all the above scenarios of nanoparticle utilization.

3.4.1 Nanoparticles Utilization to Control Fines Migration

As for scenario I in section 3.3.1, inferred from Figure 3.4 and Figure 3.5, the optimal injected nanoparticles concentration can be directly determined as that value when zero concentration of fines is yielded at the constant-state region. In the example described for scenario I, the optimal injected nanoparticles concentration is 0.00033 m^3/m^3. In scenario I, downstream of the nanoparticle adsorption front, there is no nanoparticle, therefore, no more fines to be captured without the contributions of nanoparticles. In addition, the moving velocity of nanoparticle adsorption front has the speed close to the velocity of the "salinity wave" (Lake, 2002). Therefore, as shown in Figure 3.18a, before the breakthrough of nanoparticles about $t_{D1} = 1.0$, there are no changes of effluent fines concentration, which is kept as same with the initial condition ($C_{FP,\text{initial}} = 0.02\ m^3/m^3$). Within the time range from 1.0 to 1.13, due to the nanoparticle effects, there is no fines production at the outlet ($C_{FP,eff} = 0$), i.e., the rock grains with the effects of nanoparticles have retained all newly injected fine particles. After $t_{D1} = 3.3$, the maximum retention capacity of rock grains (with respect to fines) is reached, as results, the newly injected fines cannot be attached on the rock grains any more. Since then, the injection-condition

state ($C_{FP,\text{injected}} = 0.02\ \text{m}^3/\text{m}^3$) spreads over the whole one-dimensional permeable medium, and the effluent concentration of fines also increases gradually to be 0.02 m^3/m^3 (injection condition) as well. The optimal usage of nanoparticles should be the amounts that have been injected before $t_{D3} = 3.3$, which is about 0.001 pore volume in total (very small). It is worth mentioning that the shadowed envelop ABCD in Figure 3.18a represents the cumulative reduction amounts of fines production attributed to the nanoparticle effects.

For the example of scenario II in section 3.3.2, before the breakthrough of injected fines at $t_{D1} = 1.0$, there are no fines produced at the outlet. Even after the breakthrough of injected fines, due to the positive effects of nanoparticle adsorption, there does appear a long production period with very small amounts of fines (close to zero) to be produced at the outlet, as shown in Figure 3.18b. At $t_{cr}(x_D = 1)$, the effluent concentration of fines rapidly increases equal to the injected condition ($C_{FP,\text{injected}} = 0.02\ \text{m}^3/\text{m}^3$).

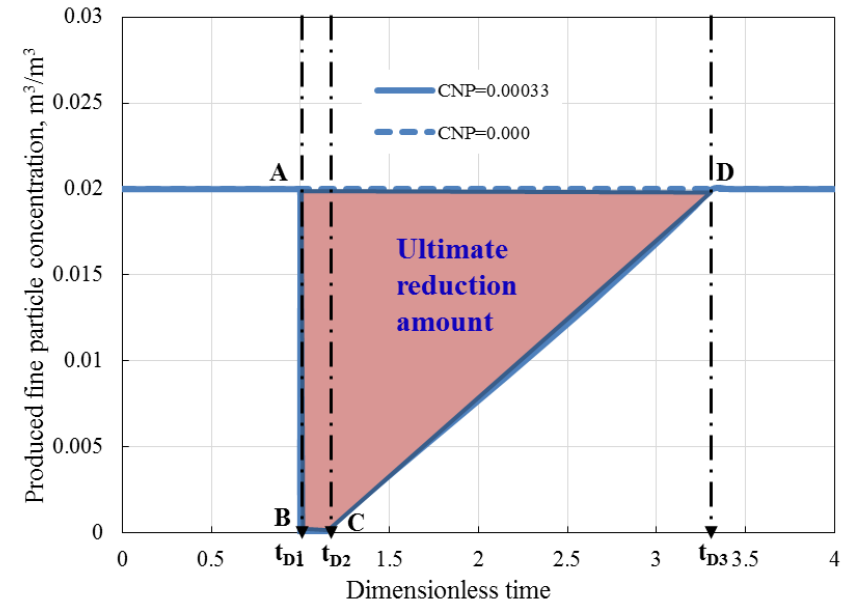
As shown in Figure 3.19, the contributions of nanoparticles to control fines migration is a function of production time. Before the breakthrough of injection-condition state ($t_{D3} = 3.3$ for scenario I and $t_{cr}(x_D = 1)$ for scenario II), the reduced amounts of fines production increases as time goes; After breakthrough, the produced fines concentration stays constant as 0.02 m^3/m^3, i.e., the attachment ability of fine particles on rock grains has reached maximum limits. Thus, no more injected fines controlled by nanoparticles can be realized.

To evaluate the efficiency of nanoparticles in controlling of fines migration, we define mitigation index (MI) as expressed in Eq. 3.64. This is the reduction percentage of

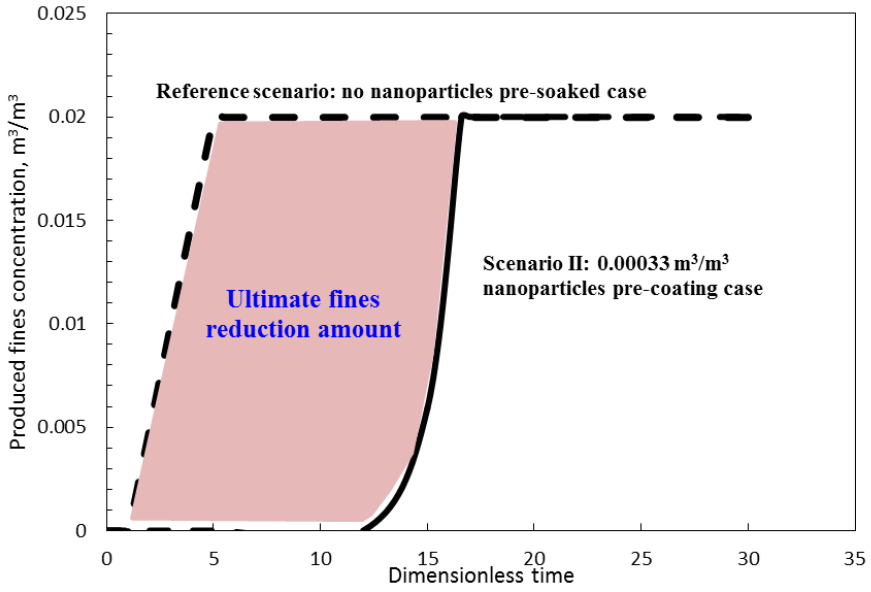
the cumulative fines production with the effects of nanoparticles utilization before the moment of the fines effluent concentration increases, becoming equal to the injected condition. For the two reference scenarios studied in this paper, nanoparticle injection can reduce fines particles production by 36.91 % and 89.9%, respectively. This comparison indicates that scenario II of pre-treat the reservoirs or fracture packs with nanoparticles has more excellent performance than scenario I of co-injection nanofluid with fines, to fixate the injected fines and prevent fines moving further. It may be attributed to the decrease of reaction efficiency between nanoparticle and fines particles, while both of them are mobile at the time of nanoparticles-fines reactions.

$$\mathrm{MI}=\left(1-\frac{C_{FP,initial}\phi(1-S_{or})AL\times t_{D1}+\int_{t_{D2}}^{t_{D3}} C_{FP,effluent}\phi(1-S_{or})ALdt}{C_{FP,initial}\phi(1-S_{or})AL\times t_{D1}+C_{FP,injection}\phi(1-S_{or})AL\times(t_{D3}-t_{D1})}\right)\times 100\%=36.9\% \quad (3.64a)$$

$$\mathrm{MI}=\frac{\int_{1}^{t_{cr}(x_D=1)} C_{FP,\mathrm{effluent}}\phi(1-S_{or})ALdt}{C_{FP,injection}\phi(1-S_{or})AL\times(t_{cr}(x_D=1)-1)}\times 100\%=89.9\% \quad \text{..... (3.64b)}$$



a. Scenario I: Co-inject nanoparticle into the injected stream of fines suspension

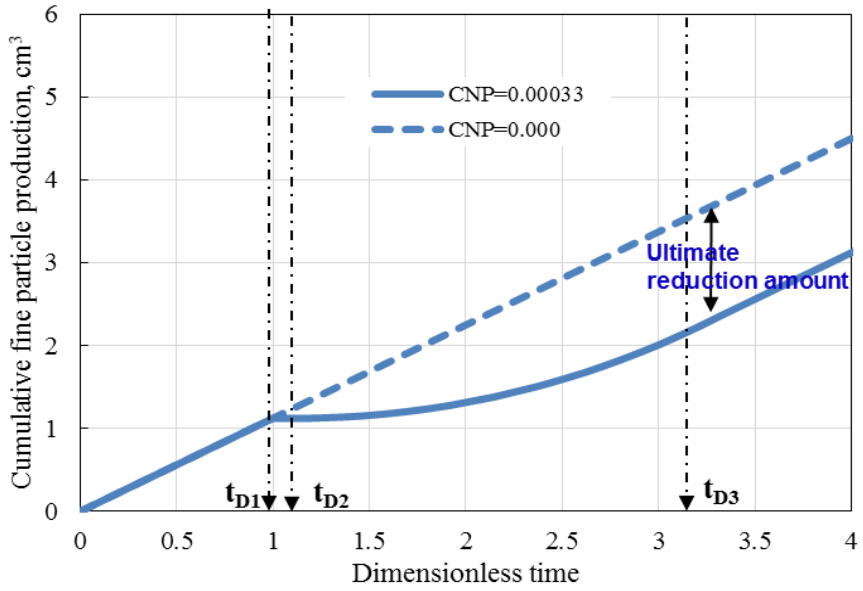


b. Scenario II: Pre-coat with nanoparticles prior to fines injection

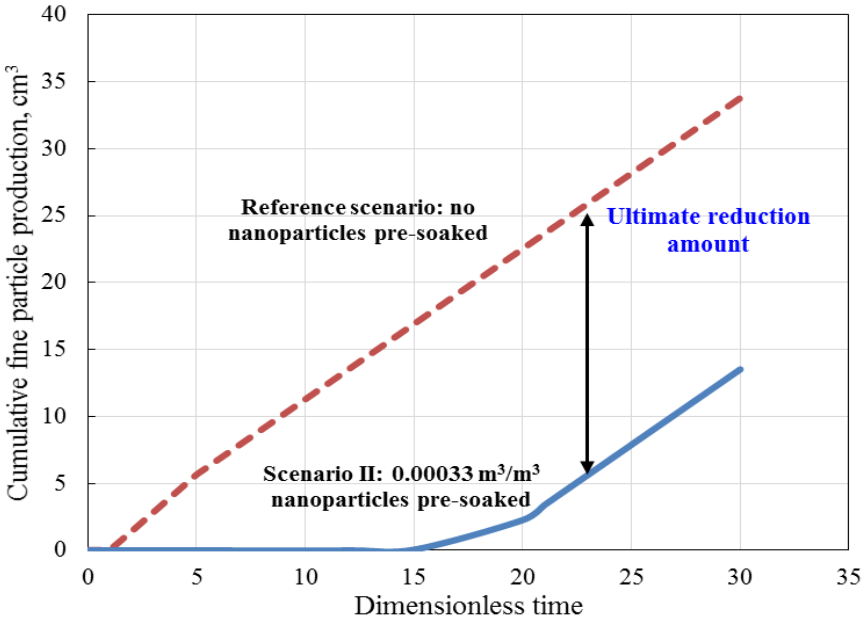
Figure 3.18 Effluent history of fine particles concentration at the outlet for different scenarios of nanoparticles utilization

(Scenario I: dash line- without nanoparticle injection; solid line- with nanoparticle injection concentration 0.00033; t_{D1}, adsorption front breakthrough time; t_{D2}, time when injected fine particles start to produce; t_{D3}, the breakthrough time of

injection point; Scenario II: dash line: no nanoparticles used to pre-coat the porous medium; solid line: apply 0.00033 concentration of nanoparticles used to pre-coat medium)



a. Scenario I: Co-inject nanoparticle into the injected stream of fines suspension



b. Scenario II: Pre-soak with nanoparticles prior to fines injection

Figure 3.19 Cumulative fine particles production volume for different scenarios of nanoparticle utilization

(Scenario I: Dash line- reference scenario without nanoparticles injection; solid line- with nanoparticles injection concentration 0.00033; t_{D1}, the breakthrough time of nanoparticles adsorption front; t_{D2}, the moment when injected fine particles start to produce; t_{D3}, the breakthrough time of injection condition; Scenario II: dash line: no nanoparticles used to pre-soak the porous medium; solid line: applying 0.00033 concentration of nanoparticles to soak porous medium)

3.4.2 Nanoparticles Utilization to Improve Well Injectivity

In section 3.3.3, as shown in Figure 3.15, prior to the arrival of steady-state condition at $t_D = 17.0$, the cumulative reduced fine particles production keeps increasing as the injection of fines suspension continues. After the breakthrough of injection condition at $t_D = 17.0$, the produced fines concentration would stay constant as 0.007 m^3/m^3, which means that the newly injected fines would not be reduced by nanoparticles any more along 1-D porous medium. To evaluate the efficiency of nanoparticles to control fines migration, we apply the mitigation index (MI) defined in Eq. 3.65 as the cumulative reduction amounts of fine particles outflow caused by the utilization of nanoparticles (case I) until the moment when the effluent fines concentration become equal to the injected condition. For two reference scenarios (case II & case III) studied in this paper, by applying nanoparticles pretreatment, the cumulative production of fine particles can be reduced by 53.8 % and 56.0%, respectively (i.e., MI=53.8% and 56.0%). It demonstrates that the pre-coated nanoparticles can bring significant reduction of fines migration and prevent the injected fines moving any further. Especially, for the higher content of clay fines in reservoir (case III), the utilization of nanoparticles can bring more significant performance to control fines migration in reservoirs.

In this chapter, assuming that the injected rates keep constant, the injection pressure drop along 1-D permeable medium will increase as the injection of suspension continues, due to the formation damage effects caused by the attachment and straining of fines particles. The impairment of formation permeability has been proposed to modify the Darcy-flow by incorporating the effects of particles attachment and straining, as shown in Eq. 2.51 and Eq. 2.52. The increase of pressure drop with constant injection rates can be characterized using Eq. 2.52.

Using the values of parameters in Table 3. into analytical solutions in section 3.2.3, the changes of injection pressure drop along the whole 1-D permeable medium are compared at different time, as shown in Figure 3.20. For all the three cases in section 3.2.3, the injection pressure drop keeps increasing as the injection continues. This phenomenon can be attributed to the continuous decline of permeability caused by the cumulation effects of fines attachment and straining from the beginning. With the aid of pre-coated nanoparticles onto rock grains, the newly injected fines can be prevented from moving any further, which help mitigating the severe formation damage along 1-D permeable medium. In addition, as inferred from Figure 3.15, the existence of nanoparticles delays significantly the breakthrough of injected condition ($C_{FP,\ injection}$=0.02) from $t_D = 1.0$ to $t_D = 17.0$. After $t_D = 17.0$, the effluent fines concentrations for all the three cases eventually become the same with the injected condition. As results, in Figure 3.20, the trend of pressure drop curves for all the three cases also become identical, which can also be confirmed by Figure.3.13 and Figure 3.14 where the attached fines concentration keeps constant and only the strained fines concentration increase linearly with time (Eq. 3.51, Eq.3.56 and Eq.3.61) for all three cases after $t_D = 17.0$.

In addition, this section also introduces the injection index to characterize the performance of nanoparticle utilization to prevent formation damage:

$$J_{injection} = \frac{Q_{inj}}{\Delta p(t_D)} = \frac{UA}{\Delta p(t_D)} \quad \text{..... (46)}$$

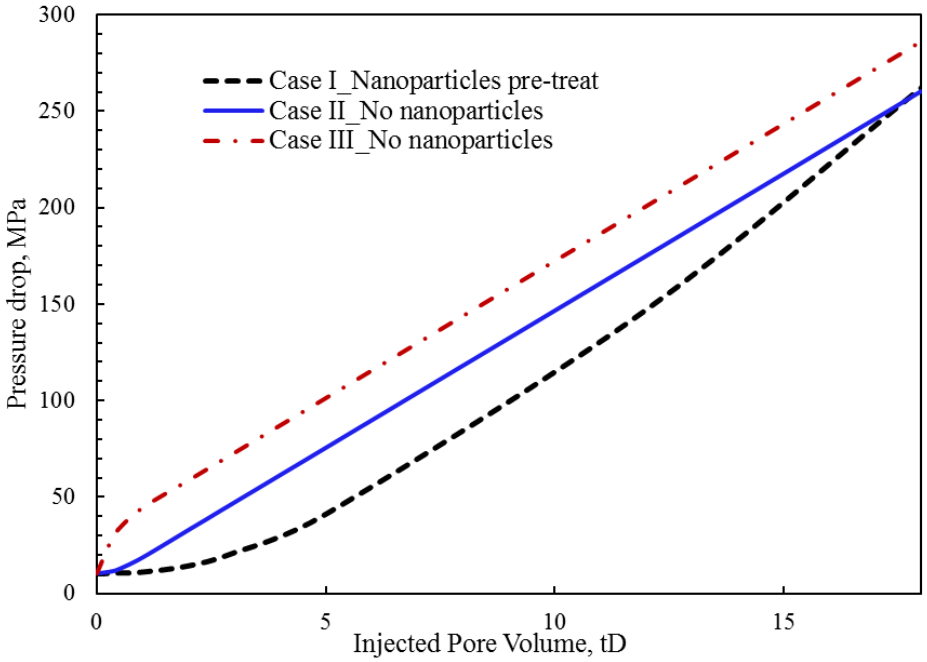


Figure 3.20 Pressure drop along 1-D permeable medium at different time for three different cases

Inferred from Figure 3.21, the injection index keeps the trend of decreasing as the injection continues. The existence of pre-coated nanoparticles can slow down the decline of well injectivity. However, the effect of nanoparticles to prevent formation damage is finite and time-dependent. With the continuous injection of fines suspension for long time, the nanoparticles performance also decrease gradually. Until $t_D = 17.0$, the injection index for all the three scenarios become same. This phenomenon can easily be explained by that even the nanoparticles have finite capacity to control fines migration, in view of the finite capacity of nanoparticles adsorption and limited low surface zeta potential of

nanoparticles. As results, the pre-coated nanoparticles can only prevent the flowing of continuous fines invasion for limited period.

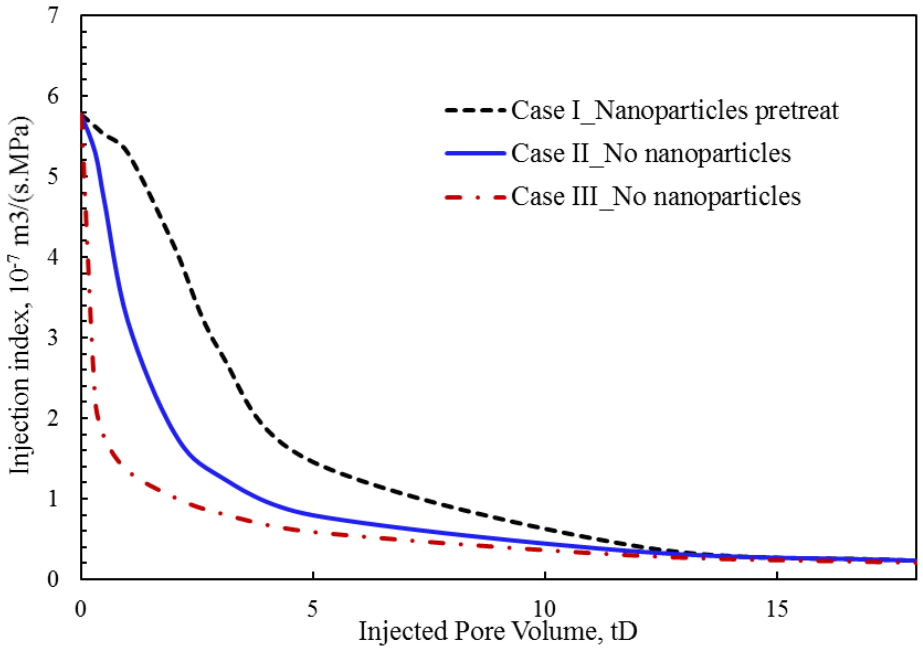


Figure 3.21 Decline of injection index with the increase of injected pore volume for three different cases

In addition, inferred from the lab experiments from Arab et al. (2013), the severe permeability impairment can be indicated by the increase of injection pressure drop. To evaluate the performance of nanoparticles to mitigate the impairment of formation damage, the changes of permeability (Eq. 2.51) are calculated as the injection continues, as shown in Figure.3.22. The comparison results of analytical solutions with experimental results confirm the accuracy of analytical solutions. The constant values of injection pressure drop from both the experimental results and analytical solutions help explain the effectiveness of nanoparticles to control fine particles migration. Because of the positive effects of pre-coated nanoparticles onto rock grains prior to the invasion of fines, the

impairment of Berea core permeability is completely remedied from the damage case without nanoparticles.

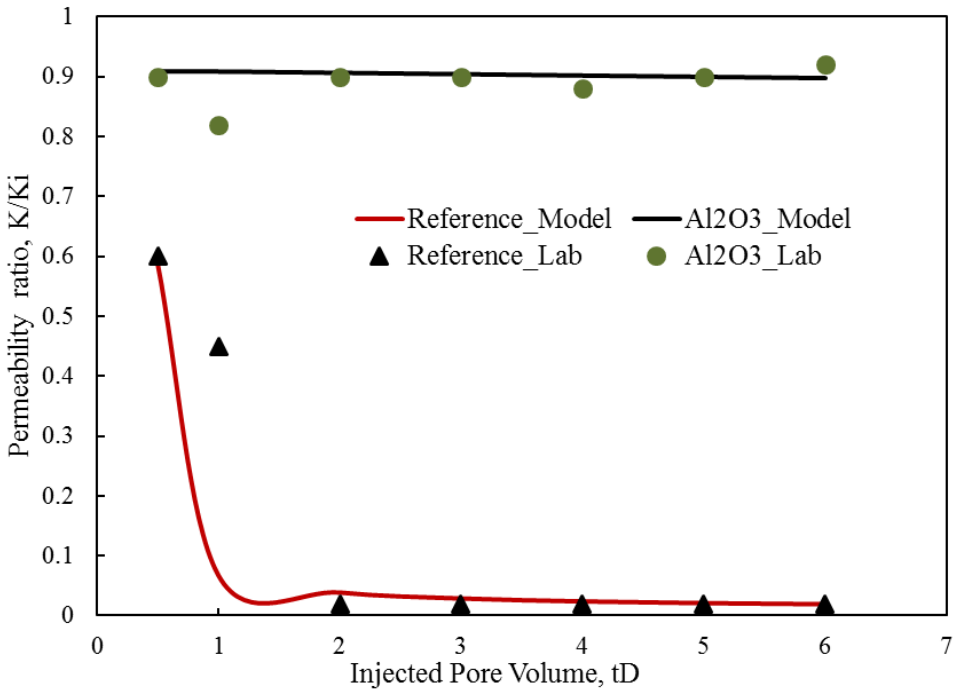


Figure 3.22 Comparison of permeability changes obtained from analytical models (solid line) and lab experimental results (discrete points) for both cases (case with nanoparticles effects; and reference case without nanoparticles)

3.5 Conclusions and Summary

This chapter provides series of analytical solutions of two-phase (one flowing and one stationary) three-component (water, nanoparticles, and fines) flow in 1-D permeable medium and evaluates the utilization of nanoparticles to control fines migration. The main outcomes of this chapter are to provide mathematical structures to evaluate different scenarios of nanoparticle utilization to control fines migration and improve well injectivity. The main conclusions are summarized, as follows:

- The maximum retention concentration of fines on rock grains, combined with advective particles flow model is applied to describe the instant detachment of fines from

rock grains when the flow velocity / fluid salinity abruptly changes. The adsorption of nanoparticles on surfaces of fines or rock grains can enhance the maximum retention concentration of fine particles on rocks, due to the decrease of repulsive forces between fine particles and rock grains.

- Only with small amount of nanoparticle injection, a satisfactory control of fines migration can be achieved; e.g., MI is 36.91% and 89.9% for scenario I and scenario II, respectively. In section 3.3.3 with effects of fine particles straining, in comparison to two reference scenarios, nanoparticles pre-flush can reduce the cumulative fines production by 53.8 % and 56.0%, respectively.

- In scenario I, the profiles of suspended, strained and attached fine particles concentration along 1-D porous medium and the effluent history of fine particles are compared for different cases of nanoparticle applications and reference cases. In scenario I, the optimal condition is that value allowing fines concentration to be zero at constant-state region. In the example, the optimal nanoparticles injection concentration is 0.00033 m^3/m^3 (almost two orders of magnitude less than fines concentration 0.02 m^3/m^3).

- In section 3.3.3, the core permeability can be severely impaired by the attachment of fine particles onto pore surfaces and particles straining into pore-throats. As the fluid injection continues, well injectivity decreases, in other words, pressure drop must increase to maintain the constant injection rate. The existence of pre-coated nanoparticles can prevent permeability impairment and decline of well injectivity.

3.6 Nomenclature

C_1= Nanoparticles in fluid phase defined in fictitious chemical reaction

C_2= Fine particles in fluid phase defined in fictitious chemical reaction

C_{12}= Fine particles with nanoparticle adsorption in fluid phase

$C_{12,attachment}$= Fine particle deposited from fluid phase to solid phase

$\hat{C}_{NP}$ = Volumetric concentration of adsorbed nanoparticles with respect to bulk volume, m^3/m^3

C_{FP}, C_{NP}= Volumetric concentration of fine particles and nanoparticles with respect to pore volume, m^3/m^3

$C_{FP,inj}$= Volumetric concentration of injected fine particles with respect to pore volume, m^3/m^3

$C_{FP,eff}$= Volumetric concentration of effluent fines at the outlet with respect to pore volume, m^3/m^3

$\hat{C}_{NP,\,NP}$ = Derivative of volumetric concentration of adsorbed nanoparticles with respect to flowing nanoparticle concentration, m^3/m^3

$\hat{C}_{NP,\,FP}$ = Derivative of volumetric concentration of adsorbed nanoparticles with respect to flowing fines concentration, m^3/m^3

F_{ei} = Electrostatic forces initially without nanoparticles effects, N

h = Surface-to-surface separation length, m, $h<<r_{fp}$

K_{NP}= Langmuir adsorption constant of nanoparticle

k_B = The Boltzmann's constant, 1.381×10^{-21} J/K

$k_{intrinsic}$= Intrinsic permeability of sand pack, mD

k_{rwor}= Relative permeability of water at residual oil condition

l = Characteristic wave length of interaction, l=100 nm

λ_1, λ_2 = Line combination coefficients

L_1, L_2 = Function of total derivative

n = Pore concentration, number/m^3

n_∞ = Bulk number density of ions, 6.022×10^{25} number/m^3

r_{FP}, r_{NP}= Radius of fine particle or nanoparticles, m

r_p = Pore radius, m

T = Absolute temperature of reservoir, K

U = Fluid velocity, m/s

V_{FP} = Total energy, J

V_{DLR} = Double electric layer repulsion energy, J

y = Ratio between drag and electrostatic force

ρ = Fluid density, kg/m^3

$\Delta\rho$ = Density difference between particle and fluid, kg/m^3

Δp = Injection pressure drop along the whole porous media, Pa

ω = Dimensionless drag force coefficient varying in the range 10~60

μ = Fluid viscosity, Pa.s

$\varsigma_{FP}, \varsigma_{NP}, \varsigma_{GS}$ = Zeta potentials for fine particles, nanoparticles and grain surfaces, mV

ϕ = Porosity of sand pack

σ_{FP} = Volumetric concentration of retained fine particles with respect to bulk volume

$\sigma_{cr,initial}$ = Critical retention concentration of fine particles without nanoparticles adsorption

σ_{cr} = Critical retention concentration of fine particles with varying nanoparticle adsorption

$\sigma_{cr,\max}$ = Critical retention concentration of fine particles with maximum nanoparticles adsorption

$\sigma_{cr,NP}$ = Derivative of the maximum retention concentration of fine particles with respect to nanoparticles concentration, m^3/m^3

x_D = Dimensionless distance

t_D = Dimensionless time or injected numbers of pore volume

β = Characteristic parameter along C_-

α = Characteristic parameter along C_+

Chapter 4: Control Two-Phase Fines Migration using Nanoparticles

4.1 Problem Statement and Assumptions

Fines migration in two-phase flow occurs in unsaturated reservoirs. In petroleum industry, as the injection of low-quality water with solid and liquid particles (produced water or waste water) continues for waterflooding, both the newly invaded fine particles and the initially existing formation fine particles bring significant formation damage and impair well performance, i.e., well injectivity and oil recovery. Plan and design of those projects related to fines migration in two-phase flow and evaluation of various mechanism by which nanoparticles control fines migration need reliable physical-based mathematical models. This need motivates us to develop exact analytical solutions for quantitative controlling two-phase fines migration problems.

The mutual relation among nanoparticles, fines and rock grains are characterized using two-step interactions process: (1) adsorption of nanoparticle onto the particles/grain surface and (2) enhanced attachment of fines; doing so, method of characteristic is applied to study the problems. In this chapter, two different scenarios of nanoparticles utilization to control fines migration are discussed, including 1) co-injection of nanoparticle-fine particles mixture into 1-D permeable medium that initially oversaturated with fine particles and 2) pre-coating /pre-treatment of the porous medium with nanoparticles prior to fines injection. Our assumptions commonly used for two-phase colloidal-suspension flows are as follows:

- One-dimensional (1D), uniform and homogeneous medium, and local thermodynamic equilibrium assumption applies.

• Four components exist (water, oil, nanoparticles, and fine particles) and three-phase (two flowing (oil/water) and one stagnant solid phase) isothermal flow takes place; No volume change occurs in aqueous phase.

• All fluids and solids are incompressible. Gravity of fluids (oil/water) are neglected; the effects of viscous force are dominated, and capillary forces is implicit in relative permeability equations.

• Langmuir isotherm adsorption of nanoparticles provides an asymptotical maximum adsorption capacity when time tends to infinite. The changes of porosity and permeability caused by nanoparticles adsorption are neglected.

• Flow velocity is sufficiently large to neglect the dispersion flow effects; Darcy's flow law is applied; therefore, hyperbolic conservation equations are obtained.

Beside those above assumptions, specifically, for the scenario of nanofluid co-injection into fluid mixture stream in section 4.2, some additional assumptions are implemented,

• The adsorbed nanoparticles onto mobile fines can only enhance the maximum attachment concentration of fine particles onto the rock and not the attachment rate of fines particles. The attachment of fine particles from pore surfaces and adsorption of nanoparticles on fines occur simultaneously but at different rates;

• In cases of limited number of mobile fines and enough small sizes of fine particles, only the attachment of fine particles is incorporated, but ignoring the straining of fines.

• The fractional flow is function of both phase saturation and retained fines (particles attachment onto pore surfaces). Ignore the changes of residual oil saturation,

but only focus on the improvement of mobility control using relative permeability of water phase.

Similarly, for the scenario of nanofluid pre-treatment prior to the invasion of low-quality fluid into reservoirs in section 4.3, some additional assumptions are implemented,

- Nanoparticles concentration already adsorbed on rock grains can have enough capacity to retained all newly injected fine particles for long time.
- Multiple mechanisms of fine particles retention are incorporated, i.e., particles straining and particles attachment.
- The fractional flow is function of both phase saturation and retained fines (fines straining and attachment). Ignore the changes of residual oil saturation, but only focus on the changes of relative permeability curve.

4.2 Nanofluid Co-Injection to Reduce Two-Phase Fines Migration

4.2.1 Model Description and Methodology

As indicated in section 3.2.1, it is desirable to introduce nanoparticles as an additive continuously into the injection fluid stream to control injected fines suspension. The co-injected nanoparticles are preferentially adsorbed on the surfaces of mobile fines, and then alter the surface potential of fine particles. Consequently, the repulsive force between fine particles and rock grains lowers down, which help fines more prone to be attached on pore surfaces. Thus, the existence of nanoparticles helps increasing the maximum (critical) retention concentration of fine particles on rock grains (Eq. 3.2). To extend the analytical modeling of co-injecting nanoparticle and fine particles in single-phase water flow, this section derives analytical solutions of nanoparticles-fine particles transport in two phase (oil and water) flow and evaluate both performance of formation

damage and enhanced oil recovery caused by fines and nanoparticles effects. Referring to section 3.3.1, the mass-balance equation of nanoparticles considering their adsorption on mobile fines, mass-balance equation of fines flow considering their attachment onto pore surface, and water component flowing through one-dimensional permeable medium can be written as:

Water component:

$$\frac{\partial f_w}{\partial x_D}+\frac{\partial S_w}{\partial t_D}=0 \quad \text{..... (4.1)}$$

Fine particles component:

$$\frac{\partial\left(C_{FP} f_w\right)}{\partial x_D}+\frac{\partial\left(S_w C_{FP}\right)}{\partial t_D}+\frac{1}{\phi}\frac{\partial \sigma_a}{\partial t_D}=0,\ \begin{cases}\sigma_a=\sigma_{cr};\ \ \sigma_{cr}<\sigma_{cr,\max}\\ \sigma_a=0;\quad \sigma_{cr}=\sigma_{cr,\max}\end{cases} \quad \text{..... (4.2)}$$

Nanoparticles component:

$$\frac{\partial\left(C_{NP} f_w\right)}{\partial x_D}+\frac{\partial\left(S_w C_{NP}\right)}{\partial t_D}+\frac{1}{\phi}\frac{\partial \hat{C}_{NP}}{\partial t_D}=0,\begin{cases}\hat{C}_{NP}=\dfrac{\hat{C}_{NP,\max} K_{NP} C_{NP}}{1+K_{NP} C_{NP}};\ \ \hat{C}_{NP}<\hat{C}_{NP,\max}\\ \hat{C}_{NP}=0;\quad \hat{C}_{NP}<\hat{C}_{NP,\max}\end{cases} \quad \text{... (4.3)}$$

The initial conditions and boundary (inlet) condition are:

$$C_{NP}(x_D,0)=0;\ C_{FP}(x_D,0)=C_{FP,initial};\ \sigma_a(x_D,0)=\sigma_{cr,initial};\ S_w=S_{wc} \quad \text{..... (4.4a)}$$

$$C_{NP}(0,t_D)=C_{NP,inj};\ C_{FP}(0,t_D)=C_{FP,inj};\ \sigma_a(0,t_D)=\sigma_{cr}(C_{NP,inj});\ S_w=1 \quad \text{..... (4.4b)}$$

The relative permeability of wetting water-phase is a function of the retained fine particles concentration onto wetting phase or non-wetting phase surfaces. To the best of our knowledge, in cases of polymer flooding or nanofluid flooding, there are already available models and evidence to confirm the wettability alteration caused by adsorption of injected substances. In this chapter, the relative permeability for wetting phase is

assumed as a monotonical increasing function of retained concentration of fine particles onto pore surfaces. The viscosity of flowing water is a function of fines concentration, which is modeled using Flory-Huggins equation (Pope et al. 1978). Apply the Taylor's expansion and leave the zero and first-order terms,

$$\frac{k_{rw}\left(S_w,\sigma_a\right)}{\mu_w\left(C_{FP}\right)}=\frac{k_{rw}\left(S_w,\sigma_{a,initial}\right)}{\left(1+\beta\sigma_a\right)\mu_w\left(1+aC_{FP}\right)} \quad \text{(4.5)}$$

The splitting method (Wagner, 1987) allows to the derivation of analytical solutions for two-phase multi-component flows by changing time to be a stream-function as a new independent variable. Pires et al. (2006) applied this method to study the analytical solutions of multi-component partially miscible gas flooding. Borazjani et al. (2016a and b) implemented the splitting method to obtain the analytical solutions of fines migration with multiple particles capture mechanisms and effects of fines migration on low salinity waterflooding. To the best of my knowledge, analytical models for two-phase flow of nanoparticles-fines considering their mutual reactions are not available now.

This chapter will introduce the splitting method for the system of nanoparticles-fine particle suspended in water-phase flow with mutual reactions among fines, nanoparticles, and rock grains. The governing system is reduced from the 3×3 system in Eq.4.1-4.3 to the 2×2 system of hyperbolic partial differential equations by the splitting method. A new system is formulated as two sub-systems, including, particles retention-kinetics auxiliary subsystem with nanoparticles and fines components and lifting system for unknown water saturation. The procedure to solve the problem includes 1) analytical solutions of both auxiliary system and lifting system, and 2) inversion of solutions by transforming back the coordinates.

4.2.2 Analytical Solutions and Derivations

First, let us introduce the concept of stream-function φ associated with the conservation law of water component in Eq.4.1 (Pires et al. 2006).

$$S_w = -\frac{\partial \varphi}{\partial x_D},\ f_w = \frac{\partial \varphi}{\partial t_D} \quad \text{..... (4.6)}$$

The corresponding differential form of two-phase flux is

$$d\varphi = f_w dt_D - S_w dx_D \quad \text{..... (4.7)}$$

Expressing the differential form dt_D from the above equation:

$$dt_D = \frac{1}{f_w} d\varphi + \frac{S_w}{f_w} dx_D \quad \text{.....}$$

(4.8)

The equality of mixed partials of t_D results in the transformation of Eq.4.5 into the coordinate of (x_D, φ), which is called the lifting equation (Borazjani et al. 2016b):

$$\frac{\partial G}{\partial x_D} + \frac{\partial F}{\partial \varphi} = 0; \quad G = \frac{1}{f_w}; \quad F = -\frac{S_w}{f_w} \quad \text{..... (4.9)}$$

Integrating both sides of mass-balance equation of fine particles in Eq. 4.1 over any arbitrary closed and simply-connected domain in the plane of (x_D, t_D) and applying Green's theorem result in:

$$\begin{aligned} &\iint_D \left[\frac{\partial \left(C_{FP} f_w \right)}{\partial x_D} + \frac{\partial \left(S_w C_{FP} \right)}{\partial t_D} + \frac{1}{\phi} \frac{\partial \sigma_a}{\partial t_D} \right] dx_D dt_D = \oint_{\partial D} C_{FP} f_w dt_D - C_{FP} S_w dx_D - \frac{1}{\phi} \sigma_a dx_D \\ &= \oint_{\partial D} C_{FP} d\varphi - \frac{1}{\phi} \sigma_a dx_D = \iint_D \left[\frac{\partial C_{FP}}{\partial x_D} + \frac{1}{\phi} \frac{\partial \sigma_a}{\partial \varphi} \right] dx_D d\varphi \end{aligned} \quad \text{..(4.10)}$$

Yield to an independent-variable transformation of mass-balance equation of fine

particles in Eq.4.2:

$$\frac{\partial C_{FP}}{\partial x_D}+\frac{1}{\phi}\frac{\partial \sigma_a}{\partial \varphi}=0 \quad \text{..... (4.11)}$$

Similar to Eq.4.10, the transformation of nanoparticles mass-balance equation is performed as:

$$\begin{aligned}&\iint_D\left[\frac{\partial\left(C_{NP}f_w\right)}{\partial x_D}+\frac{\partial\left(S_wC_{NP}\right)}{\partial t_D}+\frac{1}{\phi}\frac{\partial \hat{C}_{NP}}{\partial t_D}\right]dx_Ddt_D=\oint_{\partial D}C_{NP}f_wdt_D-C_{NP}S_wdx_D-\frac{1}{\phi}\hat{C}_{NP}\,dx_D\\&=\oint_{\partial D}C_{NP}d\varphi-\frac{1}{\phi}\hat{C}_{NP}\,dx_D=\iint_D\left[\frac{\partial C_{NP}}{\partial x_D}+\frac{1}{\phi}\frac{\partial \hat{C}_{NP}}{\partial \varphi}\right]dx_Dd\varphi\end{aligned} \quad (4.12)$$

Yield to transformed mass-balance equation of nanoparticles with new independent-variable, stream-function:

$$\frac{\partial C_{NP}}{\partial x_D}+\frac{1}{\phi}\frac{\partial \hat{C}_{NP}}{\partial \varphi}=0 \quad \text{..... (4.13)}$$

As results, the transformations of all equations describing the transport of nanoparticles and fines in system of Eq.4.2-4.3 are summarized as an auxiliary system:

$$\begin{cases}L_1=\overset{A_1}{\phi}\dfrac{\partial C_{FP}}{\partial x_D}+\overset{D_1}{\dfrac{\partial \sigma_{cr}}{\partial C_{NP}}}\dfrac{\partial C_{NP}}{\partial \varphi}=0, & (a)\\ L_2=\overset{B_2}{\dfrac{\partial \hat{C}_{NP}}{\partial C_{FP}}}\dfrac{\partial C_{FP}}{\partial \varphi}+\overset{C_2}{\phi}\dfrac{\partial C_{NP}}{\partial x_D}+\overset{D_2}{\dfrac{\partial \hat{C}_{NP}}{\partial C_{NP}}}\dfrac{\partial C_{NP}}{\partial \varphi}=0, & (b)\end{cases} \quad \text{..... (4.14)}$$

Now, method of characteristic is applied to solve the above auxiliary system. To make sure that the characteristic lines of both variables C_{NP} and C_{FP} along the same direction in a single system, a linear combination of the above two differential equations is defined as $L=\lambda_1L_1+\lambda_2L_2$ to yield:

$$L = \lambda_1 A_1 C_{FP,x_D} + \lambda_2 B_2 C_{FP,\varphi} + \lambda_2 C_2 C_{NP,x_D} + \left(\lambda_2 D_2 + \lambda_1 D_1\right) C_{NP,\varphi} = 0 \quad \text{...……..…} \quad (4.15)$$

where L_1 and L_2 are the functions of derivatives of two variables; λ_1, λ_2 are the line combination coefficients;

Inferred from Eq. A.5 in Appendix A, two characteristic directions can be obtained by setting the determinate of coefficient matrix as zero:

$$\left(\frac{d\varphi}{dx_D}\right)_1^{\pm} = \sigma_1^{\pm} = \frac{A_1 D_2 \pm \sqrt{\left(A_1 D_2\right)^2 + 4 A_1 B_2 C_2 D_1}}{2 A_1 C_2} \quad \text{……...…..…..} \quad (4.16)$$

To obtain the composition path $C_{FP}\left(C_{NP}\right)$, the coefficients of PDEs in system of Eq.4.14 are compared with Eq. A.1, and then get,

$$\frac{dC_{NP}}{dC_{FP}} = \frac{-B_2}{\sigma_{1,\pm} C_2} \quad \text{……..……...} \quad (4.17)$$

Combining Eq. 4.16 with Eq. 4.17 leads to the dynamic relation between suspended nanoparticles and suspended fines concentration, along two different characteristic directions, i.e., slow path and fast path, as shown Figure. 4.1.

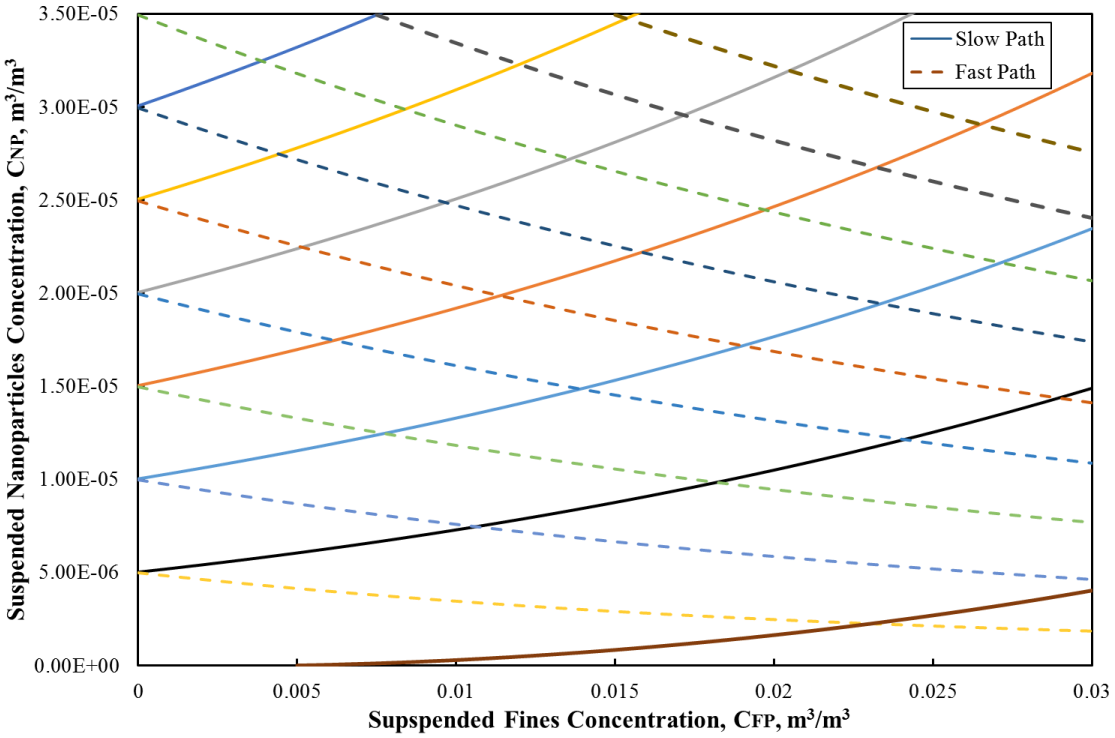


Figure 4.1 Composition diagram of suspended nanoparticles and fines concentration along the slow path and fast path in coordinate of stream-function and distance

After transforming to stream-function from time as the new independent variable, the initial conditions and boundary (inlet) conditions (Eq. 4.4) become:

$$\varphi = -S_{wc}x_D:\ C_{NP} = 0;\ C_{FP} = C_{FP,initial};\ \sigma_a = \sigma_{cr,initial};\ S_w = S_{wc} \quad \text{..... (4.18a)}$$

$$x_D = 0: C_{NP} = C_{NP,inj};\ C_{FP} = C_{FP,inj};\ \sigma_a = \sigma_{cr}(C_{NP,inj});\ S_w = 1 \quad \text{..... (4.18b)}$$

Inferred from Rankine-Hugoniot relation and concept of discontinuity, the reciprocal of characteristic velocity (Eq. 4.16) must decrease monotonically. Otherwise, it must exist a shock along the composition path from the injection condition to the initial condition. Applying the mass-balance conditions on shock waves for Eq. 4.11 and Eq. 4.13 by equating the outgoing and incoming flux equality yield to the moving velocity of shock front.

$$(\frac{d\varphi}{dx_D})_1 = \frac{[\sigma_{cr}]}{[\phi C_{FP}]} = \frac{\left[\hat{C}_{NP}\right]}{[\phi C_{FP}]} \quad \text{..... (4.19)}$$

After the suspended and retained fine particles concentrations have been known from the above solutions. Combining Eq. 4.9 with the initial and boundary conditions (Eq. 4.18) results in a hyperbolic partial differential equation of lifting system. The characteristic form of lifting equation (Eq.4.9) is:

$$\left(\frac{d\varphi}{dx_D}\right)_2 = \sigma_2 = \frac{\partial F}{\partial G} = \frac{f_w\left(S_w, \sigma_a, C_{FP}\right) - S_w \dfrac{\partial f_w\left(S_w, \sigma_a, C_{FP}\right)}{\partial S_w}}{\dfrac{\partial f_w\left(S_w, \sigma_a, C_{FP}\right)}{\partial S_w}} \quad \text{..... (4.20a)}$$

$$\frac{dS_w}{dx_D} = \frac{\dfrac{\partial f_w}{\partial \sigma_a}\left(S_w \dfrac{\partial \sigma_a}{\partial \varphi} - \dfrac{\partial \sigma_a}{\partial x_D}\right) + \dfrac{\partial f_w}{\partial C_{FP}}\left(S_w \dfrac{\partial C_{FP}}{\partial \varphi} - \dfrac{\partial C_{FP}}{\partial x_D}\right)}{\dfrac{\partial f_w}{\partial S_w}} \quad \text{..... (4.20b)}$$

Inferred from Eq. 4.16 and Eq. 4.17, the first derivative of retained fines and suspended fines concentration to stream-function and distance can be determined along the characteristic directions, respectively.

$$\frac{\partial \sigma_a}{\partial \varphi} = \frac{1}{\left(\dfrac{\partial \sigma^{\pm}}{\partial C_{FP}} \dfrac{dC_{FP}}{dC_{NP}} + \dfrac{\partial \sigma^{\pm}}{\partial C_{NP}}\right) \dfrac{dC_{NP}}{d\sigma_a} x_D} \quad \text{..... (4.21a)}$$

$$\frac{\partial \sigma_a}{\partial x_D} = \frac{-\varphi}{\left(\dfrac{\partial \sigma^{\pm}}{\partial C_{FP}} \dfrac{dC_{FP}}{dC_{NP}} + \dfrac{\partial \sigma^{\pm}}{\partial C_{NP}}\right) \dfrac{dC_{NP}}{d\sigma_a} x_D{}^2} \quad \text{..... (4.21b)}$$

$$\frac{\partial C_{FP}}{\partial \varphi} = \frac{1}{\left(\dfrac{\partial \sigma^{\pm}}{\partial C_{NP}} \dfrac{dC_{NP}}{dC_{FP}} + \dfrac{\partial \sigma^{\pm}}{\partial C_{FP}}\right) x_D} \quad \text{..... (4.21c)}$$

$$\frac{\partial C_{FP}}{\partial x_D} = \frac{-\varphi}{\left(\frac{\partial \sigma^{\pm}}{\partial C_{NP}} \frac{dC_{NP}}{dC_{FP}} + \frac{\partial \sigma^{\pm}}{\partial C_{FP}} \right) x_D{}^2} \quad \text{(4.21d)}$$

Substituting Eq.4.21 into Eq. 4.20 result in the characteristic direction along which water saturation varies. An iterative algorithm using Eq. 4.16, Eq. 4.17 and Eq. 20 is applied to get the values of different components in coordinate of $\left(x_D, \varphi\right)$, as shown in Figure 4.2. The detailed workflow is described, as follows.

Substituting the values of different parameters at the initial point of $\left(x_{D,i}, \varphi_i\right)$ into Eq. 4.20a, the characteristic velocity of lifting equation and along which the variation of water saturation (Eq. 4.20b) performs are determined. By giving a distance step Δx_D, a new set of $\left(S_w, t_D\right)$ is obtained using Eq.4.20b. As for the calculation of nanoparticles and fines concentration, firstly, substituting the initial values of nanoparticles and fines concentration into Eq.4.17yields to the composition path. Followed by, combining the result of Eq. 4.17 into Eq.4.16 determines the characteristic velocity of nanoparticles-fines concentration wave. Because the dependent variables (i.e., nanoparticles concentration and fines concentration) along the characteristic direction (Eq. 4.16) keep constant, the characteristic lines would be straight along with constant values of $\left(C_{NP}, C_{FP}\right)$. Afterwards, by equating Eq.4.16 to the slope of the connection lines between new points $\left(x_{D,i+1}, \varphi_{i+1}\right)$ and original point $\left(0,0\right)$, the values of $\left(C_{NP}, C_{FP}\right)$ at new points can be obtained. Consequently, at the new point in distance-stream function diagram, all the values of water saturation, fines concentration and nanoparticles concentration have been updated. Repeating the above workflow yields the distribution of all component

concentrations in the coordinate of (x_D, φ).

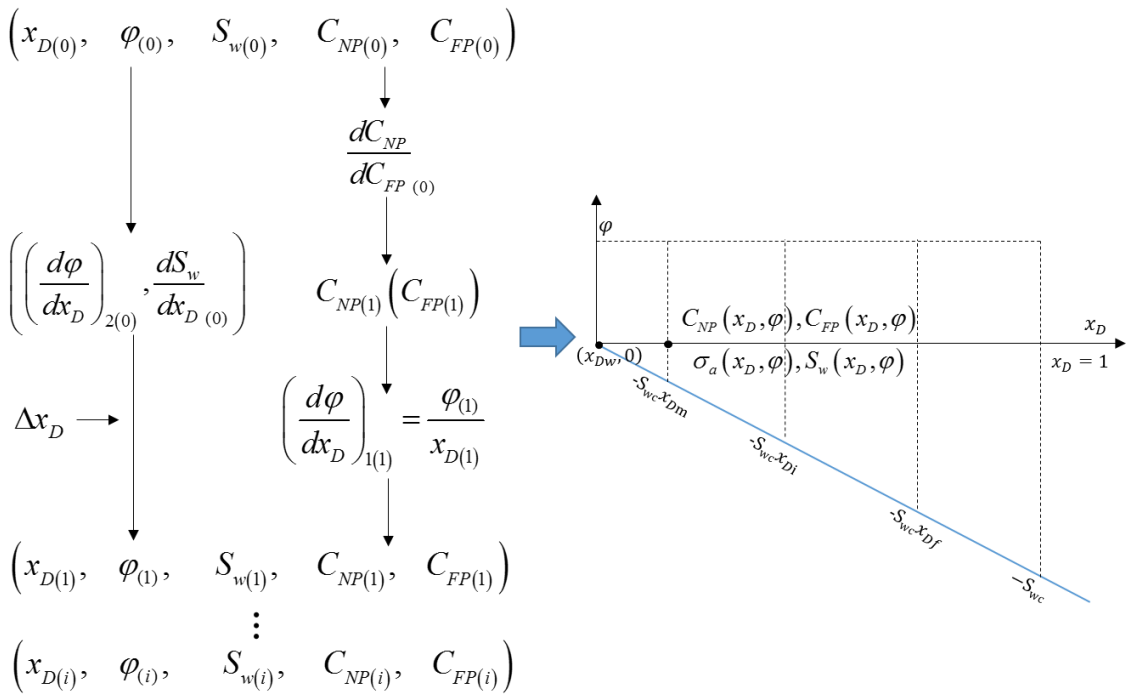


Figure 4.2 Flowchart to derive the propagation of water saturation, nanoparticles, and fines concentration in the plane of stream-function and distance

After the analytical solutions in coordinate of (x_D, φ) have been obtained, an inverse transformation of stream-function back to time as independent variable is implemented, as follows,

$$t_D = \int_{(0,0)}^{(x_D,\varphi)} \frac{1}{f_w(x_D,\varphi)} d\varphi + \frac{S_w(x_D,\varphi)}{f_w(x_D,\varphi)} dx_D \quad \text{.....} \quad (4.22)$$

Finally, combining Eq. 4.22 with the above solutions of the auxiliary and lifting system leads to the exact solutions of problem Eq. 4.1-Eq. 4.3 in coordinate of (x_D, t_D).

4.2.3 Results Discussion and Verification

To clarify the application of the above exact solutions, several examples with input values listed in Table. 4.1 are presented in this section. As inferred in Figure 4.3, the

composition path (Eq. 4.17) for two-phase flow (oil & water) and that for single-phase water flow (Eq. 4.23-24) starting from the same initial condition are different. The injected condition for single-phase flow that yields zero-concentration of fines at the constant-state is lower than that in case of two-phase flow.

For the case of nanoparticles and fines in single-phase flow, the injection condition ($C_{NP,INJ} = 1.05e^{-6}; C_{FP,INJ} = 0.02$) and initial condition ($C_{NP,INI} = 0; C_{FP,INI} = 0.02$) are defined. For the case of nanoparticles and fines in two-phase flow, the injection condition ($C_{NP,INJ} = 1.89e^{-6}; C_{FP,INJ} = 0.02$) and initial condition ($C_{NP,INI} = 0; C_{FP,INI} = 0.02$) are defined. In other words, for two-phase flowing case, the oilfield operators need to spend more nanoparticles under the condition of mobile oil than that under the residual-oil condition. The difference can be explained by combination of Eq. 4.17 and Eq. 3.23-3.24, which express the relation between nanoparticles and fines concentration for single-phase and two-phase flow, respectively.

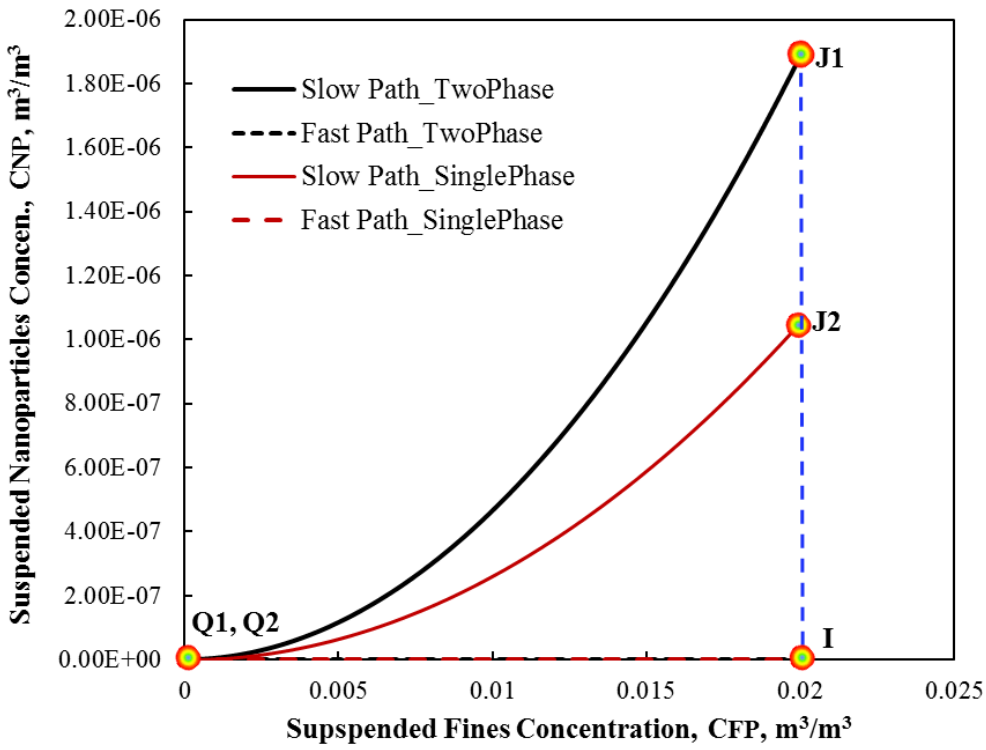


Figure 4.3 Composition path from the injection to initial condition in the example (Oil & water phase: Injection condition：C_{NP}=1.80E-6， C_{FP}=0.02；Constant-state condition：C_{NP}=1.32E-15, C_{FP}=0；Initial condition：C_{NP}=0, C_{FP}=0.02. Single water phase: Injection condition：C_{NP}=1.05E-6， C_{FP}=0.02；Constant-state condition：C_{NP}=9.93E-16, C_{FP}=0；Initial condition：C_{NP}=0, C_{FP}=0.02.)

4.2.3.1 Solutions of Auxiliary System and Lifting Equation

Along the slow path from injection point J_1 to constant-state point Q, the slopes of characteristic lines show a counterclockwise trend from -0.7752 to 0 in the domain of (x_D, φ), and thus, there is a shock from point J_1 to point Q, which is called as *c-shock1*. Followed b, along the fast path from constant-state point Q_1 to initial point I, the slopes of characteristic lines increase from 0 to 1.60, which also fans counterclockwise; thus, there is another shock from point Q1 to point I, which is named as *c-shock2*. To determine the trajectory of those two shock fronts, the compatibility condition (Hankins, 2004;

Lake, 1989) is applied for mass-balance at both sides of two c-shock fronts, as shown in Eq. 4.19. The characteristic velocities of *c-shock1* and *c-shock2* are determined as 1.38 and 0.0, respectively, as shown in Figure. 4.4.

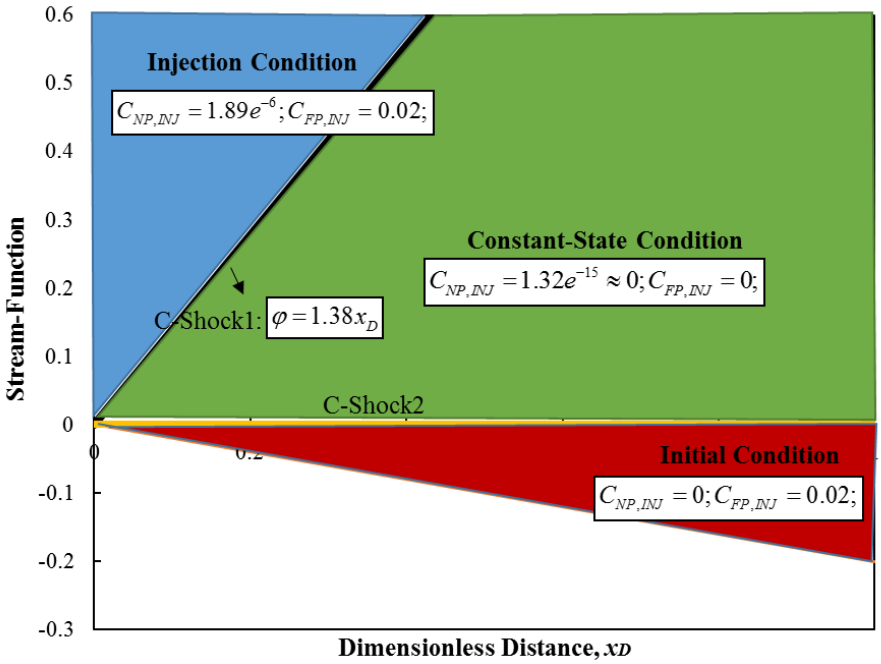


Figure 4.4 Stream-function/distance diagram with the propagation of different nanoparticles-fines condition for two-fluid phase flow

(Injection condition：C_{NP}=1.80E-6， C_{FP}=0.02；Constant-state condition：C_{NP}=1.32E-15, C_{FP}=0；Initial condition：C_{NP}=0, C_{FP}=0.02)

After the distributions of (C_{FP}, C_{NP}) in the coordinate of (x_D, φ) have been determined from the exact solutions of auxiliary system in Figure. 4.4, substituting the values of (C_{FP}, C_{NP}) into Eq. 4.20, the characteristic lines associated with different values of (C_{FP}, C_{NP}) are obtained, as shown in Figure 4.5. Around the discontinuities of particles-concentration wave, *c-shock1* and *c-shock2*, there is also a discontinuity of water saturation wave, as shown in Figure 4.5, where water saturation decrease from 0.76 upstream to 0.696 downstream of *c-shock1*, and water saturation increase from 0.66 upstream to 0.693 downstream of *c-shock2*. In the region of initial-condition, there is

another S_w-*shock* because of the discontinuity of fraction flow curve (Figure. 4.6), where water saturation decrease directly from 0.66 to the connate-water saturation 0.20.

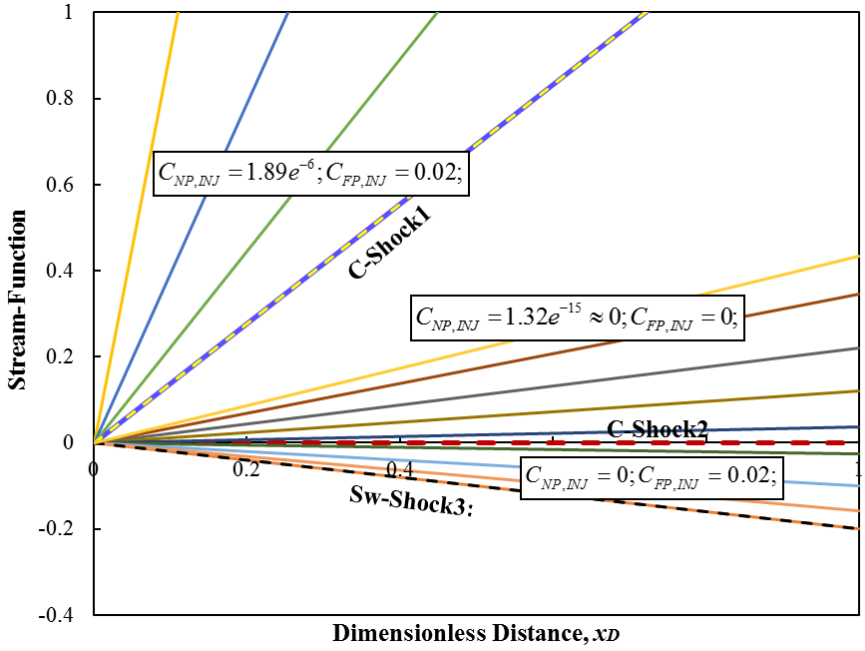


Figure 4.5 Stream-function and distance diagram with the propagation of water-saturation wave and different nanoparticles-fines concentration wave

(Injection condition：C_{NP}=1.80E-6， C_{FP}=0.02；Constant-state condition：C_{NP}=1.32E-15, C_{FP}=0；Initial condition：C_{NP}=0, C_{FP}=0.02

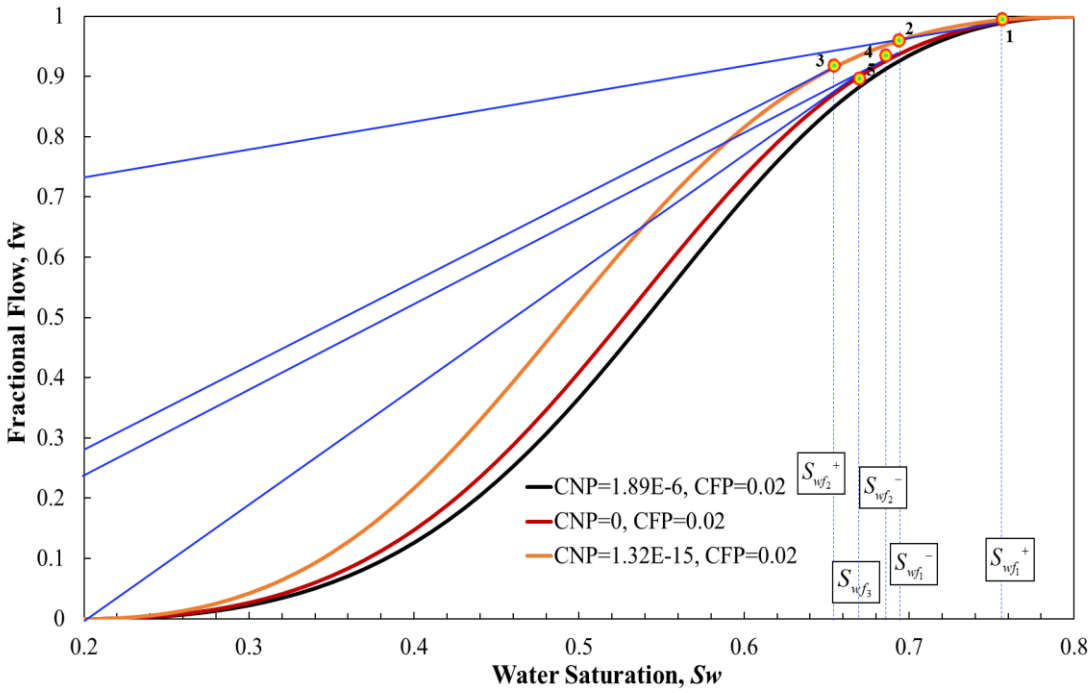
Water-saturation wave: S_{wj}=0.80, Sw_{f1}^{+}=0.76, Sw_{f1}^{-}=0.696, Sw_{f2}^{+}=0.66, Sw_{f2}^{+}=0.693, Sw_{f3}= 0.66, S_{wi} = S_{wc}=0.80)

Alternatively, the exact solutions of auxiliary system and lifting equation can be graphically determined using the switch among different fractional flow curves from the injection point to the initial point, as shown in Figure 4.6. Firstly, the rarefaction wave of water-saturation from the injection point to point 1 at the fraction flow curve ($C_{NP,INJ}=1.89e^{-6};C_{FP,INJ}=0.02$) propagate in the region of injection-condition, until reaches c-*shock*$_1$, where water saturation jump from point 1 to point 2 with $S_{wf_1}^{+}\rightarrow S_{wf_1}^{-}$ occurs. The point 2 can be determined by drawing a straight line connecting point 1 with point 2 at the fraction flow curve ($C_{NP,INJ}=1.32e^{-15};C_{FP,INJ}=0$) with the slope same with

the moving velocity of c-*shock*$_1$ *(*Eq. 4.20*)*. Followed by, it enters the region of constant-state condition with the fraction flow curve ($C_{NP,INJ}=1.32e^{-15}; C_{FP,INJ}=0$). In this region, the spreading wave of water saturation continuously varies from point 2 to point 3 $S_{wf_1}^{-} \rightarrow S_{wf_2}^{+}$, until reaches c-*shock*$_2$, where water saturation jumps to point 4 $S_{wf_2}^{-}$. The point 4 is determined by the equality between the characteristic velocity of c-*shock2* and the slope of tangent line along the fractional flow curve ($C_{NP,INJ}=0; C_{FP,INJ}=0.02$).

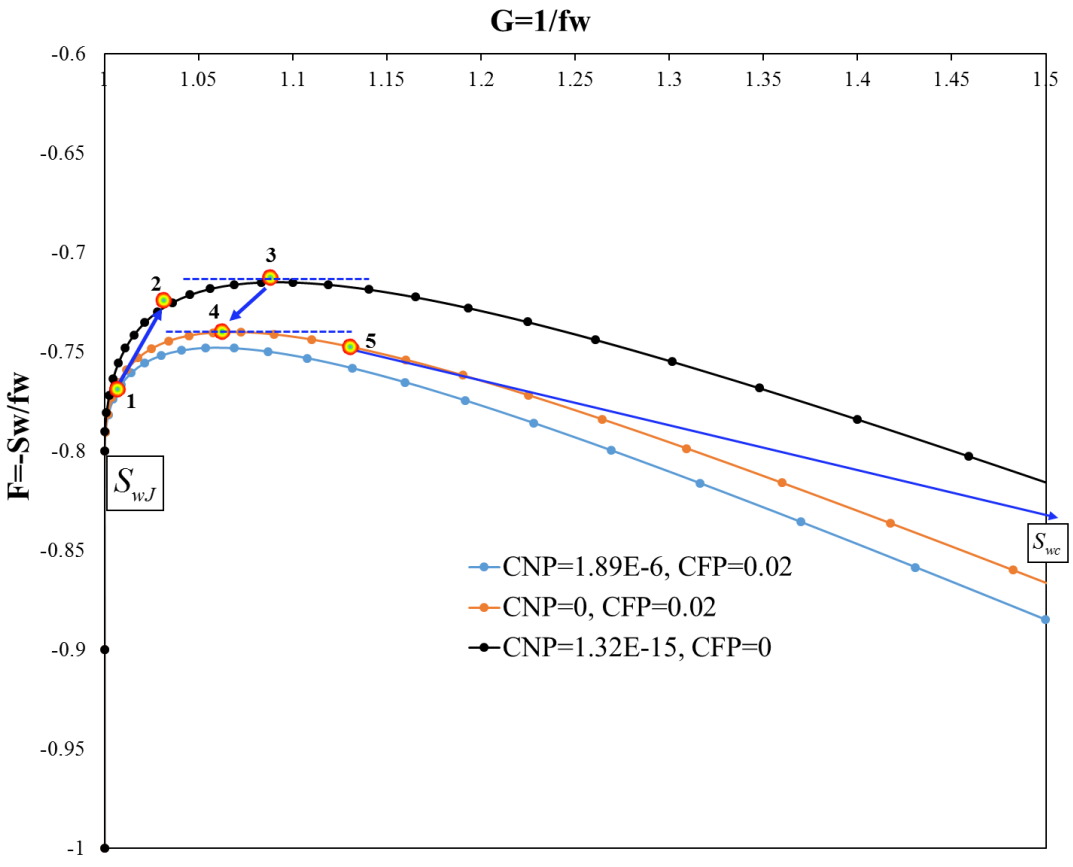
In addition, because the characteristic velocity in the plane *of* (U, F) curve with ($C_{NP,INJ}=1.32e^{-15}; C_{FP,INJ}=0$) obtained by Eq. 4.20 is infinite at point 3, the point 4 can be determined by finding a tangent line of U-F curve with ($C_{NP,INJ}=0; C_{FP,INJ}=0.02$) whose slope as zero. In the initial-condition region, there is a sequence of rarefaction water-saturation waves from point 4 to point 5 until S_w-*shock*, where the jump $S_{wf_3} \rightarrow S_{wc}$ occurs to reach the initial conditions.

Finally, the exact solutions of water saturation, nanoparticles and fines concentration from both auxiliary system and lifting system are obtained in coordinate of (x_D, φ).



(a) Fraction flow curves with different nanoparticles-fines concentration and water

saturations variation in the analytical solutions



(b) Solutions of lifting system in the plane of (*U*, *F*) and corresponding points of water saturation in fractional flow curve

Figure 4.6 Graphical solution of nanoparticles and fines concentration in oil-water flow along 1-D porous media

(a. Fraction flow curves with different nanoparticles-fines concentration and water saturations variation; b. Solutions of lifting system in the domain of (*U*, *F*) and corresponding points of water saturation in fractional flow curve)

4.2.3.2 Inversed Mapping of Solutions

Inferred by Eq. 4.22, the calculations of $t_D\left(x_D,\varphi\right)$ for each point in coordinate of $\left(x_D,\varphi\right)$ in Figure 4.5 after the distributions of $\left(C_{FP},C_{NP},S_w\right)$ have been determined from the solutions of above auxiliary system and lifting equation. In Figure 4.5, the values of

nanoparticles and fines concentration keep constant within different regions, respectively. As results, water saturation (S_w) and fraction flow function (f_w) are also constant along the characteristic lines in different regions in Figure 4.5. Hence, the explicit formula of independent variable t_D can be transformed back by integrating Eq. 4.22,

$$t_D = \left(\frac{1}{f_w} \left(\frac{d\varphi}{dx_D} \right)_{2(S_w, C_{FP}, C_{NP})} + \frac{S_w}{f_w} \right) x_D \quad \text{..... (4.23)}$$

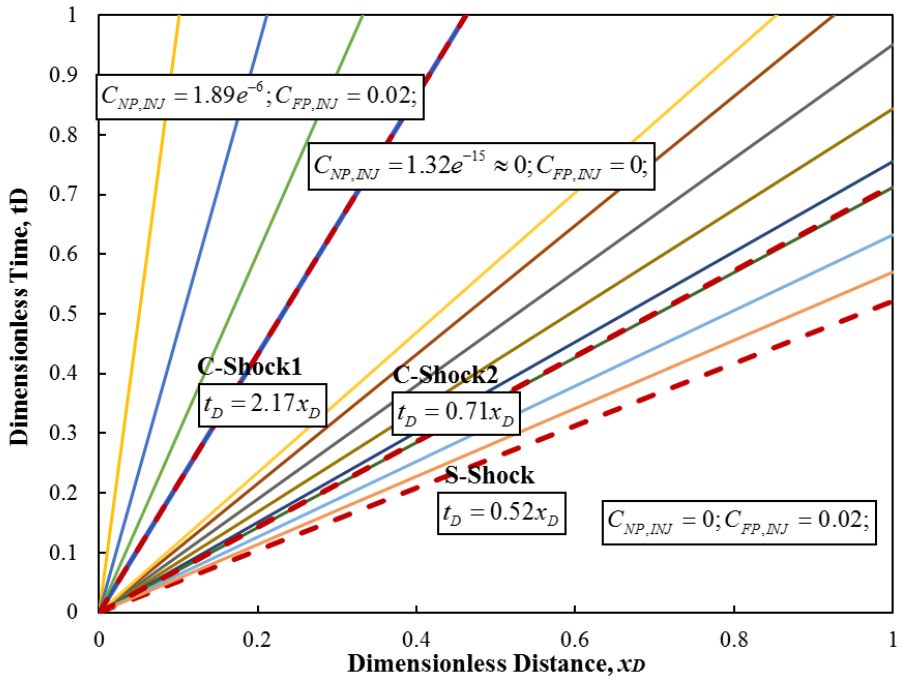
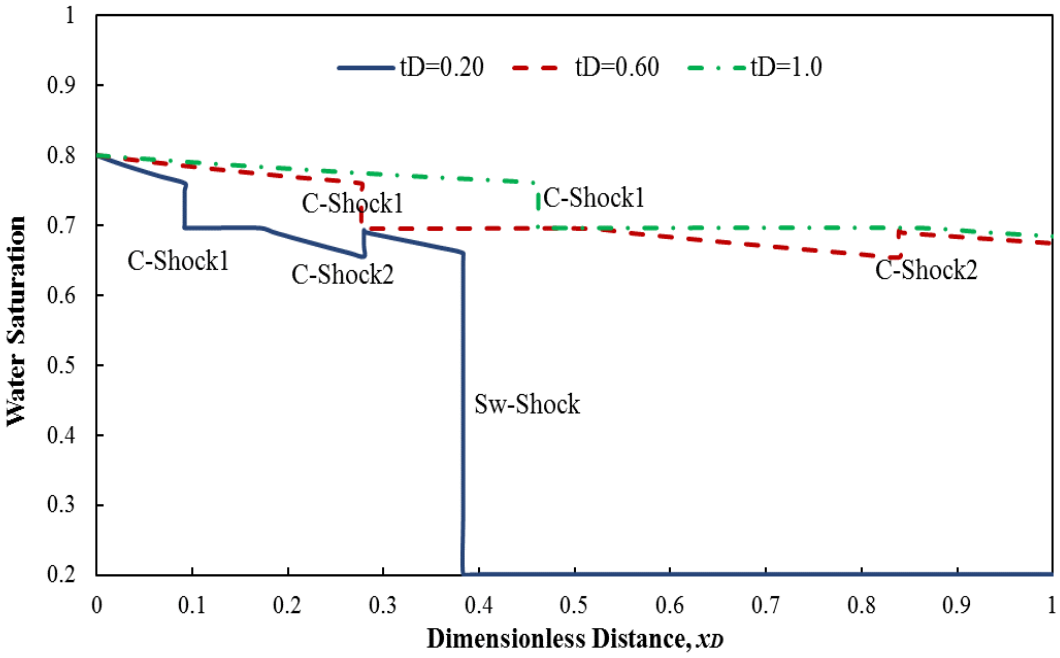


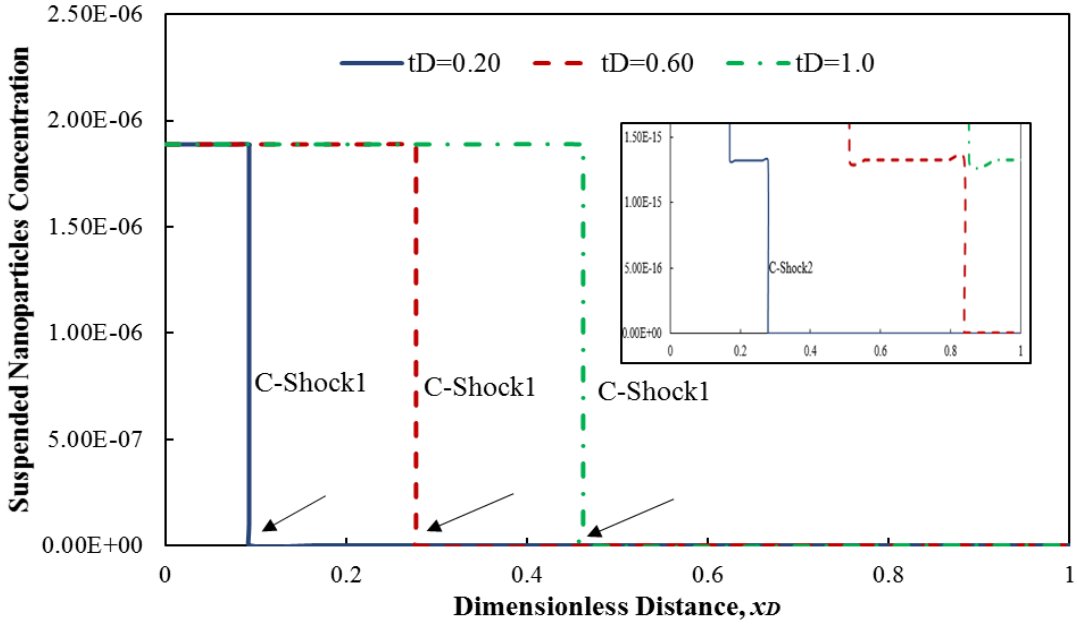
Figure 4.7 Distance-time diagram of nanoparticles-fines transport in oil-water flow in the coordinate of (x_D, t_D)

Where the characteristic velocity is calculated using Eq.4.20a with specific values of water saturation, fines concentration and nanoparticles concentration. Because the concentration of those three components along the characteristic lines in Figure 4.7 are kept as constant, the inversed transformation of $\varphi(x_D, t_D)$ yields to a straight-line image of $t_D(x_D, \varphi)$, as shown in Figure 4.7. The moving velocities of c-*shock*$_1$, c-*shock*$_2$, and

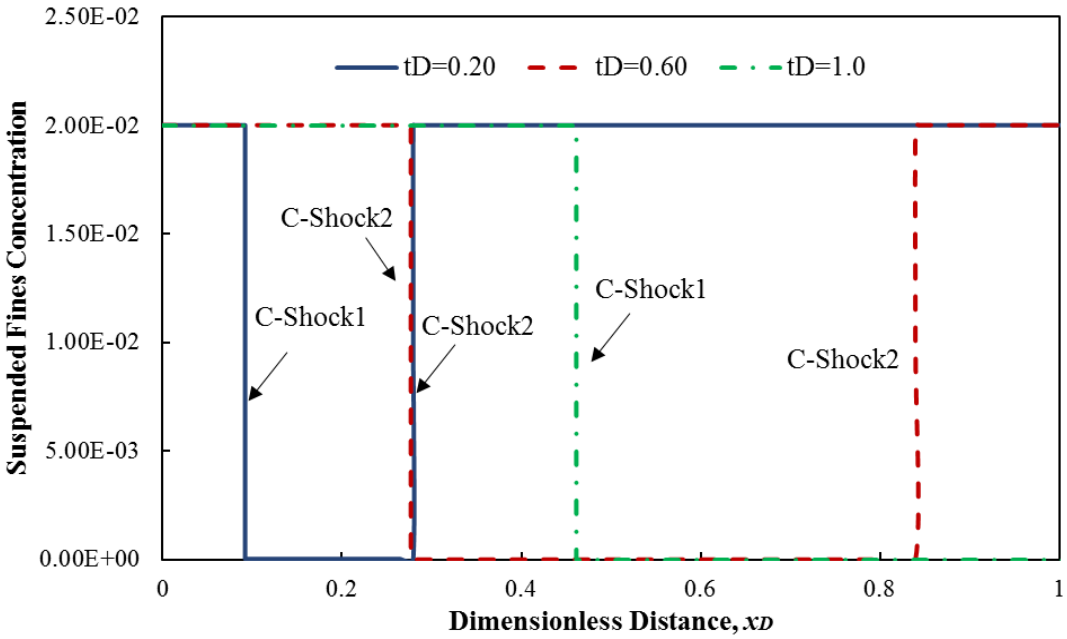
S_w-shock change to be 2.17, 0.71 and 0.52, respectively, in coordinate of (x_D, t_D).



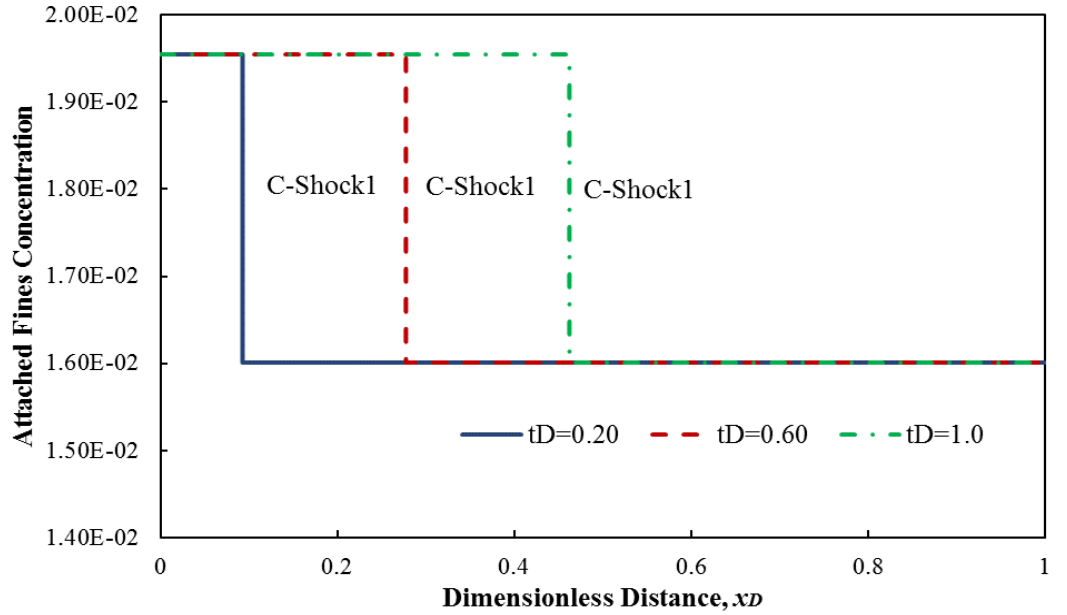
(a) Profile of water saturation along 1-D permeable medium at different moments (t_D=0.20, 0.60 and 1.0)



(b) Profile of suspended nanoparticles concentration along 1-D permeable medium at different moments (t_D=0.20, 0.60 and 1.0)



(c) Profile of suspended fines concentration along 1-D permeable medium at different moments (t_D=0.20, 0.60 and 1.0)



(d) Profile of attached fines concentration along 1-D permeable medium at different moments (t_D=0.20, 0.60 and 1.0)

Figure 4.8 Profile of water saturation, suspended nanoparticles, suspended fines and attached fines concentration in oil-water flow along 1-D porous medium

In the distance-time diagram of Figure 4.7, the intersection points of horizontal lines (t_D=*const*.) with the characteristic lines with different set of (C_{FP}, C_{NP}, S_w) correspond to the profile of component concentration along 1-D porous medium, as shown in Figure 4.8. Indicated by Figure 4.8, three shock fronts exist, i.e., *c-shock*$_1$, *c-shock*$_2$ and S_w-*shock*, which separate into different zones in Figure 4.7. At the moment of (t_D=*0.20*), the breakthrough of injected water has not occurred yet. Later, at both moments of (t_D=*0.60, 1.0*), the injected water has already reached the outlet. The existence of fines migration and nanoparticles utilization leads to the formulation of a "oil-bank" in the region between *c-shock*$_1$ and *c-shock*$_2$. The "oil-bank" is followed by a spreading wave derived from fractional flow curve at injection conditions of (C_{FP}, C_{NP}). The effects of injected nanoparticles on both fines migration control and improvement of waterflooding performance will be discussed in next section.

4.2.3.3 Evaluation on Nanoparticles Contributions

Figure 4.9 presents the profile of fines concentration along 1-D porous medium at the same moment of 0.60 for cases with and without nanoparticles. It is worth mentioning that the differences between two cases, i.e., the rectangular envelop, represents the reduction of fines migration only attributed to the positive contributions of nanoparticles.

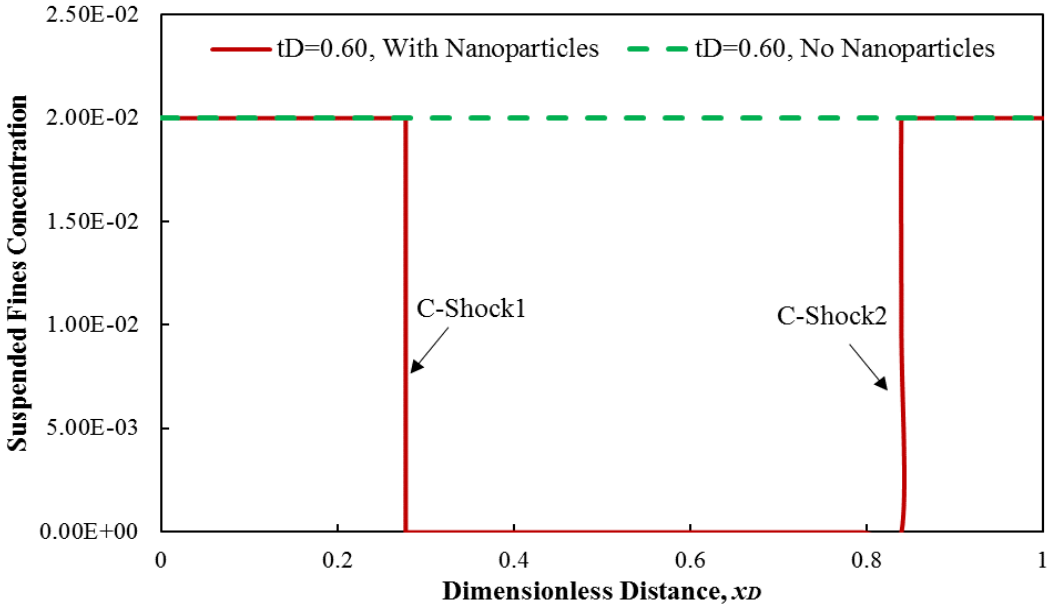


Figure 4.9 Suspended fines concentration profile in oil-water flow along 1-D porous medium (Dash line: without nanoparticles injection; Solid line: with nanoparticles injection. The difference between two lines represents the reduction number of mobile fines attributed to nanoparticles effects)

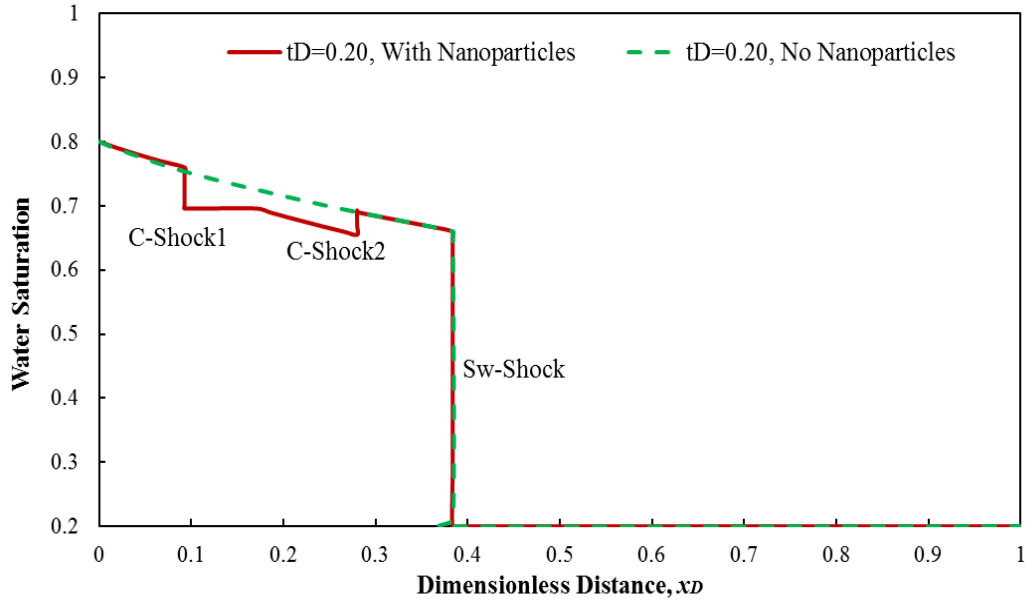


Figure 4.10 Profile of water saturation in oil-water flow along 1-D porous medium (Dash line: without nanoparticles injection; Solid line: with nanoparticles injection. The difference between two lines represents the reduction amount of water saturation or oil-bank attributed to nanoparticles effects)

Figure 4.10 presents the profile of water saturation along 1-D porous medium at the same moment of 0.60 for both cases with and without nanoparticles, respectively. The positive contribution of nanoparticles brings the reduction of water saturation between *c-shock1* and *c-shock2*, which leads to the formulation of a "oil-bank". Inferred from the improved fines attachment onto pore surfaces by nanoparticles co-injection () and the relation between the decrease of water-phase relative permeability and fines attachment (Eq. 4.5), the enhanced waterflooding performance can be attributed to the effects of nanoparticles co-injection to control fines migration.

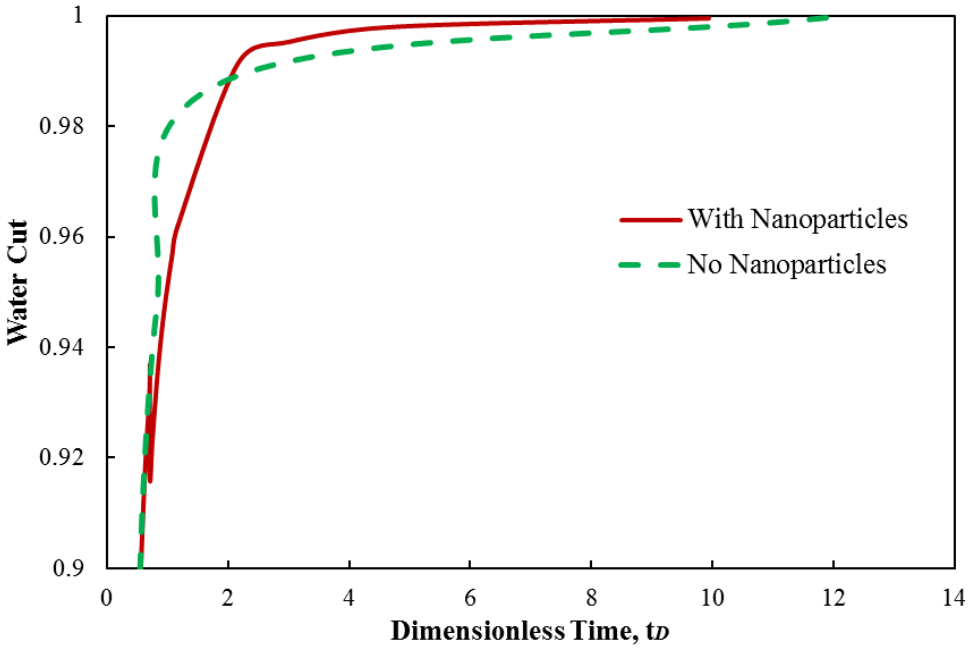


Figure 4.11 Water-cut history accounting for effects of fines migration and nanoparticles utilization
(Dash line: without nanoparticles injection; Solid line: with nanoparticles injection)

Figure 4.11 presents the curve of water-cut at different moments for both cases with and without nanoparticles, respectively. As indicated by Eq. 4.5, the performance of fines

migration control by nanoparticles utilization can be confirmed by the reduction of relative permeability of water-phase, which delays the increase of water production. The utilization of nanoparticles brings more attachment of water-wet fine particles, as results, further decrease the flow capacity of water phase. As shown in Figure. 4.11, even though nanoparticles co-injection does not delay the breakthrough of injected water which is determined by the fractional flow curve at the initial condition, the long-term curve of water-cut can be changed significantly by nanofluid utilization, especially prior to the breakthrough moment of *c-shock*$_1$, as shown in Figure 4.11.

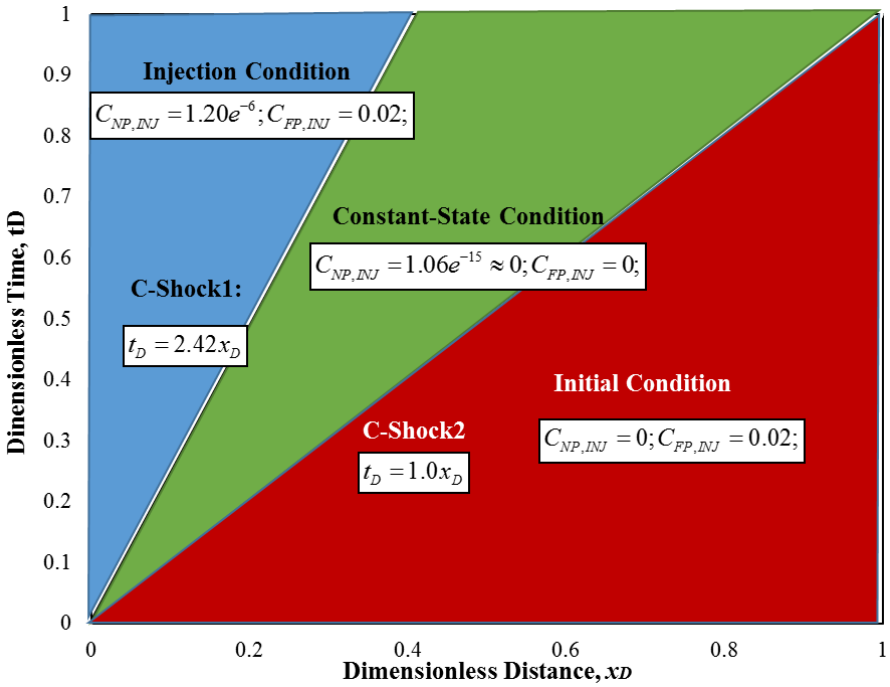
4.2.3.4 Phase Effects on Nanoparticles Performance

As indicated by Figure 4.3, in single-phase (water) flow, the composition paths between nanoparticles and fines concentration are different from that in two-phase (oil & water) flow. In other words, to mitigate the same amounts of mobile fines in porous medium initially, less amounts of nanoparticles are required for the case of single-phase flow. In addition, because of phase saturation on fraction flow, performances of nanoparticles to mitigate fines migration are different between single-phase flow and two-phase flow. In this section, the comparison of nanoparticles contributions under the same initial and boundary conditions will be discussed for the cases of different phase-saturation (e.g., single-phase: $S_{wi}=1-S_{or}$; two-phase: $S_{wi}=S_{wc}$, $S_{oi}=1-S_{wc}$).

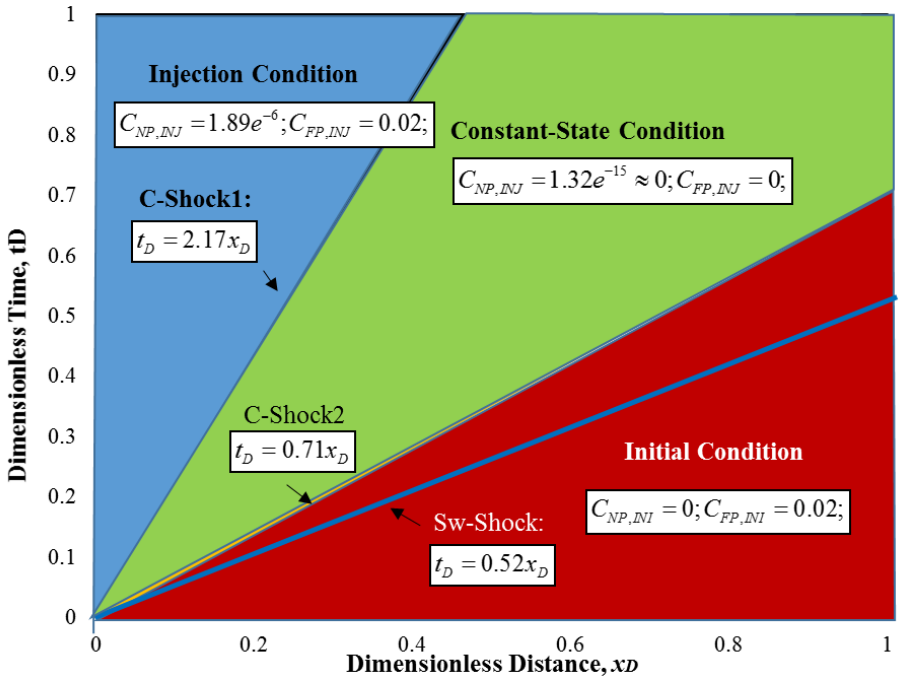
In single-phase flow, the movement of *c-shock1* and *c-shock2* slows down in comparison with those in two-phase flow. The values of suspended nanoparticles concentration and fines concentration in different regions are also different from those in two-phase flow, as shown in Figure 4.12. In different regions of Figure 4.12a, the nanoparticles and fines concentrations are determined as, injection condition：

C_{NP}=1.20E-6， C_{FP}=0.02； constant-state condition： C_{NP}=1.06E-15, C_{FP}=0； initial condition： C_{NP}=0, C_{FP}=0.02. By placing horizontal lines with constant time to pass through different zones in Figure 4.12 a and b, the intersection points correspond to the profile of nanoparticles and fines concentration along 1-D porous medium at that moment.

As shown in Figure 4.13, the decrease of moving velocity of *c-shock1* along with a discontinuity of nanoparticles concentration wave can be attributed to the increase of nanoparticles adsorption onto flowing fines in single-phase flow. The enhanced efficiency of nanoparticles adsorption brings more significant control on fines migration by altering the surface potential of mobile fines. It explains why more excellent performance of nanoparticle co-injection to mitigate fines migration can be achieved in single-phase flow, comparted to the case of two-phase flow, as shown in Figure 4.3.



(a) Single-phase flow case



(b) two-phase flow case

Figure 4.12 Stream-function/distance diagram with the propagation of different nanoparticles-fines condition in water and two-phase flow in coordinate of (x_D, t_D)

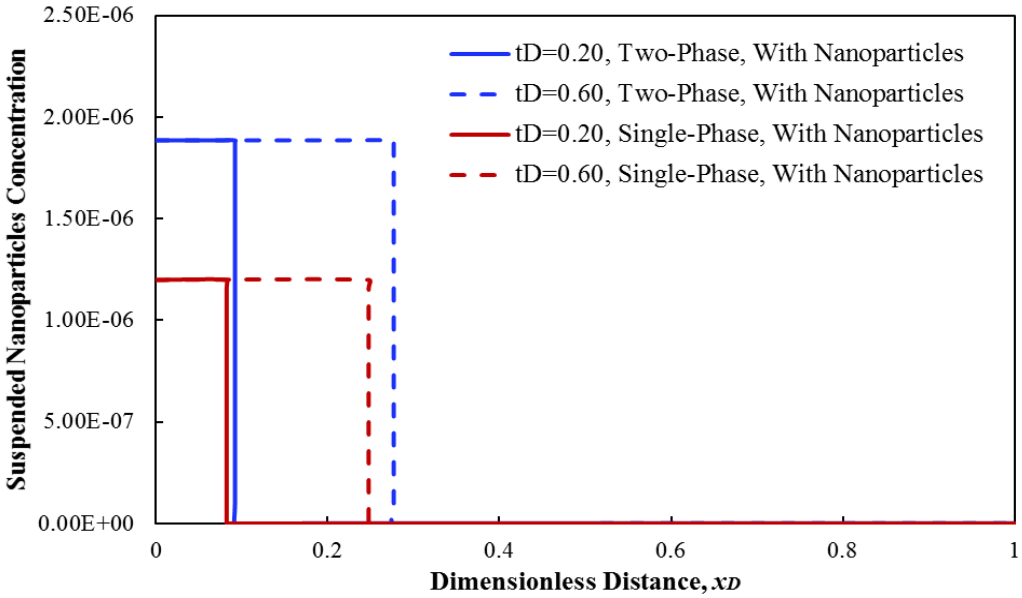
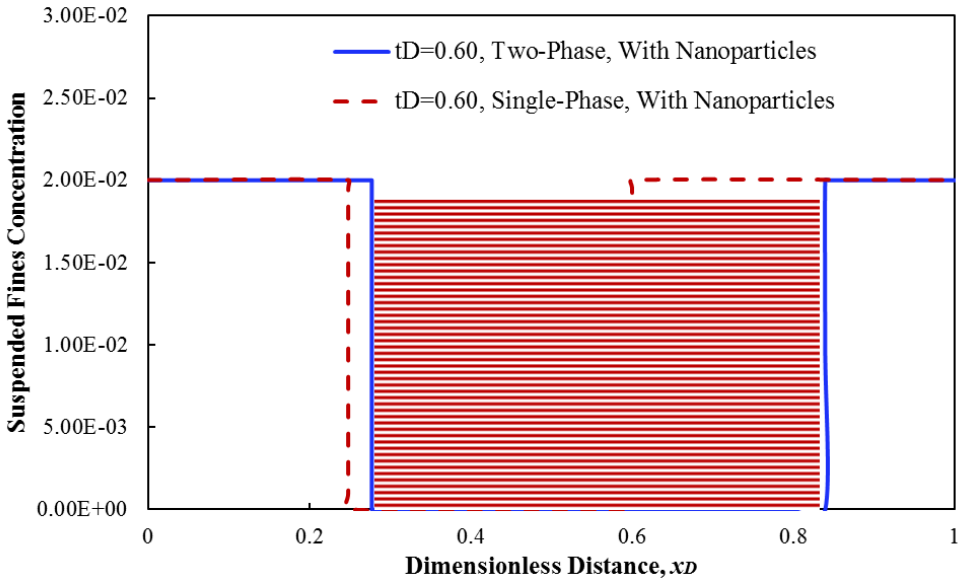


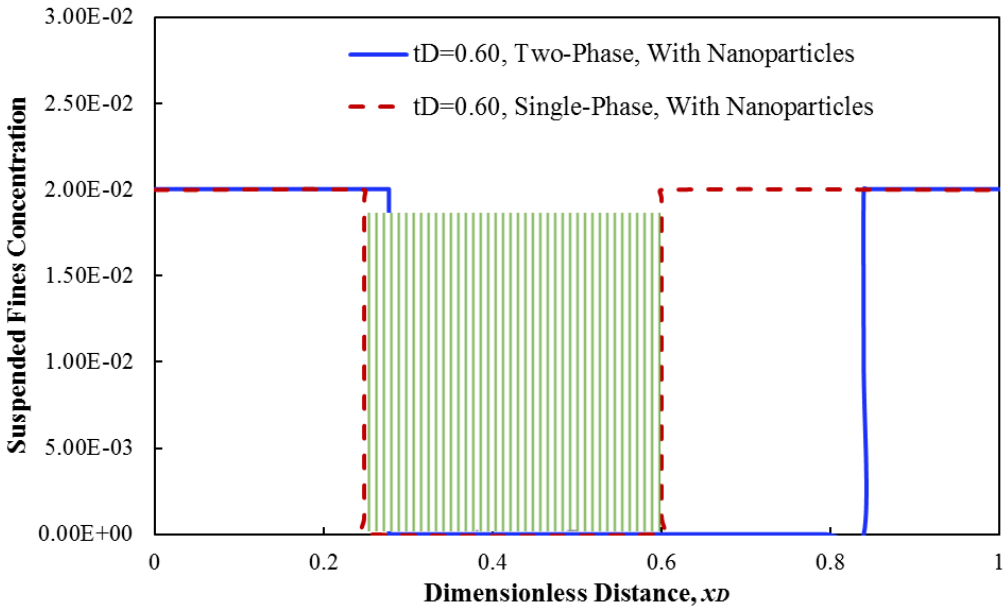
Figure 4.13 Comparison of suspended nanoparticles concentration profile in water flow and in oil-water flow along 1-D porous medium

The shadowed areas in Figure 4.14 represent the reduction of mobile fines concentration attributed to nanoparticles co-injection in both single-phase and two-phase flow. It seems that there are more fines (absolute values) reduced by nanoparticles in two-phase flowing case, because of larger concentration of nanoparticles co-injection. The reduction efficiency of mobile fines in single-phase flow is similar to that of two-phase flow case while considering the difference of injected nanoparticles concentration. The reduction efficiency (RE) of mobile fines is defined as the cumulative reduction of fines concentration per unit concentration of nanoparticles co-injection, as shown in Eq. 4.24. In Figure 4.14, the reduction efficiency for single-phase flow is 9.78×10^{3} and the reduction efficiency for two-phase flow is 9.91×10^{3} at the same moment of $t_D = 0.60$,

$$RE = \frac{\int_0^1 \left(C_{FP,\text{no}-nanoparticle}\left(x_D, t_D\right) - C_{FP,with-nanoparticle}\left(x_D, t_D\right) \right) dx_D}{\int_0^{t_D} C_{NP,\text{INJ}}\, dt_D} \quad \text{..... (4.24)}$$



(a) The shadowed envelop with horizontal lines represents the reduction of suspended fines by nanoparticles in two-phase flow



(b) The shadowed envelop with vertical lines represents the reduction of suspended fines by nanoparticles in single-phase flow

Figure 4.14 Comparison of suspended fines concentration profile in water flow and in oil-water flow along 1-D porous medium

4.2.3.5 Verification with Numerical Simulations

Finite-difference method is implemented to calculate the numerical solutions of Eq. 4.1-4.4. Backward difference and implicit formulation are used to make sure that the solution is unconditionally stable. For each time step, the mass-balance equations of water saturation, fines and nanoparticles are approximated as,

$$S_{wi}^{\,n} = \frac{\Delta t_D}{\Delta x_D}\left(f_{wi}^{\,n+1} - f_{wi-1}^{\,n+1}\right) + S_{wi}^{\,n+1}$$

$$S_{wi-1}^{\,n} C_{FPi}^{\,n} + \frac{1}{\phi}\sigma_{ai}^{\,n} = \frac{\Delta t_D}{\Delta x_D} f_{wi-1}^{\,n}\left(C_{FPi}^{\,n+1} - C_{FPi-1}^{\,n+1}\right) + S_{wi-1}^{\,n} C_{FPi}^{\,n+1} + \frac{1}{\phi}\sigma_{ai}^{\,n+1} \quad \text{..... (4.25)}$$

$$S_{wi-1}^{\,n} C_{NPi}^{\,n} + \frac{1}{\phi}\hat{C}_{NPi}^{\,n} = \frac{\Delta t_D}{\Delta x_D} f_{wi}^{\,n}\left(C_{NPi}^{\,n+1} - C_{NPi-1}^{\,n+1}\right) + S_{wi-1}^{\,n} C_{FPi}^{\,n+1} + \frac{1}{\phi}\hat{C}_{NPi}^{\,n+1}$$

for grid blocks i, where f_{wi} is a function of both S_{wi} (water saturation at grid block i) and attached fines concentration σ_a. In order to use the more accurate f_w in each time step n,

simple-iteration method is employed, and f_w is evaluated using several iterations after the water saturation has been calculated.

The comparison between the semi-analytic solutions and finite-difference solutions is presented in Figure 4.15-4.17. Due to the inevitable numerical dispersion effects introduced by grid discretization in finite-difference method, the shape of shock in finite-difference solution spreads. As the interval of grid width decreases, the dispersion effects can be decreased (Rossen et al. 2011). In this paper, the grid size is set as 0.01. At the moment of $t_D = 0.20$, the rarefaction-wave regions (upstream and downstream around shock front) of water saturation profile show excellent match of the above semi-analytical solutions with numerical simulations.

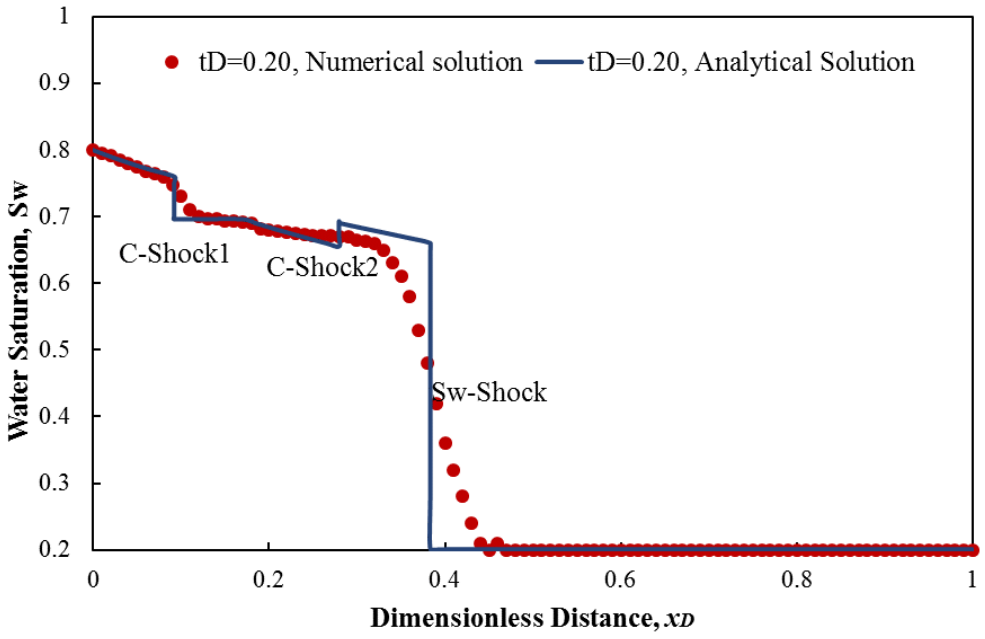


Figure 4.15 Comparison of water saturation profile in oil-water flow along 1-D porous medium at the same moment (injected-pore-volume=0.2) (Discrete points: finite-difference with 100 grid blocks; Solid line: analytical solution with Δx_D =0.01)

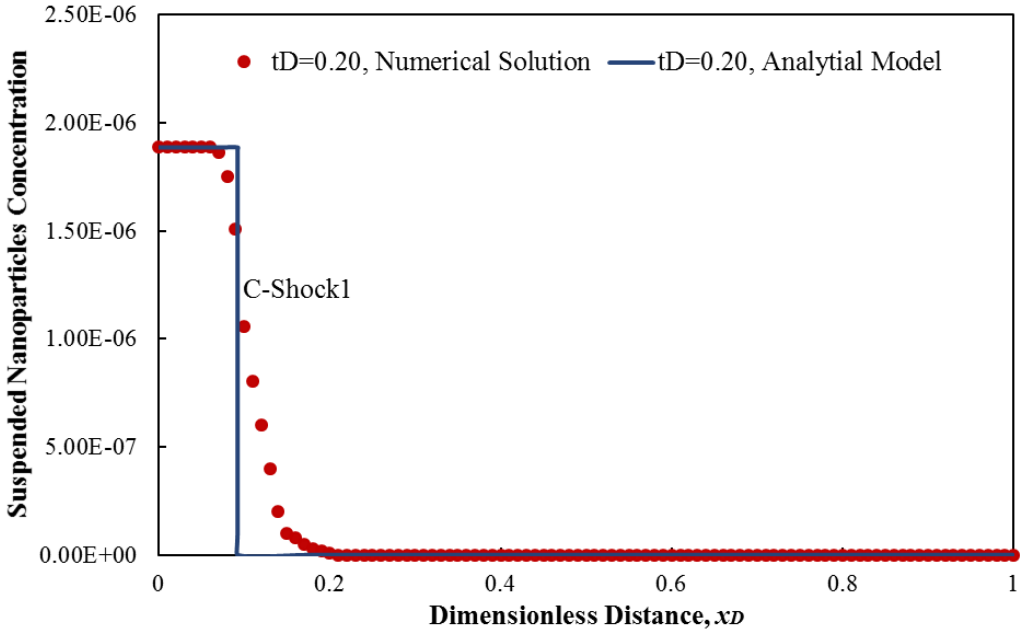


Figure 4.16 Comparison of suspended nanoparticles profile in oil-water flow along 1-D porous medium with injected-pore-volume as 0.2

(Discrete points: finite-difference with 100 grid blocks; Solid line: analytical solution withΔx_D =0.01)

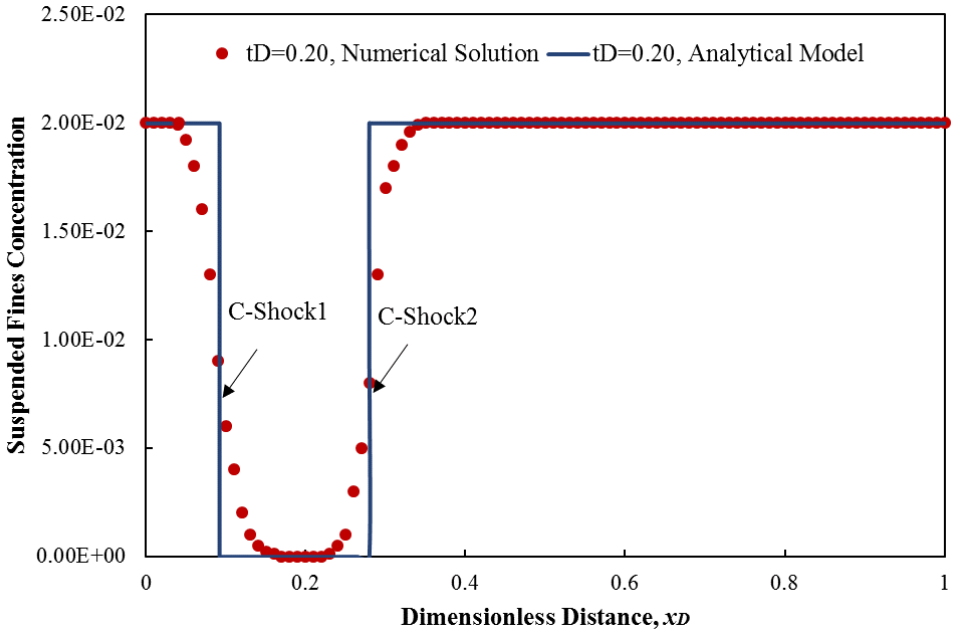


Figure 4.17 Comparison of suspended fines profile in oil-water flow along 1-D porous medium with injected-pore-volume as 0.2)

Table 4-1 Values of parameters used the examples in section 4.2

Nanoparticles Langmuir adsorption constant K, m^3/m^3	1000	Fine particle density, ρ_{FP}, kg/m^3	2000
Water viscosity, μ_w, mPa.s	1.0	Bulk number density of ions, n_∞, number/m^3	6.022×10^{25}
Force lever of drag force and normal force, l_d, l_n, m	l_d / l_n=1.73	Nanoparticle radius, r_{NP}, nm	20
Atomic collision diameter, nm,	0.5	Boltzmann's constant, k_B, J/K	1.381×10^{-21}
Fine particle radius, r_{FP}, μm	1.0	Hamaker constant, A_{132}, J	7.73×10^{-21}
Pore size radius, r_p, μm	10	Inverse Debye length, κ, m^{-1}	7.3×10^{8}
Flow velocity, U, m/s	0.004	Surface-to-surface separation length, h, m	$h<<r_s$
Porosity, ϕ, decimal	0.15	Dimensionless drag empirical coefficient	5.0
Residual oil saturation, S_{or}, decimal	0.20	Absolute temperature of reservoir, T, K	398
Nanoparticle surface Zeta potential, ς_{NP}, mV	-1.0	Lifting force coefficient, χ	640
Fine particle surface Zeta potential, ς_{FP}, mV	-20	Formation damage coefficient for straining, β_a	500
Grain surface Zeta potential, ς_{GS}, mV	-30	Connate water saturation, S_{wc}	0.20
Liquid density, ρ_l, kg/m^3	1000	Oil viscosity, μ_o, mPa.s	10
Characteristic wave length of interaction, l, nm	100	Length of 1-D sand pack, L, m	0.5
Fines concentration-dependent constant, a	30		

4.3 Nanofluid Pre-Flush to Control Fines Migration in Two-Phase Radial Flow

4.3.1 Model Description and Governing System

In this section, fines migration in two-phase radial flow system is discussed by incorporating the multiple particles capture mechanisms, i.e., fines attachment and straining. The performances of cases with different nanofluid pre-treatment radius are characterized. The assumptions associated with physical problem have been listed in section 4.1. Governing equations for mass-balance of water, fine particles, and nanoparticles are derived, as follows,

Water component:

$$\frac{\partial f_w}{\partial x_D}+\frac{\partial S_w}{\partial t_D}=0 \quad \text{……..…..} \quad (4.21)$$

Fine particles component:

$$\frac{\partial\left(C_{FP} f_w\right)}{\partial x_D}+\frac{\partial\left(C_{FP} S_w\right)}{\partial t_D}+\frac{\partial S_a}{\partial t_D}+\frac{\partial S_s}{\partial t_D}=0 \quad \text{……..…..} \quad (4.22)$$

Kinetics equations for particles attachment and straining:

$$\frac{\partial S_a}{\partial t_D}=\begin{cases}\dfrac{\Lambda_a C_{FP} f_w}{2\sqrt{x_D}}; \ \sigma_a<\sigma_{cr}\left(x_D, C_{NP}\right)\\ \sigma_{cr}\left(x_D, C_{NP}\right)\end{cases} \quad \text{…….……..…..…..} \quad (4.23)$$

$$\frac{\partial S_s}{\partial t_D}=\frac{\Lambda_s C_{FP} f_w}{2\sqrt{x_D}} \quad \text{…….....…..} \quad (4.24)$$

Modify Darcy-flow law by accounting for the damage of permeability caused by the attachment and straining behavior of mobile fines,

$$1=x_D\left(\frac{k_{rw}}{\left(1+\phi\beta_a S_a+\phi\beta_s S_s\right)\mu_w}+\frac{k_{ro}}{\mu_o}\right)\frac{\partial P}{\partial x_D} \quad \text{.....……..……..} \quad (4.25)$$

Here, introduce the following dimensionless variables for simplification,

$$x_D = \left(\frac{r}{r_e}\right)^2;\ t_D = \frac{qt}{\phi\pi r_e^{\,2}};\ \Lambda_a = r_e\lambda_a;\ \Lambda_s = r_e\lambda_s;\ S_a = \frac{\sigma_a}{\phi};\ S_s = \frac{\sigma_s}{\phi};\ P = \frac{4k_0\pi}{q}\,p$$

Lemon et al. (2011) extended Dietz's two-dimensional layer cake reservoirs model to evaluate the water-cut curve with and without fines migration. The effects of fines migration on water-cut are analogous to that of polymer flooding ruled as mobility controlled by the resistance factor by polymer adsorption. Hence, the formation damage effects of both attached and strained fines are incorporated into the retardation term in the relative permeability of water, as shown,

$$f_w\left(S_w, S_s, S_a\right) = \left(1 + \frac{k_{ro}\mu_w\left(1 + \phi\beta_s S_s + \phi\beta_a S_a\right)}{k_{rw}\mu_o}\right)^{-1} \quad \text{..... (4.26)}$$

The two-phase (oil & water) flow effects are represented by the following relative permeability functions depending on phase saturations.

$$k_{rw} = k_{rw}^0\left(\frac{S_w - S_{wc}}{1 - S_{wc} - S_{or}}\right)^{n_w}$$
$$k_{ro} = k_{ro}^0\left(\frac{S_o - S_{or}}{1 - S_{wc} - S_{or}}\right)^{n_0} \quad \text{..... (4.27)}$$

Where, $k_{rw}^0 = k_{ro}^0 = 1;\ n_w = n_o = 2$

The positive effects of nanoparticle concentration on the attachment of fine particles have been characterized in Eq.3.4. However, in radial flow system, flow velocity depends on distances even for the condition with constant injection flux, as below:

$$U = \frac{q}{2\pi r} \quad \text{..... (4.28)}$$

Now, let us determine the initial conditions for the above problem. As per the assumption of maximum retention concentration in Chapter 2, the release of the initial attached fines concentration occurs instantly while over than the maximum limits. Figure. 2.2 also indicates the negative relationship (Eq. 2.19) between the attached fines concentration and flow velocity defined in Eq. 4.28. As shown in Figure 4.18, around the well vicinity of $r < \frac{q}{2\pi U_m}$, all the initially attached fines before the start of injection are released instantly because of the high flow velocity. Within the range with medium flow velocity, $\frac{q}{2\pi U_m} < r < \frac{q}{2\pi U_i}$, the instant released fines concentration equates to the difference between the initial attached fines concentration and the maximum retention concentration of fines at that location. In the remote area of $r > \frac{q}{2\pi U_i}$ from the wellbore, there are no fines to be released because of sufficiently slow velocity.

In view of the differences of released fines concentration at different locations, it is desirable to optimize the radius of nanofluid pre-treatment to maximize the efficiency of nanoparticles treatment. In this chapter, cases with 0.01 nanofluid pre-treatment and reference case without nanofluid utilization are compared, as shown in Figure 4.18. The initial conditions and boundary conditions inferred by the above descriptions can be listed, as follows.

Scenario A: without nanofluids treatment

$$C_{FP}(x_D,0)=\begin{cases} S_{ai}, & x_{Dw}<x_D<\left(\dfrac{q}{2\pi U_m r_e}\right)^2=x_{Dm} \\ S_{ai}-S_a(x_D), & x_{Dm}=\left(\dfrac{q}{2\pi U_m r_e}\right)^2<x_D<\left(\dfrac{q}{2\pi U_i r_e}\right)^2=x_{Di} \\ 0, & x_{Di}=\left(\dfrac{q}{2\pi U_i r_e}\right)^2<x_D<1 \end{cases}$$

$$S_a(x_D,0)=\begin{cases} 0, & x_{Dw}<x_D<\left(\dfrac{q}{2\pi U_m r_e}\right)^2=x_{Dm} \\ S_a(x_D), & x_{Dm}=\left(\dfrac{q}{2\pi U_m r_e}\right)^2<x_D<\left(\dfrac{q}{2\pi U_i r_e}\right)^2=x_{Di} \\ S_{ai}, & x_{Di}=\left(\dfrac{q}{2\pi U_i r_e}\right)^2<x_D<1 \end{cases} \quad (4.29a)$$

$$S_s(x_D,0)=0; S_w(x_D,0)=S_{wc}; C_{FP}(x_{Dw},t_D)=C_0; S_a(x_{Dw},t_D)=0; S_s(x_{Dw},t_D)=\frac{\Lambda_s C_0 t_D}{2\sqrt{x_{Dw}}}$$

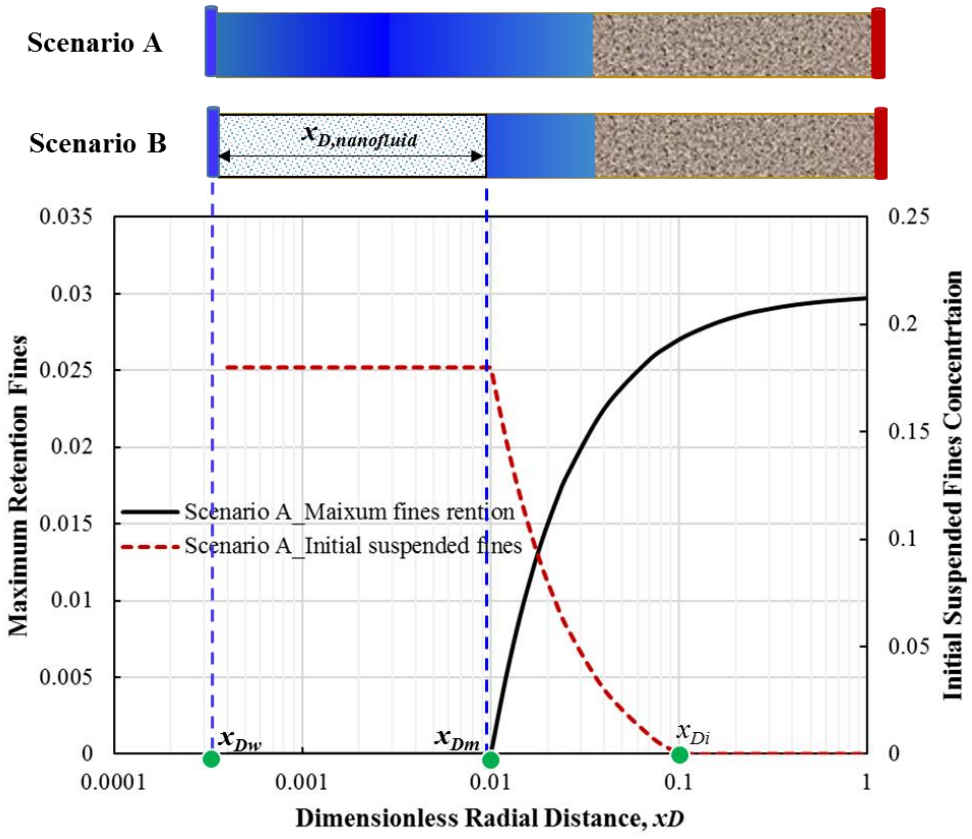


Figure 4.18 Maximum retention concentration of fines at different radial locations, and scheme of different nanoparticles pre-treatment radius

As assumed above, the adsorption of nanoparticle can control the detachment of fines effectively for a sufficiently long time, i.e., there are no fines to be released freely within the range of nanoparticles treatment. Even along with the injection of newly fines, within the nanofluid treatment range, the rock grains can still have capacity to capture more fine particles, until the maximum retention concentration of fines enhanced by nanofluids has been reached after sufficiently long time. The initial condition of suspended fines concentration and maximum capacity of rock grains to capture fines after nanofluid treatment are calculated, as shown in Figure 4.19.

Scenario B: Nanofluid treatment only limited to the region with zero initially attached fines concentration: $x_{D,nanofluid} = x_{Dm}$:

$$C_{FP}\left(x_D,0\right)=\begin{cases}0, & x_{Dw}<x_D<x_{Dm}\\ S_{ai}-S_a\left(x_D\right), & x_{Dm}<x_D<x_{Di}\\ 0, & x_{Di}<x_D<1\end{cases}$$

$$S_a\left(x_D,0\right)=\begin{cases}S_{ai}, & x_{Dw}<x_D<x_{Dm}\\ S_a\left(x_D\right), & x_{Dm}<x_D<x_{Di}\\ S_{ai}, & x_{Di}<x_D<1\end{cases} \qquad \text{…….. (4.29b)}$$

$$S_s\left(x_D,0\right)=0; \quad S_w\left(x_D,0\right)=S_{wc}$$

$$C_{FP}\left(x_{Dw},t_D\right)=C_0;\ S_a\left(x_{Dw},t_D\right)=\frac{\Lambda_a C_0}{2\sqrt{x_{Dw}}}t_D+S_{ai};\ \ S_s\left(x_{Dw},t_D\right)=\frac{\Lambda_s C_0}{2\sqrt{x_{Dw}}}t_D;$$

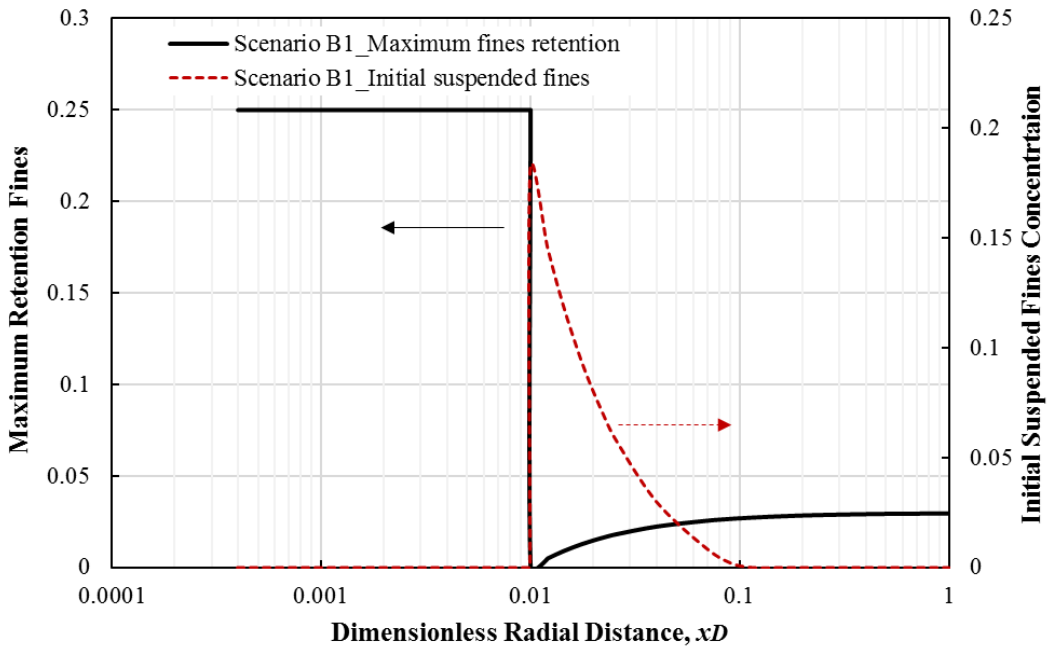


Figure 4.19 The initial suspended fines concentration and maximum fines retention with 0.01nanofluid treatment range

4.3.2 Analytical Solutions and Derivations

The transformations of stream-function analogous to the Sec. 4.2.2 are performed for Eq.4.21-4.22. The mass-balance equation of water component in new coordinate:

$$\frac{\partial G}{\partial x_D}+\frac{\partial F}{\partial \varphi}=0; \quad G=\frac{1}{f_w}; \quad F=-\frac{S_w}{f_w} \qquad \text{(4.30)}$$

Integrating both sides of fine particles mass-balance equation considering fines attachment and straining in Eq. 4.22 over any arbitrary closed and simply-connected domain in the plan of (x_D, t_D) and applying Green's theorem result in:

$$\iint_D \left[\frac{\partial\left(C_{FP} f_w\right)}{\partial x_D}+\frac{\partial\left(S_w C_{FP}\right)}{\partial t_D}+\frac{\partial S_a}{\partial t_D}+\frac{\partial S_s}{\partial t_D}\right] dx_D dt_D = \oint_{\partial D} C_{FP} f_w dt_D - C_{FP} S_w dx_D - S_a dx_D - S_s dx_D$$
$$= \oint_{\partial D} C_{FP} d\varphi - \left(S_a+S_s\right) dx_D = \iint_D \left[\frac{\partial C_{FP}}{\partial x_D}+\frac{\partial\left(S_a+S_s\right)}{\partial \varphi}\right] dx_D d\varphi \qquad \text{(4.31)}$$

A transformation of fines mass-balance equation with new stream-function:

$$\frac{\partial C_{FP}}{\partial x_D}+\frac{\partial S_a}{\partial \varphi}+\frac{\partial S_s}{\partial \varphi}=0 \quad \text{……...……...……} \quad (4.32)$$

The stream-function transformation of kinetics equations for particles attachment and straining are derived as:

$$\begin{aligned}&\iint_D\left[\frac{\partial S_a}{\partial t_D}-\frac{\Lambda_a C_{FP} f_w}{2\sqrt{x_D}}\right]dx_D dt_D=\oint_{\partial D} S_a dx_D+\frac{\Lambda_a C_{FP}}{2\sqrt{x_D}}\, f_w dx_D dt_D\\&=\oint_{\partial D} S_a dx_D+\frac{\Lambda_a C_{FP}}{2\sqrt{x_D}}dx_D f_w dt_D=\iint_D\left[\frac{\partial S_a}{\partial \varphi}-\frac{\Lambda_a C_{FP}}{2\sqrt{x_D}}\right]dx_D d\varphi\end{aligned} \quad \text{……..…..…..} \quad (4.33)$$

$$\frac{\partial S_a}{\partial \varphi}=\frac{\Lambda_a C_{FP}}{2\sqrt{x_D}} \quad \text{……...…….....…..} \quad (4.34)$$

The transformation of strained fines concentration is analogous to Eq.4.33,

$$\frac{\partial S_s}{\partial \varphi}=\frac{\Lambda_s C_{FP}}{2\sqrt{x_D}} \quad \text{…….....….....} \quad (4.35)$$

After applying transformation, the initial conditions need to be updated from $t_D=0$ to $\varphi=-S_{wc}x_D+S_{wc}x_{Dw}$. The initial and boundary conditions for scenario A in new coordinate become $\left(x_D,\varphi\right)$, as below:

$$\begin{aligned}&C_{FP}\left(x_D,-S_{wc}x_D+S_{wc}x_{Dw}\right)=\begin{cases}S_{ai}, & x_{Dw}<x_D<x_{Dm}\\ S_{ai}-S_a\left(x_D\right), & x_{Dm}<x_D<x_{Di}\\ 0, & x_{Di}<x_D<1\end{cases}\\&S_a\left(x_D,-S_{wc}x_D+S_{wc}x_{Dw}\right)=\begin{cases}0, & x_{Dw}<x_D<x_{Dm}\\ S_a\left(x_D\right), & x_{Dm}<x_D<x_{Di}\\ S_{ai}, & x_{Di}<x_D<1\end{cases}\\&S_s\left(x_D,-S_{wc}x_D+S_{wc}x_{Dw}\right)=0;\;\; S_w\left(x_D,-S_{wc}x_D+S_{wc}x_{Dw}\right)=S_{wc}\\&C_{FP}\left(x_{Dw},\varphi\right)=C_0;\;\; S_a\left(x_{Dw},\varphi\right)=0;\;\; S_s\left(x_{Dw},\varphi\right)=\frac{\Lambda_s C_0\varphi}{2\sqrt{x_{Dw}}}\end{aligned} \quad \text{……...} \quad (4.36)$$

As results of transformation, system Eq.4.21-4.24 evolves into a lifting equation (Eq.4.30) and auxiliary system (Eq.4.32). Next step. method of characteristic is applied to solve the above transformed system in coordinate of (x_D, φ).

4.3.2.1 Scenario A: No Nanofluid Treatment

As described above about initial conditions of scenario A, the maximum retention concentration of fines is velocity-dependent or distance-dependent. In the range of $x_{Dw} < x_D < x_{Di}$, even though there is continuous injection of new fines, there is no more room for the re-attachment of fine particles onto rock grains. Only after entering the zone of $x_{D_i} < x_D < 1$, where there is available room for fines attachment, the new injected fines can be attached onto pore surfaces, until the maximum retention concentration of fines is reached. It indicates that there are two different zones separated by an "erosion front" (Bedrikovetsky 2014), only ahead of which the attachment of fines occurs.

Referred to the derivation procedure of Bedrikovetsky (2017), it is the first step to derive the analytical solutions behind the erosion front, where there are no changes of attached fines concentration which keeps constant as maximum fines retention concentration. Substituting the straining kinetics of Eq.4.35 into fines mass-balance equation of Eq. 4.32 leads to,

$$\frac{\partial C_{FP}}{\partial x_D} + \frac{\Lambda_s C_{FP}}{2\sqrt{x_D}} = 0 \quad \text{(4.37)}$$

The characteristics forms of Eq. 4.37 in zone I, II and III (Figure 4.20) are,

$$\frac{d\varphi}{dx_D} = 0; \quad \frac{dC_{FP}}{dx_D} = -\frac{\Lambda_s C_{FP}}{2\sqrt{x_D}} \quad \text{(4.38)}$$

It indicates that the characteristic velocity of fines concentration wave is infinite, and the trajectory of saturation-concentration *c-shock* can be only along the *x*-axis. Above the *x*-axis, it is the propagation of concentration waves of injected conditions. In the zones below the *x*-axis are the regions with concentration wave corresponding to non-uniform initial condition (Figure. 4.19), the characteristic lines propagate along the horizontal direction only. The initial conditions at $t_D = 0$ is transformed along the initial-condition line using the new stream-function described in Sec. 4.2.2.

$$\varphi = -S_{wc} x_D + S_{wc} x_{Dw} \quad \text{(4.39)}$$

The concentration waves of suspended fine particles in zone I, II and VII propagate from the initial-condition line with the initial data in the range of $\left[0, S_{wc}\left(x_{Dw} - x_{Dm}\right)\right]$ in Eq. 4.36. The second ODE in Eq. 4.38 can be solved by separation of variables.

$$C_{FP,I} = S_{ai} \exp\left(-\Lambda_s\left(\sqrt{x_D} - \sqrt{x_{Dw} - \frac{\varphi}{S_{wc}}}\right)\right) \quad \text{(4.40)}$$

In zone I, the strained fines concentration is determined from equation of straining kinetics, as shown in Eq.4.35. Integrating the suspended fines concentration C_{FP} in variable of φ from the initial conditions results in the solutions of strained fines concentration:

$$S_{s,I} = -\frac{S_{ai}}{\sqrt{x_D}} S_{wc}\left[\left(\sqrt{x_{Dw} - \frac{\varphi}{S_{wc}}} - \frac{1}{\Lambda_s}\right)\exp\left(\Lambda_s\left(\sqrt{x_{Dw} - \frac{\varphi}{S_{wc}}} - \sqrt{x_D}\right)\right) + \frac{1}{\Lambda_s} - \sqrt{x_D}\right] \quad \text{(4.41)}$$

Similarly, in zone III, the suspended fines concentration can be determined by integrating Eq. 4.38 from initial conditions in range of $\left[S_{wc}\left(x_{Dw} - x_{Dm}\right), S_{wc}\left(x_{Dw} - x_{Di}\right)\right]$ The strained fines concentration is obtained by integrating suspended fines concentration

from the initial values for the right side of Eq. 4.35.

Suspended fines:

$$C_{FP,III}=\left(S_{ai}-S_{cr}\left(x_{Dw}-\frac{\varphi}{S_{wc}}\right)\right)\exp\left(-\Lambda_s\left(\sqrt{x_D}-\sqrt{x_{Dw}-\frac{\varphi}{S_{wc}}}\right)\right) \quad \text{(4.42a)}$$

Strained fines:

$$S_{s,III}=-\frac{S_{ai}}{\sqrt{x_D}}S_{wc}\left[\left(\sqrt{x_{Dw}-\frac{\varphi}{S_{wc}}}-\frac{1}{\Lambda_s}\right)\exp\left(\Lambda_s\left(\sqrt{x_{Dw}-\frac{\varphi}{S_{wc}}}-\sqrt{x_D}\right)\right)+\frac{1}{\Lambda_s}-\sqrt{x_D}\right] \quad \text{(4.42b)}$$
$$-\frac{\Lambda_s\exp\left(-\Lambda_s\sqrt{x_D}\right)}{2\sqrt{x_D}}\int_{-S_{wc}x_D+S_{wc}x_{Dw}}^{\varphi}S_{cr}\left(\sqrt{x_{Dw}-\frac{\varphi}{S_{wc}}}\right)\exp\left(\Lambda_s\sqrt{x_{Dw}-\frac{\varphi}{S_{wc}}}\right)d\varphi$$

Attached fines: $S_{a,III}=S_{cr}\left(x_D\right)$ ……. (4.42c)

To worth mentioning, inferred from straining kinetics in Eq. 4.35, the strained concentration at specific location in zone II is the sum of the integration of suspended fines concentration across zone III and II from the initial-condition line in range of $\left[S_{wc}\left(x_{Dw}-x_{Dm}\right),S_{wc}\left(x_{Dw}-x_{Di}\right)\right]$. Hence, the strained fines concentration in zone II is expressed as,

$$S_{s,II}=\frac{\Lambda_s}{2\sqrt{x_D}}\left(\int_{-S_{wc}x_D+S_{wc}x_{Dw}}^{-S_{wc}x_{Dm}+S_{wc}x_{Dw}}C_{FP,III}d\varphi+\int_{-S_{wc}x_{Dm}+S_{wc}x_{Dw}}^{\varphi}C_{FP,II}d\varphi\right) \quad \text{(4.43)}$$

In zone II, VII and VIII, the trajectories of suspended and attached fines concentration waves keep same with those in zone I. Analogously, the trajectories of suspended and attached fines are same with those in zone III. In addition, the over-saturated attached fines concentrations can be determined by the maximum retention concentration of fines at different locations. The difference between zone VII and VIII is the appearance of erosion front which catch up with the characteristic line (

$\varphi = S_{wc}\left(x_{Dw} - x_{Dm}\right)$) at the point of $\left(x_{Df_1}, S_{wc}\left(x_{Dw} - x_{Df_1}\right)\right)$.

Suspended and attached fines concentration in zone II, VII and VIII are expressed as

$$C_{FP,II}, C_{FP,VII}, C_{FP,VIII} = S_{ai}\exp\left(-\Lambda_s\left(\sqrt{x_D} - \sqrt{x_{Dw} - \frac{\varphi}{S_{wc}}}\right)\right) \quad \text{(4.44)}$$

$$S_{a,II}, S_{a,VII}, S_{a,VIII} = S_{cr}\left(x_D\right)$$

Suspended and attached fines concentration in zone VI are expressed as,

$$C_{FP,VI} = \left(S_{ai} - S_{cr}\left(\sqrt{x_{Dw} - \frac{\varphi}{S_{wc}}}\right)\right)\exp\left(-\Lambda_s\left(\sqrt{x_D} - \sqrt{x_{Dw} - \frac{\varphi}{S_{wc}}}\right)\right);\ S_{a,VI} = S_{cr}\left(x_D\right). \quad \text{(4.45)}$$

Strained fines concentration in zone VI can be determined by the continuous integration of suspended fines concentration across zone 0, IX and VI from the initial-condition line,

$$S_{s,VI} = \frac{\Lambda_s}{2\sqrt{x_D}}\left(\int_{-S_{wc}x_{Di}+S_{wc}x_{Dw}}^{\varphi_{cr}} C_{FP,IX}\,d\varphi + \int_{\varphi_{cr}}^{\varphi} C_{FP,\mathrm{VI}}\,d\varphi\right) \quad \text{(4.46)}$$

Similarly, strained fines concentration in zone VII is determined by the sum of continuous integration of suspended fines concentration across zone 0, IX, VI and VII from the initial-condition line,

$$S_{s,VII} = \frac{\Lambda_s}{2\sqrt{x_D}}\left(\int_{-S_{wc}x_{Di}+S_{wc}x_{Dw}}^{\varphi_{cr}} C_{FP,IX}\,d\varphi + \int_{\varphi_{cr}}^{-S_{wc}x_{Dm}+S_{wc}x_{Dw}} C_{FP,\mathrm{VI}}\,d\varphi + \int_{-S_{wc}x_{Dm}+S_{wc}x_{Dw}}^{\varphi} C_{FP,\mathrm{VII}}\,d\varphi\right). \quad \text{(4.47)}$$

Analogously, strained fines concentration in zone VIII is determined as,

$$S_{s,VIII} = \frac{\Lambda_s}{2\sqrt{x_D}}\left(\int_{-S_{wc}x_{Di}+S_{wc}x_{Dw}}^{\varphi_{cr}} C_{FP,IX}\,d\varphi + \int_{\varphi_{cr}}^{\varphi} C_{FP,\mathrm{VIII}}\,d\varphi\right) \quad \text{(4.48)}$$

After the analytical solutions of suspended fines, attached fines and strained fines concentration behind the erosion front have been determined above, now it is the turn to determine the trajectory of erosion front, where the discontinuities of the first-derivative

of concentration occur, where the equilibrium maximum retention concentration switches to the non-equilibrium particles attachment kinetics.

As indicated by Eq. 4.34-4.35, the suspended fines concentrations and fines attachment rates can be expressed by fines straining rates, as shown below,

$$C_{FP}=\frac{2\sqrt{x_D}}{\Lambda_a}\frac{\partial S_a}{\partial \varphi};\quad \frac{\partial S_s}{\partial \varphi}=\frac{\Lambda_s}{\Lambda_a}\frac{\partial S_a}{\partial \varphi} \quad \text{(4.49)}$$

Substituting Eq. 4.49 into the mass-balance equation Eq.4.32 results in,

$$\frac{\partial}{\partial \varphi}\left(\frac{\partial}{\partial x_D}\left(\frac{2\sqrt{x_D}}{\Lambda_a}S_a\right)\right)+\frac{\partial}{\partial \varphi}\left(S_a+\frac{\Lambda_s}{\Lambda_a}S_a\right)=0 \quad \text{(4.50)}$$

Integrating both sides of Eq. 4.41 in φ and combining the initial conditions at $\varphi=-S_{wc}x_D+S_{wc}x_{Dw}$ result in,

$$\frac{\partial}{\partial x_D}\left(\frac{2\sqrt{x_D}}{\Lambda_a}S_a\right)+\left(1+\frac{\Lambda_s}{\Lambda_a}\right)S_a=\left(1+\frac{\Lambda_s}{\Lambda_a}\right)S_{ai}+\frac{\partial}{\partial x_D}\left(\frac{2\sqrt{x_D}}{\Lambda_a}S_{ai}\right) \quad \text{(4.51)}$$

$$\frac{\partial S_a}{\partial x_D}=\frac{1}{2\sqrt{x_D}}\left(\Lambda_a+\Lambda_s+\frac{1}{\sqrt{x_D}}\right)\left(S_{ai}-S_a\right) \quad \text{(4.52)}$$

Meanwhile, along the erosion front, the attached fines concentration should be equal to the maximum retention concentration of fines at different locations.

$$S_{cr}\left(x_{D,cr}\right)=S_a\left(x_{D,cr},\varphi\right) \quad \text{(4.53)}$$

Taking the derivative of both sides in x_D results in,

$$\frac{dS_{cr}}{dx_D}=\frac{d\varphi_{cr}}{dx_D}\frac{\partial S_a}{\partial \varphi}+\frac{\partial S_a}{\partial x_D} \quad \text{(4.54)}$$

Substituting both Eq. 4.34 and Eq.4.52 into Eq. 4.54 results in the formulation of the moving velocity of erosion front, as follows,

$$\frac{d\varphi_{cr}}{dx_{D,cr}}=\frac{2\sqrt{x_{D,cr}}\,\frac{dS_{cr}\left(x_{D,cr}\right)}{dx_{D,cr}}-\left(\Lambda_a+\Lambda_s+\frac{1}{\sqrt{x_{D,cr}}}\right)\left(S_{ai}-S_{cr}\left(x_{D,cr}\right)\right)}{\Lambda_a C_{FP}\left(x_{D,cr}\right)} \quad \text{..... (4.55)}$$

The continuous suspended fines concentration around the erosion front has been proved by Bedrikovetsky (2014). Hence, the S_a and C_{FP} along the trajectory of erosion front are those values at which the trajectories in zones VI and VIII intersects with erosion front, which have been presented in Eq. 4.44 and Eq. 4.45.

Then, the trajectory of erosion front is now expressed as,

$$\varphi_{cr}=S_{wc}\left(x_{Dw}-x_{Di}\right)+\frac{d\varphi_{cr}}{dx_{D,cr}}\left(x_{D,cr}-x_{Di}\right) \quad \text{..... (4.56)}$$

Now, it comes to the analytical solutions ahead of the erosion front where fines attachment still occurs. Substituting both the fines attachment and straining into the mass-balance equation, Eq. 4. 32 results in,

$$\frac{\partial C_{FP}}{\partial x_D}+\frac{C_{FP}}{2\sqrt{x_D}}\left(\Lambda_a+\Lambda_s\right)=0 \quad \text{..... (4.57)}$$

The characteristic forms of this PDE in zone IX and zone XII can be presented as,

$$\frac{d\varphi}{dx_D}=0;\ \ \frac{dC_{FP}}{dx_D}=-\frac{C_{FP}}{2\sqrt{x_D}}\left(\Lambda_a+\Lambda_s\right) \quad \text{..... (4.58)}$$

The characteristic velocity of fines concentration wave is infinite, and the characteristic lines in zone IX and Zone X are expressed as,

$$\varphi=\varphi_{cr0} \quad \text{..... (4.59)}$$

Where, φ_{cr0} are the intersection points of characteristic lines in both Zone IX and Zone X with the erosion front, and can be determined by combing Eq. 4.59 with Eq. 4.56, as

shown below.

$$\varphi_{cr} = -S_{wc}x_{D0} + S_{wc}x_{Dw} + \frac{d\varphi_{cr}}{dx_D}\left(x_{cr} - x_{D0}\right) \quad \text{(4.60)}$$

Suspended and attached fines concentration in zone IX and XII are expressed as,

$$C_{FP,IX}, C_{FP,XII} = C_{FP}\left(x_{cr}, \varphi_{cr}\right)\exp\left[-\left(\Lambda_a + \Lambda_s\right)\left(\sqrt{x_D} - \sqrt{x_{cr}}\right)\right] \quad \text{(4.61)}$$

$$S_{a,IX}, S_{a,XII} = S_{ai} + \left(S_{cr}\left(x_{D,cr}\right) - S_{ai}\right)\sqrt{\frac{x_{cr}}{x_D}}\exp\left(\left(\Lambda_a + \Lambda_s\right)\left(\sqrt{x_{cr}} - \sqrt{x_D}\right)\right) \quad \text{(4.62)}$$

Strained fines concentration in zone IX and XII are expressed as,

$$S_{s,IX} = \frac{\Lambda_s}{2\sqrt{x_D}}\left(\int_{-S_{wc}x_{Di}+S_{wc}x_{Dw}}^{\varphi} C_{FP,IX}\, d\varphi\right) \quad \text{(4.63)}$$

$$S_{s,XII} = \frac{\Lambda_s}{2\sqrt{x_D}}\left(\int_{-S_{wc}x_{Di}+S_{wc}x_{Dw}}^{\varphi} C_{FP,XII}\, d\varphi\right) \quad \text{(4.64)}$$

The erosion front catch up with the injection water front at $\left(x_{Df_2}, 0\right)$. The suspended solutions in zone IV, V, X_1, X_2 and XI behind the front of injected water (also behind the erosion front) can be obtained by integrating the second equation of Eq. 4.38 from the boundary condition of Eq. 4.36.

$$C_{FP} = C_0\exp\left(-\Lambda_s\sqrt{x_D}\right) \quad \text{(4.65)}$$

The formulas of attached fines concentration in zone IV, V, X_1, X_2 and XI are directly defined by the corresponding maximum retention concentration of fines at different locations. Because there are no room for fines re-attachment behind the erosion front in zone IV, V, X_1, X_2 and XI.

$$S_{a,IV} = 0;\ S_{a,V} = S_{cr}\left(x_D\right);\ S_{a,X_1} = S_{cr}\left(x_D\right);\ S_{a,X_2} = S_{cr}\left(x_D\right);\ S_{a,XI} = S_{cr}\left(x_D\right) \quad \text{(4.66)}$$

The strained fines concentration in zone IV, V, X and XI are determined by the

continuous integration of suspended fines concentration across different zones from their corresponding initial conditions, as shown in Figure 4.20.

Strained fines in zone IV is expressed as:

$$S_{s,IV} = -\frac{S_{ai}}{\sqrt{x_D}} S_{wc} \left[\left(\sqrt{x_{Dw}} - \frac{1}{\Lambda_s} \right) \exp\left(\Lambda_s \left(\sqrt{x_{Dw}} - \sqrt{x_D} \right) \right) + \frac{1}{\Lambda_s} - \sqrt{x_D} \right] + \frac{\Lambda_s C_0 \varphi}{2\sqrt{x_D}} \exp\left(-\Lambda_s \sqrt{x_D} \right) \quad (4.67)$$

Strained fines in zone V is expressed as:

$$S_{s,V} = \frac{\Lambda_s}{2\sqrt{x_D}} \left(\int_{-S_{wc}x_D + S_{wc}x_{Dw}}^{-S_{wc}x_{Dm} + S_{wc}x_{Dw}} C_{FP,III} d\varphi + \int_{-S_{wc}x_{Dm} + S_{wc}x_{Dw}}^{0} C_{FP,\mathrm{II}} d\varphi + \int_{0}^{\varphi} C_{FP,\mathrm{V}} d\varphi \right) \quad (4.68)$$

Strained fines concentration in zone X_1, zone X_2 and zone XI are expressed as,

$$S_{s,X_1} = \frac{\Lambda_s}{2\sqrt{x_D}} \left(\int_{-S_{wc}x_{Di} + S_{wc}x_{Dw}}^{\varphi_{cr}} C_{FP,IX} d\varphi + \int_{\varphi_{cr}}^{-S_{wc}x_{Dm} + S_{wc}x_{Dw}} C_{FP,\mathrm{VI}} d\varphi + \int_{-S_{wc}x_{Dm} + S_{wc}x_{Dw}}^{0} C_{FP,\mathrm{VII}} d\varphi + \int_{0}^{\varphi} C_{FP,X_1} d\varphi \right)$$

(4.69)

$$S_{s,X_2} = \frac{\Lambda_s}{2\sqrt{x_D}} \left(\int_{-S_{wc}x_{Di} + S_{wc}x_{Dw}}^{\varphi_{cr}} C_{FP,IX} d\varphi + \int_{\varphi_{cr}}^{0} C_{FP,\mathrm{VIII}} d\varphi + \int_{0}^{\varphi} C_{FP,X_2} d\varphi \right) \text{..... (4.70)}$$

$$S_{s,XI} = \frac{\Lambda_s}{2\sqrt{x_D}} \left(\int_{-S_{wc}x_{Di} + S_{wc}x_{Dw}}^{\varphi_{cr}} C_{FP,XII} d\varphi + \int_{\varphi_{cr}}^{\varphi} C_{FP,\mathrm{XI}} d\varphi \right) \text{..... (4.71)}$$

As derived above, the summary of analytical solutions of suspended, attached and strained fines concentration of scenario A are presented in Table. 4.2-4.4.

4.3.2.2 Scenario B: Nanofluid Treatment radius: 0.01

After transformation, the initial conditions of scenario B-1 are set from $t_D = 0$ to $\varphi = -S_{wc}x_D + S_{wc}x_{Dw}$ in the coordinate of (x_D, φ). The maximum retention capacity of fine particles is enhanced significantly by pre-coated nanoparticles, i.e., within the range of nanofluid treatment $x_{D,nanofluid} = x_{Dm}$. The attachment of fines can keep under-saturated

for a sufficiently long time, due to the positive effects of nanofluid treatment. The boundary and initial conditions for scenario B-1 become,

$$C_{FP}\left(x_D,-S_{wc}x_D+S_{wc}x_{Dw}\right)=\begin{cases}0, & x_{Dw}<x_D<x_{D,nanofluid}\\ S_{ai}-S_a\left(x_D\right), & x_{D,nanofluid}<x_D<x_{Di}\\ 0, & x_{Di}<x_D<1\end{cases}$$

$$S_a\left(x_D,-S_{wc}x_D+S_{wc}x_{Dw}\right)=\begin{cases}S_{ai}, & x_{Dw}<x_D<x_{D,nanofluid}\\ S_a\left(x_D\right), & x_{D,nanofluid}<x_D<x_{Di}\\ S_{ai}, & x_{Di}<x_D<1\end{cases} \quad \text{..... (4.72)}$$

$$S_s\left(x_D,-S_{wc}x_D+S_{wc}x_{Dw}\right)=0;\quad S_w\left(x_D,-S_{wc}x_D+S_{wc}x_{Dw}\right)=S_{wc}$$

$$C_{FP}\left(x_{Dw},\varphi\right)=C_0;\ S_a\left(x_{Dw},\varphi\right)=\frac{\Lambda_a C_0}{2\sqrt{x_{Dw}}}\varphi+S_{ai};\ \ S_s\left(x_{Dw},\varphi\right)=\frac{\Lambda_s C_0}{2\sqrt{x_{Dw}}}\varphi$$

Similar to scenario A, the characteristic lines also keep along with the horizontal direction. The concentration waves of suspended fines in zone I, II, VII and VIII propagate from the initial-condition defined in Eq. 4.72. The suspended, attached and strained fines concentration are presented as,

$$\begin{aligned}&C_{FP,I}=C_{FP,II}=C_{FP,\mathrm{VII}}=C_{FP,\mathrm{VIII}}=0\\ &S_{s,I}=0;\ S_{a,\mathrm{I}}=S_{ai};\ S_{a,II},S_{a,\mathrm{VII}},S_{a,\mathrm{VIII}}=S_{cr}\left(x_D\right)\end{aligned} \quad \text{..... (4.73)}$$

Because nanofluid treatment is only limited to the range of $x_{D,nanofluid}\le x_{Dm}$. It does mean that in scenario B, there are no changes for the propagation of concentration waves within the range of $x_{Dm}<x_D<1$, when compared to those of scenario A. In other words, the analytical solutions of zone III and zone VI keep same with scenario A. However, due to the changes of solutions in zone I, II, VII and VIII, the analytical solutions of suspended, strained and attached fines concentration in other zones need to be updated as follows,

$$S_{s,II}=\frac{\Lambda_s}{2\sqrt{x_D}}\int_{-S_{wc}x_D+S_{wc}x_{Dw}}^{-S_{wc}x_{D,nanofluid}+S_{wc}x_{Dw}}C_{FP,III}\,d\varphi \quad \text{..... (4.74)}$$

$$S_{s,VII} = \frac{\Lambda_s}{2\sqrt{x_D}}\left(\int_{-S_{wc}x_{Di}+S_{wc}x_{Dw}}^{\varphi_{cr}} C_{FP,IX}\,d\varphi + \int_{\varphi_{cr}}^{-S_{wc}x_{D,nanofluid}+S_{wc}x_{Dw}} C_{FP,\mathrm{VI}}\,d\varphi\right) \quad (4.75)$$

$$S_{s,VIII} = \frac{\Lambda_s}{2\sqrt{x_D}}\int_{-S_{wc}x_{Di}+S_{wc}x_{Dw}}^{\varphi_{cr}} C_{FP,IX}\,d\varphi \quad (4.76)$$

$$C_{FP,IX}, C_{FP,XII} = C_{FP}\left(x_{cr}, \varphi_{cr}\right)\exp\left[-\left(\Lambda_a + \Lambda_s\right)\left(\sqrt{x_D} - \sqrt{x_{cr}}\right)\right] \quad (4.77)$$

$$S_{a,IX}, S_{a,XII} = S_{ai} + \left(S_{cr}\left(x_{D,cr}\right) - S_{ai}\right)\sqrt{\frac{x_{cr}}{x_D}}\exp\left(\left(\Lambda_a + \Lambda_s\right)\left(\sqrt{x_{cr}} - \sqrt{x_D}\right)\right) \quad (4.78)$$

$$S_{s,IX} = \frac{\Lambda_s}{2\sqrt{x_D}}\left(\int_{-S_{wc}x_{Di}+S_{wc}x_{Dw}}^{\varphi} C_{FP,IX}\,d\varphi\right) \quad (4.79)$$

$$S_{s,XII} = \frac{\Lambda_s}{2\sqrt{x_D}}\left(\int_{-S_{wc}x_{Di}+S_{wc}x_{Dw}}^{\varphi} C_{FP,XII}\,d\varphi\right) \quad (4.80)$$

In addition, above the horizontal axis, because the range of $x_{Dw} < x_D < x_{Dm}$ has been treated by nanofluids, there are still available rooms for the attachment of newly injected fines onto rock grains. However, in the range of $x_{Dm} < x_D < x_{cr}$, there are no room for the fines re-attachment. Incorporated with the different behaviors of fines attachment at different locations, the suspended fines concentration in zone IV, V, X_1, X_2 and XI behind the front of injected water (also behind the erosion front) can be obtained by integrating the second equation of Eq. 4.38 from the boundary conditions defined in Eq. 4.72.

$$C_{FP,IV} = C_0\exp\left(-\left(\Lambda_s + \Lambda_a\right)\left(\sqrt{x_D} - \sqrt{x_{Dw}}\right)\right) \quad (4.81)$$

$$C_{FP,V}, C_{FP,\mathrm{X_1}}, C_{FP,\mathrm{X_2}}, C_{FP,\mathrm{XI}} = C_0\exp\left(-\left(\Lambda_s + \Lambda_a\right)\left(\sqrt{x_{D,nanofluid}} - \sqrt{x_{Dw}}\right)\right)\exp\left(-\Lambda_s\left(\sqrt{x_D} - \sqrt{x_{D,nanofluid}}\right)\right) \quad (4.82)$$

In zone IV, V, X_1, X_2 and XI, the attached fines concentrations are obtained by

integrating Eq. 4.52 using separation of variables. The strained fines concentrations are obtained by integrating the suspended fines concentrations across different corresponding flow zones vertically from the initial-condition line.

$$S_{a,IV} = S_{ai} + \frac{\Lambda_a C_0 \varphi}{2\sqrt{x_D}} \exp\left(\left(\Lambda_a + \Lambda_s\right)\left(\sqrt{x_{Dw}} - \sqrt{x_D}\right)\right) \ldots\ldots\ldots\ldots\ldots\ldots\ldots\ldots\ldots \quad (4.83)$$

$$S_{s,IV} = \frac{\Lambda_s C_0 \varphi}{2\sqrt{x_D}} \exp\left(\left(\Lambda_a + \Lambda_s\right)\left(\sqrt{x_{Dw}} - \sqrt{x_D}\right)\right) \ldots\ldots\ldots\ldots\ldots\ldots\ldots\ldots\ldots \quad (4.84)$$

$$S_{a,V} = S_{cr}\left(x_D\right);\ S_{a,X_1} = S_{cr}\left(x_D\right);\ S_{a,X_2} = S_{cr}\left(x_D\right);\ S_{a,XI} = S_{cr}\left(x_D\right) \ldots\ldots\ldots\ldots\ldots\ldots \quad (4.85)$$

$$S_{s,V} = \frac{\Lambda_s}{2\sqrt{x_D}}\left(\int_{-S_{wc}x_D + S_{wc}x_{Dw}}^{-S_{wc}x_{D,nanofluid} + S_{wc}x_{Dw}} C_{FP,III}\, d\varphi + \int_0^{\varphi} C_{FP,\mathrm{V}}\, d\varphi\right) \ldots\ldots\ldots\ldots\ldots\ldots\ldots\ldots \quad (4.86)$$

$$S_{s,X_1} = \frac{\Lambda_s}{2\sqrt{x_D}}\left(\int_{-S_{wc}x_{Di} + S_{wc}x_{Dw}}^{\varphi_{cr}} C_{FP,IX}\, d\varphi + \int_{\varphi_{cr}}^{-S_{wc}x_{D,nanofluid} + S_{wc}x_{Dw}} C_{FP,\mathrm{VI}} d\varphi + \int_0^{\varphi} C_{FP,X_1} d\varphi\right) \ldots\ldots\ldots\ldots\ldots \quad (4.87)$$

$$S_{s,X_2} = \frac{\Lambda_s}{2\sqrt{x_D}}\left(\int_{-S_{wc}x_{Di} + S_{wc}x_{Dw}}^{\varphi_{cr}} C_{FP,IX}\, d\varphi + \int_0^{\varphi} C_{FP,X_2} d\varphi\right) \ldots\ldots\ldots\ldots\ldots\ldots\ldots\ldots\ldots \quad (4.88)$$

$$S_{s,XI} = \frac{\Lambda_s}{2\sqrt{x_D}}\left(\int_{-S_{wc}x_{Di} + S_{wc}x_{Dw}}^{\varphi_{cr}} C_{FP,XII}\, d\varphi + \int_{\varphi_{cr}}^{\varphi} C_{FP,\mathrm{XI}} d\varphi\right) \ldots\ldots\ldots\ldots\ldots\ldots\ldots\ldots\ldots \quad (4.89)$$

The summary of analytical solutions of suspended, attached and strained fines concentration are presented in Table. 4.5-4.7 for nanofluid treatment scenario B-1

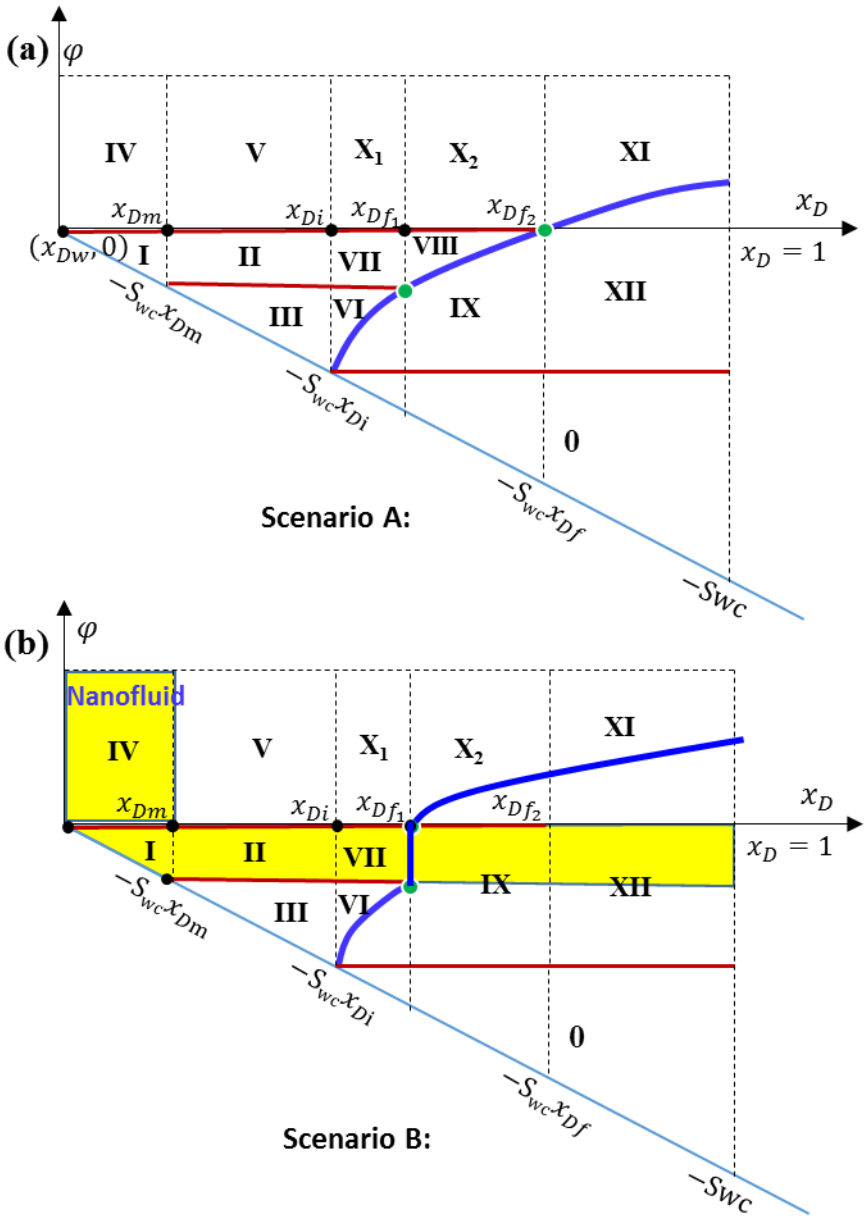


Figure 4.20 Stream-function and distance diagram with the structure of analytical solutions within different flow zones for both scenario A and scenario B (a: scenario A without nanofluid effects; b, c and d: scenarios with different nanofluid treatment radius)

Table 4-2 The summary of suspended fines concentration in different flow zones in the plane of (φ, x_D) for the scenario A in Figure 4.20

	Domain	Suspended fines concentration
0	$x_{Di} < x_D < 1$ $S_{wc}\left(x_{Dw} - x_D\right) < \varphi < S_{wc}\left(x_{Dw} - x_{Di}\right)$	0
I	$x_{Dw} < x_D < x_{Dm}$ $S_{wc}\left(x_{Dw} - x_D\right) < \varphi < 0$	$S_{ai}\exp\left(-\Lambda_s\left(\sqrt{x_D} - \sqrt{x_{Dw} - \frac{\varphi}{S_{wc}}}\right)\right)$
II	$x_{Dm} < x_D < x_{Di}$ $S_{wc}\left(x_{Dw} - x_{Dm}\right) < \varphi < 0$	$S_{ai}\exp\left(-\Lambda_s\left(\sqrt{x_D} - \sqrt{x_{Dw} - \frac{\varphi}{S_{wc}}}\right)\right)$
III	$x_{Dm} < x_D < x_{Di}$ $S_{wc}\left(x_{Dw} - x_D\right) < \varphi < S_{wc}\left(x_{Dw} - x_{Dm}\right)$	$\left(S_{ai} - S_{cr}\left(\sqrt{x_{Dw} - \frac{\varphi}{S_{wc}}}\right)\right)\exp\left(-\Lambda_s\left(\sqrt{x_D} - \sqrt{x_{Dw} - \frac{\varphi}{S_{wc}}}\right)\right)$
IV	$x_{Dw} < x_D < x_{Dm}$ $\varphi > 0$	$C_0\exp\left(-\Lambda_s\left(\sqrt{x_D} - \sqrt{x_{Dw}}\right)\right)$
V	$x_{Dm} < x_D < x_{Di}$ $\varphi > 0$	$C_0\exp\left(-\Lambda_s\left(\sqrt{x_D} - \sqrt{x_{Dw}}\right)\right)$
VI	$x_{Di} < x_D < x_{Df_1}$ $\varphi_{cr} < \varphi < S_{wc}\left(x_{Dw} - x_{Dm}\right)$	$\left(S_{ai} - S_{cr}\left(\sqrt{x_{Dw} - \frac{\varphi}{S_{wc}}}\right)\right)\exp\left(-\Lambda_s\left(\sqrt{x_D} - \sqrt{x_{Dw} - \frac{\varphi}{S_{wc}}}\right)\right)$
VII	$x_{Di} < x_D < x_{Df_1}$ $S_{wc}\left(x_{Dw} - x_{Dm}\right) < \varphi < 0$	$S_{ai}\exp\left(-\Lambda_s\left(\sqrt{x_D} - \sqrt{x_{Dw} - \frac{\varphi}{S_{wc}}}\right)\right)$
VIII	$x_{Df_1} < x_D < x_{Df_2}$ $\varphi_{cr} < \varphi < 0$	$S_{ai}\exp\left(-\Lambda_s\left(\sqrt{x_D} - \sqrt{x_{Dw} - \frac{\varphi}{S_{wc}}}\right)\right)$
X1	$x_{Di} < x_D < x_{Df_1}$ $\varphi > 0$	$C_0\exp\left(-\Lambda_s\left(\sqrt{x_D} - \sqrt{x_{Dw}}\right)\right)$
X2	$x_{Df_1} < x_D < x_{Df_2}$ $\varphi > 0$	$C_0\exp\left(-\Lambda_s\left(\sqrt{x_D} - \sqrt{x_{Dw}}\right)\right)$
IX	$x_{Di} < x_D < x_{Df_2}$ $S_{wc}\left(x_{Dw} - x_{Di}\right) < \varphi < \varphi_{cr}$	$C_{FP}\left(x_{cr}, \varphi_{cr}\right)\exp\left[-\left(\Lambda_a + \Lambda_s\right)\left(\sqrt{x_D} - \sqrt{x_{cr}}\right)\right]$
XI	$x_{Df_2} < x_D < 1$ $\varphi > \varphi_{cr}$	$C_0\exp\left(-\Lambda_s\left(\sqrt{x_D} - \sqrt{x_{Dw}}\right)\right)$
XII	$x_{Df_2} < x_D < 1$ $S_{wc}\left(x_{Dw} - x_{Di}\right) < \varphi < \varphi_{cr}$	$C_{FP}\left(x_{cr}, \varphi_{cr}\right)\exp\left[-\left(\Lambda_a + \Lambda_s\right)\left(\sqrt{x_D} - \sqrt{x_{cr}}\right)\right]$

Table 4-3 The summary of attached fines concentration in different flow zones in the plane of (φ, x_D) for the scenario A in Figure 4.20

	Domain	Attached fines concentration
0	$x_{Di} < x_D < 1$ $S_{wc}\left(x_{Dw} - x_D\right) < \varphi < S_{wc}\left(x_{Dw} - x_{Di}\right)$	S_{ai}
I	$x_{Dw} < x_D < x_{Dm}$ $S_{wc}\left(x_{Dw} - x_D\right) < \varphi < 0$	0
II	$x_{Dm} < x_D < x_{Di}$ $S_{wc}\left(x_{Dw} - x_{Dm}\right) < \varphi < 0$	$S_{cr}\left(x_D\right)$
III	$x_{Dm} < x_D < x_{Di}$ $S_{wc}\left(x_{Dw} - x_D\right) < \varphi < S_{wc}\left(x_{Dw} - x_{Dm}\right)$	$S_{cr}\left(x_D\right)$
IV	$x_{Dw} < x_D < x_{Dm}$ $\varphi > 0$	0
V	$x_{Dm} < x_D < x_{Di}$ $\varphi > 0$	$S_{cr}\left(x_D\right)$
VI	$x_{Di} < x_D < x_{Df_1}$ $\varphi_{cr} < \varphi < S_{wc}\left(x_{Dw} - x_{Dm}\right)$	$S_{cr}\left(x_D\right)$
VII	$x_{Di} < x_D < x_{Df_1}$ $S_{wc}\left(x_{Dw} - x_{Dm}\right) < \varphi < 0$	$S_{cr}\left(x_D\right)$
VIII	$x_{Df_1} < x_D < x_{Df_2}$ $\varphi_{cr} < \varphi < 0$	$S_{cr}\left(x_D\right)$
X1	$x_{Di} < x_D < x_{Df_1}$ $\varphi > 0$	$S_{cr}\left(x_D\right)$
X2	$x_{Df_1} < x_D < x_{Df_2}$ $\varphi > 0$	$S_{cr}\left(x_D\right)$
IX	$x_{Di} < x_D < x_{Df_2}$ $S_{wc}\left(x_{Dw} - x_{Di}\right) < \varphi < \varphi_{cr}$	$S_{ai} + \left(S_{cr}\left(x_{D,cr}\right) - S_{ai}\right)\sqrt{\frac{x_{cr}}{x_D}}\exp\left(\left(\Lambda_a + \Lambda_s\right)\left(\sqrt{x_{cr}} - \sqrt{x_D}\right)\right)$
XI	$x_{Df_2} < x_D < 1$ $\varphi > \varphi_{cr}$	$S_{cr}\left(x_D\right)$
XII	$x_{Df_2} < x_D < 1$ $S_{wc}\left(x_{Dw} - x_{Di}\right) < \varphi < \varphi_{cr}$	$S_{ai} + \left(S_{cr}\left(x_{D,cr}\right) - S_{ai}\right)\sqrt{\frac{x_{cr}}{x_D}}\exp\left(\left(\Lambda_a + \Lambda_s\right)\left(\sqrt{x_{cr}} - \sqrt{x_D}\right)\right)$

Table 4-4 The summary of strained fines concentration in different flow zones in the plane of (φ, x_D) for the scenario A in Figure 4.20

	Strained fines concentration
0	0
I	$-\frac{S_{ai}}{\sqrt{x_D}} S_{wc}\left[\left(\sqrt{x_{Dw}-\frac{\varphi}{S_{wc}}}-\frac{1}{\Lambda_s}\right)\exp\left(\Lambda_s\left(\sqrt{x_{Dw}-\frac{\varphi}{S_{wc}}}-\sqrt{x_D}\right)\right)+\frac{1}{\Lambda_s}-\sqrt{x_D}\right]$
II	$\frac{\Lambda_s}{2\sqrt{x_D}}\left(\int_{-S_{wc}x_D+S_{wc}x_{Dw}}^{-S_{wc}x_{Dm}+S_{wc}x_{Dw}} C_{FP,III}\,d\varphi+\int_{-S_{wc}x_{Dm}+S_{wc}x_{Dw}}^{\varphi} C_{FP,II}\,d\varphi\right)$
III	$-\frac{S_{ai}}{\sqrt{x_D}} S_{wc}\left[\left(\sqrt{x_{Dw}-\frac{\varphi}{S_{wc}}}-\frac{1}{\Lambda_s}\right)\exp\left(\Lambda_s\left(\sqrt{x_{Dw}-\frac{\varphi}{S_{wc}}}-\sqrt{x_D}\right)\right)+\frac{1}{\Lambda_s}-\sqrt{x_D}\right]$ $-\frac{\Lambda_s\exp\left(-\Lambda_s\sqrt{x_D}\right)}{2\sqrt{x_D}}\int_{-S_{wc}x_D+S_{wc}x_{Dw}}^{\varphi} S_{cr}\left(\sqrt{x_{Dw}-\frac{\varphi}{S_{wc}}}\right)\exp\left(\Lambda_s\sqrt{x_{Dw}-\frac{\varphi}{S_{wc}}}\right)d\varphi$
IV	$-\frac{S_{ai}}{\sqrt{x_D}} S_{wc}\left[\left(\sqrt{x_{Dw}}-\frac{1}{\Lambda_s}\right)\exp\left(\Lambda_s\left(\sqrt{x_{Dw}}-\sqrt{x_D}\right)\right)+\frac{1}{\Lambda_s}-\sqrt{x_D}\right]+\frac{\Lambda_s C_0\varphi}{2\sqrt{x_D}}\exp\left(-\Lambda_s\sqrt{x_D}\right)$
V	$\frac{\Lambda_s}{2\sqrt{x_D}}\left(\int_{-S_{wc}x_D+S_{wc}x_{Dw}}^{-S_{wc}x_{Dm}+S_{wc}x_{Dw}} C_{FP,III}\,d\varphi+\int_{-S_{wc}x_{Dm}+S_{wc}x_{Dw}}^{0} C_{FP,II}\,d\varphi+\int_{0}^{\varphi} C_{FP,V}\,d\varphi\right)$
VI	$\frac{\Lambda_s}{2\sqrt{x_D}}\left(\int_{-S_{wc}x_{Di}+S_{wc}x_{Dw}}^{\varphi_{cr}} C_{FP,IX}\,d\varphi+\int_{\varphi_{cr}}^{\varphi} C_{FP,VI}\,d\varphi\right)$
VII	$\frac{\Lambda_s}{2\sqrt{x_D}}\left(\begin{array}{l}\int_{-S_{wc}x_{Di}+S_{wc}x_{Dw}}^{\varphi_{cr}} C_{FP,IX}\,d\varphi+\int_{\varphi_{cr}}^{-S_{wc}x_{Dm}+S_{wc}x_{Dw}} C_{FP,VI}\,d\varphi \\ +\int_{-S_{wc}x_{Dm}+S_{wc}x_{Dw}}^{\varphi} C_{FP,VII}\,d\varphi\end{array}\right)$
VIII	$\frac{\Lambda_s}{2\sqrt{x_D}}\left(\int_{-S_{wc}x_{Di}+S_{wc}x_{Dw}}^{\varphi_{cr}} C_{FP,IX}\,d\varphi+\int_{\varphi_{cr}}^{\varphi} C_{FP,VIII}\,d\varphi\right)$
X1	$\frac{\Lambda_s}{2\sqrt{x_D}}\left(\begin{array}{l}\int_{-S_{wc}x_{Di}+S_{wc}x_{Dw}}^{\varphi_{cr}} C_{FP,IX}\,d\varphi+\int_{\varphi_{cr}}^{-S_{wc}x_{Dm}+S_{wc}x_{Dw}} C_{FP,VI}\,d\varphi \\ +\int_{-S_{wc}x_{Dm}+S_{wc}x_{Dw}}^{0} C_{FP,VII}\,d\varphi+\int_{0}^{\varphi} C_{FP,X_1}\,d\varphi\end{array}\right)$
X2	$\frac{\Lambda_s}{2\sqrt{x_D}}\left(\int_{-S_{wc}x_{Di}+S_{wc}x_{Dw}}^{\varphi_{cr}} C_{FP,IX}\,d\varphi+\int_{\varphi_{cr}}^{0} C_{FP,VIII}\,d\varphi+\int_{0}^{\varphi} C_{FP,X_2}\,d\varphi\right)$
IX	$\frac{\Lambda_s}{2\sqrt{x_D}}\left(\int_{-S_{wc}x_{Di}+S_{wc}x_{Dw}}^{\varphi} C_{FP,IX}\,d\varphi\right)$
XI	$\frac{\Lambda_s}{2\sqrt{x_D}}\left(\int_{-S_{wc}x_{Di}+S_{wc}x_{Dw}}^{\varphi_{cr}} C_{FP,XII}\,d\varphi+\int_{\varphi_{cr}}^{\varphi} C_{FP,XI}\,d\varphi\right)$
XII	$\frac{\Lambda_s}{2\sqrt{x_D}}\left(\int_{-S_{wc}x_{Di}+S_{wc}x_{Dw}}^{\varphi} C_{FP,XII}\,d\varphi\right)$

Table 4-5 The summary of suspended fines concentration in different flow zones in the plane of (φ, x_D) for the scenario B in Figure 4.20

Zone	Suspended fines concentration
0	0
I	0
II	0
III	$\left(S_{ai}-S_{cr}\left(\sqrt{x_{Dw}-\frac{\varphi}{S_{wc}}}\right)\right)\exp\left(-\Lambda_s\left(\sqrt{x_D}-\sqrt{x_{Dw}-\frac{\varphi}{S_{wc}}}\right)\right)$
IV	$C_0\exp\left(-\left(\Lambda_s+\Lambda_a\right)\left(\sqrt{x_D}-\sqrt{x_{Dw}}\right)\right)$
V	$C_0\exp\left(-\Lambda_s\left(\sqrt{x_D}-\sqrt{x_{D,nanofluid}}\right)-\left(\Lambda_s+\Lambda_a\right)\left(\sqrt{x_{D,nanofluid}}-\sqrt{x_{Dw}}\right)\right)$
VI	$\left(S_{ai}-S_{cr}\left(\sqrt{x_{Dw}-\frac{\varphi}{S_{wc}}}\right)\right)\exp\left(-\Lambda_s\left(\sqrt{x_D}-\sqrt{x_{Dw}-\frac{\varphi}{S_{wc}}}\right)\right)$
VII	0
VIII	0
X1	$C_0\exp\left(-\Lambda_s\left(\sqrt{x_D}-\sqrt{x_{D,nanofluid}}\right)-\left(\Lambda_s+\Lambda_a\right)\left(\sqrt{x_{D,nanofluid}}-\sqrt{x_{Dw}}\right)\right)$
X2	$C_0\exp\left(-\Lambda_s\left(\sqrt{x_D}-\sqrt{x_{D,nanofluid}}\right)-\left(\Lambda_s+\Lambda_a\right)\left(\sqrt{x_{D,nanofluid}}-\sqrt{x_{Dw}}\right)\right)$
IX	$C_{FP}\left(x_{cr},\varphi_{cr}\right)\exp\left[-\left(\Lambda_a+\Lambda_s\right)\left(\sqrt{x_D}-\sqrt{x_{cr}}\right)\right]$
XI	$C_0\exp\left(-\Lambda_s\left(\sqrt{x_D}-\sqrt{x_{D,nanofluid}}\right)-\left(\Lambda_s+\Lambda_a\right)\left(\sqrt{x_{D,nanofluid}}-\sqrt{x_{Dw}}\right)\right)$
XII	$C_{FP}\left(x_{cr},\varphi_{cr}\right)\exp\left[-\left(\Lambda_a+\Lambda_s\right)\left(\sqrt{x_D}-\sqrt{x_{cr}}\right)\right]$

Table 4-6 The summary of attached fines concentration in different flow zones in the plane of (φ, x_D) for the scenario B in Figure 4.20

	Domain	Attached fines concentration
0	$x_{Di} < x_D < 1$ $S_{wc}\left(x_{Dw} - x_D\right) < \varphi < S_{wc}\left(x_{Dw} - x_{Di}\right)$	S_{ai}
I	$x_{Dw} < x_D < x_{D,nanofluid}$ $S_{wc}\left(x_{Dw} - x_D\right) < \varphi < 0$	S_{ai}
II	$x_{Dm} < x_D < x_{Di}$ $S_{wc}\left(x_{Dw} - x_{D,nanofluid}\right) < \varphi < 0$	$S_{cr}\left(x_D\right)$
III	$x_{D,nanofluid} < x_D < x_{Di}$ $S_{wc}\left(x_{Dw} - x_D\right) < \varphi < S_{wc}\left(x_{Dw} - x_{Dm}\right)$	$S_{cr}\left(x_D\right)$
IV	$x_{Dw} < x_D < x_{D,nanofluid}$ $\varphi > 0$	$S_{ai} + \frac{\Lambda_a C_0 \varphi}{2\sqrt{x_D}} \exp\left(\left(\Lambda_a + \Lambda_s\right)\left(\sqrt{x_{Dw}} - \sqrt{x_D}\right)\right)$
V	$x_{D,nanofluid} < x_D < x_{Di}$ $\varphi > 0$	$S_{cr}\left(x_D\right)$
VI	$x_{Di} < x_D < x_{Df_1}$ $\varphi_{cr} < \varphi < S_{wc}\left(x_{Dw} - x_{D,nanofluid}\right)$	$S_{cr}\left(x_D\right)$
VII	$x_{Di} < x_D < x_{Df_1}$ $S_{wc}\left(x_{Dw} - x_{D,nanofluid}\right) < \varphi < 0$	$S_{cr}\left(x_D\right)$
VIII	$x_{Df_1} < x_D < x_{Df_2}$ $\varphi_{cr} < \varphi < 0$	$S_{cr}\left(x_D\right)$
X1	$x_{Di} < x_D < x_{Df_1}$ $\varphi > 0$	$S_{cr}\left(x_D\right)$
X2	$x_{Df_1} < x_D < x_{Df_2}$ $\varphi > 0$	$S_{cr}\left(x_D\right)$
IX	$x_{Di} < x_D < x_{Df_2}$ $S_{wc}\left(x_{Dw} - x_{Di}\right) < \varphi < \varphi_{cr}$	$S_{ai} + \left(S_{cr}\left(x_{D,cr}\right) - S_{ai}\right)\sqrt{\frac{x_{cr}}{x_D}} \exp\left(\left(\Lambda_a + \Lambda_s\right)\left(\sqrt{x_{cr}} - \sqrt{x_D}\right)\right)$
XI	$x_{Df_2} < x_D < 1$ $\varphi > \varphi_{cr}$	$S_{cr}\left(x_D\right)$
XII	$x_{Df_2} < x_D < 1$ $S_{wc}\left(x_{Dw} - x_{Di}\right) < \varphi < \varphi_{cr}$	$S_{ai} + \left(S_{cr}\left(x_{D,cr}\right) - S_{ai}\right)\sqrt{\frac{x_{cr}}{x_D}} \exp\left(\left(\Lambda_a + \Lambda_s\right)\left(\sqrt{x_{cr}} - \sqrt{x_D}\right)\right)$

Table 4-7 The summary of strained fines concentration in different flow zones in the plane of (φ, x_D) for the scenario B in Figure 4.20

Zone	Strained fines concentration
0	0
I	0
II	$\frac{\Lambda_s}{2\sqrt{x_D}}\int_{-S_{wc}x_D+S_{wc}x_{Dw}}^{-S_{wc}x_{D,nanofluid}+S_{wc}x_{Dw}} C_{FP,III}\,d\varphi$
III	$-\frac{S_{ai}}{\sqrt{x_D}}S_{wc}\left[\left(\sqrt{x_{Dw}-\frac{\varphi}{S_{wc}}}-\frac{1}{\Lambda_s}\right)\exp\left(\Lambda_s\left(\sqrt{x_{Dw}-\frac{\varphi}{S_{wc}}}-\sqrt{x_D}\right)\right)+\frac{1}{\Lambda_s}-\sqrt{x_D}\right]$ $-\frac{\Lambda_s\exp\left(-\Lambda_s\sqrt{x_D}\right)}{2\sqrt{x_D}}\int_{-S_{wc}x_D+S_{wc}x_{Dw}}^{\varphi} S_{cr}\left(\sqrt{x_{Dw}-\frac{\varphi}{S_{wc}}}\right)\exp\left(\Lambda_s\sqrt{x_{Dw}-\frac{\varphi}{S_{wc}}}\right)d\varphi$
IV	$\frac{\Lambda_s C_0\varphi}{2\sqrt{x_D}}\exp\left(\left(\Lambda_a+\Lambda_s\right)\left(\sqrt{x_{Dw}}-\sqrt{x_D}\right)\right)$
V	$\frac{\Lambda_s}{2\sqrt{x_D}}\left(\int_{-S_{wc}x_D+S_{wc}x_{Dw}}^{-S_{wc}x_{D,nanofluid}+S_{wc}x_{Dw}} C_{FP,III}\,d\varphi+\int_0^{\varphi} C_{FP,\mathrm{V}}\,d\varphi\right)$
VI	$\frac{\Lambda_s}{2\sqrt{x_D}}\left(\int_{-S_{wc}x_{Di}+S_{wc}x_{Dw}}^{\varphi_{cr}} C_{FP,IX}\,d\varphi+\int_{\varphi_{cr}}^{\varphi} C_{FP,\mathrm{VI}}\,d\varphi\right)$
VII	$\frac{\Lambda_s}{2\sqrt{x_D}}\left(\int_{-S_{wc}x_{Di}+S_{wc}x_{Dw}}^{\varphi_{cr}} C_{FP,IX}\,d\varphi+\int_{\varphi_{cr}}^{-S_{wc}x_{D,nanofluid}+S_{wc}x_{Dw}} C_{FP,\mathrm{VI}}\,d\varphi\right)$
VIII	$\frac{\Lambda_s}{2\sqrt{x_D}}\int_{-S_{wc}x_{Di}+S_{wc}x_{Dw}}^{\varphi_{cr}} C_{FP,IX}\,d\varphi$
X1	$\frac{\Lambda_s}{2\sqrt{x_D}}\left(\int_{-S_{wc}x_{Di}+S_{wc}x_{Dw}}^{\varphi_{cr}} C_{FP,IX}\,d\varphi+\int_{\varphi_{cr}}^{-S_{wc}x_{D,nanofluid}+S_{wc}x_{Dw}} C_{FP,\mathrm{VI}}\,d\varphi+\int_0^{\varphi} C_{FP,\mathrm{X_1}}\,d\varphi\right)$
X2	$\frac{\Lambda_s}{2\sqrt{x_D}}\left(\int_{-S_{wc}x_{Di}+S_{wc}x_{Dw}}^{\varphi_{cr}} C_{FP,IX}\,d\varphi+\int_0^{\varphi} C_{FP,\mathrm{X_2}}\,d\varphi\right)$
IX	$\frac{\Lambda_s}{2\sqrt{x_D}}\left(\int_{-S_{wc}x_{Di}+S_{wc}x_{Dw}}^{\varphi} C_{FP,IX}\,d\varphi\right)$
XI	$\frac{\Lambda_s}{2\sqrt{x_D}}\left(\int_{-S_{wc}x_{Di}+S_{wc}x_{Dw}}^{\varphi_{cr}} C_{FP,XII}\,d\varphi+\int_{\varphi_{cr}}^{\varphi} C_{FP,\mathrm{XI}}\,d\varphi\right)$
XII	$\frac{\Lambda_s}{2\sqrt{x_D}}\left(\int_{-S_{wc}x_{Di}+S_{wc}x_{Dw}}^{\varphi} C_{FP,XII}\,d\varphi\right)$

Substitute the above determined solutions of suspended, attached and retained fine particles concentrations into the conservation law of water-phase (Eq. 4.30) in coordinate of (x_D, φ). And then, combining with the initial and boundary conditions of water-phase (Eq. 4.29) can result in a hyperbolic partial differential equation (Eq.4.30) with only one unknowns, water saturation. The characteristic forms of this PDE are expressed as:

$$\frac{d\varphi}{dx_D} = \frac{\partial F}{\partial G} = \frac{f_w(S_w, S_s, S_a) - S_w \dfrac{\partial f_w(S_w, S_s, S_a)}{\partial S_w}}{\dfrac{\partial f_w(S_w, S_s, S_a)}{\partial S_w}} \quad \text{...…….....….. (4.90a)}$$

$$\frac{dS_w}{dx_D} = \frac{\dfrac{\partial f_w(S_w, S_s, S_a)}{\partial S_a}\left(S_w \dfrac{\partial S_a}{\partial \varphi} - \dfrac{\partial S_a}{\partial x_D}\right) + \dfrac{\partial f_w(S_w, S_s, S_a)}{\partial S_s}\left(S_w \dfrac{\partial S_s}{\partial \varphi} - \dfrac{\partial S_s}{\partial x_D}\right)}{\dfrac{\partial f_w}{\partial S_w}} \quad \text{……..... (4.90b)}$$

In Eq. 4.90b, the first derivatives of attached fines and strained fines concentration in stream-function can be expressed as functions of suspended fines concentration using the corresponding kinetics equation of Eq. 4.34 and Eq. 4.35. The first derivatives of attached and strained fines concentration to distance can be determined by the above solutions of strained and attached fines in Table 4.3, 4.4, 4.6 and 4.7.

In case that the attachment of fines has not reached the maximum limit, Eq.4.90b can be updated as,

$$\frac{dS_w}{dx_D} = \frac{\dfrac{\partial f_w(S_w, S_s, S_a)}{\partial S_a}\left(S_w \dfrac{\Lambda_a C_{FP}}{2\sqrt{x_D}} - \dfrac{\partial S_a}{\partial x_D}\right) + \dfrac{\partial f_w(S_w, S_s, S_a)}{\partial S_s}\left(S_w \dfrac{\Lambda_s C_{FP}}{2\sqrt{x_D}} - \dfrac{\partial S_s}{\partial x_D}\right)}{\dfrac{\partial f_w(S_w, S_s, S_a)}{\partial S_w}} \quad \text{.... (4.91a)}$$

In case that the fines attachment has reached the maximum limit, but the maximum retention of fines is distance-dependent, thus, Eq.4.90b can be expressed as,

$$\frac{dS_w}{dx_D}=\frac{\frac{\partial f_w\left(S_w,S_s,S_a\right)}{\partial S_a}\left(S_w\frac{\partial \sigma_{cr}}{\partial \varphi}-\frac{\partial \sigma_{cr}}{\partial x_D}\right)+\frac{\partial f_w\left(S_w,S_s,S_a\right)}{\partial S_s}\left(S_wS_w\frac{\Lambda_s C_{FP}}{2\sqrt{x_D}}-\frac{\partial S_s}{\partial x_D}\right)}{\frac{\partial f_w\left(S_w,S_s,S_a\right)}{\partial S_w}}. \quad (4.91b)$$

After the analytical solutions in coordinate of $\left(x_D,\varphi\right)$ have been obtained, by substituting the characteristic lines of Eq. 4.90a into Eq. 4.22, the inversed transformation of stream-function back to time is achieved along the characteristic lines, as follow,

$$t_D=\int_0^{x_D}\frac{1}{\frac{\partial f_w\left(S_w,S_s,S_a\right)}{\partial S_w}}dx_D \quad \text{....} \quad (4.92)$$

This inverse mapping depends on the initial and boundary conditions.

Substituting Eq. 4.92 into the above solutions of the auxiliary and lifting system can result in the exact solutions of the problem of Eq. 4.21-Eq. 4.29 in Lagrangian coordinate of $\left(x_D,t_D\right)$.

Inferred from Eq. 4.32, Eq. 4.34-35 in this section, and works delivered by Borazjani (2016b), the attached and strained fines concentration waves are always continuous in the domain of $\left(x_D,\varphi\right)$. However, as for the waves of suspended fines and water saturation, there are saturation-concentration c-shock & saturation s-shock along the porous media. Th c-shock has been identified by the above exact solutions of suspended fines concentrations across different zones for different cases. The mass-balance conditions on shock waves (Hugoniot-Rankine condition) are applied for Eq. 4.32, and Eq. 4.34-35. As results, the velocity of saturation s-shock front is obtained as,

$$\left[\frac{d\varphi}{dx_D}\right]_{C_{FP}}=\frac{F^+-F^-}{G^+-G^-} \quad \text{....} \quad (4.93)$$

"-" and "+" indicates the values outgoing and incoming the shock front.

In addition, in Figure 4.20, along the horizontal axis $\varphi = 0$, there is an injected fines front, i.e., downstream of which, the initial condition of fines migration exists, and upstream of which, fines particles concentrations are determined by injected conditions.

4.3.3 Results and Discussions

4.3.3.1 Effects of Fines Migration on Two-Phase Flow

First, to evaluate the effects of fines migration and associated fines attachment and fines straining behaviors, a reference scenario without fines migration effects is presented for comparison. It does mean the ignorance of fines straining and attachment in fraction flow function of Eq. 4.26.

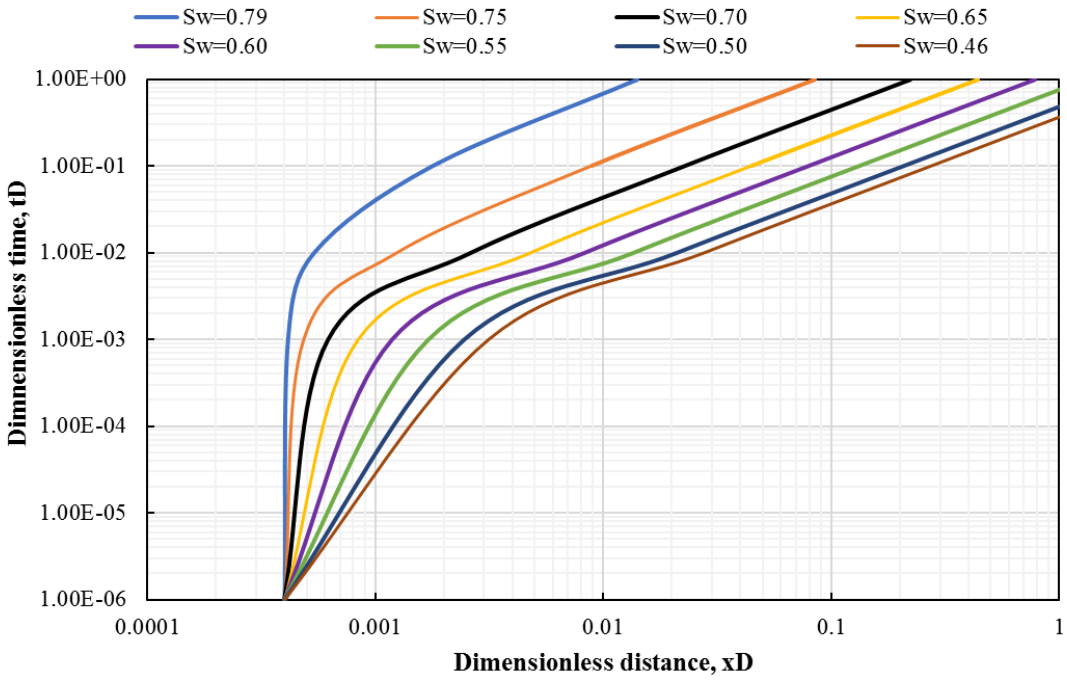


Figure 4.21 Time-distance diagram indicates the propagation of different water saturation waves (no fines migration effects)

The time-distance diagram for the case without fines migration is presented in Figure 4.21. The profile of water saturation in asymmetric system at different moments can be achieved by finding the intersection points of horizontal lines (t_D=const.) with the characteristic lines of different water saturation waves.

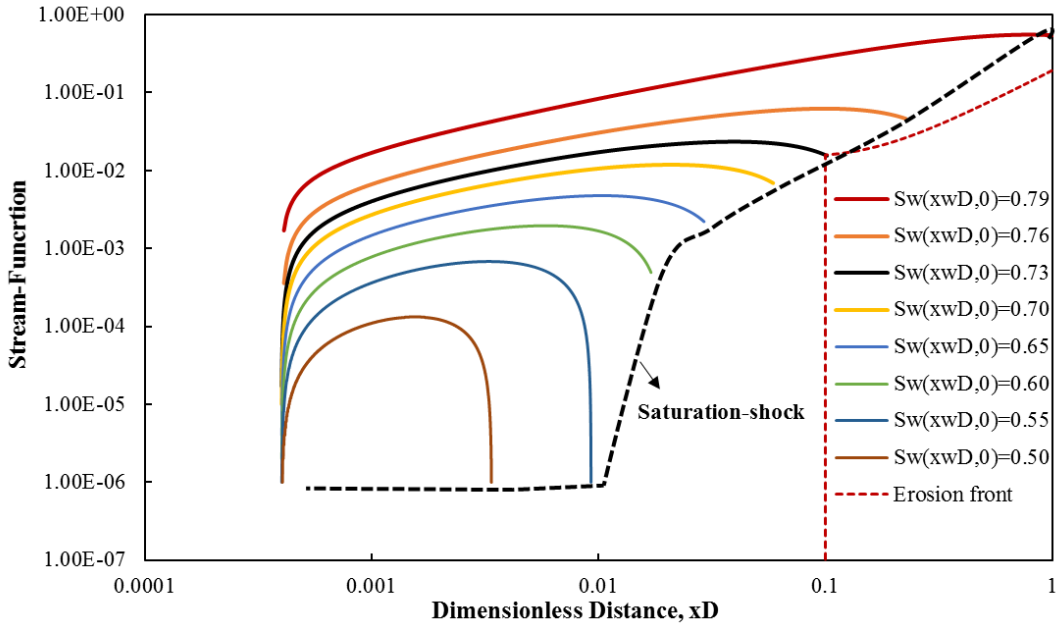


Figure 4.22 Stream-function and distance diagram indicates the propagation of water saturation waves (with fines migration in two-phase flow)
(Black dash-line: water saturation shock. Red dash-line: erosion front)

As for scenario A with fines migration in two-phase flow, according to the sets of analytical solutions defined in section 4.3.2, the diagram of stream-function and distance (two independent variables in auxiliary system and lifting equations) is applied to describe the propagation of water saturation waves which originate from the same injection point. The ends of different characteristic lines (propagation of water saturation wave) reflect the values of front-saturation along the saturation-shock. The line connecting those points with front-saturation values represents the movement path of water saturation shock. The red dashed line in Figure 4.22 indicates the trajectory of

erosion front (upstream, no fines attachment occurs; and downstream, fines attachment occurs). As indicated in Figure 4.22, the erosion front always moves faster than water saturation shock-front. In other words, the propagation of erosion front does not affect the movement of water saturation waves. The below analysis can also reflect this finding.

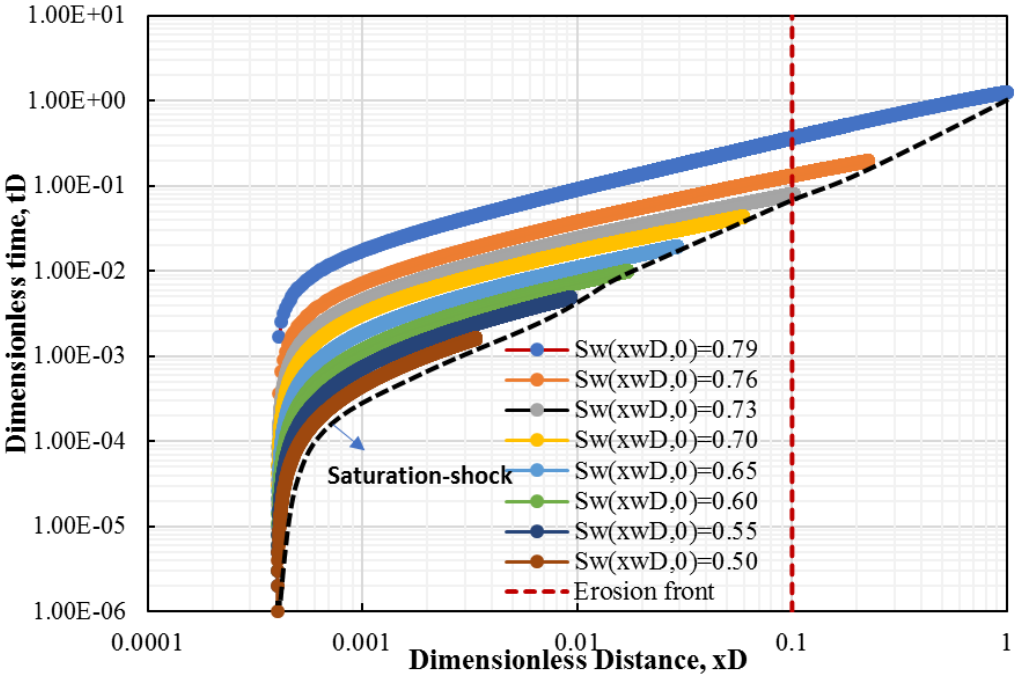
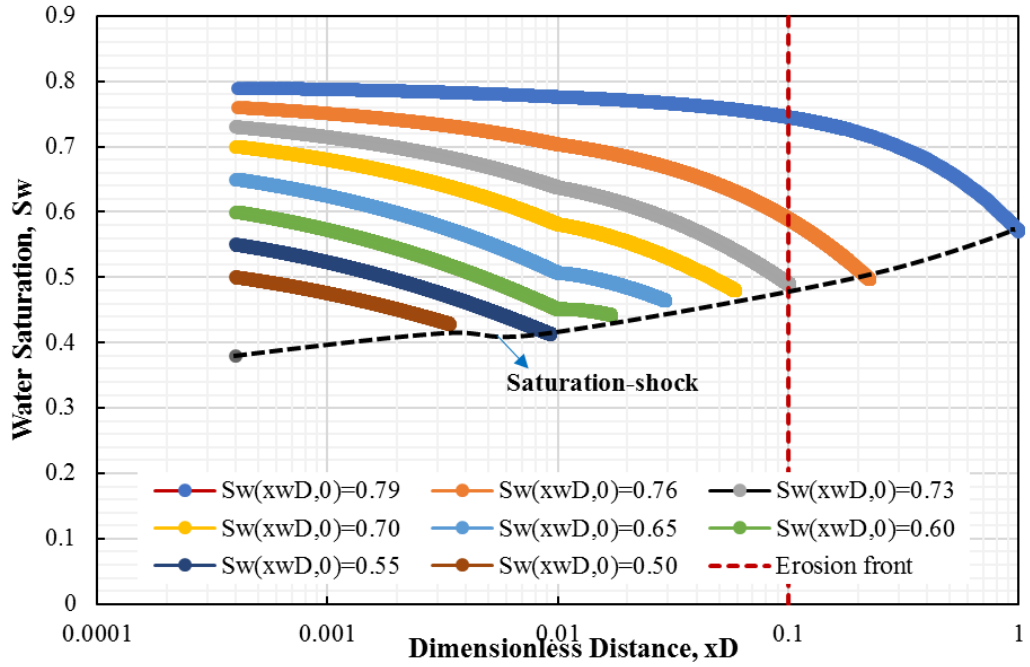


Figure 4.23 Time-distance diagram indicating the propagation of different water saturation waves in coordinate of dimensionless distance and time (with fines migration in two-phase flow)
(Black dash-line: water saturation shock. Red dash-line: erosion front)

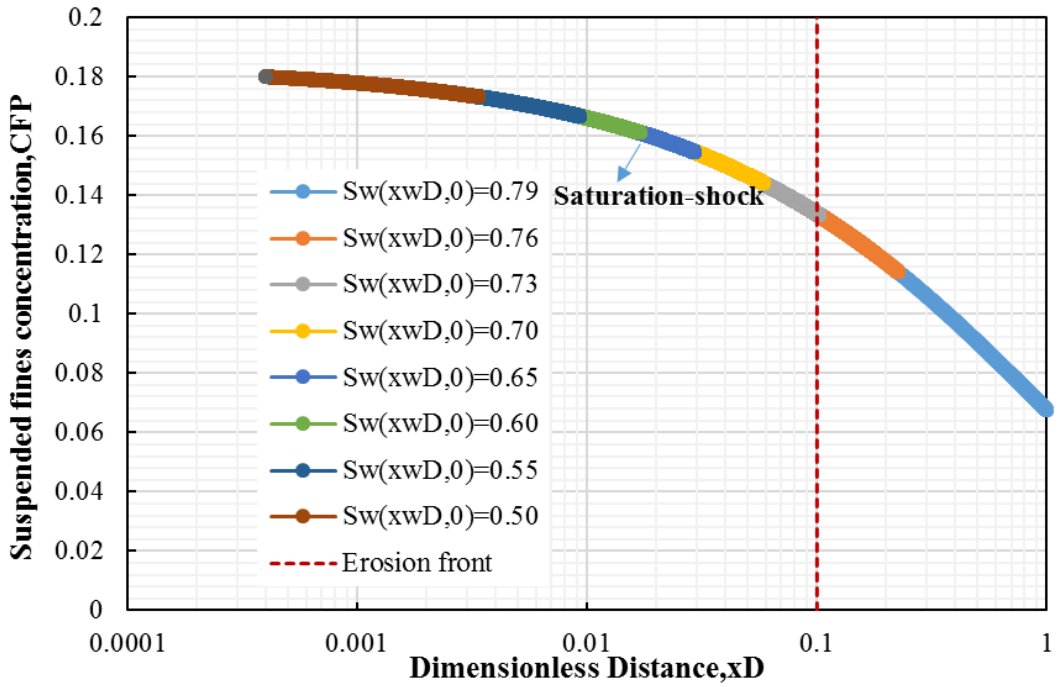
By applying the inverse transformation back to time from the stream-function as independent variables, the diagram of dimensionless time and distance can be achieved. The trajectory of erosion front becomes along the vertical direction, which indicates the erosion front is stationary at distance of 0.1. The black dash-line in Figure 4.23 represents the movement of water-saturation shock. As indicated, the values of front-saturation along the shock of water saturation change with distance, which is attributed to the

dependency of fines migration effects on the radial distance. The intensities of fines migration, attachment and straining are more severe near the injection well because of higher flow velocity in radial flow.

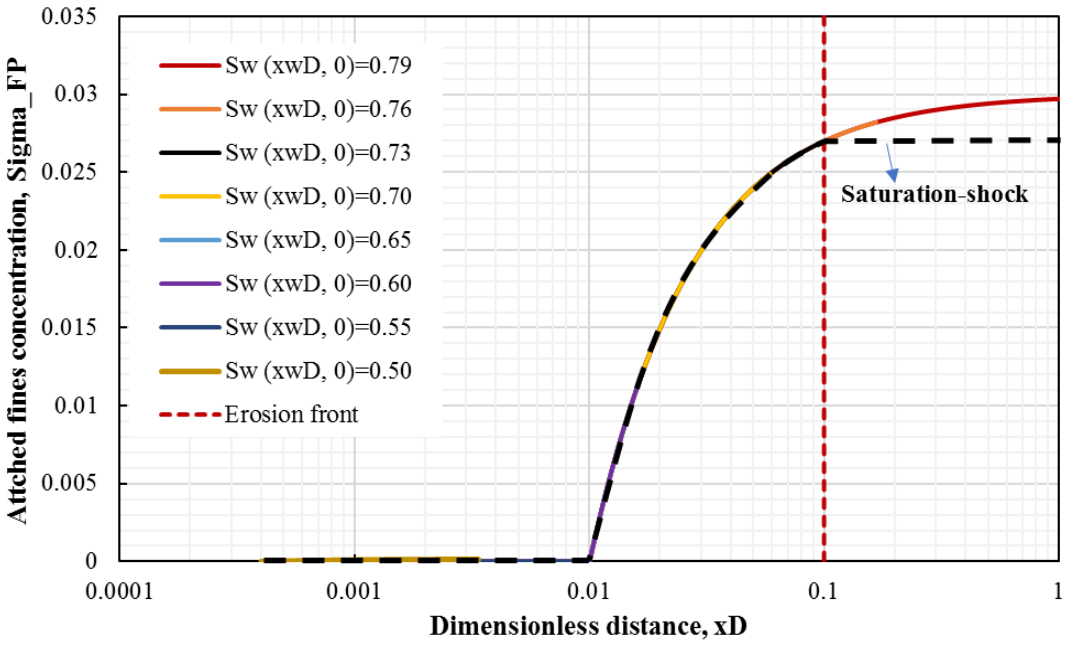
The changes of dependent variables (i.e., water saturation, suspended fines concentration, attached fines concentration and strained fines concentration) along the characteristic lines are presented in Figure 4.24. The erosion front and water saturation shock are also included into Figure 4.24. The combination of Figure 4.23 with Figure 4.24 provides us to obtain the MOC analytical solutions of fines migration in two-phase flow. The detailed workflow is described as follows. Firstly, draw different horizontal lines with constant time intersecting through the set of characteristic lines, and then find out the positions of different water saturation waves by reading out the values of intersection points. Followed by, the values of water saturation, suspended fines, attached fines and strained fines concentration are determined by placing the specific locations of different saturation waves from Figure 4.23 to Figure 4.24.



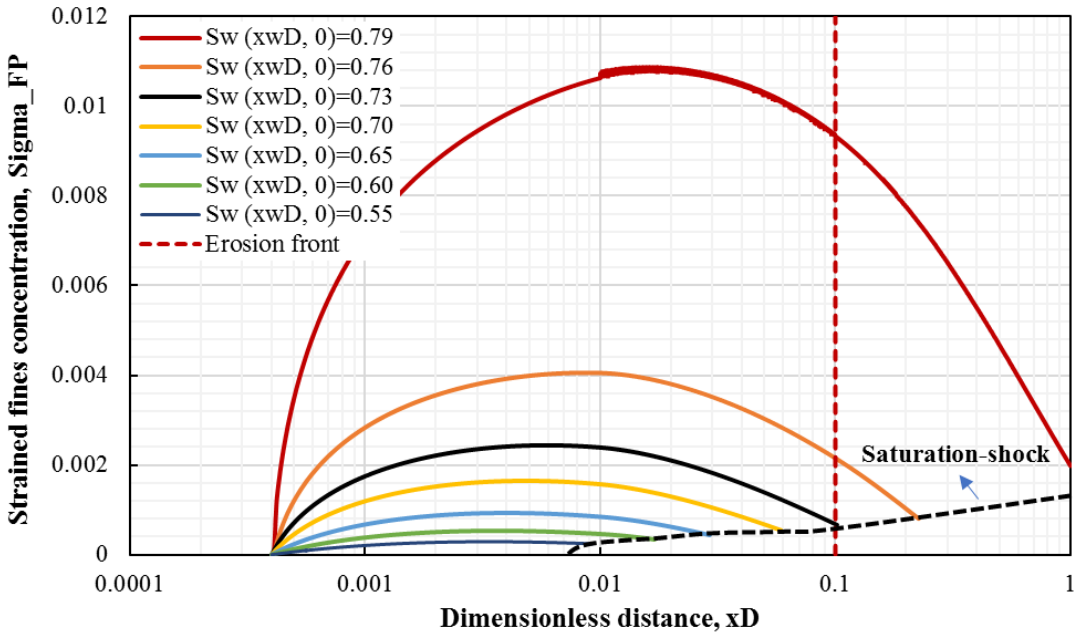
a. The variation of water saturation along the characteristic lines in Figure 4.23



b. The variation of suspended fines along the characteristic lines in Figure 4.23



c. The variation of attached fines along the characteristic lines in Figure 4.23



d. The variation of strained fines along the characteristic lines in Figure 4.23

Figure 4.24 The variation of water saturation, suspended fines, attached fines and strained fines concentration along the characteristic lines

Hence, the profiles of water saturation in the radial flow system at different time (injected pore-volume) are presented in Figure 4.25. The solutions of the scenario without fines migration in two-phase flow are also derived from Figure 4.21, and compared to demonstrate the effects of fines migration.

The effects of fines migration (fines attachment, fines straining and fines suspension) can slow down the movement of injected water saturation significantly. The values of front-saturation along the water-saturation shock also varies with locations because of fines migration. However, the differences of front-saturation values between both scenarios decreases as the movement of shock front continues toward the outlet. This can be attributed the attenuation of fines migration where the slower velocity occurs near the outlet in radial flow system, as indicated in Figure 4.18-19.

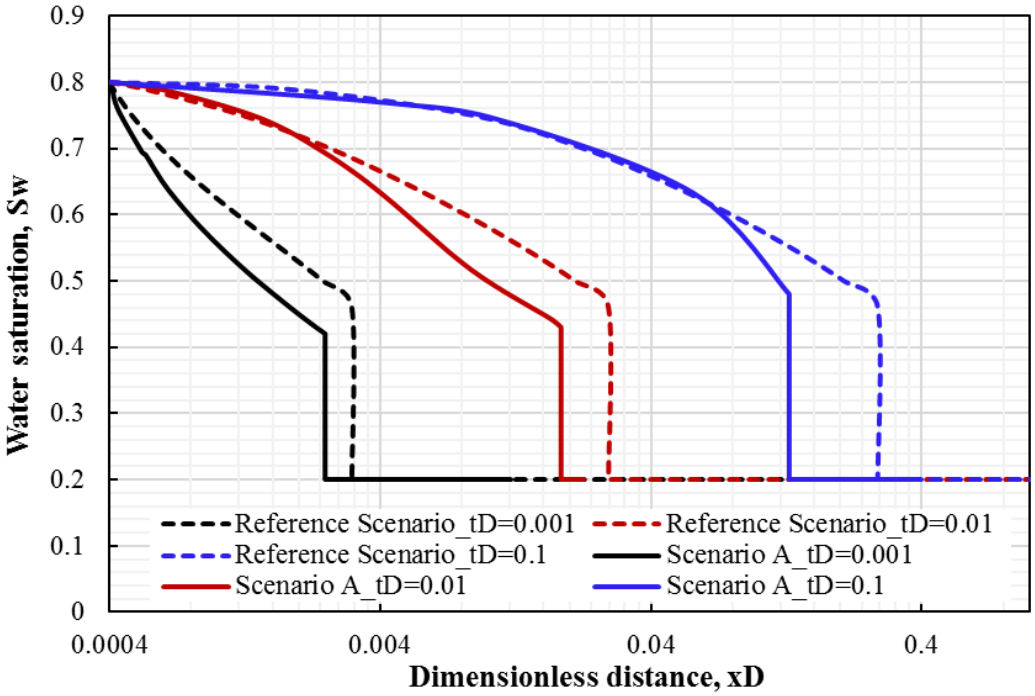


Figure 4.25 Comparison of water saturation profile between the scenario with fines migration and that with no fines migration in two-phase radial flow system

4.3.3.2 Performance of Nanofluid to Control Fines Migration in Two-Phase Flow

In this section, the performance of nanofluid treatment to control fines migration and enhance oil recovery will be examined. The range of nanofluid treatment is defined as 0.01, as shown in Figure 4.18. Because of the positive effects of nanofluid, the capacity of rock grains to capture migrating fines is enhanced significantly, from zero to 0.25. In other words, there are no fines detachment near the injection end for long time. The initial distribution of suspended fines and maximum capacity of rock grains to retain mobile fines after nanofluid treatment has been presented in Figure 4.19.

In Figure 4.26, the diagram of stream-function and distance is presented to demonstrate the trajectories of different water-saturation waves, and the movement of both erosion front and saturation-shock. Different from the scenario A in Figure 4.22, the trajectory of erosion front movement pass through the set of saturation waves. In other words, the erosion front is not always ahead of water saturation waves. As results, the existence of erosion front brings effects on the propagation of water-saturation waves, which is also confirmed in the diagram of distance and time in Figure 4.27. In the following figures, the range of nanofluid is highlighted from the injection point (0.0004) to the point of zero fines attachment in case without nanofluids (0.01). Figure 4.27 indicates the time-distance diagram for scenario B with nanofluid treatment. Figure 4.28 indicates the changes of water saturation, suspended fines, attached fines and strained fines along the different characteristic lines. The integration of Figure 4.27 with Figure 4.28 results in the analytical solutions of scenario B with nanofluid treatment effects.

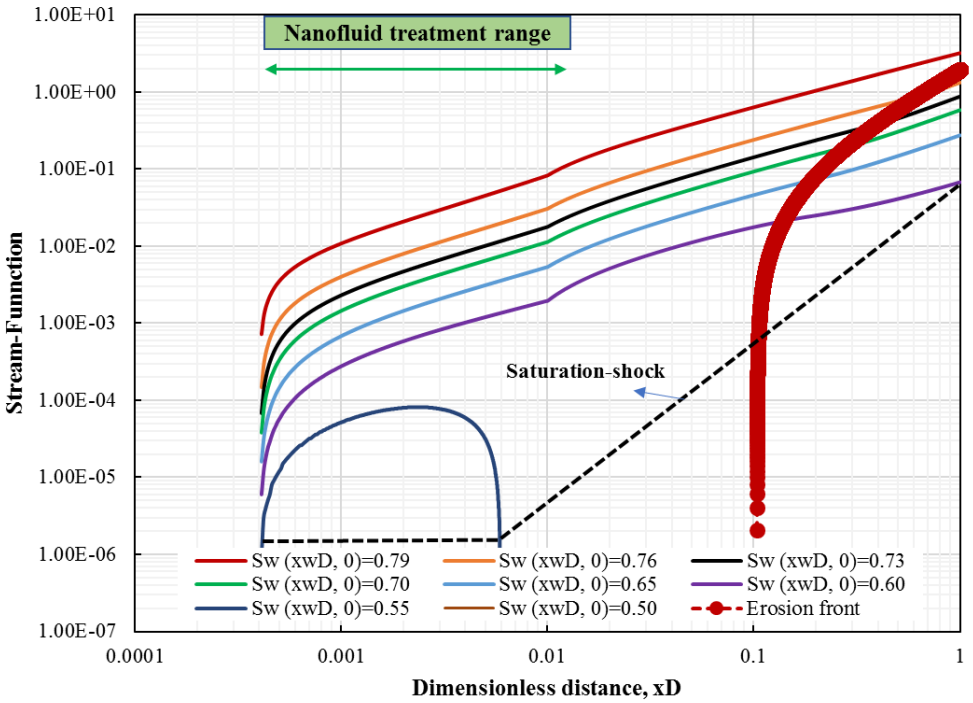


Figure 4.26 Stream-function and distance diagram indicating the propagation of water saturation waves (with nanofluids in two-phase radial flow)
(Black dash-line: water saturation shock. Red dash-line: erosion front)

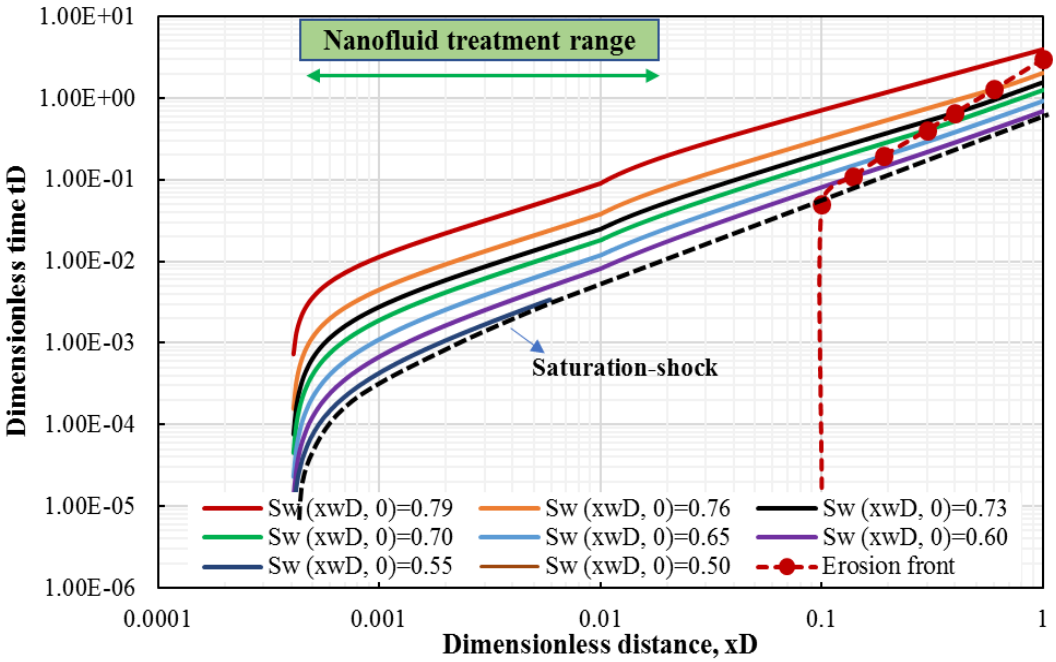
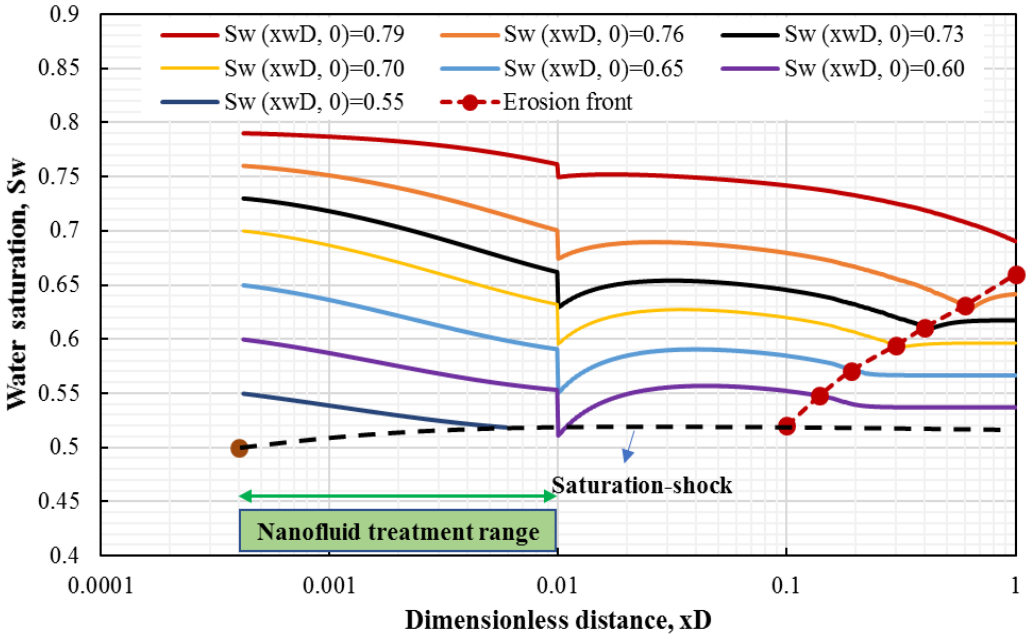
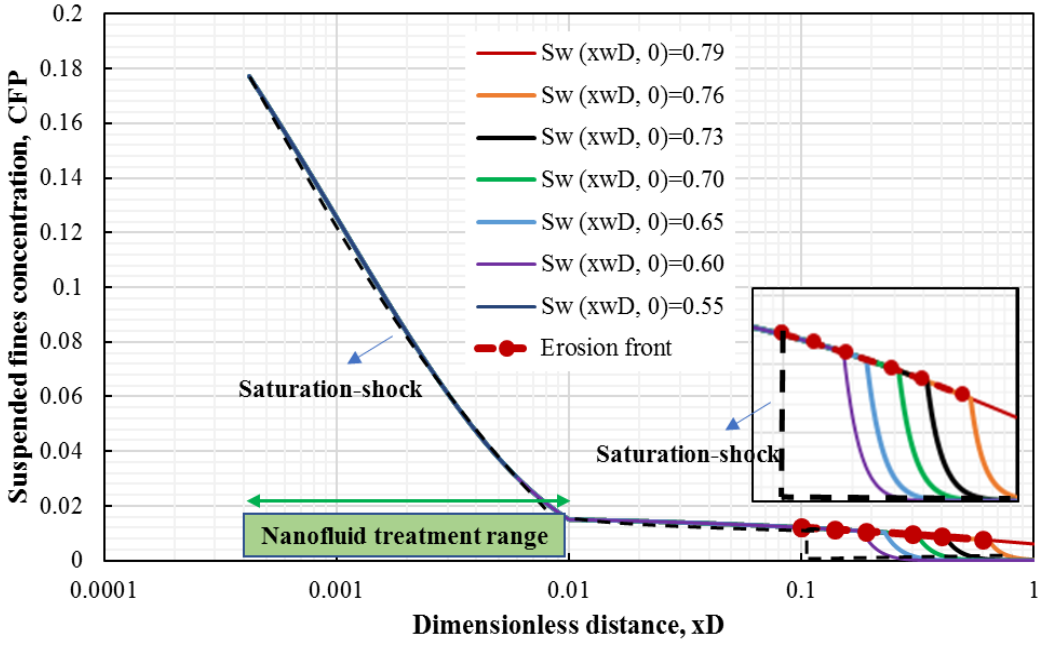


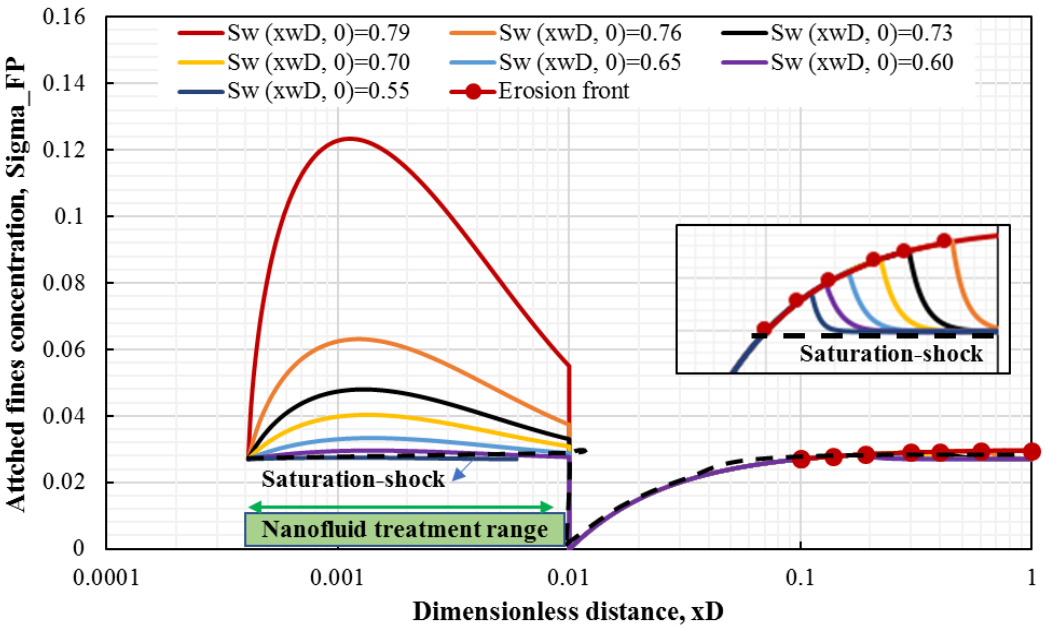
Figure 4.27 Time-distance diagram indicating the propagation of different water saturation waves (with nanofluids in two-phase flow)
(Black dash-line: water saturation shock. Red dash-line: erosion front)



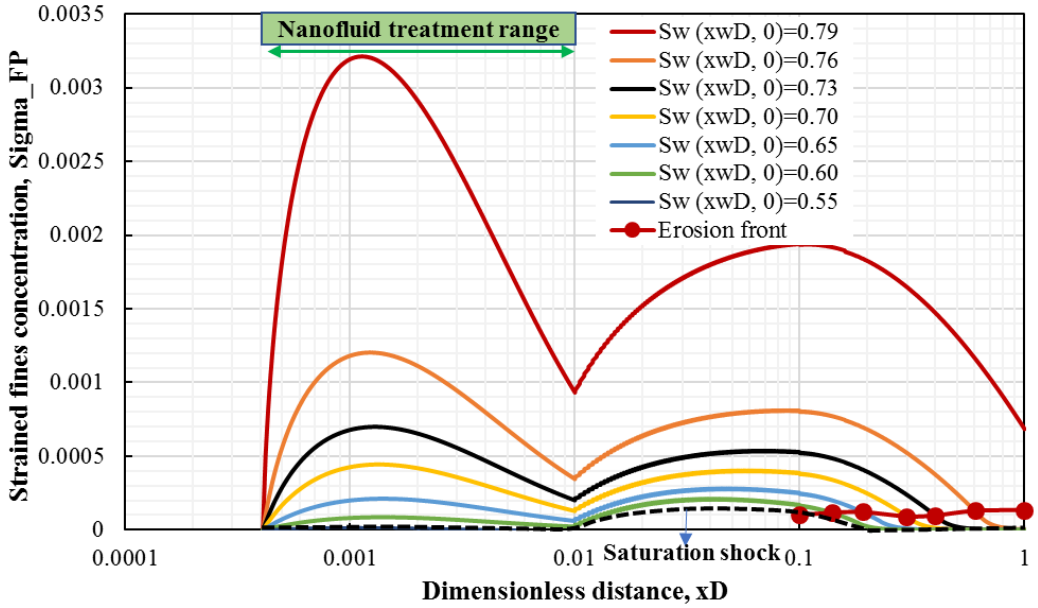
a. The variation of water saturation along the characteristic lines in Figure 4.27



b. The variation of suspended fines along the characteristic lines in Figure 4.27



c. The variation of attached fines along the characteristic lines in Figure 4.27



d. The variation of strained fines along the characteristic lines in Figure 4.27

Figure 4.28 The variation of water saturation, suspended fines, attached fines and strained fines concentration along different characteristic lines

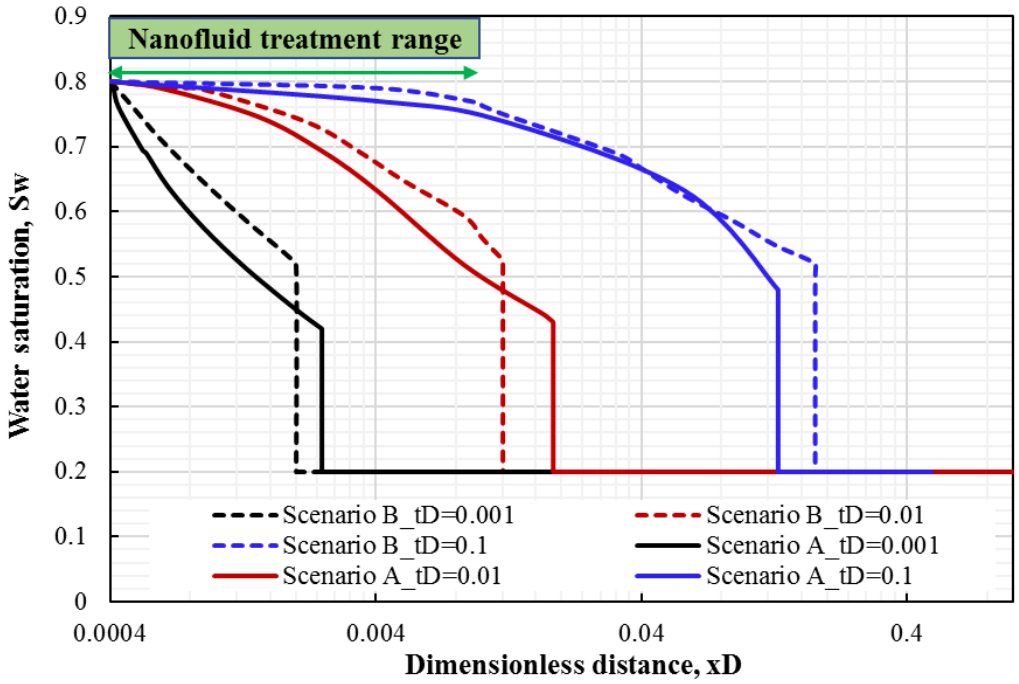


Figure 4.29 Distributions of water saturation in the radial flow system at different time for both cases with and without nanofluid treatment

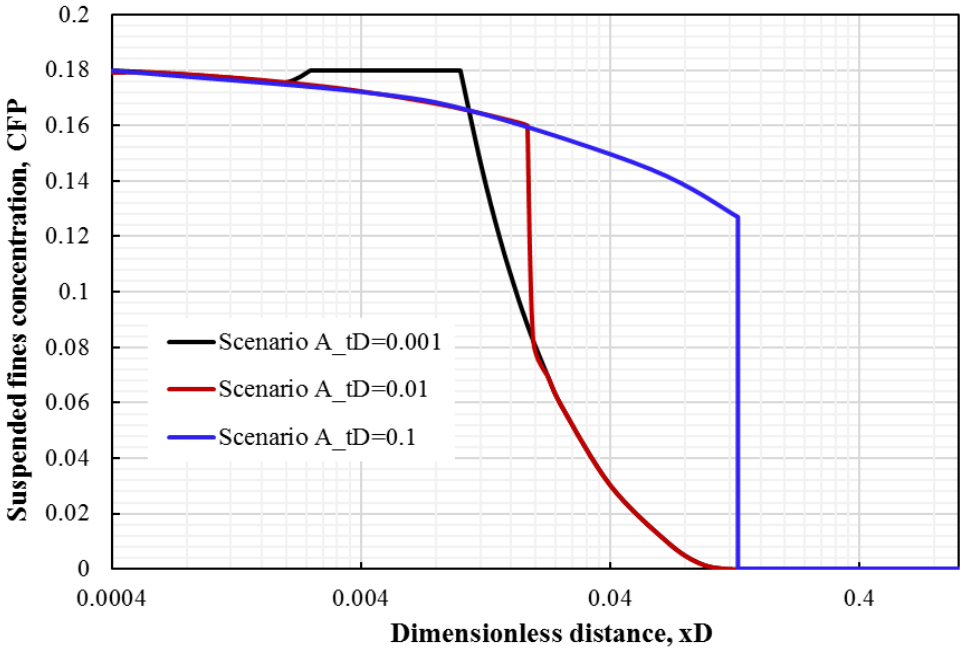
Figure 4.29 presents the comparison of water saturation profile in the radial flow system between scenario A without nanofluid and scenario B with nanofluid to control fines migration. By comparing Figure 4.29 with Figure 4.25, the usage of nanofluids can slow down the movement of injected fluid through enhancing attachment of mobile fines within the range of nanofluid treatment, and hence preventing the mobile fines moving further. However, in the remote region with slower velocity, the water-saturation shock of scenario B with nanofluid treatment surpasses that of scenario A. This finding can be explained by the attenuation of fines attachment and straining effects caused by the decreases of mobile fines after the injected fluids has passed through the nanofluid-treated region. Consequently, the decrease of fines attachment and straining effects mitigates the impairment of water-phase relative permeability. As results, after nanofluid treatment,

the movement of water saturation shock in regions close to the outlet overtakes that of the case without nanofluids.

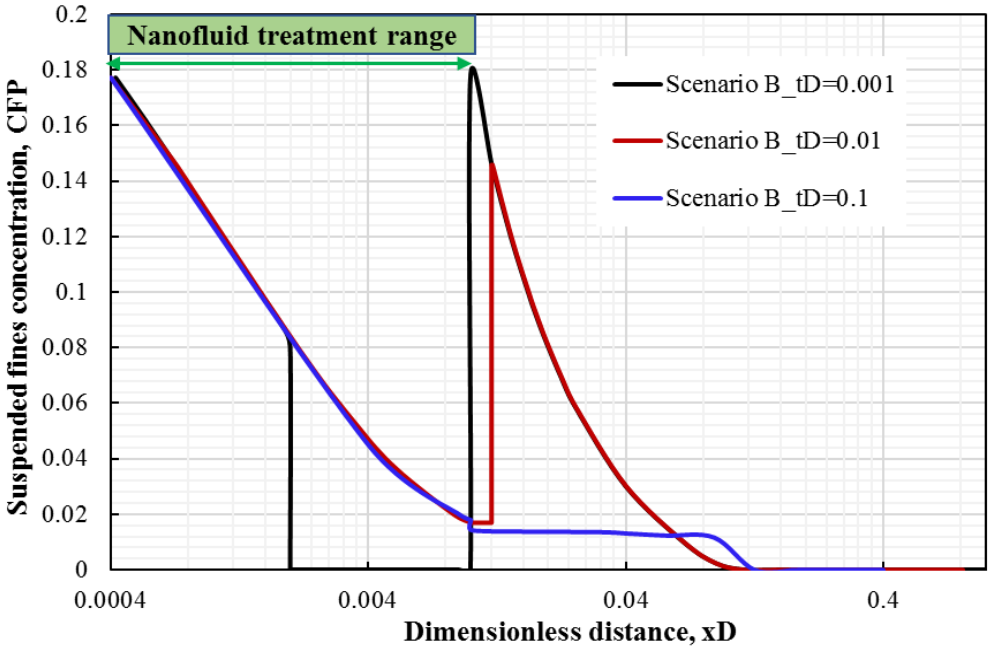
Th effects of nanofluid to control fines migration are indicated by Figure 4.30, Figure 4.31, and Figure 4.32. In Figure 4.30, because of nanofluid treatment within the range of 0.01 near the injection end, the amounts of suspended fines decrease significantly. Especially, by comparing Figure 4.30 a and Figure 4.30b, within the range of 0.01, the steady-state (no changes of values with time) the concentration of suspended fines is less than that of case without nanofluids. Figure 4.31 a and b indicate the different performance of fines attachment at different time for cases with and without nanofluid treatment. Attributed to the contributions of nanofluid, the attachment of fines within the range of nanofluid treatment is enhanced very significantly. However, in the case without nanofluid treatment, no fines can be attached onto rock grains because of the higher flowing velocity near the injection end. In addition, as shown in Figure 4.32, because there are more amounts of fines to be attached onto rock grains after nanofluid treatment, thus, the amounts of strained fines decrease. In view of the stronger formation damage effects of fines straining than that of fines attachment, formation damage can be significantly mitigated by nanofluid treatment to reduce fines straining.

After the distributions of strained fines and attached fines concentration in the radial flow system have been determined at different time, integrating the equation of pressure gradient in Eq. 4.25 can result in the changes of injection pressure drop as the two-phase fines suspension flow continues.

$$\Delta p = \frac{q}{4\pi k_0}\int_{x_{Dw}}^{1} \frac{1}{x_D\left(\dfrac{k_{rw}}{\left(1+\phi\beta_a S_a+\phi\beta_s S_s\right)\mu_w}+\dfrac{k_{ro}}{\mu_o}\right)}dx_D \quad \text{..... (4.94)}$$

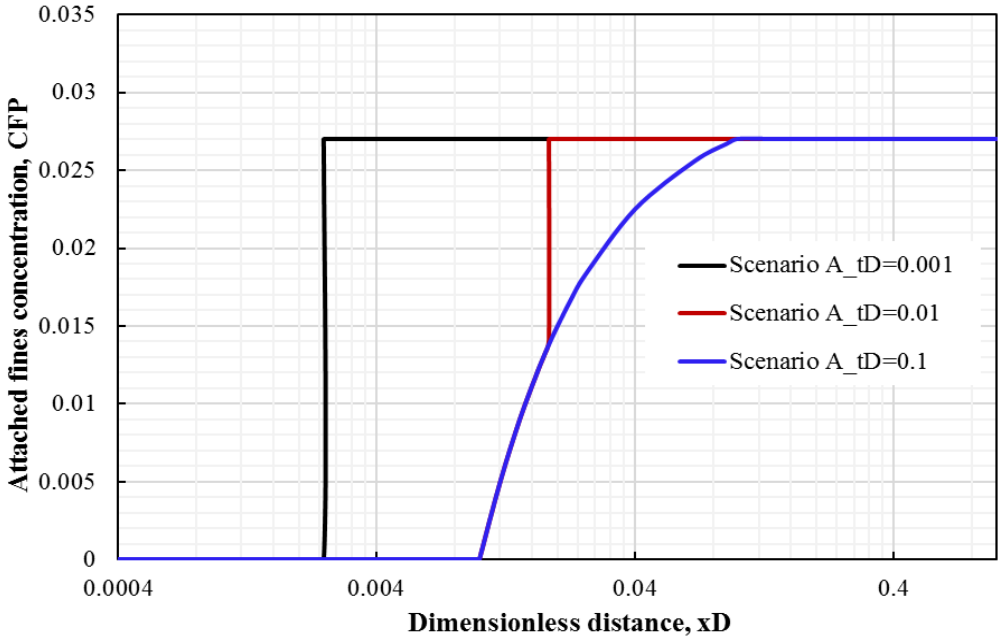


a. The distribution profile of suspended fines in the radial system for case without nanofluid retreatment

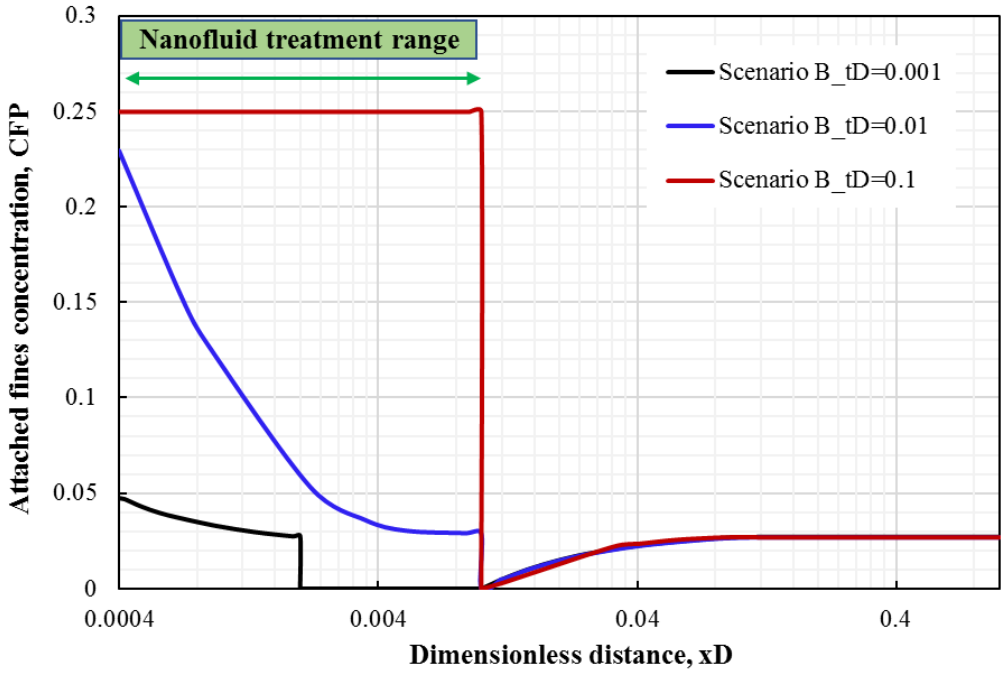


b. The distribution profile of suspended fines in the radial system for case with nanofluid retreatment range as 0.01

Figure 4.30 Distributions of suspended fines concentration in the radial flow system at different time for both cases with and without nanofluid treatment



a. The distribution profile of attached fines in the radial system for case without nanofluid retreatment



b. The distribution profile of attached fines in the radial system for case with nanofluid retreatment range as 0.01

Figure 4.31 Distributions of attached fines concentration in the radial flow system at different time for both cases with and without nanofluid treatment

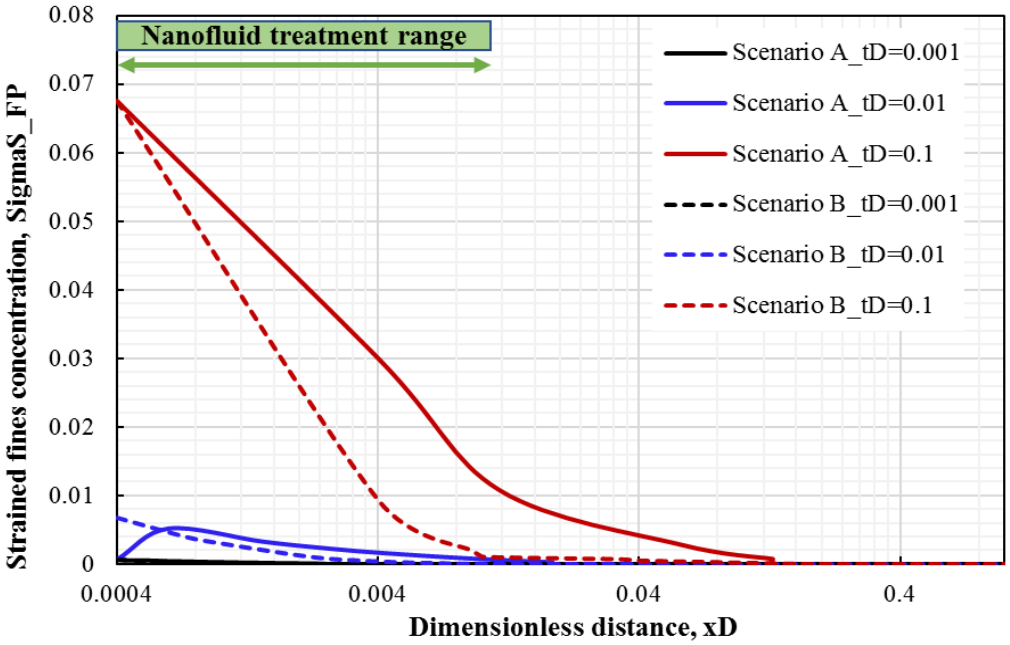


Figure 4.32 Distributions of strained fines concentration in the radial flow system at different time for both cases with and without nanofluid treatment

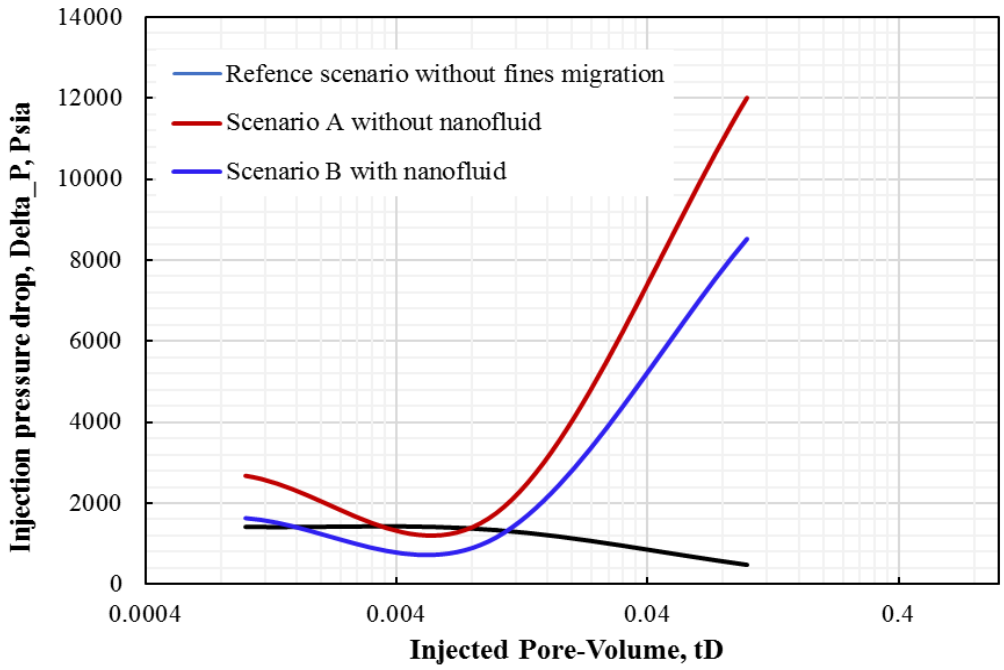


Figure 4.33 Comparison of injection pressure drop changes for two scenarios with and without nanofluid to control fines migration in two-phase radial flow

Figure 4.33 presents the comparison of injection pressure drop among three cases, they are, reference scenarios without fines migration, scenario A with fines migration but without nonfluid treatment, and scenario B with nanofluid to control fines migration in two-phase radial flow. The effects of fines migration and associated fines attachment and straining can bring significant formation damage, which is characterized by the increase of injection pressure drop as the injection continues. The existence of nanofluids can help mitigating the formation damage caused by fines migration. As the injection of fines suspension continues with constant rates, the positive effects of nanofluid to mitigate fines migration mitigate the increase of injection pressure drop.

All above analysis reflects the positive effects of nanofluid treatment to control the movement of fine particles in two-phase flow.

4.4 Conclusions and Summary

This chapter provides the exact solutions of two different nanoparticles utilization to control fines migration in two-phase flow, including 1) co-injection of nanoparticle-fine particles mixture into 1-D permeable medium that initially oversaturated with fine particles and 2) pre-coating /pre-treatment with nanoparticles prior to fines injection in radial flow system. The main conclusions and contributions are listed as below:

- The application of splitting method for the 3×3 system of nanoparticles-fine particles transport in two-phase flow results in a 2×2 subsystem of nanoparticles-fines transport and lifting equation of water phase.

- The procedure to solve the problem of fines-nanoparticles transport in two-phase flow includes 1) analytical solutions of both auxiliary system and lifting system, and 2) inversion of solution by transforming the coordinates.

- The utilization of nanoparticles can bring more fines attachment, as results, further decrease the flow capacity of water phase. The positive contributions of nanoparticles to enhance oil recovery of waterflooding are confirmed by the formulation of a “oil-bank”. The increase of water-cut can also be controlled significantly by nanofluid utilization.

- The composition paths between nanoparticles and fines concentration in single-phase water flow are different from that in two-phase (oil & water) flow. In other words, to mitigate the same amounts of mobile fines in porous medium, less amounts of nanoparticles are required for the case in single-phase water flow. However, the reduction efficiency of nanofluid in single-phase flow is similar to that in two-phase flow case while considering the differences of injected nanoparticles concentration.

- In two-phase radial flow system, the effects of fines migration (fines attachment, fines straining and fines suspension) can slow down the movement of injected water significantly. The values of front-saturation along the water-saturation shock decrease. This can be attributed the attenuation of fines migration in radial flow system where the slower velocity occurs in remote region from the injection end.

- In the remote region from the injection end with slower velocity, the movement of injected water surpasses that of scenario without nanofluid treatment. This can be explained by the attenuation of fines attachment and straining caused by the decrease of mobile fines after passing through the nanofluid-treated region.

- The phenomena of fines migration and associated fines attachment and straining can bring significant formation damage, which is characterized by the increase of injection pressure drop, as the injection continues. The existence of nanofluid help mitigating the increase trend of injection pressure drop caused by fines migration.

4.5 Nomenclature

C_{FP} = Volumetric concentration of fine particles with respect to pore volume, m^3/m^3

$C_{FP,inj}$ = Volumetric concentration of injected fines with respect to pore volume, 0.18 m^3/m^3

C_{NP} = Volumetric concentration of nanoparticles with respect to pore volume, 0.18 m^3/m^3

f_w = Fractional flow function

S_w = Water saturation, decimal

S_{wc} = Connate water saturation, decimal

S_{or} = Residual oil saturation, decimal

β_a = Formation damage coefficient of fines attachment, 5

β_s = Formation damage coefficient of fines straining, 1000

k_0 = Intrinsic permeability of sand pack, 400mD

k_{rw} = Relative permeability of water phase

k_{ro} = Relative permeability of oil phase

r_e = Radius of reservoir boundary, 0.5m

r_w = Wellbore radius, 0.01m

q = Well injection rate per formation height, 0.00054 m^2/s

U = Fluid velocity, m/s

U_m = The maximum flowing velocity to retain fines, m/s

U_i = Flowing velocity in the example, m/s

μ_w = Water viscosity, Pa.s

μ_o = Oil viscosity, Pa.s

ϕ = Porosity of sand pack, 0.15

x_D = Dimensionless distance

φ = Stream-function, as independent variable

t_D = Dimensionless time or injected numbers of pore volume

σ_s = Strained retention concentration of fine particles

σ_a = Volumetric concentration of retained fine particles with respect to bulk volume

$\sigma_{cr,\max}$ = Maximum retention concentration of fines onto rock grains

Δp = Pressure drop along the porous media, Pa

Chapter 5: Combined Nanofluids with Low-Salinity Waterflooding

5.1 Problem Statement and Assumption

Low-salinity waterflooding (LSW) has been justified as a very promising EOR method (i.e., improving oil recovery by 5-38%, compared to conventional, high-salinity water flooding) in numerous experimental studies and field trials for both tertiary (residual oil) and secondary (initial water condition) modes of water flooding (Bernad 1967; Tripathi et al. 2007; Hourshad et al. 2012 and Behruz et al. 2013). The physical mechanisms of lower salinity water to enhance oil recovery have been extensively investigated during the past decades. The summary of those diverse mechanisms behind low salinity effects include the following: 1) wettability alteration toward more water-wet conditions by releasing original mixed-wet particles (Tang et al. 1999; Alagic et al. 2010; and Skauge 2008); 2) reduction of interfacial tension due to mineral dissolution and ion-exchange reactions (McGuire et al. 2005 and Lager et al. 2006); 3) reduction of residual oil by multi-component ionic exchange among crude oil, connate brine and clay particles (Sorbie et al. 2010); and 4) local pH increase at water-clay interface to desorb organic materials from pore surfaces (Austad et al. 2008; Aksulu et al. 2012). Despite the extensive previous investigations of low salinity water flooding, i.e., the alterations of rock wettability, fluid relative permeability, and residual oil saturation (all of which bring positive effects on oil recoveries), no single mechanism has been a widely conclusive form in either experiments or field trials. (Boussour et al. 2009; Behruz et al. 2013).

However, the problem of fines migration induced by chemical environments of low-salinity fluid has aroused great debates. Accompanying the above interpreted EOR mechanisms associated with LSWF (Aksulu et al. 2012), fines migration may carry small

amount of residual oil by the detachment of oil-coated particles from rock grains, which improve the displacement efficiency (Bernard, 1967). In addition, the reduction of local water-phase effective permeability in water-swept areas caused by the blockage of high permeability layers provides a simple mobility-control method to enhance the sweep efficiency (Lemon, 2011; Zeinijahromi, 2011, 2012, 2013). However, fines migration and their size exclusion effects can also result in severe damage to reservoir permeability near wells causing the decline of well injectivity (productivity in case of production well), which leads to the understanding of avoiding fines migration in reservoirs. During low salinity water flooding, the majority of pressure loss is attributed to the tremendously large flow within the vicinity of wells. Therefore, evoking the debates between the pros and cons of fines migration, it is desirable to control fines migration to take advantages of its positive effects far from the wellbore and minimize its weaknesses near wellbore. The best strategy to avoid fines migration is to keep them stagnant at their original location/sources through either limiting flow rate (less than the critical rates) or somehow settling them.

It has been shown that nanoparticles can effectively enhance attractive forces between fine particles and grain surfaces through changing the surface zeta potentials of fine particles, and significantly mitigating formation damage caused by fine particles and clogging pore-throats (Huang, 2008b; Ju, 2006). In practice, this chapter not only provides an analytical model to confirm the feasibility of nanoparticle application to reduce fines migration, but also presents improvement analysis of LSW flooding performance with nanoparticles application.

The aim of this study includes the following: 1) evaluate the mutual interactions among nanofluid, fines and low-salinity waterflooding performance; 2) extend the mathematical foundation toward designing nanofluid-slug pre-flush to enhance well injectivity while keeping the mobility-control assisted by fines migration to improve low-salinity waterflooding performance (both EOR and well injectivity) in multi-layered heterogeneous reservoirs; and 3) the comparisons between new derived semi-analytical solutions and finite-different numerical simulation.

The detachment of fines can enhance displacement efficiency by reducing the residual oil saturation, and the blockages of released fines in already-swept zones improve the volumetric sweep efficiency by impairing the relative permeability of water phase. However, well injectivity is also impaired significantly due to the loss of water effective permeability near wells caused by fines migration. Our study aims to deliver analytical solutions to evaluate the mutual interactions among nanofluid, fines and low -salinity water. Several assumptions commonly used for fractional flow function and suspension flow theory are itemized as (Lake 1989; Moghanloo 2010 and 2015; Yuan et al. 2016c).

- Two-layered, uniform, and areal homogeneous medium and local thermodynamic equilibrium assumption applies; each layer has its own petrophysical and fluid properties, i.e., porosity, permeability, relative permeability, residual oil saturation and initial conditions. It is further assumed that the layers have no cross-flow communications in the vertical direction.

- Four-components exist (water, oil, nanoparticles, and fine particles) and three-phase (two flowing (oil/water) and one stagnant solid phase) isothermal flow takes place;

No volume changes occur in aqueous phase upon particles mixing, detachment and straining effects.

- All fluids and solids are incompressible. Gravity of fluids (oil/water) are neglected; the effects of viscous force dominates, and capillary force is implicit in the relative permeability curve.
- Langmuir isotherm adsorption of nanoparticles is assumed to provide an asymptotical adsorption capacity when time tends to infinite. The changes of porosity and permeability caused by small-sized nanoparticles adsorption are neglected.
- Flow velocity is sufficiently large to neglect the dispersion flow effects; Darcy's flow law is applied; therefore, hyperbolic conservation equations are obtained.
- During low salinity water flooding (LSWF), the detachment of fines can be attributed to the changes of maximum retention concentration of fines onto rock grains.
- Nanoparticles with lower surface potential are adsorbed on the pore surfaces or mobile fines, thereby, enhancing the maximum attachment concentration of fine particles, but cannot modify the attachment rates of particles onto rock grains.
- The instant straining of particles is assumed after fine particles are detached from the pore surfaces, i.e., the strained fines concentration is equal to the reduction of maximum retention concentrations of fine particles caused by changes of water composition and flow velocity.
- The fractional flow function depends on both phase saturation and straining/plugging of pore-throats by fines. Ignore the changes of residual oil saturation caused by low salinity water, but only focus on the improvement of mobility control induced by fines migration.

5.2 Nanofluid Improve Performance of Low-Salinity Waterflooding

5.2.1 Maximum Retention Concentration in Two-phase Flow

As the injection of low-salinity water continues, the changes of flowing fluid properties (i.e., fluid salinity, fluid density, and flow velocity etc.) will affect the torque balance among the types of mechanical forces on fines deposited onto pore-surfaces. The forces acting on a single particle located on the rock grain surfaces (pore walls) are: the drag force F_d from viscous water flow, the electrostatic force F_e, the lifting force F_l, and the buoyancy F_g, (Fig. 1). The mechanical equilibrium posed on fines define a critical value for fines deposition, which is named as the maximum retention concentration. The maximum retention concentration of particles in single-phase water flow has been developed by Bedrikovetsky (2011) and Yuan (2015b) in different types of porous medium. However, during low-salinity waterflooding, water saturation is dynamically changing but not keeping constant, which makes the maximum retention concentration model in single-phase not applicable for two-phase flow scenarios. In view of water-wet fine particles can only be dissolved in water phase, and thus, the effective drag force on fines is controlled by the flowing velocity of water phase. Considering the velocity difference between water phase and oil phase, the water-cut is introduced into the drag and lifting force exerted on fines particles. As results, the maximum retention concentration of fine particles in two-phase flow is introduced as follows.

The modified formulation of drag and lifting forces in Eq. 2.1 and Eq. 2.3 by introducing the fraction flow of water phase can be expressed as,

Drag force: $$F_d = \frac{\omega \pi \mu_w r_{FP}^{\ 2} q f_w}{4\pi\phi(r_P - r_C)r} \quad \text{..... (5.1)}$$

Lifting force: $F_l = \chi r_{FP}^{\ 3} \sqrt{\dfrac{\rho\mu\left(\dfrac{qf_w}{2\pi r}\right)^3}{8\phi^3(r_P - r_C)^3}}$ ……..……... (5.2)

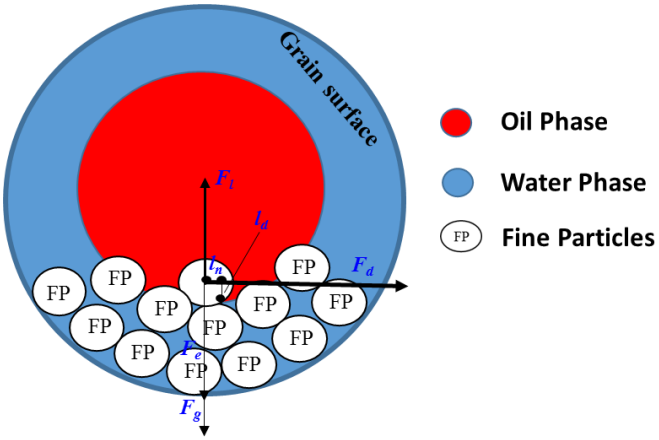


Figure 5.1 Forces and momentum vectors exerted on fines in water-oil flow

The injection of low-salinity water would bring changes of the chemical environment in porous media. During low-salinity waterflooding, the injected low-salinity fluid would gradually sweep out the reservoir fluids with higher salinity. In the environment of lower salinity, where smaller amounts of ions exist. Thus, according to Debye-Huckel theory, the Deby-length (Double layer thickness in Gouy-Chapman theory) (Eq. 5.3) increases; As results, the repulsive energy among particles increase, and the bonding force among particles attenuates. Therefore, the effects of fluid salinity can be reflected by changes of the inverse Debye-length, κ, m^{-1} (Elimelech et al. 1995).

$$\kappa = 0.73\times10^{11}\sqrt{\sum\left|\frac{C_{mi,initial}S_{wc} + C_{mi,injected}\left(S_w - S_{wc}\right)}{S_w}\right| z_i^{\ 2}} \quad \text{……..…. (5.3)}$$

where, C_{mi} is the molar i^{th} ion concentration in water phase (injected and initial conditions), moles/m^3; $Z_i$is a valence of i^{th} ion. As the saturation of injected low salinity

water increases, the inverse Debye-length would decrease; thereby, the electrostatic repulsive force would increase, as shown in Eq. 5.4.

$$V_{DLR} = \frac{128\pi r_{FP} n_{\infty} k_B T}{\kappa^2} \varsigma_{FP} \varsigma_{GS} e^{-\kappa h} \quad \text{..... (5.4)}$$

As low-salinity water saturation increases, the particles surface-surface distance, *h*, would also increase from the minimum value to some distance where the electrostatic force reaches minimum, where the detachment of fines from pore surfaces starts. The detachment condition is determined by which the detachment force torque exceeds the maximum torque of the attachment force torque at the maximum particles separation distance, as shown in Eq. 2.11. The maximum particles separation distance can be determined by which the second-derivative of total energy (Eq. 2.5) become zero. Figure 5.2 presents the impacts of water salinity on the particles separation distance, *h*. With the decrease of fluid salinity, the particles separation distance would increase, as results, the bonding force among particles would decrease. The smaller the particles separation distance is, the stronger the particles bonds with each other. When the particles separation distance is sufficiently small, flocculation will occur.

Therefore, it is through the increase of electric repulsive force that low-salinity water affects the maximum retention concentration (Eq. 2.11). In addition, for individual cylindrical shaped pores, in water-oil two phase flow, the maximum retention concentration of fine particles onto rock grains in two-phase flow is expressed as:

$$\sigma_{cr}(S_w, r) = \left[1 - \left(\frac{\mu_w r_{FP}^2 \frac{q f_w}{2\pi r}}{2\phi S_w r_P F_e y} \right)^2 \right] \phi S_w (1 - \phi_c) \quad \text{..... (5.5)}$$

y is the ratio between drag and electrostatic force and can be obtained numerically by solving the following equation:

$$1+\frac{4\pi r_{FP}^{\ 3}}{3F_e}\Delta\rho g-\frac{\chi\sqrt{\rho F_e}}{\mu_w}y^{3/2}-\sqrt{3}\omega\pi y=0 \quad \cdots\cdots\cdots\

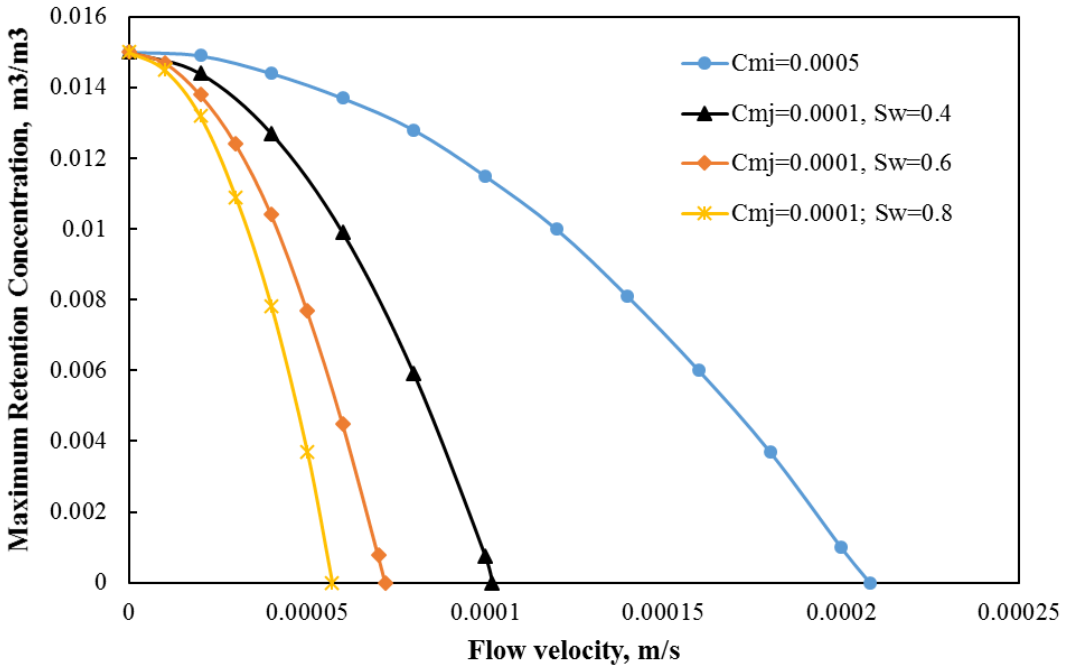


Figure 5.3 The effects of low-salinity water saturation on the maximum retention concentration of fine particles onto rock grains

5.2.2 Fractional Flow Function Considering Particles Straining

The formation damage coefficient of fines straining is much greater than that of fines attachment, i.e., the detachment/attachment of fines only leads to small changes of permeability, while the straining/plugging of pore-throats bring more significant damage of permeability. Here, in this section, only the effects of fines straining are incorporated into the retardation term in fractional flow function.

$$f_w\left(S_w,\sigma_s\right)=\left(1+\frac{K_{ro}\mu_w\left(1+\beta\sigma_s\right)}{K_{rw}\mu_o}\right)^{-1} \quad \text{..... (5.7)}$$

The multiphase flow effects are represented by the relative-permeability function. Different from conventional waterflooding, low-salinity waterflooding can help decreasing residual-oil saturation and enhancing oil recovery as a ternary method.

$$k_{rw} = k_{rw}^{0}\left(\frac{S_w - S_{wc}}{1 - S_{wc} - S_{or}}\right)^{n_w}$$
$$k_{ro} = k_{ro}^{0}\left(\frac{S_o - S_{or}}{1 - S_{wc} - S_{or}}\right)^{n_0} \quad \text{..... (5.8)}$$

Hereby, as per the assumptions of an instant straining of those detached fines, the concentration of strained particles is equal to the detached fine particles concentration (subtracts the maximum retention concentration of fine particles from the initial attached fines concentration at different condition of low-salinity water saturation).

Substituting Eq. 5.5 into Eq.5.7, a new formula of fractional flow equation considering fines migration during low-salinity waterflooding is introduced as,

$$f_w\left(S_w, x_D\right) = \left(1 + \frac{K_{ro}\mu_w\left(1 + \beta\left(\sigma_{cr,initial}\left(0, S_{wc}\right) - \left[1 - \left(\frac{\mu_w r_{FP}^2 q f_w}{4\pi\phi r_P F_e y}\right)^2 \frac{1}{x_D r_e^2}\right]\phi\left(1 - \phi_c\right)\right)\right)}{K_{rw}\mu_o}\right)^{-1} \quad (5.9)$$

where, x_D is dimensionless distance; t_D is dimensionless time or injected pore-volume;

$$x_D = \left(\frac{r}{r_e}\right)^2 \;;\; t_D = \frac{qt}{\phi\pi r_e^2}$$

Eq.5.9 is an implicit equation about water cut, f_w. An iteration algorithm is necessary to calculate the fraction flow versus water saturation at different radial locations, as shown in Figure 5.4. At the locations close to the injection well, the fractional flow curves show downward, which means the decrease of water-cut because of fines migration only in water-phase. In addition, the flood-front water saturation obtained by Welge method (Welge 1952) increases, which is caused by the attenuation of fines migration with the

increase of distance away from the injection well. A detailed explanation of fines migration affecting on the performance of low-salinity waterflooding is discussed later.

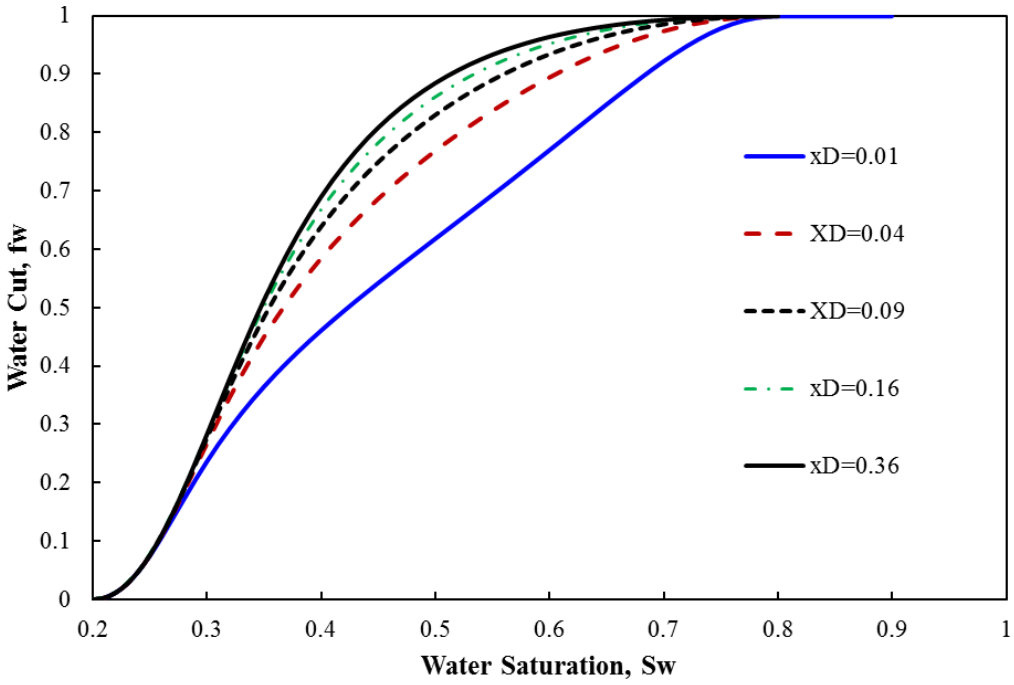


Figure 5.4 Comparisons of fractional flow curves at different distances from injection wells considering the effects of fines straining

5.2.3 Mechanistic Assumption of Nanoparticles to Control Fines Migration

During low-salinity waterflooding, especially in many unconsolidated reservoirs, the induced fines migration leads to the blockages of flow paths. In addition, as shown in Figure 5.5, the majority of pressure loss occurs in the vicinity of wells for a radial flow system. The larger flow velocity near injection well leads to more amounts of fines detachment and migration, as results, which would exaggerate the pressure loss in the regions near vertical wells. To prevent the negative effects of low-salinity waterflooding, as indicated in chapter 3 and chapter 4, the pre-treatment with nanofluid slugs prior to

low-salinity water injection is proposed as an effective remediation to fixate the injected or formation fines induced by low-salinity water at their original locations.

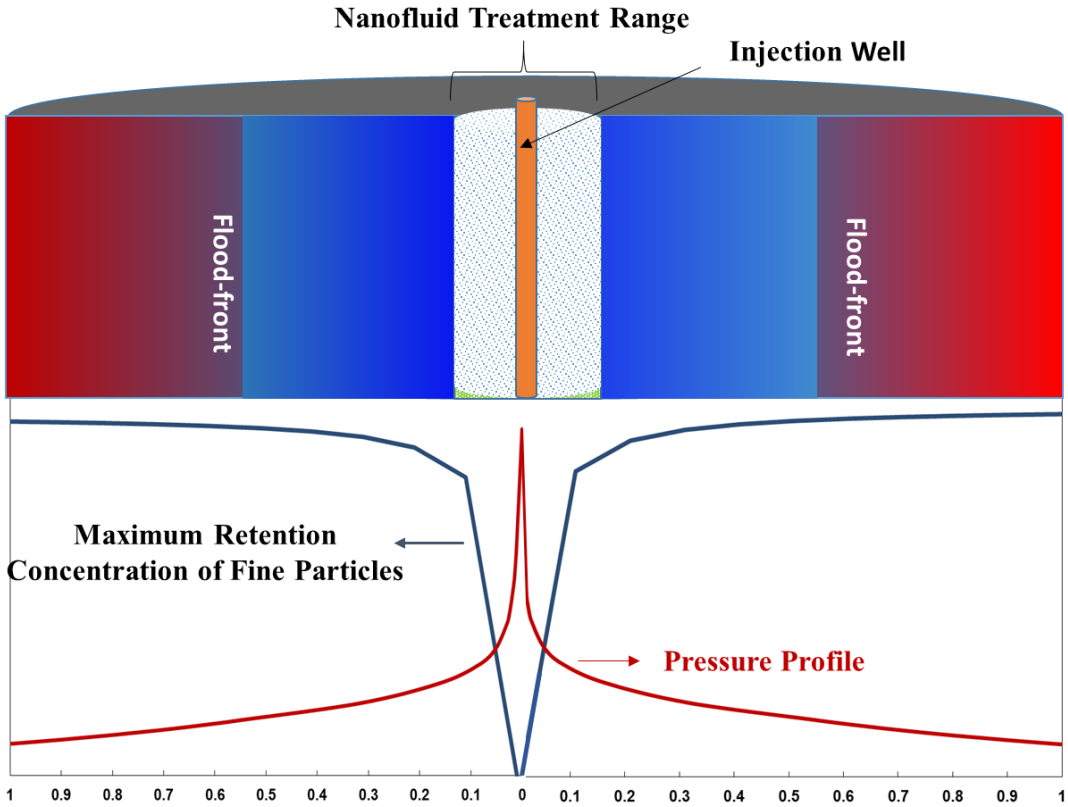


Figure 5.5 Schematic profile of nanofluid pretreatment, pressure drop, phase saturation, and maximum retention concentration of fines in radial flow

5.2.4 Governing Equations and Semi-Analytical Solutions

Inferred from the assumptions of nanoparticles effects in Eq. 3.1, the double-layer repulsive force between fine particles and rock grains is a function of nanoparticles adsorption concentration onto fines. Nanoparticles with very small surface potential leads to the decrease of repulsive forces between fine particles and rock grains. Thereby, the maximum retention concentration of fine particles is enhanced, as shown in Eq. 3.2.

The mass-balance equation of fine particles and water flowing by considering the detachment and straining effects of fine particles can be written as (pseudo-two-phase: water (solids only exist in water phase)/oil; three-component: water/oil/fines):

$$\begin{cases} \dfrac{\partial S_{wi}}{\partial t_D} + \left(\dfrac{\partial f_{wi}}{\partial S_{wi}}\right)_{x_D} \dfrac{\partial S_{wi}}{\partial x_D} + \left(\dfrac{\partial f_{wi}}{\partial x_D}\right)_{S\,wi} = 0 \\ \dfrac{q}{4\pi x_D} = \dfrac{k_0}{1+\beta\sigma_s}\left(\dfrac{k_{rw}}{\mu_w} + \dfrac{k_{ro}}{\mu_o}\right)\dfrac{\partial p}{\partial x_D} \end{cases} \quad \text{..... (5.10)}$$

The initial conditions and boundary (inlet) conditions are defined as:

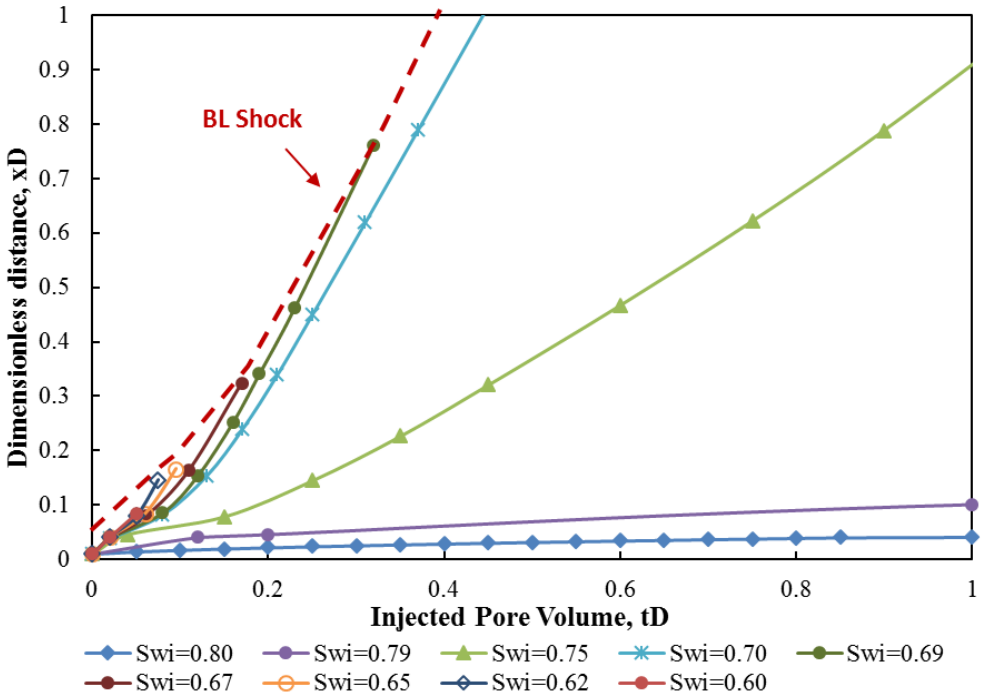
$$\sigma_a(r,0) = \sigma_{cr,initial}(U,\ S_{wc});\ \ \sigma_s(r,0) = \sigma_{cr,initial}(0,\ S_{wc}) - \sigma_{cr,initial}(U,\ S_{wc});\qquad S_w = S_{wc}$$
$$\sigma_a(0,t) = \sigma_{cr,initial}(U,\ 1\text{-}S_{or});\ \ \sigma_s(0,t) = \sigma_{cr,initial}(0,\ S_{wc}) - \sigma_{cr,initial}(U,\ 1\text{-}S_{or});\quad S_w = 1$$

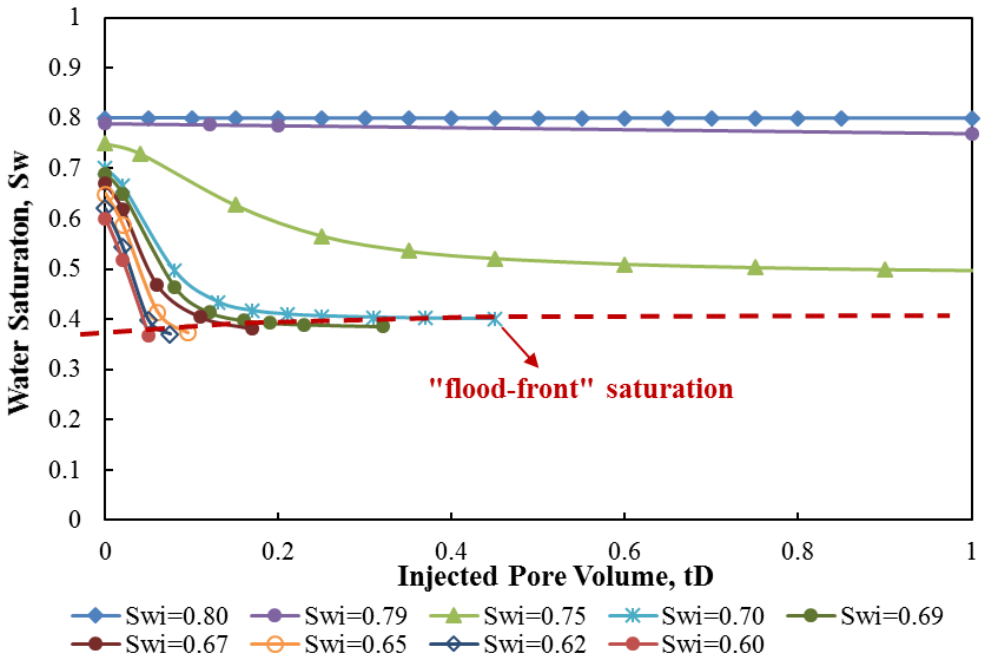
The above system is a problem of first-order quasi-linear partial differential equations. Method of Characteristic (MOC) is applied to solve this problem. Inferred from Eq.5.10, the characteristic directions and the variations of water saturation along the characteristic lines are expressed as,

$$\frac{dx_D}{dt_D} = \left(\frac{\partial f_{wi}}{\partial S_w}\right)_{x_D};\quad \frac{dS_{wi}}{dt_D} = \left(\frac{\partial f_{wi}}{\partial x_D}\right)_{S_w i} \quad \text{.....(5.11)}$$

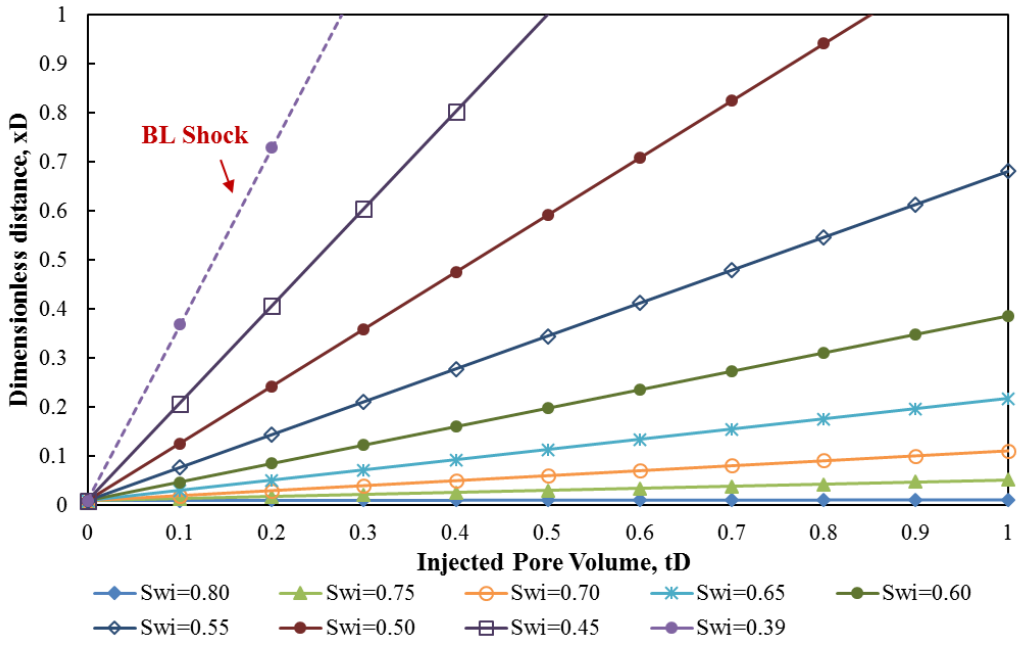
By combining with fraction flow function (Eq. 5.9), the slopes of characteristic lines, and along which the changes of water saturation can be evaluated using a computer code. As shown in Figure 5.6, the effects of fines migration cause low-salinity waterflooding significantly different from conventional water flooding (with no changes of fluid salinity) as a classical Buckley-Leverett problem. As for the conventional waterflooding case (Figure.5.6b), the characteristic lines of different water saturation waves are always straight (characteristic velocity of specific water-saturation wave is constant, and along the characteristic lines there are no changes of water saturation). However, in the presence of fines migration, the classic Buckley-Leverett waterflooding theory needs to be

modified. The characteristic lines are no longer straight, and along which water saturation also would not keep constant.





(a) Low-salinity waterflooding cases considering fines migration effects (Modified Buckley-Leverett Problem)



(b) Conventional waterflooding cases (Buckley-Leverett Problem)

Figure 5.6 Comparison of analytical solutions (Distance-time diagram and composition variation along characteristic lines) between low-salinity waterflooding and conventional waterflooding cases considering fines migration

To obtain water saturation distribution in radial flow system and water-cut history at the outlet, etc., firstly, draw vertical lines with constant injected pore-volume (for example, t_D=0.2) passing those paths of water-saturation waves in the distance-time diagram (first of Figure 5.6a). The values of vertical axis (dimensionless distance, x_D) of those intersected points are found out. Afterwards, water saturation distribution can be read out from the points where different lines of specific time intersecting with the characteristic lines (second of Fig.5.6a). The comparisons of water saturation distribution between conventional waterflooding and low-salinity waterflooding at the same injected pore-volume (0.2) are shown in Figure5.7. It indicates that the effects of fines migration on decreasing the effective water-phase permeability (Eq.16) can significantly slow down

the movement of flooding water. In other words, the breakthrough of injected water is delayed, and the duration of oil production without water is extended.

Finite-difference method is implemented to calculate the numerical solutions of Eq. 5.10. Backward difference is used to make sure that the solution is unconditionally stable. For each time step, the following finite-difference equations are solved,

$$S_{wii}^{\,n+1} = \left(1 - \left(\frac{\partial f_{wi}}{\partial S_w}\right)_i^{n+1} \frac{\Delta t_D}{\Delta x_D}\right) S_{wii}^{\,n} + \frac{\Delta t_D}{\Delta x_D}\left(\frac{\partial f_{wi}}{\partial S_w}\right)_i^{n+1} S_{wii-1}^{\,n} - \Delta t_D \left(\frac{\partial f_{wi}}{\partial x_D}\right)_i^{n+1} \quad \text{……..……..} \quad (5.12)$$

for grid blocks *i*, where f_w is a function of both S_{wi} (water saturation at grid block i) and dimensionless distance x_D. To obtain more accurate value of f_w in each time step n, a simple-iteration method is employed that f_w is updated via several iterations after saturation is calculated.

The comparison results between the semi-analytic solution and finite-difference numerical solution are presented in Figure 5.7. Due to the inevitable numerical dispersion effects of finite-difference methods, the shape of shock from finite-difference solution spreads. As the interval of grid width decreases, the dispersion effects can decrease. The rarefaction-wave region (downstream behind shock front) of water saturation profile shows an excellent agreement between the analytical solutions and finite-difference numerical simulations.

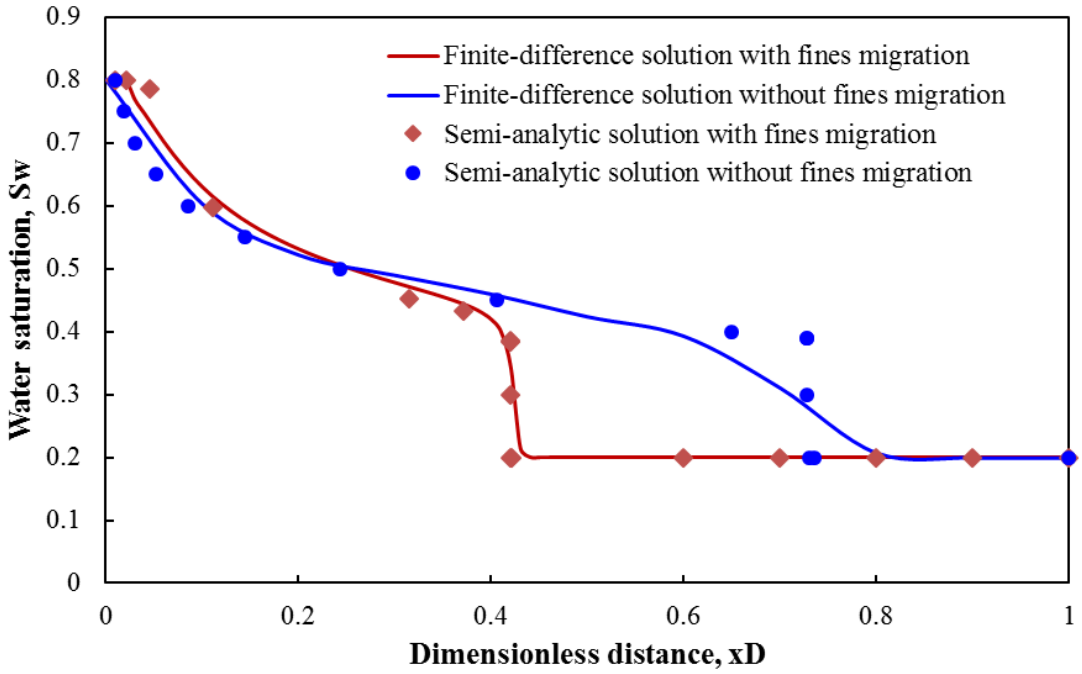


Figure 5.7 Comparison of water saturation profile at the same injected pore-volume (0.2) of conventional waterflooding cases and low-salinity waterflooding cases considering fines migration effects

5.2.5 Effects of Nanofluids Treatment on Low-Salinity Waterflooding

Because of larger flow velocity near wells, more fine particles are prone to be detached from rock grains. Figure 5.8 presents the variation of maximum retention concentration of fine particles with the increase of distance away from the injection wells. Within the near-wellbore region (less than about x_D=0.2, as shown in Figure 5.8), the maximum retention concentrations of fines have a rapid decrease, which exaggerates problem of fines detachment and straining. The blockage of pore-throats the detached fine particles exaggerates the pressure loss. However, beyond this region, there are very small changes of maximum retention of fines. Even with the changes of water saturation, the maximum retention concentration of fines does not change very largely. It does mean

that the problem of in-situ fines detachment and migration is not very severe and even negligible in the remote region away from wells.

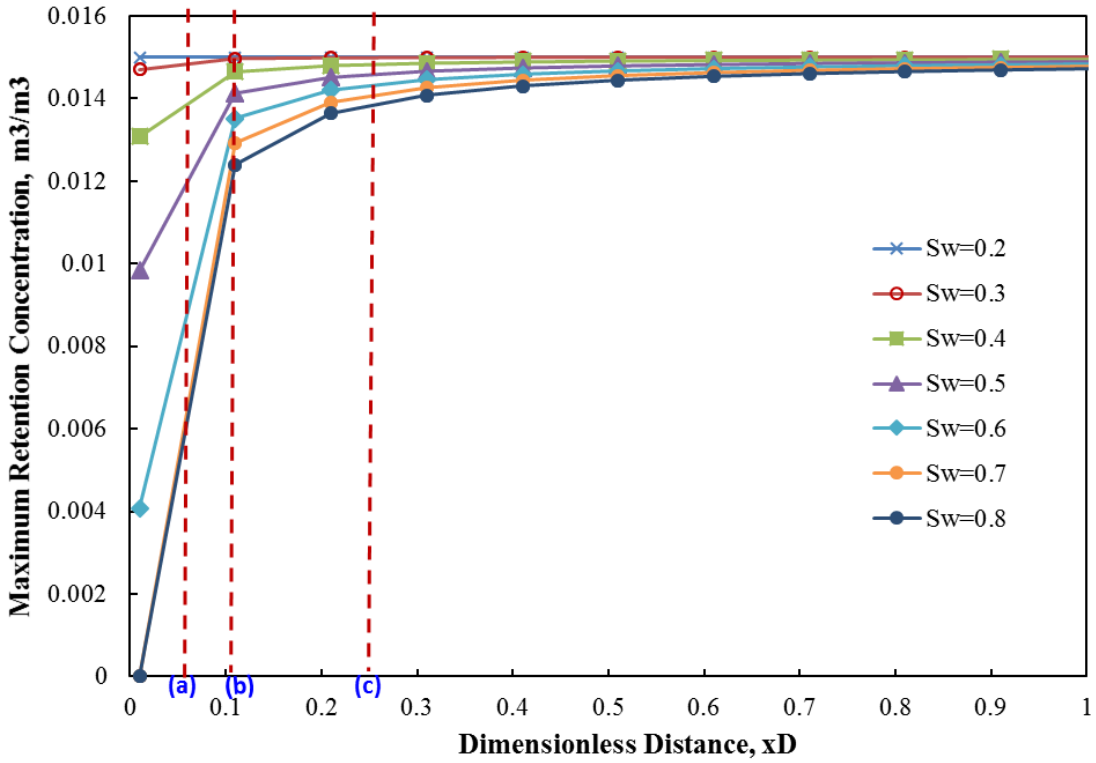


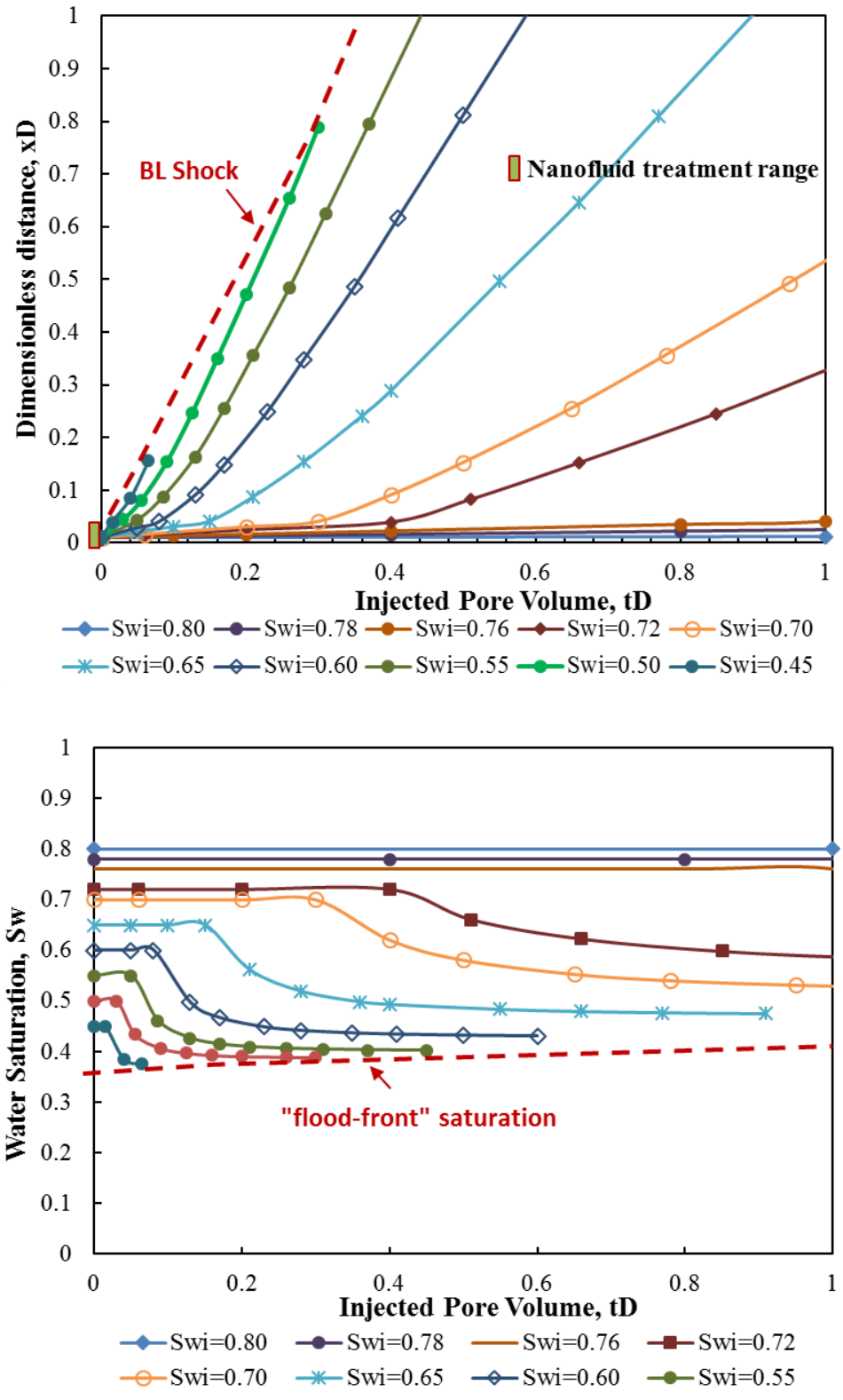
Figure 5.8 Variation of maximum retention concentration of fine particles with the changes of distance from well (in radial coordinate)

Despite the enhanced displacement efficiency (slow moving velocity of injected water front) by fines migration during low-salinity waterflooding, fines migration brings troublesome formation damage (fines straining), and thereby the damage of well injectivity/productivity. In view that the majority of pressure loss occurs in the near-wellbore region, therefore, it is profitable to introduce nanofluid-slug prior to low-salinity water injection to prevent fines moving further. Meanwhile, it is also desirable to keep advantages of fines migration to enhance oil recovery in deep reservoirs. In this section,

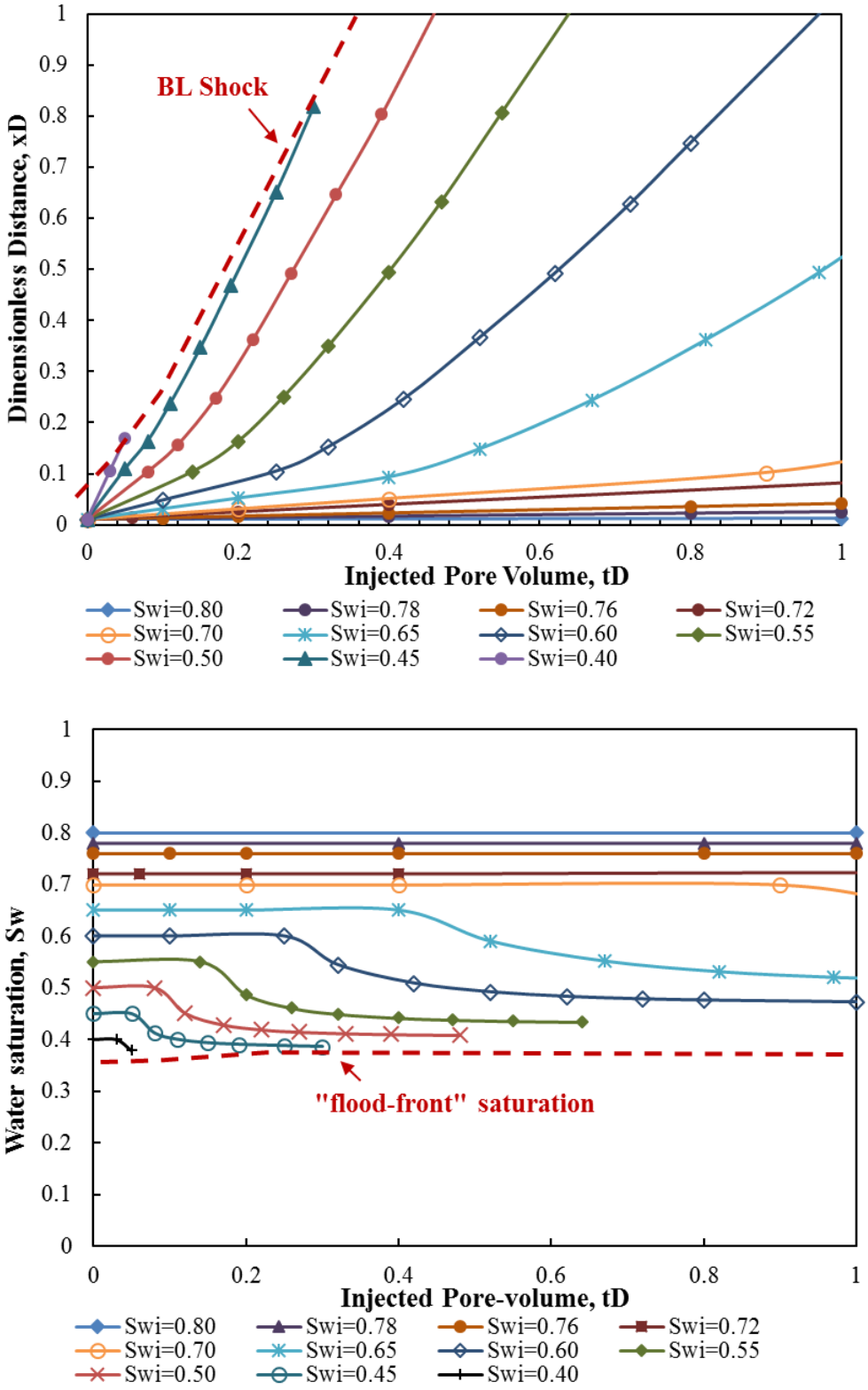
three cases with different nanofluid treatment ranges (0.05, 0.10 and 0.25) are compared to demonstrate the effects of nanofluid, as shown in Figure 5.8.

Inferred from Figure 5.9, the different ranges of nanofluid treatment could bring effects on the movement of water-saturation wave (the slope of characteristic lines) and the variation of water saturation along the characteristic lines. The larger treatment range of nanofluid can enlarge the region with no fines migration/straining effects. As results, the propagation velocity of water-saturation wave throughout the treated region becomes close with that of the case without fines migration. With the increase of nanofluid treatment range, within which the variation of water saturation along characteristic lines become smaller, in other words, the characteristic lines become straighter because of the decrease of fines migration.

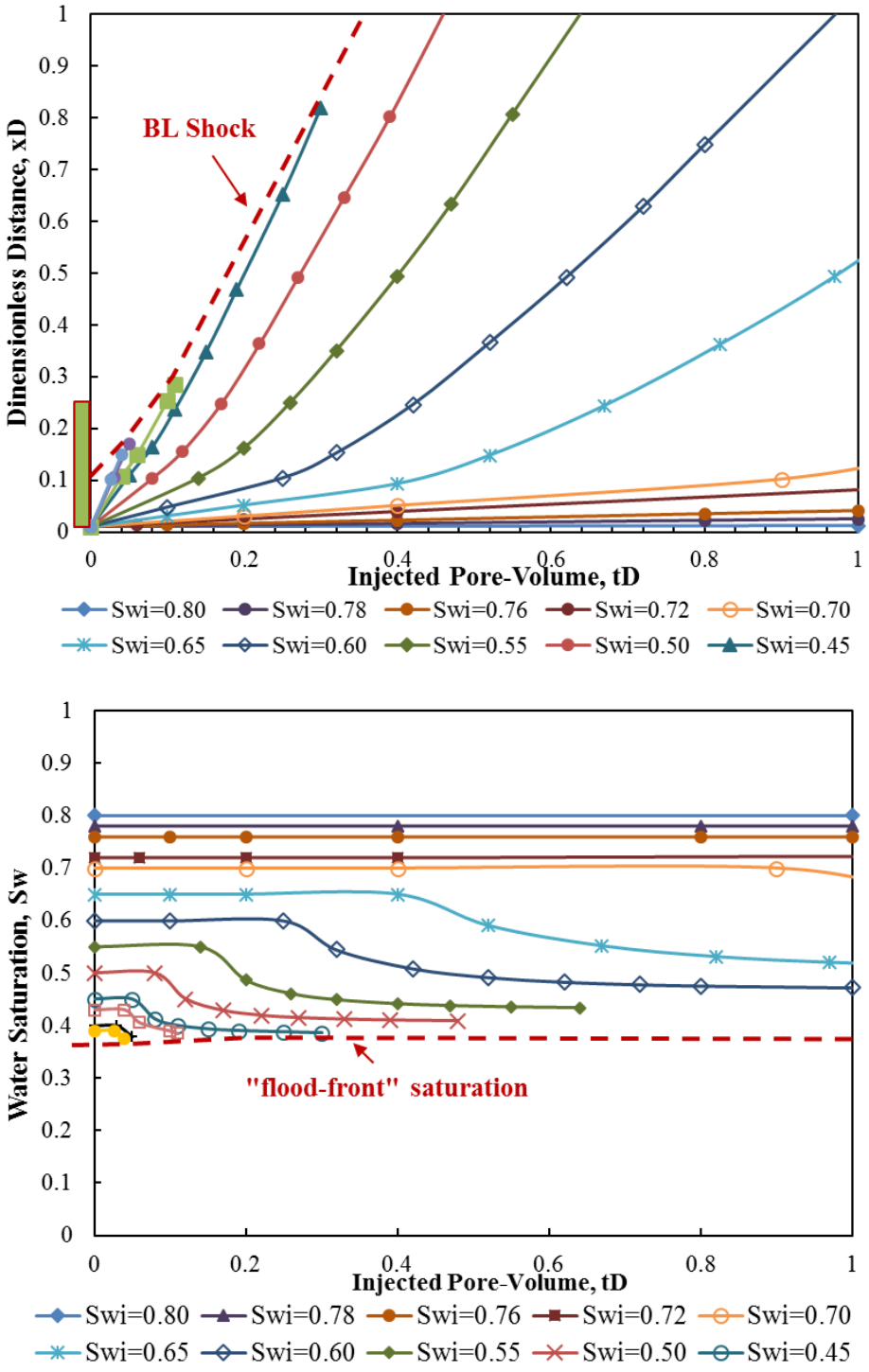
Figure 5.10 presents the profile of water saturation in radial flow system for three different cases of nanofluid treatment at the same injected pore-volume (0.2). As the range of nanofluid treatment increases, the movement of injected water accelerates. It means that the breakthrough of injected water can be accelerated as a negative result by preventing fines migration using nanofluid. The comparison of water saturation profile calculated from analytical solutions and finite-difference numerical solutions for cases with different nanofluids treatment ranges shows an excellent agreement, which confirms the accuracy of our analytical solutions.



(a) With 0.05 nanofluid treatment range prior to low-salinity waterflooding



(b) With 0.10 nanofluid treatment range prior to low-salinity waterflooding



(c) With 0.10 nanofluid treatment range prior to low-salinity waterflooding

Figure 5.9 Comparison of analytical solutions (distance-time diagram and composition variation along characteristic lines) of low-salinity waterflooding with different nanofluid treatment ranges (0.05; 0.10; 0.25)

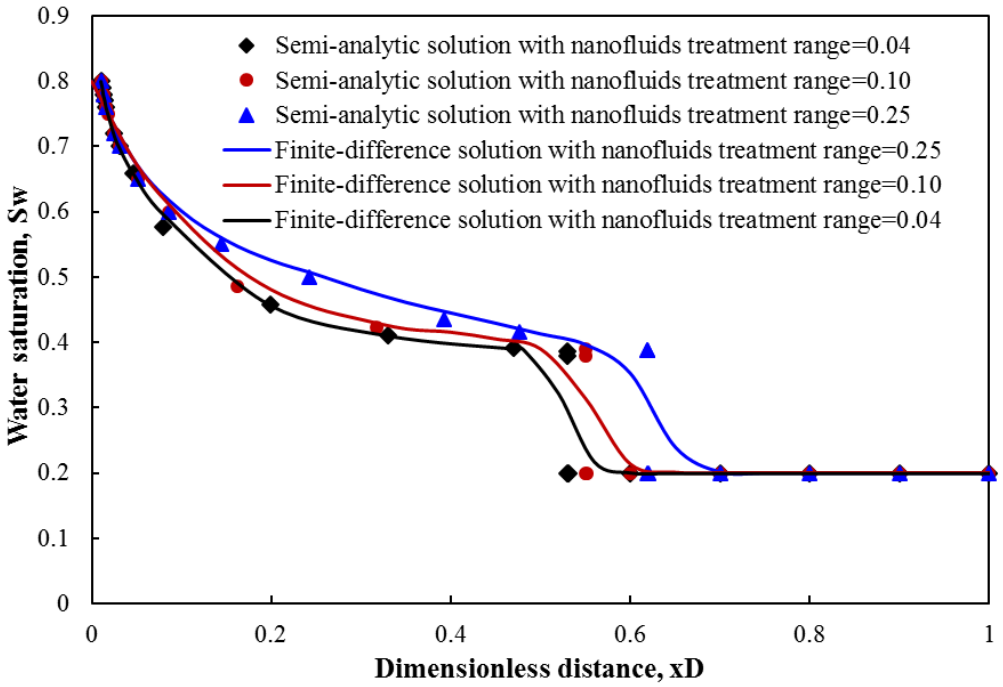


Figure 5.10 Comparison of water saturation profile for cases with different nanofluid treatment ranges (0.05; 0.10; 0.25) prior to low-salinity waterflooding

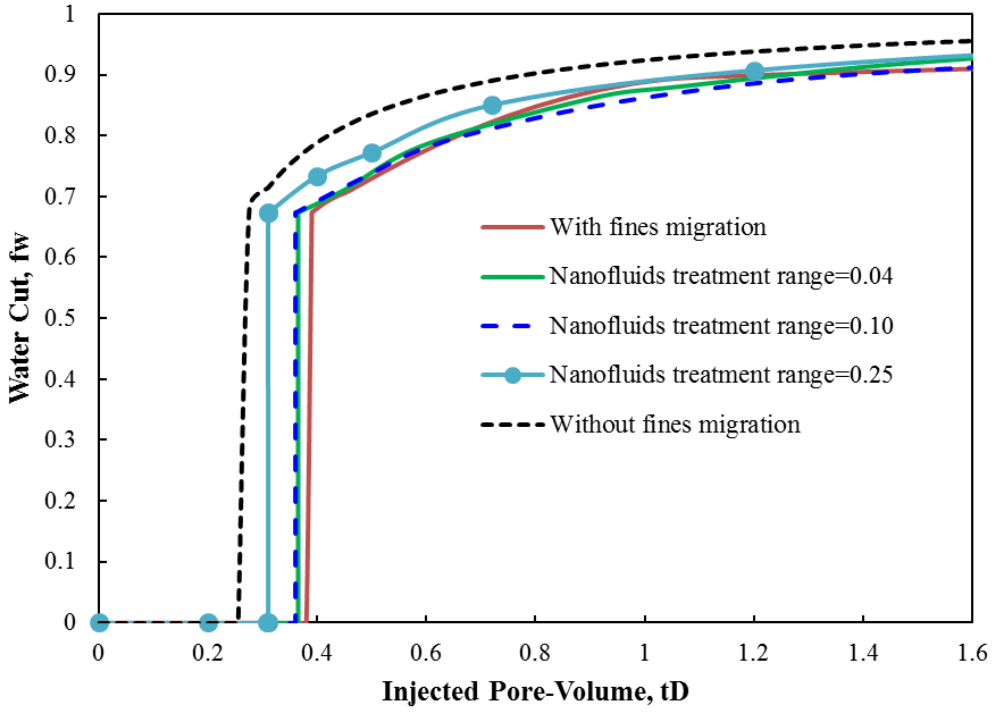


Figure 5.11 Comparison of water-cut history of low-salinity waterflooding with different nanofluid treatment ranges (0.05; 0.10; 0.25)

In Figure 5.11, the water-cut history during low-salinity waterflooding at the outlet are compared for cases with different nanofluid treatment ranges. The induced fines migration and straining during low-salinity waterflooding can effectively delay the breakthrough of injected water, and elongate the duration of oil production with no water. In addition, as the nanofluid treatment range increases from 0.04 to 0.25, the breakthrough of injected water is brought forward, approaching to that of conventional waterflooding without fines migration. In addition, even the breakthrough of injected water has been moved forward because of the reduction of fines migration, the curves of water-cut after nanofluid treatment at the later period of production have no significant increases. It does mean that the nanofluid pre-treatment may help accelerating the breakthrough of injected water, however, it does not bring significant increase of water production, compared with the case without nanofluid treatment.

Besides, another significant positive effect of nanofluid is to mitigate increase of injection pressure by preventing formation damage caused by fines migration. Here, the pressure drop is expressed by the integrating of pressure gradient (Eq.5.10) along the whole reservoirs from the injection end to the production end.

$$\Delta p = \int_0^1 \frac{q\left(1+\beta\sigma_s\right)}{4\pi x_D k_0 \left(\frac{k_{rw}}{\mu_w}+\frac{k_{ro}}{\mu_o}\right)} dx_D \quad \text{..... (5.13)}$$

By integration both negative and positive effects of nanofluid treatment, it can be confirmed that nanofluid is desirable to treat the near-wellbore region for the improvement of low-salinity waterflooding performance, as shown in Figure. 5.12.

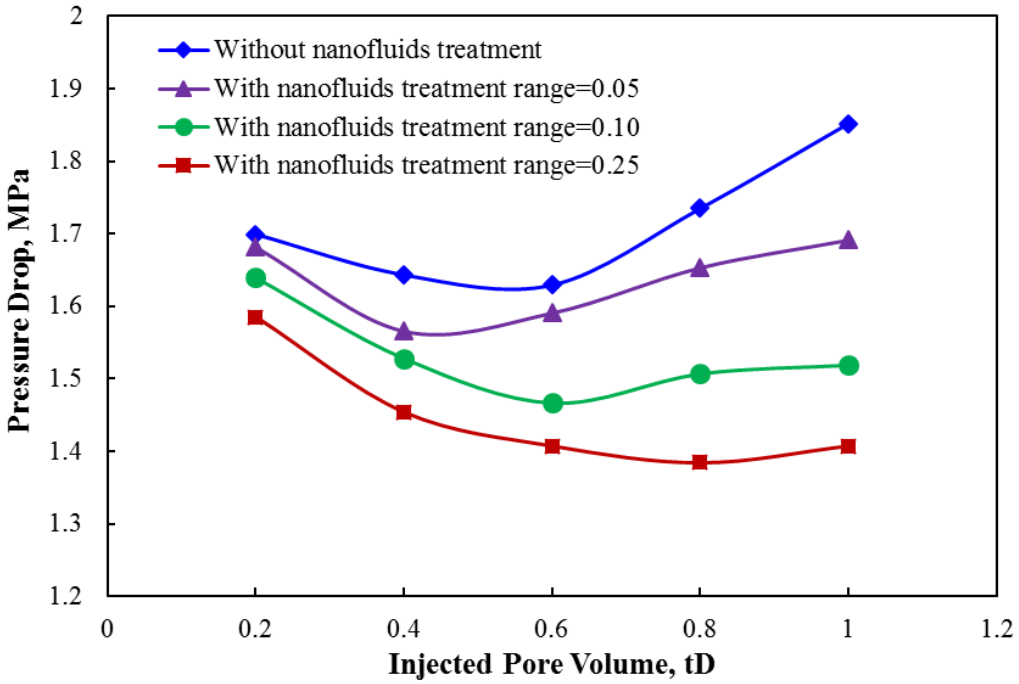


Figure 5.12 Comparison of injection pressure drop for low-salinity waterflooding with different nanofluid treatment range

(a: without nanofluid treatment; b: with nanofluids treatment range=0.05; c: with nanofluid treatment range=0.10 and d: with nanofluid treatment range=0.25)

The utilization of nanofluid slug injection prior to low-salinity water injection can mitigate the problems of fines migration at the vicinity of wells. Thus, the increase of injection pressure drop can greatly be controlled as the low-salinity waterflooding continues. With the increase of nanofluids treatment range, the decreases of injection pressure drop at the different times are enhanced. However, the decreasing trend of pressure drop slows down. This can be explained by that the problem of fine migration weakens with the increase of distance away from the injection well. Thus, the excessively large range of nanofluids treatment does not bring more significant effects. The comparison of pressure drop among different cases of nanofluid treatment indicates the existence of optimal nanofluid treatment range prior to low- salinity water injection. To

determine the optimal value by weighting the balance between decreasing pressure drop and enhancing oil recovery, the recovery factors of different nanofluids treatment cases are defined as Eq.5.14. The comparison results for different cases are presented in Figure 5.13. At the early production period, the oil recovery of low-salinity waterflooding with fines migration is slightly less than that of conventional water flooding (without fines migration) due to the slower movement of injected water to displace the resident oil. However, as for long-term flooding process, the recovery factors of low-salinity waterflooding exceeds that of conventional waterflooding because the reduction of water-phase relative permeability caused by fines migration. Nanofluid treatment can help increasing the early-time recovery of low-salinity waterflooding by accelerating the moving speed of injected water to displace resident oil before the breakthrough of injected water. However, the oil recovery at later life of production is adversely reduced due to the regained water-phase flow capacity by nanofluid. In addition, after the breakthrough of injected water, the performance of low-salinity waterflooding can be reduced by the increase of nanofluids treatment range. Therefore, by making balance between the maintenance of injected pressure drop in Figure 5.12 and impairment of recovery factor in Figure 5.13 caused by nanofluid treatment, the optimal nanofluid treatment range is determined to be 0.10, approximately. In practical, this optimal value provides valuable insights for oilfield operators to approximate the optimal nanofluids treatment prior to low-salinity water flooding.

$$\overline{S_w} = \int_{x_1=0}^{x_2=1} S_w dx_D \frac{1}{x_2 - x_1} = \int_0^1 S_w dx_D; \quad RF = \frac{\overline{S_w} - S_{wc}}{1 - S_{or} - S_{wc}} \quad \text{..... (5.14)}$$

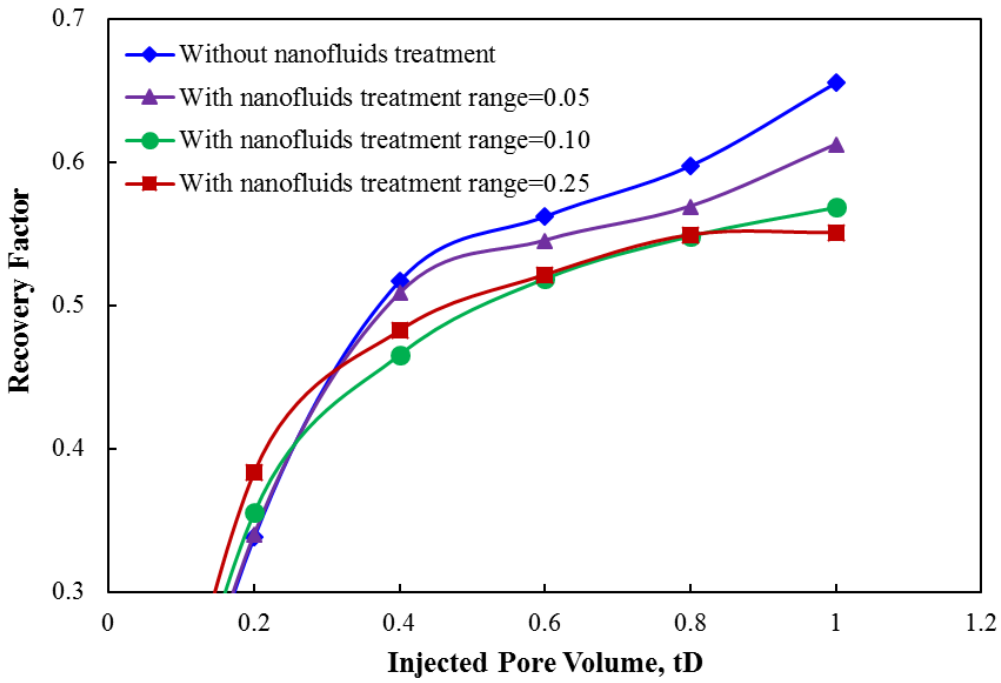


Figure 5.13 Comparison of recovery factor for low-salinity waterflooding with different nanofluid treatment ranges
(a: without nanofluid treatment; b: with nanofluids treatment range=0.05; c: with nanofluid treatment range=0.10 and d: with nanofluid treatment range=0.25)

5.3 Combine Nanofluid with Low-Salinity Waterflooding in Layered Reservoirs

5.3.1 Description of Layered Radial Flow System

The aim of this section is to extend the above mathematical foundation in single-layered system toward the study of low-salinity waterflooding in multi-layered heterogeneous system. The outcomes can eventually help designing nanofluid-slug pre-treatment to maintain well injectivity while improving sweep efficiency by fines migration-assisted mobility control effectively.

In a multi-layered radial flow system, the total flow mobility (both water- and oil-phase) at different locations can be expressed as for different layers,

$$\lambda_t = \frac{k_0}{(1+\beta\sigma_s)}\left(\frac{k_{rw}}{\mu_w}+\frac{k_{ro}}{\mu_o}\right) \quad \text{..... (5.15)}$$

In addition, by substituting Eq.5.15 into Eq.5.9, the modified fractional flow functions of two layers, f_{wi} (i=1, 2), are obtained with the effects of fines migration during low-salinity waterflooding.

The injection pressure drop at different time by integrating pressure gradient from the injection end to the production end. Because the total mobility is different for each layer, firstly, the flow mobility along each layer is calculated. Afterwards, by combining the condition of constant injection rates in total, a harmonic mean of flow mobility for the multi-layered system are obtained, as below:

$$\left.\begin{aligned}
\Delta p_1(t_D) &= q_1(t_D)\int_0^1 \frac{dx_D}{4\pi x_D \lambda_{t1}} \\
\Delta p_2(t_D) &= q_2(t_D)\int_0^1 \frac{dx_D}{4\pi x_D \lambda_{t2}} \\
\Delta p(t_D) &= q_t(t_D)\int_0^1 \frac{dx_D}{4\pi x_D \lambda_t}
\end{aligned}\right\} \xrightarrow{q_t(t_D)=Const.} \frac{1}{\int_0^1 \frac{dx_D}{4\pi x_D \lambda_{t1}}} + \frac{1}{\int_0^1 \frac{dx_D}{4\pi x_D \lambda_{t2}}} = \frac{1}{\int_0^1 \frac{dx_D}{4\pi x_D \lambda_t}} \quad (5.16)$$

The total injection rate is assumed as constant, but the injection pressure drop changes with time because of the changes of formation damage caused by fines migration as low-salinity waterflooding continues. Therefore, the real-time injection pressure drop for the whole system is expressed in Eq.5.17.

$$\Delta p(t_D) = \frac{q_t(t_D)}{\frac{1}{\int_0^1 \frac{dx_D}{4\pi x_D \lambda_{t1}}} + \frac{1}{\int_0^1 \frac{dx_D}{4\pi x_D \lambda_{t2}}}} \quad \text{..... (5.17)}$$

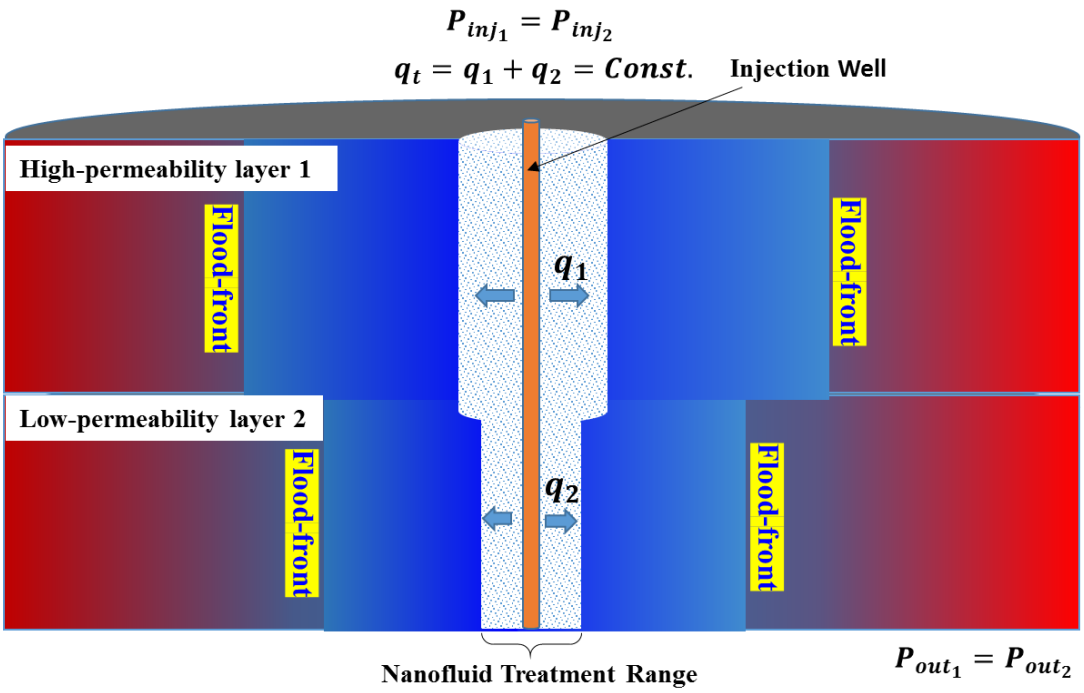


Figure 5.14 Schematic profile of nanofluid pretreatment, pressure drop, phase saturation, and retention concentration of fines particles during low-salinity waterflooding in two-layered heterogenous reservoirs.

5.3.2 Fines Migration-Assisted Mobility Control in Layered System

For an example of two-layered heterogeneous system (Figure 5.14) during low-salinity waterflooding, the ratio of permeability between two parallel layers is set as 2.0, i.e., 0.4 Darcy for high-permeability layers and 0.2 Darcy for low-permeability reservoirs, respectively. The other properties of two layers are assumed as the same. During the injection of low-salinity water, the values of injection pressure for two layers are always identical, but changes with time for the reasons of constant injection rates. The pressure at the outlet pressure is kept as constant. Even though the total injection rate is fixed as constant, the fractional rates of water entering each layer change with time because of the different total mobility along each layer. Here, to demonstrate the advantages of low-

salinity waterflooding, a reference scenario of conventional water flooding without fines migration is presented for comparison. The performance of mobility-control is characterized as the ratio of displacement fronts' advancing locations along each layer, as shown in Eq.5.18. The fractional rates of water flowing into each layer are also analyzed, as waterflooding continues.

$$R=\frac{x_{fD1}}{x_{fD2}}=\frac{x_{fD10}+\left(\frac{\partial f_w}{\partial S_w}\right)_{S_{wf}} t_{D1}}{x_{fD20}+\left(\frac{\partial f_w}{\partial S_w}\right)_{S_{wf}} t_{D2}} \quad \text{..... (5.18)}$$

In addition, as indicated by the maximum retention concentration of fines in Eq. 5.5, flow velocity affects the detachment of fines and the accompanying fines straining (equal to the detachment of fines). As results, due to the different mobility of each layer, the flow rates along each layer change differently as the injection continues. The derivation of MOC analytical solutions for two-layer heterogeneous system is more complicated than the case of single-layer flow system in section 5.2 (which assume the flow rate always keeps constant). To solve this problem, the changes of total mobility need to be evaluated at different time and flow rates needs to be updated for each layer. By substituting the updated total mobility and flow rates into Eq. 5.11, the time-distance diagram and saturation-time diagram are presented to obtain the graphical solutions of our problems. The detailed workflow to obtain analytical solution for low-salinity waterflooding in two-layered heterogeneous flow system is shown in Figure 5.15.

As indicated in section 5.2, during low-salinity waterflooding, the characteristic lines will not keep straight, and along which water saturation also keeps changing. According to the workflow shown in Figure 5.15, the propagation of water saturation waves at

different injected pore-volume is obtained as shown in Figure 5.16. Compared with the Buckley-Leverett problem of conventional waterflooding with no fines migration effects, where the strained fines concentration in Eq.5.7 is zero, the propagation of low-salinity water slows down, which delays the breakthrough of the injected water. In addition, the moving velocities of flood-front (Eq. 5.18) along each layer change with time. The mobility-control caused by fines migration makes the water-flood front of each layer uniform after the injection of certain amounts of water (after $t_D=0.3$). The allocation of injection rates is determined by the changing mobility along each layer. At the early period of low-salinity waterflooding, a larger percentage of injected water enters the high-permeability layer, as shown in Figure 5.17. The flood-front along the high-permeability layer propagates much faster, as shown in Figure 5.16. However, in view of Eq.5.3 and Eq.5.5, with the accumulation of low-salinity water injected into the high-permeability layer, more significant formation damage is induced by amounts of fines detachment and straining as consequences of high flow rates and decreasing fluid salinity within high-permeability layer. As results, both the advancing speed of flood-front and fraction of injected water flowing into high-permeability layer decreases gradually.

As low-salinity waterflooding continues, the flow fractions of the injected water entering each later become same, and that the movement of flood-front along each layer become uniform gradually. These positive results are attributed to the mobility-control effects assisted by fines migration in radial heterogeneous system, as shown in Figure 5.15 and Figure 5.16.

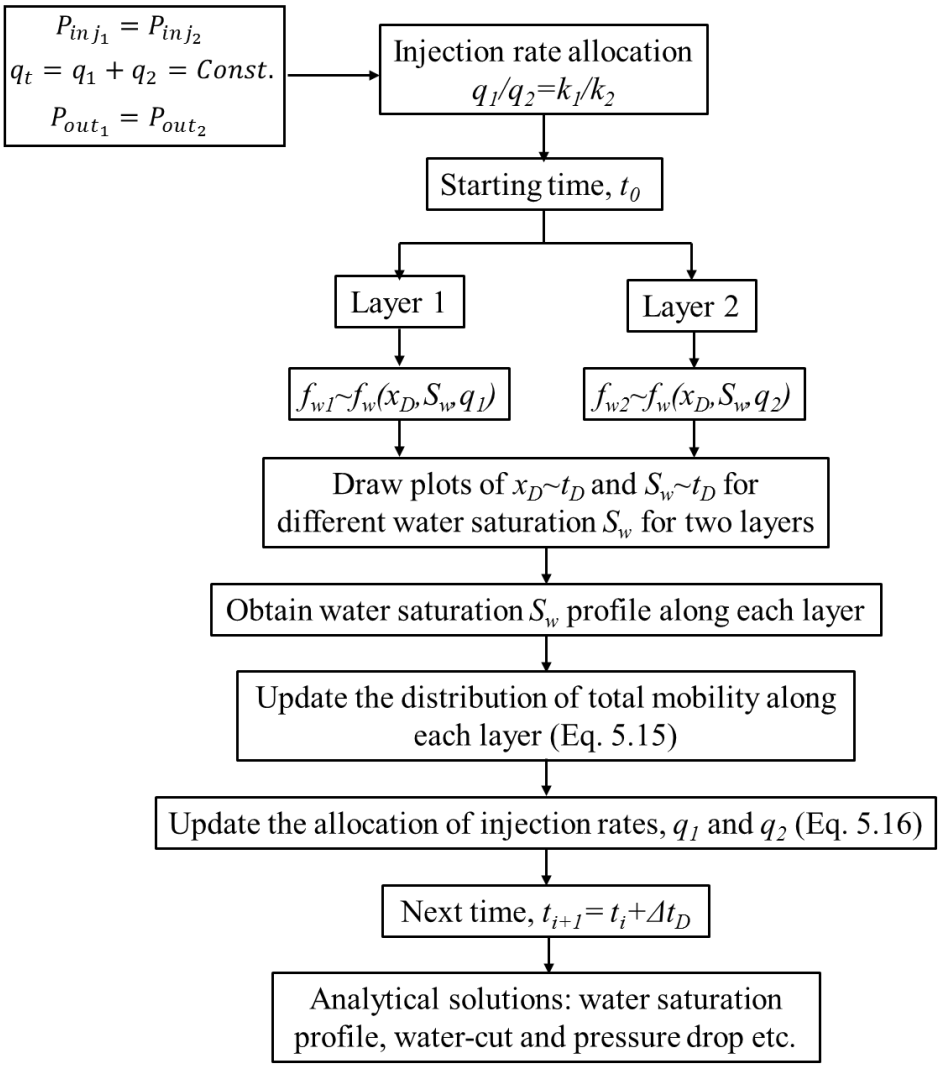


Figure 5.15 Workflow of analytical solutions for two-layered heterogeneous system with fines migration-assisted mobility control during low-salinity waterflooding

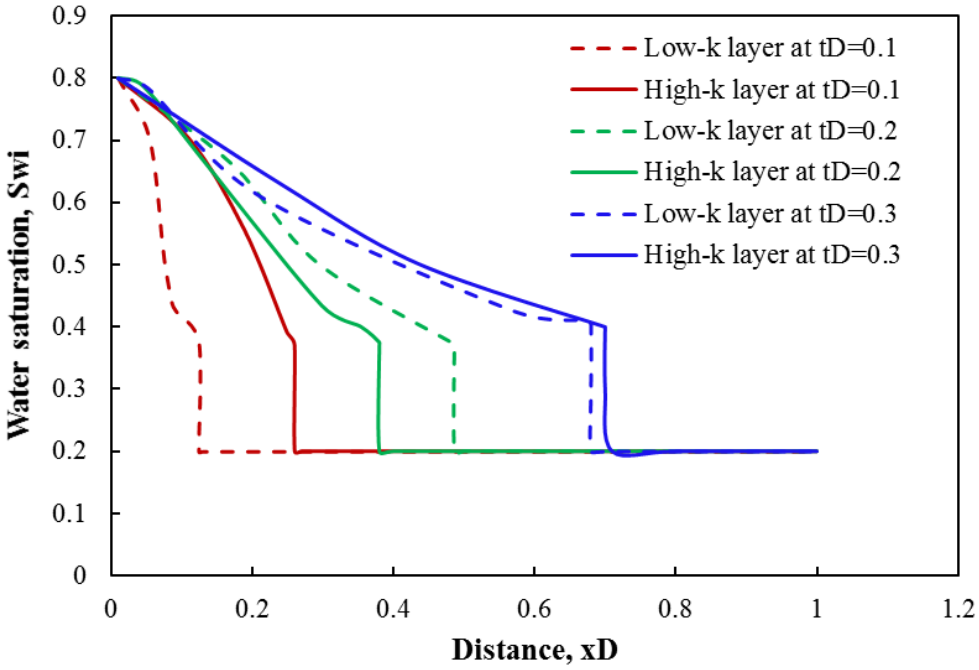


Figure 5.16 Water saturation profiles along each layer at different times

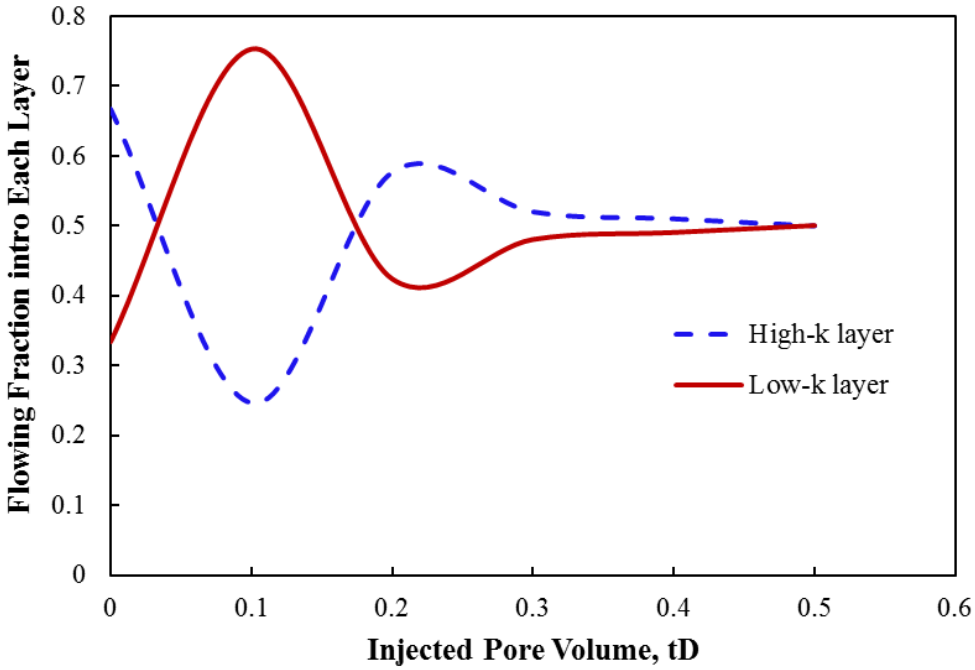


Figure 5.17 Changes of injected fluid fraction entering each layer at different times

5.3.3 Combine Nanofluid with Low-Salinity Waterflooding

On the one hand, the problem of fines migration induced by low-salinity water can provide a simple approach of mobility control to improve the sweep efficiency of injected water. However, on the other hand, the straining effects of fines can bring significant damage of formation permeability. As results, the well injectivity is impaired with the increase of injection pressure drop. The increase of pressure drop would bring troubles on the management of surface facilities with loss of economic profits.

As shown in Figure 5.13, prior to the start of low-salinity waterflooding into radial heterogeneous system, a slug containing nanoparticles is injected to modify the surface potential of rock grains. The capacity of rock grains to retain fine particles is enhanced, as consequences. Figure 5.18 presents the maximum retention concentration of fine particles changing with the increase of distance away from the injection well. At the early period of injection, the flow velocities along each layer are different because of the difference of total mobility along each layer. The distributions of the maximum retention concentration of fines along each layer are also not same. Within the near-wellbore region (less than about x_D=0.1 for low-permeability layer and x_D=0.2 for high-permeability layer), there are more rapid decreases of maximum retention concentration of fines, compared with that in the remote areas. In view of the majority of pressure drop caused by fines migration, in this section, the efficiency of combining nanofluid-slug pretreatment with low-salinity waterflooding will be examined in layered heterogeneous radial flow system. The example of nanofluid treatment is presented with different nanofluid treatment ranges into each layer, i.e.,0.10 and 0.20 for each layer, respectively.

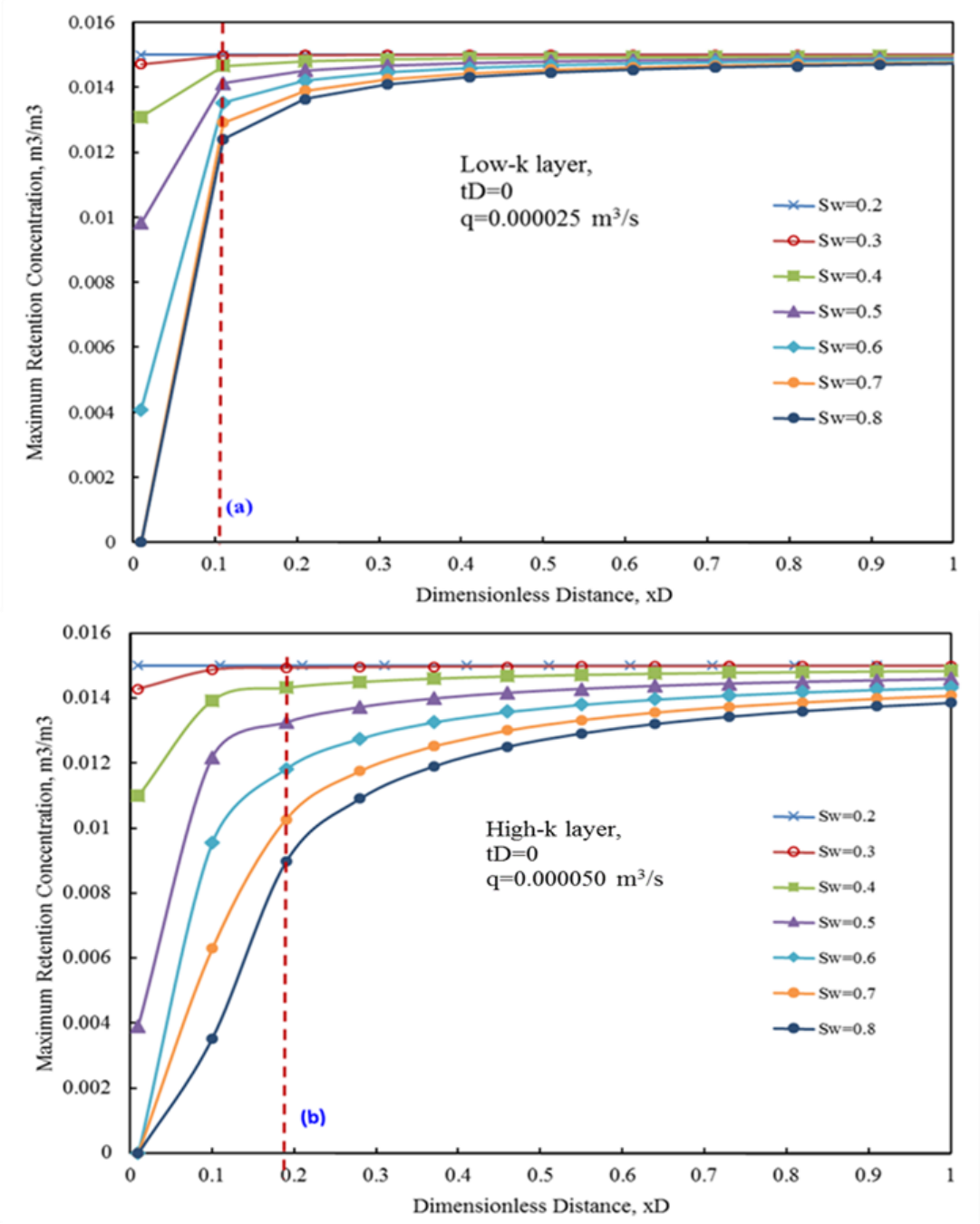


Figure 5.18 The maximum retention concentration of fine particles changing with distances away from the injection well

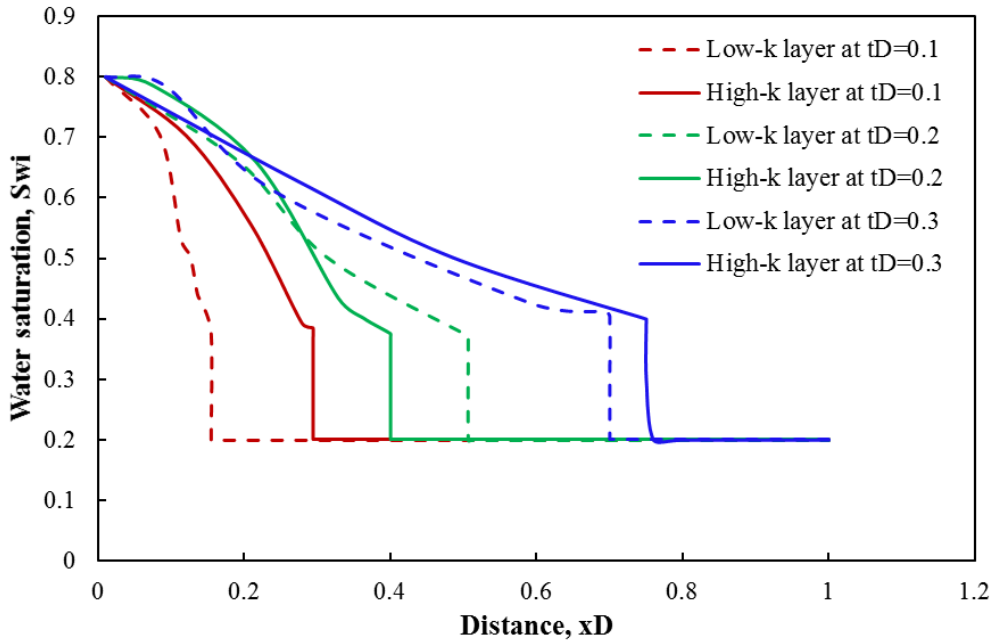


Figure 5.19 The propagation of water saturation profile along each layer at different time for case with nanofluid treatment prior to waterflooding

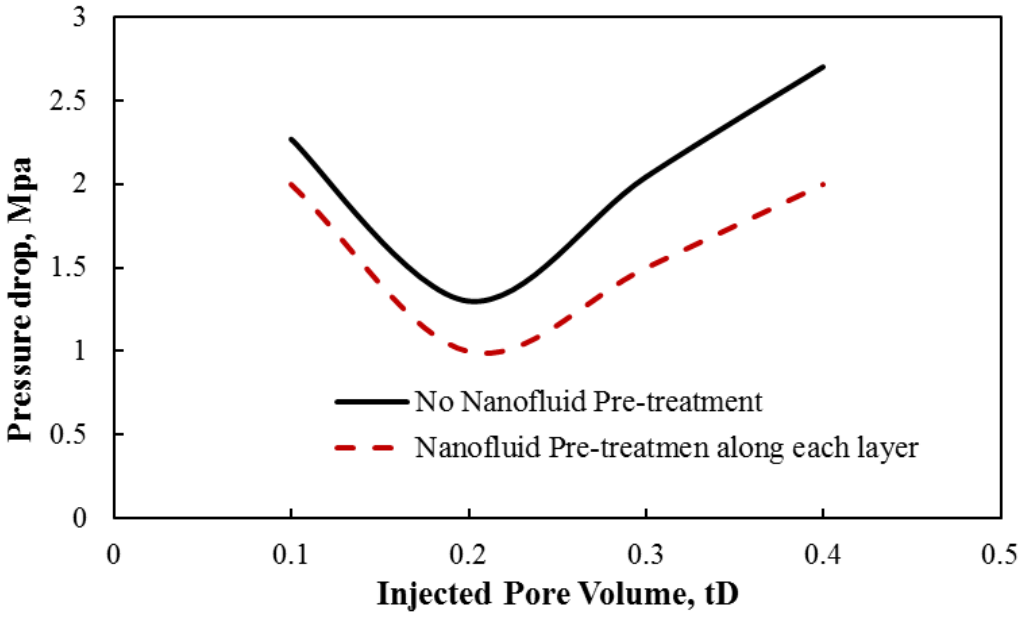


Figure 5.20 The comparison of injection pressure drop for cases with and without nanofluid pre-treatment cases

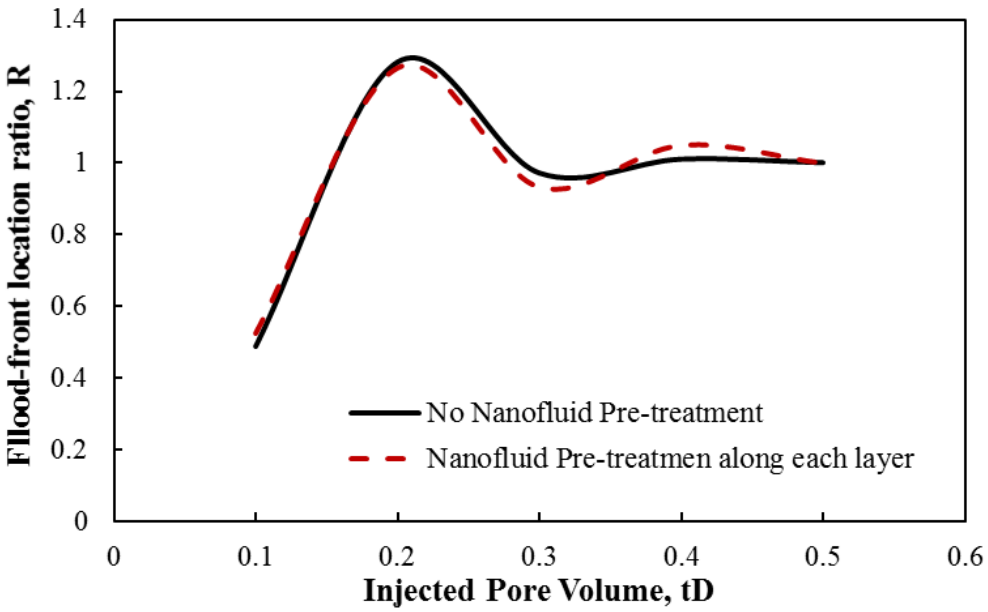


Figure 5.21 The comparison of location ratio of front movement along each layer for cases with and without nanofluid pre-treatment cases

After nanofluid treatment into each layer, the movement of water-saturation wave accelerates, and therefore, the breakthrough of injected water comes earlier, as shown in Figure 5.19. However, the increase of injection pressure drop has been controlled due to the mitigation of formation damage near wells by nanofluid treatment, as shown in Figure 5.20. In addition, despite the changes of the propagation velocity of flood front along each layer, the ratio of front-location along each layer, *R*, has no significant changes, as shown in Figure 5.21. It does mean that nanofluid pre-treatment each layer within the near-well region does not affect the improvement of sweep efficiency by fines migration assisted mobility control for layered heterogeneous reservoirs, but can help decreasing the increase of injection pressure and maintaining well injectivity. The only negative effect of nanofluid treatment within near-well region is to bring forward the breakthrough of injected water, and shorten the duration of oil production without water.

5.4 Conclusions and Summary

This chapter provides semi-analytic solutions to evaluate nanofluid treatment prior to low-salinity waterflooding in both single-layer and two-layer heterogeneous reservoirs. The semi-analytic solutions are proven through numerical finite-difference simulations. The significant findings are concluded below:

- The maximum retention concentration of fine particles is dependent upon both water quality and flow velocity. The capacity of fines attached onto rock grains is weakened as low-salinity water saturation increases. Fines particles near the wellbore are more susceptible to detachment due to the sizable pressure drop caused by the larger flow velocity adjacent to the wells.
- The induced fines migration by low-salinity water delays water breakthrough and extends the duration of oil production without water. Fines migration can help improving mobility-control within each heterogenous reservoir layer, and creating an even fraction of injected fluid flowing into each layer. However, fines migration can also lead to troublesome formation damage resulting in the decline of well injectivity.
- Nanofluid treatment prior to low salinity water injection can help controlling fines migration adjacent to injection wells, and significantly maintaining long-term well injectivity. In addition, nanofluid treatment has the capacity to bring forward the breakthrough of injected water, but has minimal effects on the improved sweep efficiency by fines migration in layered heterogeneous reservoirs.

Chapter 6: Contributions and Recommendations

This chapter entails the main contributions of this dissertation and offers the recommendation for future research.

6.1 Major Contributions

- The mechanical equilibrium of particles and maximum retention concentration model are extended to study transport of both nanoparticles and fine particles. Adsorption/detachment and straining behavior of nanoparticles and their associated effects on formation permeability are quantified by analytical solutions. The important parameters pertinent to transport and capture of nanoparticles are characterized, i.e., the maximum adsorption concentrations, reversible or detachment adsorption concentrations, nanoparticles adsorption and straining rates, and formation damage coefficients.

- An application of the method of characteristics (MOC) is examined to evaluate the effectiveness of nanoparticles to mitigate fines migration in single-phase water flow. Semi-analytic MOC solutions are developed for two different scenarios of nanoparticles utilization to control fines migration: (1) co-injection of nanoparticles with fines suspension into one-dimensional permeable medium and (2) pre-coating porous medium with nanoparticles before injection.

- Analytical transport solutions of nanoparticles/fine particles in two-phase (oil and water) flow is derived while accounting for interactions among fines, nanoparticles, and rock grains. The splitting method will be implemented to separate the 3×3 system into a 2×2 auxiliary system containing only particles (nanoparticles & fines) and one lifting equation containing phase saturation, in the transformed plane of distance and stream-function. After the analytical solutions of auxiliary system and lifting equation are

obtained, an inverse transformation is applied to obtain the actual solutions of nanoparticles-fines transport in oil-water phase flow.

- Both the performance of formation damage mitigation and enhanced oil recovery caused by the integrated effects of fines migration and nanoparticles utilization are evaluated for two different nanoparticles utilization to control fines migration in two-phase flow, including 1) co-injection of nanoparticle-fine particles mixture into 1-D permeable medium initially oversaturated with fine particles and 2) pre-coating /pre-treatment with nanoparticles prior to fines injection in a radial flow system.
- In radial flow through single-layer homogenous system, analytical solutions are derived to confirm the feasibility of nanoparticle application to improve low-salinity waterflooding performance. The maximum retention concentration of fine particles is extended to two-phase flow. A new formulation for fraction flow function considering fines straining in water-phase is presented. The semi-analytical solutions of low salinity water flooding without/with fines migration and nanofluid pre-treatment are derived and verified by numerical simulations.
- In layered reservoirs, nanofluid-slug pre-flush is introduced to both maintain well injectivity and improve sweep efficiency by fines migration-assisted mobility control during low-salinity waterflooding. An axisymmetric radial flow model and fraction flow analysis are applied to interpret the improvement of mobility control and well injectivity. A graphic workflow is also presented to analyze an example of nanofluid treatment for nanofluid-fines-assisted low-salinity waterflooding.

6.2 Recommendation for Future Work

The proposed future research topics based on the outcomes of this dissertation are listed as follows:

- Extension of both experiments and analytical solutions of nanoparticles transport in Chapter 2 to two-phase or multi-phase flow.
- Extension of analytical solutions of nanoparticles to control fines migration in Chapter 3 and Chapter 4 by considering,
    - Multi-phase multi-component flow (coal powders migration in coal-bed methane; tertiary low-salinity waterflooding or chemical flooding in reservoirs suffers from the problem of fines migration).
    - More fines capture mechanisms (particles straining, attachment, and size exclusion etc.).
- Extension of analytical models to be more generalized and realistic for field applications through developing a novel simulator.

References

Abduwani, F. A. H., Bedrikovetsky, P., and Farajzadeh, R., et al., 2005. External Filter Cake Erosion: Mathematical Model and Experimental Study, Paper SPE-94635-MS presented at *SPE European Formation Damage Conference*. 25-27 May, Sheveningen, The Netherlands.

Abdelrahman, I. E., and Ahmed, M. A. 2015. Understanding the Mechanism of Nanoparticles Applications in Enhanced Oil Recovery. Paper SPE-175806-MS presented at *SPE North Africa Technical Conference and Exhibition*, 14-16 September, Cairo, Egypt.

Abousleiman, Y. N., Tran, M. H., and Hoang, B. O., et al. 2009. Geomechanics Field and Laboratory Characterization of Woodford Shale: The Next Gas Play. Paper SPE-110120-MS presented at *SPE Annual Technical Conference and Exhibition*, 11-14 November Anaheim, California, USA.

Achinta, B., and Belhaj, H., 2016, Application of Nanotechnology by Means of Nanoparticles and Nano-dispersions in Oil Recovery- A Comprehensive Review. *Journal of Natural Gas Science and Engineering*, 34: 1284-1309.

Adkins, S., Gohil, D., and Dickson, J., et al. 2007. Water-in-carbon Dioxide Emulsions Stabilized with Hydrophobic Silica Particles, *Physical Chemistry Chemical Physics*, 9: 6333-6343.

Ahmadi, M., Pourafshari, P., and Ayatollahi, S., 2011. Zeta Potential Investigation and Mathematical Modeling of Nanoparticles Deposited on the Rock Surface to Reduce Fine Migration, Paper SPE-142633-MS presented at *SPE Middle East Oil and Gas Show and Conference*, 25-28 September, Manama, Bahrain.

Alagic, E., and Skauge, A. 2010. Combined Low Salinity Brine Injection and Surfactant Flooding in Mixed-wet Sandstone Cores. *Energy Fuels*, 24(06): 3551-3559.

Aksulu, H., Hamso, D., and Strand, S., et al. 2012. The Evaluation of Low Salinity Enhanced Oil Recovery Effects in Sandstone: Effects of Temperature and pH Gradient. *Energy Fuels*, 26: 3497-3503.

Aminzadeh, B., DiCarlo, D. A., and Chung, D. H., et al. 2012. Effect of Nanoparticles on Flow Alteration during CO2 Injection. Paper SPE-160052-MS presented at the *SPE Annual Technical Conference and Exhibition*, 8-10 October San Antonio, Texas, USA.

Arab, D., and Pourafshary, P., 2013. Nanoparticles-Assisted Surface Charge Modification of the Porous Medium to Treat Colloidal Particles Migration Induced by Low Salinity Water Flooding. *Colloids and Surfaces A: Physicochemical and Engineering Aspects*, 436, 803-814.

Assef, Y., Arab, D., and Pourafshary, P. 2014. Application of Nanofluid to Control Fines Migration to Improve the Performance of Low Salinity Water Flooding and Alkaline Flooding. *Journal of Petroleum Science and Engineering*. 124: 331-340.

Bera, A., Mandal, A., and Kumar, T., 2015. The Effect of Rock-Crude Oil-Fluid Interactions on Wettability Alteration of Oil-Wet Sandstone in the Presence of Surfactants. *Pet. Sci. Tech*. 33 (5): 542-549.

Austad T. Rezaeidoust, A., and Puntervold, T. 2008. Chemical Mechanisms of Low Salinity Water Flooding in Sandstone Reservoirs. Paper SPE 129767 presented at *SPE Improved Oil Recovery Symposium*, Apr 24-28, Tulsa, Oklahoma.

Bedrikovetsky, P., et al. 2011. Modified Particle Detachment Model for Colloidal Transport in Porous Media. *Transport in Porous Media*, 86(2): 353-383.

Bedrikovetsky Pavel, et al. 2014. Analytical Model for Fines Migration During Water Injection. *Transport in Porous Media,* 101:161-189.

Behruz, S. S., and Skauge, A. 2013. Enhanced Oil Recovery (EOR) by Combined Low Salinity Water/Polymer Flooding. *Energy Fuels*, 27 (3): 1223–1235.

Berlin, J. M., Yu, J., and Lu, W., et al., 2011. Engineered Nanoparticles for Hydrocarbon Detection in Oil-field Rocks. *Energy Environ. Sci.,* 4: 505-509.

Bernard, G. G. 1967. Effect of Floodwater Salinity on Recovery of Oil from Cores Containing Clays, Paper SPE-1725-MS presented at *SPE California Regional Meeting*. Los Angeles, 26-27 October, Los Angeles, California.

Borazjani, S., Behr, A., and Genolet, L., et al. 2016a. Effects of Fines Migration on Low Salinity Waterflooding: Analytical Modelling. *Transport in Porous Media*, 116 (01): 213-249.

Borazjani, S., and Bedrikovetsky, P., 2016b. Exact Solutions for Two-Phase Colloidal-Suspension Transport in Porous Media. *Applied Mathematical Modelling*, in press, http://dx.doi.org/10.1016/j.apm.2016.12.023.

Boussour, S., Cissokho, M., and Cordier, P., et al. 2009, Oil Recovery by Low Salinity Water Injection: Laboratory Results on Outcrop and Reservoir Cores. Pape SPE 119835 presented at *SPE Annual Technical Conference and Exhibition*, 8-11 Jun, Amsterdam, The Netherland.

Chatterjee, R., Mitra, S., and Bhattacharjee, S. 2011. Particle Deposition onto Janus and Patchy Spherical Collectors. *Langmuir*, 27, 8787–8797.

Cheng, X. 2005. Study of C60 Transport in Porous Media and the Effect of Absorbed C60 on Naphthalene Transport. *Journal of Materials Research*, 20(12): 3244-3254.

Civan, F. 2007. *Reservoir Formation Damage (Fundamentals, Modeling, Assessment, and Mitigation),* 2nd Edition. Gulf Professional Publishing, Oxford.

Civan, F., 2010a. Temperature Effect on Power for Particle Detachment from Pore Wall Described by An Arrhenius-type Equation. *Transport in Porous Media*, 67, 329–334.

Civan, F., 2010b. Non-Isothermal Permeability Impairment by Fines Migration and Deposition in Porous Media including Dispersive Transport. *Transport in Porous Media*, 85(1), 233–258.

Contreras, O., Hareland, G., and Husein, M., et al. 2014. Application of In-house Prepared Nanoparticles as Filtration Control Additive to Reduce Formation Damage. Paper SPE-168116-MS presented at *SPE International Symposium and Exhibition on Formation Damage Control*, 26-28 February, Lafayette, Louisiana, USA.

Courant, R. H., D. 1962. *Methods of Mathematical Physics: Vol. II. Partial Differential Equations*. New York City, New York: Wiley-Interscience Publishers Inc.

Crews, J. B., and Gomaa, A.M., 2012. Nanoparticle-assisted Surfactant Micellar Fluids: An Alternative to Crosslinked Polymer Systems. Paper SPE-157055-MS presented at *SPE International Oilfield Nanotechnology Conference*, 12-14 June, Noordwyk, The Netherlands.

Dábrowski, W. 1988. Consequences of the Mass Balance Simplification in Modelling Deep Filtration. *Water Research*, 22(10): 1219-1227.

Dominguez, J. G., and Willhite, G. P. 1977. Retention and Flow Characteristics of Polymer Solutions in Porous Media. *SPE Journal*, 17(02): 111-121.

Dullien, F. A. L. 2012. *Porous Media: Fluid Transport and Pore Structure*: Elsevier Science.

Elimelech, M., Gregory, J., and Jia, X., & Williams, R. A. 1995. *Particle Deposition & Aggregation: xiii-xv*. Woburn: Butterworth-Heinemann.

Esmaeilzadeh, P., Bahramian, A., and Fakhroueian, Z., 2011. Adsorption of Anionic, Cationic and Nonionic Surfactants on Carbonate Rock in presence of ZrO2 nanoparticles. *Phys. Procedia*. 22: 63-67.

Ezeudoh, C., Zandvliet, M., and Jenakumo, T., et al., 2014. Enhancing Recovery by Concurrent Water and Gas Injection: Case Study of a Deepwater Turbidite Reservoir, *SPE Nigeria Annual International Conference and Exhibition*. 5-7 August, Lagos, Nigeria.

Ezeukwu, T., Thomas, R.L., and Gunneroed, T., 1998. Fines Migration Control in High-Water-Cut Nigerian Oil Wells: Problems and Solutions, Paper SPE-39482-MS presented at *SPE Formation Damage Control Conference*. 18-19 February, Lafayette, Louisiana.

Gonzenbach, U. Studart, A. and Tervoort, E., et al. 2007. Tailoring the Microstructure of Particle-Stabilized Wet Foams, *Langmuir*, 23: 1025-1032.

Gregory, J. 1981. Approximate Expressions for Retarded Van der Waals Interaction. *Journal of Colloid and Interface Science*, 83(1): 138-145.

Gruesbeck, C. 1982. Entrainment and Deposition of Fine Particles in Porous Media. *SPE Journal*, 22(6): 847-856.

Gruedes, R. G., Al-Abduwani, F., and Bedrikovetsky. 2006. Injectivity Decline under Multiple Particles Capture Mechanisms. Paper SPE-98623-MS presented at *SPE International Symposium and Exhibition on Formation Damage Control*, 15-17 February, Lafayette, Louisiana, USA.

Gurluk, M.R., Nasr-El-Din, H.A., and Crews, J., 2013a. Enhancing the Performance of Viscoelastic Surfactant Fluids using Nanoparticles. Paper SPE-164900-MS presented at *EAGE Annual Conference & Exhibition*, 10-13 June, London, UK.

Habibi, A., Pourafshari, P., and Ayatollahi. 2011. Reduction of Fines Migration by Nanofluids Injection, An Experimental Study, *SPE Journal*, 18(02): 309-318.

Hankins, N. P. 2004. Application of coherence theory to a reservoir enhanced oil recovery simulator. *Journal of Petroleum Science and Engineering*, 42(1): 29-55.

Herzig, J. P. 1970. Flow of Suspensions through Porous Media—Application to Deep Filtration. *Industrial & Engineering Chemistry*, 62(5): 8-35.

Hendraningrat, L., Li, S., and Torseter, O. 2012. A Glass Micromodel Experimental Study of Hydrophilic Nanoparticles Retention for EOR Project. Paper SPE-15916-MS presented at *SPE Russian Oil and Gas Exploration and Production Technical Conference and Exhibition*, 16-18 October, Moscow, Russia.

Hendraningrat, L., and Torseter, O. 2015. Metal Oxide-based Nanoparticles: Revealing Their Potential to Enhance Oil Recovery in Different Wettability Systems. *Applied Nanoscience* 5: 181-199.

Holden, H., Risebro, N. H., *Front tracking for hyperbolic conservation laws*, Springer, Berlin, 2013.

Hourshad, M., and Jerauld, G. 2012. Mechanistic Modeling of the Benefit of Combining Polymer with Low Salinity Water for Enhanced Oil Recovery. Paper SPE-153161-MS presented at *SPE Improved Oil Recovery Symposium*, 14-18 April, Tulsa, Oklahoma, USA.

Huang, T., Crews, B. J. and Willingham, R. J. 2008a. Nanoparticles for Formation Fines Fixation and Improving Performance of Surfactant Structure Fluids, *International Petroleum Technology Conference*. Kuala Lumpur, Malaysia.

Huang, T., Crews, J., and Willingham, J. R., 2008b. Using Nanoparticles Technology to Control Fine Migration, Paper SPE-115384-MS presented at *SPE Annual Technical Conference and Exhibition*, 21-24 September, Denver, Colorado, USA.

Huang, T., Evans, B. A., and Crews, J. B., et al. 2010. Field Case Study on Formation Fines Control with Nanoparticles in Offshore Applications. Paper SPE-13508-MS presented at *SPE Annual Technical Conference and Exhibition*, 19-22 September, Florence, Italy.

Huang T., Han, J., and Agrawal, G., et al. 2015. Coupling Nanoparticles with Water flooding to Increase Water Sweep Efficiency for High Fines-Containing Reservoir – Lab and Reservoir Simulation Results. Paper SPE-174802-MS presented at *SPE Annual Technical Conference and Exhibition*, 28-30, September, Houston, Texas, USA.

Israelachvili, J. N. 2011. *Intermolecular and Surface Forces*: Revised Third Edition: Elsevier Science.

Jahagirdar, S. R., 2008. Oil-microbe Detection Tool Using Nano Optical Fibers. Paper SPE-113357-MS presented at the *SPE Western Regional and Pacific Section AAPG Joint Meeting*, 29 March-4 April Bakersfield, California, USA.

Ju, B., Fan, T., and Ma, M., 2006. Enhanced Oil Recovery by Flooding with Hydrophilic Nanoparticles. *China Particuology*, 4(1): 41-46.

Ju, B., and Fan, T., 2009. Experimental Study and Mathematical Model of Nanoparticles Transport in Porous Media. *Powder Technology*, 192(2): 195-202.

Kapusta, S., Balzano, L., and Riele, P., 2011. Nanotechnology Application in Oil and Gas Exploration and Production. Paper SPE-15152-MS presented at *International Petroleum Technology Conference*, 15-17 November, Bangkok, Thailand.

Keller, A. A., Wang, H., and Zhou, D., et al. 2010. Stability and Aggregation of Metal Oxide Nanoparticles in Natural Aqueous Matrices. *Environment Science Technology* 44(06): 1962-1967.

Khilar, K, C., and Fogler, H., 1998. *Migration of Fines in Porous Media*. Springer Netherlands.

Lake, L. W. 1989. *Enhanced oil recovery*. United States: Old Tappan, NJ; Prentice Hall Inc.

Lake, L. W., Bryant, L. S., and Araque-Martinez, N. A. 2002. Geochemistry and Fluid Flow: Elsevier.

Lemon, P. 2011. Effects of Injected-Water Salinity on Waterflood Sweep Efficiency Through Induced Fines Migration. *Journal of Canadian Petroleum Technology*, 50: 9-10.

Li, S., Hendraningrat, L. and Torsæter, O. 2013. Improved Oil Recovery by Hydrophilic Silica Nanoparticles Suspension 2-Phase Flow Experimental Studies. Paper IPTC-16707 presented at *International Petroleum Technology Conference*, 26-28 March, Beijing, China.

Li, S., Jiang, M., and Torsæter, O. 2014. An Experimental Investigation of EOR Mechanisms for Nanoparticles Fluid in Glass Micromodel. Paper SCA2014-022 presented at the *International Symposium of the Society of Core Analysts*, 8-11 September 2014, Avignon, France.

Li, S., and Torsæter, O. 2015a. Experimental Investigation of the Influence of Nanoparticles Adsorption and Transport on Wettability Alteration for Oil Wet Berea Sandstone. SPE-172539-MS presented at the *SPE Middle East Oil & Gas Show and Conference*, 8-11 March 2015, Manama, Bahrain.

Li, S., Jiang, M., and Torsæter, O. 2015b. An Experimental Investigation of Nanoparticles Adsorption Behavior during Transport in Berea Sandstone. SCA2015-029 presented at *International Symposium of the Society of Core Analysts* held in St. John's Newfoundland and Labrador, Canada, 16-21 August 2015.

Lin, K., Pryadko, L., and Waler, S., et al. 2009. Attachment and Detachment Rate Distributions in deep-bed filtration. *Physical Review E*. 79(04): 046321-1-046321-12.

Logan, D. J. 2001. *Transport Modeling in Hydrogeochemical Systems*. New York: Springer.

Massoudieh, A., and Ginn, T.R., 2010. Colloid-facilitated Contaminant Transport in Unsaturated Porous Media, Chapter 8 in *Modelling of Pollutants in Complex Environmental System*. Vol. II. ILM Publications, Glensdale.

McDonald, M. J., 2012. A Novel Potassium Silicate for Use in Drilling Fluids Targeting Unconventional Hydrocarbons. Paper SPE-162180-MS presented at *SPE Canadian Unconventional Resources Conference*, 30 October-1 November, Calgary, Alberta, Canada.

Moghadam, T. F., and Azizian, S., 2014. Effect of ZnO Nanoparticles on the Interfacial Behavior of Anionic Surfactant at Liquid/Liquid Interfaces. *Colloids Surf. A* 457: 333-339.

Moghanloo, R. G., and Lake, L. W. 2010. Simultaneous Water-Gas-Injection Performance under Loss of Miscibility, Paper SPE-129966-MS presented at *SPE Improved Oil Recovery Symposium*. 24-28 April, Tulsa, Oklahoma.

Moghanloo, R. G., 2012a. *Modeling the Fluid Flow of Carbon Dioxide through Permeable Media*. The University of Texas at Austin, Austin, Texas.

Moghanloo, R. G., and Lake, W. L. 2012b. Applying Fractional Flow Theory under Loss of Miscibility. *SPE Journal*, 17(3): 661-670.

Moghanloo, R. G., and Javadpour, F. 2014. Applying Method of Characteristics to Determine Pressure Distribution in 1D Shale-Gas Samples. *SPE Journal*, 19(03): 361-372.

Moghanloo, R. G., Dadmohammadi, Y., and Yuan, B., et al. 2015. Applying Fractional Flow Theory to Evaluate CO2 Storage Capacity of an Aquifer. *Journal of Petroleum Science and Engineering*, 125, 154–161.

Muecke, T. W. 1979. Formation Fines and Factors Controlling Their Movement in Porous Media. *Journal of Petroleum Technology*, 31(02): 144-151.

Nguyen, P. D., Weaver, J., D., and Rickman, R. D., et al. 2007. Controlling Formation Fines at Their Sources to Maintain Well Productivity. *SPE Production & Operations*, 22(02): 202-216.

Noh, M., and Lake, L. W. 2004. Implications of Coupling Fractional Flow and Geochemistry for CO2 Injection in Aquifers, Paper SPE-89341-MS presented *at SPE/DOE Symposium on Improved Oil Recovery*. 17-21 April, Tulsa, Oklahoma.

O'Brien. 2014. Langmuir Analysis of Nanoparticle Polyvalency in DNA-Mediated Adsorption. *Angewandte Chemie International Edition*, 53(36): 9532-9538.

Ochi, J. 1998. Permeability Decrease in Sandstone Reservoirs by Fluid Injection: Hydrodynamic and Chemical effects. *Journal of Hydrology*, 208(3–4): 237-248.

Ogolo, N.A., Olafuyi, O.A., and Onyekonwu, M. O., 2012. Enhanced Oil Recovery Using Nanoparticles. Paper SPE-160847-MS presented at *SPE Saudi Arabia Section Technical Symposium and Exhibition*, 8-11 April, Al-Khobar, Saudi Arabia.

Ofurhie, M. A., Lufadeju, A. O., and Agha, G. U., et al. 2002. Turbidite Depositional Environment in Deepwater of Nigeria, Paper OTC-14068-MS presented at *Offshore Technology Conference*. 6-9 May, Houston, Texas.

Pang, X., Boul, P.J., and Jimenez, W., 2014. Nanosilicas as Accelerators in Oil Well Cementing at Low Temperatures. *SPE Drilling & Completion*. 29 (01), 98-105.

Penberthy, W. L. 1992. *Sand control*: Henry L. Doherty Memorial Fund of AIME, Society of Petroleum Engineers.

Prigiobbe V., Worthen J. A., and Johnston P. K., et al. 2016. Transport of Nanoparticles-Stabilized CO2-Foam in Porous Media. *Transport Porous Media*, 111: 265-285.

Pires, P. A., Bedrikovetsky, P., and Sharpiro, A. A. 2006. A Splitting Technique for Analytical Modeling of Two-Phase Multicomponent Flow in Porous Media. *Journal of Petroleum Science and Engineering*, 51: 54-67.

Pope, G. A., and Nelson, R. C. 1978. A Chemical Flooding Compositional Simulator. *SPE Journal*, 18(05): 339-354.

Rhee, H. K., Aris, R., and Amundson, R. N. 2001. *First-order Partial Differential Equations, Volume 2: Theory and Application of Hyperbolic Systems of Quasilinear Equations*. Dover Publications, Inc. Mineola, New York.

Rosenbrand, E., Haugwitz, C., and Jacobsen, P. S. M., et al. 2014. The Effect of Hot Water Injection on Sandstone Permeability. *Geothermics*, 50: 155-166.

Senger B., Schaaf P., and Vogel J.C. et al. 1992. Influence of Bulk Diffusion on Adsorption of Hard Spheres on A Flat Surface. *Journal of Chemistry Physics*. 97(05): 3813-3820.

Santos, A., and Bedrikovetsky, P., 2006. A Stochastic Model for Particulate Suspension Flow in Porous Media. *Transport in Porous Media*. 62 (01):23-53.

Santra, A.K., Boul, P., and Pang, X., 2012. Influence of nanomaterials in Oil Well Cement Hydration and Mechanical Properties. Paper SPE-156937-MS presented at *SPE International Oilfield Nanotechnology Conference and Exhibition*, 12-14 June, Noordwyk, The Netherlands.

Sarkar, A. K., and Sharma, M. M., 1990. Fines Migration in Two-Phase Flow. *Journal of Petroleum Technology*, 42(05): 646-652.

Saripalli, K. P., and Sharma, M. M., and Bryant, S. L., Modeling Injection Well Performance during Deep-Well Injection of Liquid Wastes. *Journal of Hydrology*, 227: 41-55.

Shapiro, A. A., Bedrikovetsky, P. G., 2008. Elliptic Random-Walk Equation for Suspension and Tracer Transport in Porous Media. *Physical A: Statistical Mechanics and its Application*, 387(24): 5963-5978.

Sharma, M. M. 1987. Transport of Particulate Suspensions in Porous Media: Model formulation. *AIChE Journal*, 33, 1636-1643.

Sharma, M. M., Chenevert, M. E., and Guo, Q., et al. 2012. A New Family of Nanoparticles Based Drilling Fluids. Paper SPE-160045-MS presented *at SPE Annual Technical Conference and Exhibition*, 8-10 October San Antonio, Texas, USA.

Skauge, A. 2008. Microscopic Diversion: A New EOR Technique. 29th IEA Workshop &Symposium. Beijing China.

Song, Y.Q., and Marcus, C., 2007. Hyperpolarized Silicon Nanoparticles: Reinventing Oil Exploration? *Schlumberger Presentation*.

Sorbie, K. S., and Collins, I. R. 2010. A Proposed Pore-scale Mechanism for How Low Salinity Water Flooding Works. Paper SPE 129833 presented at *SPE Improved Oil Recovery Symposium*, 24-28 April, Tulsa, Oklahoma.

Tang, G. Q., and Morrow, N. R. 1999. Influence of Brine Composition and Fines Migration on Crude Oil/Brine/Rock Interactions and Oil Recovery. *Journal of Petroleum Science and Engineering*. 24: 99-111.

Tripathi, I., and Mohanty, K. K. 2007. Flow Instability Associated with Wettability Alteration. Paper SPE 110202 presented at *SPE Annual Technical Conference and Exhibition*, Nov 11-14, Anaheim CA.

Tufenkji, N. 2007. Colloid and Microbe Migration in Granular Environments: A Discussion of Modelling Methods, *Colloidal Transport in Porous Media*: 119-142: Springer Berlin Heidelberg.

Vafai, K. 2005. *Handbook of Porous Media* (Second Edition). New York: CRC Press, Taylor & Francis Group.

Van Zanten, R., Lawrence, B., and Henzler, S.J. 2010. Using Surfactant Nanotechnology to Engineer Displacement Packages for Cementing Operations. Paper SPE-127885-MS

presented at *IADC/SPE Drilling Conference and Exhibition*, USA, 2-4 February New Orleans, Louisiana.

Wagner, H. D. 1987. Equivalence of the Euler and Lagrangian Equations of Gas Dynamics for Weak Solutions. *Journal of Differential Equations*, 68: 118-136.

Wang, W., Yuan, B., and Su, Y., et al. 2016. Nanoparticles Adsorption/Detachment Behaviors and Its Effects on Permeability of Berea Cores: Experiments and Analytical Modeling. Paper SPE-181285-MS presented at *SPE Annual Technical Conference and Exhibition*, 26 – 28 September, in Dubai, U.A.E.

Welge H. J. A Simplified Method for Computing Oil Recovery by Gas or Water Drive. 1952. *Journal of Petroleum Technology*, 4(04): 91-98.

You, Z., Badalyan, A., and Bedrikovetsky, P., et al. 2015. Modeling of Productivity Decline in Geothermal Reservoirs due to Fines Migration-induced Formation Damage. *Proceedings World Geothermal Congress*, 19-25 April, Melbourne, Australia.

Yu, J., An, C., and Mo, D., et al. 2012. Study of Adsorption and Transportation Behavior of Nanoparticles in Three Different Porous media. Paper SPE-153337-MS presented at the *Eighteenth SPE Improved Oil Recovery Symposium*, 14-18 April. Tulsa, Oklahoma.

Yuan, B., Su, Y., and Moghanloo, R. G., et al. 2015a. A New Analytical Multi-Linear Solution for Gas Flow toward Fractured Horizontal Well with Different Fracture Intensity. *Journal of Natural Gas Science and Engineering*, 23, 227-238.

Yuan, B., Moghanloo, R. G., and Purachet. P., 2015b. Applying Method of Characteristics to Study Utilization of Nanoparticles to Reduce Fines Migration in Deepwater Reservoirs. SPE-174192-MS presented at *SPE European Formation Damage Conference and Exhibition*, 3-5 June, Budapest, Hungary.

Yuan, B., Moghanloo, R. G., Zheng, D., 2016a. Analytical Modeling of Nanofluid Injection to Improve the Performance of Low Salinity Water Flooding. Paper OTC-26363-MS presented at *Offshore Technology Conference Asia*, 22-25 March, Kuala Lumpur, Malaysia.

Yuan, B., Moghanloo, R. G., 2016b. Analytical Solution of Nanoparticles Utilization to Reduce Fines Migration in Porous Medium, *SPE Journal*, 21(06): 2317-2332.

Yuan, B., Moghanloo, R. G., and Wang, K. 2016c. Injectivity Improvement by Nanofluid Preflush during Low Salinity Water Flooding. Paper IPTC-18611-MS presented at *10th International Petroleum Technology Conference*. 14 – 16 November, Bangkok, Thailand.

Yuan, B., Moghanloo, R. G., Zheng, D. 2016d. Enhanced Oil Recovery by Combined Nanofluid and Low Salinity Water Flooding in Multi-Layer Heterogeneous Reservoirs. Paper SPE-181392-MS presented at *SPE Annual Technical Conference and Exhibition*, 26 – 28 September, Dubai, U.A.E.

Yuan, B., Bedrikovetsky, P., and Huang, T., et al. 2016e. Special Issue: Formation Damage during Enhanced Gas and Liquid Recovery. *Journal of Natural Gas Science and Engineering*, 36: 1051-1054.

Yuan, B., Wang, W., and Rouzbeh, G. M., et al. 2017. Permeability Reduction of Berea Cores Owing to Nanoparticles Adsorption onto the Pore Surfaces: Mechanistic Modeling and Lab Experiments. *Energy & Fuels*, 31(01): 795-804.

Yuan, H., and Shapiro, A. A. 2011. A Mathematical Model for Non-Monotonic Deposition Profile for Deep Bed Filtration Systems. *Chem. Eng. J.* 1661(1): 105-115.

Zeinijahromi, A., Lemon, P., and Bedrikovetsky, P., 2011. Effects of Induced Fines Migration on Water Cut during Waterflooding. *Journal of Petroleum Science and Engineering*, 78(3–4): 609-617.

Zeinijahromi, A., Vaz, A., and Bedrikovetsky, P., 2012. Well Impairment by Fines Migration in Gas Fields. *Journal of Petroleum Science and Engineering*, 88–89: 125-135.

Zeinijahromi, A., Nguyen, T. K. P., and Bedrikovetsky, P., 2013. Mathematical Model for Fines-Migration-Assisted Waterflooding with Induced Formation Damage. *SPE Journal*, 18(03): 518-533.

Zhang, T., Murphy, M., and Yu, H., et al., 2013. Investigation of Nanoparticles Adsorption during Transport in Porous Media. Paper SPE-166346-MS presented at the *SPE Annual Technical Conference and Exhibition*. USA, 30 September-2 October 2013, New Orleans, Louisiana.

Zhang, J., Li, L., and Wang, S. 2015. Novel Micro and Nanoparticle-based Drilling Fluids: Pioneering Approach to Overcome the Borehole Instability Problem in Shale Formation. Paper SPE-176991-MS presented at the *SPE Asia Pacific Unconventional Resources Conference and Exhibition*, 9-11 November, Brisbane, Australia.

Appendix A

Consider a general system of quasilinear first-order PDEs for two dependent variables (Rhee et al. 2001), C_1 and C_2, with two independent variables, x_D and t_D,

$$\begin{aligned} L_1 &= A_1 \frac{\partial C_1}{\partial x_D} + B_1 \frac{\partial C_1}{\partial t_D} + C_1 \frac{\partial C_2}{\partial x_D} + D_1 \frac{\partial C_2}{\partial t_D} + E_1 = 0 \\ L_2 &= A_2 \frac{\partial C_1}{\partial x_D} + B_2 \frac{\partial C_1}{\partial t_D} + C_2 \frac{\partial C_2}{\partial x_D} + D_2 \frac{\partial C_2}{\partial t_D} + E_2 = 0 \end{aligned} \quad \text{.....(A.1)}$$

Where $A_1, B_1, C_1, D_1, E_1, A_2, B_2, C_2, D_2, E_2$ are given continuous functions of , C_1, C_2, x_D and t_D with as many continuous derivatives. The two PDEs are always independent with each other and quasilinear since all the derivatives are linear in first-order.

The above PDEs above are homogeneous if $E_1, E_2 = 0$. They are also called reducible while they are homogeneous and the coefficients are only functions of C_1 C_2. For different cases of multi-phase multi-component flow with adsorption and chemical reactions, the functions of E_1, E_2 depends on the assumption of equilibrium or non-equilibrium reaction theory.

To ensure the characteristic lines of both variables C_1 and C_2, along the same direction, a linear combination of the above two equations is defined, as $L = \lambda_1 L_1 + \lambda_2 L_2$ to yield:

$$L = (\lambda_1 A_1 + \lambda_2 A_2)\frac{\partial C_1}{\partial x_D} + (\lambda_1 B_1 + \lambda_2 B_2)\frac{\partial C_1}{\partial t_D} + (\lambda_1 C_1 + \lambda_2 C_2)\frac{\partial C_2}{\partial x_D} + (\lambda_1 D_1 + \lambda_2 D_2)\frac{\partial C_2}{\partial t_D} + (\lambda_1 E_1 + \lambda_2 E_2) = 0 \quad \text{(A.2)}$$

where L_1 and L_2 are the functions of derivatives of two variables; and λ_1, λ_2 are the line combination coefficients. If the directed derivatives of C_1 and C_2 will be collinear, it is necessary that:

$$\frac{dt_D}{dx_D} = \frac{\lambda_1 B_1 + \lambda_2 B_2}{\lambda_1 A_1 + \lambda_2 A_2} = \frac{\lambda_1 D_1 + \lambda_2 D_2}{\lambda_1 C_1 + \lambda_2 C_2} = \sigma \quad \text{..... (A.3)}$$

In matrix form, the system of Eq. A.3 can be written as:

$$\begin{vmatrix} A_1\sigma - B_1 & A_2\sigma - B_2 \\ C_1\sigma - D_1 & C_2\sigma - D_2 \end{vmatrix} \begin{vmatrix} \lambda_1 \\ \lambda_2 \end{vmatrix} = 0 \quad \text{.....(A.4)}$$

If there are nontrivial values of λ_1, λ_2 , it becomes an eigenvalue problem; the determinate of coefficient matrix should be zero. Therefore, two characteristic directions can be obtained as:

$$\sigma^{\pm} = \frac{\left(A_1D_2 - A_2D_1 + B_1C_2 - B_2C_1\right) \pm \sqrt{\left(A_1D_2 - A_2D_1 + B_1C_2 - B_2C_1\right)^2 - 4\left(A_1C_2 - A_2C_1\right)\left(B_1D_2 - B_2D_1\right)}}{2\left(A_1C_2 - A_2C_1\right)} \quad \text{(A.5)}$$

If the discriminant is a positive number,

$$\left(A_1D_2 - A_2D_1 + B_1C_2 - B_2C_1\right)^2 - 4\left(A_1C_2 - A_2C_1\right)\left(B_1D_2 - B_2D_1\right) > 0$$

This quadratic equation has two real roots and there are two families of characteristics C_+ and C_- presented in form of $\alpha(x_D, t_D) = \text{const}$ and $\beta(x_D, t_D) = \text{const}$, which are called as characteristic parameters. When the discriminant is zero or negative, the system is parabolic and elliptic, accordingly.

Since there are two characteristic directions for hyperbolic system of equations, there will be two different family of characteristics generated by two distinct values. The

subscript ± in Eq. A.5 indicates the corresponding terms to two roots of Eq. A.4. The characteristic lines form a curvilinear map that serves as the possible solution route; the unique solution for different sets of initial and boundary conditions can be obtained along these characteristics lines.

Total derivatives of (C_1, C_2) in $x_D - \varphi$ domain will be only functions of ζ along each characteristic, $\alpha(x_D, t_D)$ and $\beta(x_D, t_D)$,

$$C_{1,\xi} = \frac{\partial C_1}{\partial x_D}\frac{\partial x_D}{\partial \xi} + \frac{\partial C_1}{\partial t_D}\frac{\partial \varphi}{\partial \xi} = C_{1,x_D} x_{D,\xi} + C_{1,t_D} t_{D,\xi}$$
$$C_{2,\xi} = \frac{\partial C_2}{\partial x_D}\frac{\partial x_D}{\partial \xi} + \frac{\partial C_2}{\partial t_D}\frac{\partial \varphi}{\partial \xi} = C_{1,x_D} x_{D,\xi} + C_{2,t_D} t_{D,\xi} \quad \text{..... (A.6)}$$

Replacing the coefficients of C_{1,t_D} and C_{2,t_D} in Eq. A.2 by the numerators in Eq. A.3 and substitution of total derivatives from Eq. A.6:

$$\left(\lambda_1 A_1 + \lambda_2 A_2\right) C_{1,\xi} + \left(\lambda_1 C_1 + \lambda_2 C_2\right) C_{2,\xi} + \left(\lambda_1 E_1 + \lambda_2 E_2\right) x_{D,\xi} = 0 \text{ .....} \quad \text{(A.7)}$$

Alternatively, replace the coefficients of C_{1,x_D} and C_{1,x_D} in Eq. A.2 by the numerators in Eq. A.3 and substitution of total derivatives from Eq. A.6:

$$\left(\lambda_1 B_1 + \lambda_2 B_2\right) C_{1,\xi} + \left(\lambda_1 D_1 + \lambda_2 D_2\right) C_{2,\xi} + \left(\lambda_1 E_1 + \lambda_2 E_2\right) t_{D,\xi} = 0 \text{ ..... (A.8)}$$

For system of hyperbolic partial differential equations, two roots to the system of Eq. A.7-A.8 and two roots obtained from the system of Eq. A.4 form the four-coupled ordinary differential equations that may be integrated simultaneously for (C_1, C_2) and (x_D, t_D) from an initial curve. The system of four above equation is summarized as,

$$\begin{cases} \left(A_1C_{1,\xi}+C_1C_{2,\xi}+E_1x_{D,\xi}\right)\lambda_1+\left(A_2C_{1,\xi}+C_2C_{2,\xi}+E_2x_{D,\xi}\right)\lambda_2=0 \\ \left(B_1C_{1,\xi}+D_1C_{2,\xi}+E_1t_{D,\xi}\right)\lambda_1+\left(B_2C_{1,\xi}+D_2C_{2,\xi}+E_2t_{D,\xi}\right)\lambda_2=0 \\ \left(A_1\sigma_{\pm}-B_1\right)\lambda_1+\left(A_2\sigma_{\pm}-B_2\right)\lambda_2=0 \\ \left(C_1\sigma_{\pm}-D_1\right)\lambda_1+\left(C_2\sigma_{\pm}-D_2\right)\lambda_2=0 \end{cases} \quad \text{……..……..…} \quad \text{(A.9)}$$

For non-trial value of two unknowns $\lambda_1 \ \lambda_2$, we can choose any two equations from the system A-9, and set the determinant of the coefficient matrix be zero. The below system A-10 is the determinant of coefficient matrix of A-9.

$$\begin{cases} \left(A_2B_1-A_1B_2\right)C_{1,\xi}+\left[\left(A_2C_1-A_1C_2\right)\sigma_{\pm}+\left(B_1C_2-B_2C_1\right)\right]C_{2,\xi}+\left[\left(A_2E_1-A_1E_2\right)\sigma_{\pm}+\left(B_1E_2-B_2E_1\right)\right]x_{D,\xi}=0 \\ \left[\left(A_1C_2-A_2C_1\right)\sigma_{\pm}+\left(A_2D_1-A_1D_2\right)\right]C_{1,\xi}+\left(C_2D_1-C_1D_2\right)C_{2,\xi}+\left[\left(C_2E_1-C_1E_2\right)\sigma_{\pm}+\left(D_1E_2-D_2E_1\right)\right]x_{D,\xi}=0 \\ \left[\left(A_2B_1-A_1B_2\right)\sigma_{\pm}\right]C_{1,\xi}+\left[\left(A_2D_1-A_1D_2\right)\sigma_{\pm}+\left(B_1D_2-B_2D_1\right)\right]C_{2,\xi}+\left[\left(A_2E_1-A_1E_2\right)\sigma_{\pm}+\left(B_1E_2-B_2E_1\right)\right]t_{D,\xi}=0 \\ \left[\left(B_1C_2-B_2C_1\right)\sigma_{\pm}+\left(B_2D_1-B_1D_2\right)\right]C_{1,\xi}+\left(C_2D_1-C_1D_2\right)C_{2,\xi}+\left[\left(C_2E_1-C_1E_2\right)\sigma_{\pm}+\left(D_1E_2-D_2E_1\right)\right]t_{D,\xi}=0 \end{cases}$$

(A-10)

As for the system of A-11, it is a coupled four-equation system with four unknows, $C_{1,\xi} \ C_{2,\xi} \ t_{D,\xi} \ x_{D,\xi}$. To obtain non-zero solutions, the determinant of coefficient matrix must be zero for system A-10, in matrix form,

$$\begin{pmatrix} \left(A_2B_1-A_1B_2\right) & \left[\left(A_2C_1-A_1C_2\right)\sigma_{\pm}+\left(B_1C_2-B_2C_1\right)\right] & \left[\left(A_2E_1-A_1E_2\right)\sigma_{\pm}+\left(B_1E_2-B_2E_1\right)\right] & 0 \\ \left[\left(A_1C_2-A_2C_1\right)\sigma_{\pm}+\left(A_2D_1-A_1D_2\right)\right] & \left(C_2D_1-C_1D_2\right) & \left[\left(C_2E_1-C_1E_2\right)\sigma_{\pm}+\left(D_1E_2-D_2E_1\right)\right] & 0 \\ \left[\left(A_2B_1-A_1B_2\right)\sigma_{\pm}\right] & \left[\left(A_2D_1-A_1D_2\right)\sigma_{\pm}+\left(B_1D_2-B_2D_1\right)\right] & 0 & \left[\left(A_2E_1-A_1E_2\right)\sigma_{\pm}+\left(B_1E_2-B_2E_1\right)\right] \\ \left[\left(B_1C_2-B_2C_1\right)\sigma_{\pm}+\left(B_2D_1-B_1D_2\right)\right] & \left(C_2D_1-C_1D_2\right) & 0 & \left[\left(C_2E_1-C_1E_2\right)\sigma_{\pm}+\left(D_1E_2-D_2E_1\right)\right] \end{pmatrix} \begin{pmatrix} C_{NP,\xi} \\ C_{FP,\xi} \\ x_{D,\xi} \\ t_{D,\xi} \end{pmatrix}=0$$

(A-11)

Combining the zero determinant of coefficient matrix in Eq. A-4, and apply matrices transformation, the simplest form of coefficient matric for Eq. A-11 become, as follows,

$$\begin{pmatrix} (A_2B_1 - A_1B_2) & \left[(A_2C_1 - A_1C_2)\sigma_{\pm} + (B_1C_2 - B_2C_1)\right] & \left[(A_2E_1 - A_1E_2)\sigma_{\pm} + (B_1E_2 - B_2E_1)\right] & 0 \\ 0 & 0 & 0 & 0 \\ 0 & 0 & 1 & -\sigma_{\pm} \\ 0 & 0 & 0 & 0 \end{pmatrix} \begin{pmatrix} C_{NP,\xi} \\ C_{FP,\xi} \\ x_{D,\xi} \\ t_{D,\xi} \end{pmatrix} = 0$$

(A-12)

Therefore, the composition diagram is determined along the fast path and slow path respectively, and obtain the composition path $C_{FP}\left(C_{NP}\right)$,

$$\begin{aligned} &(A_2B_1 - A_1B_2)C_{1,\xi} + \left[(A_2C_1 - A_1C_2)\sigma_{\pm} + (B_1C_2 - B_2C_1)\right]C_{2,\xi} \\ &+ \left[(A_2E_1 - A_1E_2)\sigma_{\pm} + (B_1E_2 - B_2E_1)\right]x_{D,\xi} = 0 \end{aligned} \quad \text{..... (A-13)}$$

The existences of non-homogeneous terms (E_1, E_2) make the derivation of $C_{FP}\left(C_{NP}\right)$ difficult. In fact, for cases of two-phase multi-component flow with different assumptions of chemical reactions or adsorptions, the non-homogeneous terms are different. In view of the scopes of this dissertation, we summarize the simplification cases of the above general system of hyperbolic PDEs, as shown in Table A.1.

The amounts of fines detachment and sizes of fine particles with respect to pore-throat sizes are small enough to ignore the straining behavior of fines into pore-throats (Civan 2016). Nanoparticles equilibrium Langmuir Adsorption onto surfaces is assumed. The state of mobile or stationary depends on the strategy of nanofluid treatment, stationary for nanofluid pre-treatment case & mobile for co-injection case. The effects of phase saturation are also incorporated into different cases with residual oil or mobile water & oil phase. Nanoparticles transport in two-phase colloidal-suspension flow is simulated to evaluate the performance of enhanced oil recovery.

Table A-1 Summary of assumptions of nanoparticles, fine particles, water, and oil behaviors in different cases of nanofluid application to control fines migration, maintain well injectivity and improve oil recovery

<table>
<tr><td rowspan="2">Cases</td><td colspan="6">Components</td></tr>
<tr><td>Nanoparticles</td><td colspan="3">Fines particles</td><td>Water</td><td>Oil</td></tr>
<tr><td>Sec. 3.3.1</td><td>Equilibrium Langmuir Adsorption onto Mobile Fines</td><td rowspan="6">Multi-layer Adsorption Kinetics onto Rock Grains</td><td>No Straining</td><td rowspan="6">Mobile</td><td rowspan="6">Mobile</td><td rowspan="3">Residual</td></tr>
<tr><td>Sec. 3.3.2</td><td rowspan="2">Equilibrium Langmuir Adsorption onto Stationary Grains</td><td rowspan="2">Straining</td></tr>
<tr><td>Sec. 3.3.3</td></tr>
<tr><td>Sec. 4.2</td><td>Equilibrium Langmuir Adsorption onto Mobile Fines</td><td>No Straining</td><td rowspan="3">Mobile</td></tr>
<tr><td>Sec. 4.3</td><td rowspan="2">Equilibrium Langmuir Adsorption onto Stationary Grains</td><td rowspan="2">Straining</td></tr>
<tr><td>Sec. 5.2-5.3</td></tr>
</table>

Appendix B

In scenario II, the MOC solution for the condition of "under-saturated" porous medium, $\sigma_{cr,\text{initial}} < \sigma < \sigma_{cr,\max}$, substituting the particles capture kinetics equation into mass-balance equation, Eq.3.11, yields to:

Suspended fine particles:

$$\frac{\partial C_{FP}}{\partial x_D} + \frac{\partial C_{FP}}{\partial t_D} + \lambda C_{FP} L = 0 \quad \text{(B.1)}$$

Retained fine particles:

$$\frac{\partial \sigma_{FP}}{\partial x_D} + \frac{\partial \sigma_{FP}}{\partial t_D} + \lambda L\left(\sigma_{FP} - \sigma_{cr,\text{initial}}\right) = 0 \quad \text{(B.2)}$$

Applying the approach of MOC, the following ordinary differential equations are obtained, along the characteristic line:

$$\frac{dx_D}{dt_D} = 1: \ \frac{dC_{FP}}{dt_D} = -\lambda C_{FP} L; \ \frac{d\sigma_{FP}}{dt_D} = \lambda L\left(\sigma_{cr,\text{initial}} - \sigma_{FP}\right) \quad \text{(B.3)}$$

Combined with the boundary condition, Eq. 3.12, leads to the solution of suspended fines and retained fines concentration in zone I and zone II, as shown in Fig. B-1:

$$0 < t_D < t_{Dc}$$

$$\begin{cases} \text{Zone I } (x_D > t_D): C_{FP} = 0; \quad \sigma_{FP} = \sigma_{cr,\text{initial}} \\ \text{Zone II } (x_D < t_D): \\ C_{FP} = C_0 \exp\left(-\lambda L x_D\right); \\ \sigma_{FP} = \left[\lambda \phi L (1 - S_{or}) C_0 \left(t_D - x_D\right)\right] \exp\left(-\lambda L x_D\right) + \sigma_{cr,\text{initial}} \end{cases} \quad \text{(B.4)}$$

The time t_{DC} is the moment when the retained fines concentration on rock grains at the inlet reaches the maximum value, $\sigma_{cr,\max}$, as shown in Eq. 3.4c.

$$t_{Dc} = \frac{\sigma_{cr,\max} - \sigma_{cr,initial}}{\lambda\phi L(1-S_{or})C_0} \quad \text{..... (B.5)}$$

At this moment, "attached front" appears, the retained and suspended fines concentration along the characteristic line in Fig.B-1 can be obtained, respectively.

$$\begin{cases} t_D = t_{Dc} \\ \sigma = \left(\sigma_{cr,\max} - \sigma_{cr,\text{initial}}\right)\exp\left(-\lambda L x_D\right) + \sigma_{cr,\text{initial}} \\ C_{FP} = C_0 \exp\left(-\lambda L x_D\right) \end{cases} \quad \text{..... (B.6)}$$

Based on the continuity condition derived by (Bedrikovetsky, 2011), around the "erosion front" $C^+ = C^- = C_0$, the following differential equations can be derived,

$$\frac{\partial\sigma_{FP}}{\partial x_D} + \frac{dt_D}{dx_{cr}}\frac{\partial\sigma_{FP}}{\partial t_D} = \frac{d\sigma_{\max}}{dx_D} = 0 \quad \text{..... (B.7)}$$

Where, the attachment of fine particles can be presented by particles capture kinetics,

$$\frac{\partial\sigma_{FP}}{\partial t_D} = \lambda\phi L(1-S_{or})C_0 \quad \text{..... (B.8)}$$

Substituting Eq. B.8 into Eq. B.7 results in,

$$\frac{\partial\sigma_{FP}}{\partial x_D} = -\lambda\phi L(1-S_{or})C_0 - \lambda L\left(\sigma_{cr,\max} - \sigma_{cr,\text{initial}}\right) \quad \text{..... (B.9)}$$

Then, the moving velocity of the "erosion front" is determined by,

$$\frac{dx_{cr}}{dt_D} = \frac{\phi(1-S_{or})C_0}{\phi(1-S_{or})C_0 + \left(\sigma_{cr,\max} - \sigma_{cr,\text{initial}}\right)} \quad \text{..... (B.10)}$$

Therefore, the trajectory of particles erosion front can be represented as:

Distance form:

$$x_{cr} = \frac{\phi(1-S_{or})C_0}{\phi(1-S_{or})C_0 + \left(\sigma_{cr,\max} - \sigma_{cr,\text{initial}}\right)}\left(t_D - \frac{\sigma_{cr,\max} - \sigma_{cr,initial}}{\lambda\phi L(1-S_{or})C_0}\right) \quad \text{..... (B.11a)}$$

Time form:

$$t_{cr}=\frac{\phi(1-S_{or})C_0+\left(\sigma_{cr,\max}-\sigma_{cr,\text{initial}}\right)}{\phi(1-S_{or})C_0}x_D+\frac{\sigma_{cr,\max}-\sigma_{cr,initial}}{\lambda\phi L(1-S_{or})C_0}\text{……..……..…(B-11b)}$$

Inferred from Eq. B.1, the slopes of characteristic lines in zone III are unity, therefore, the characteristic lines that start from any intersection points with the erosion front can be represented as:

$$\text{Line III: } x_D-x_{cr}=t_D-t_{cr}\ \text{……..……..…… (B.12)}$$

Combining Eq. B.12 and Eq.B.11, the start points on the erosion front at zone III can be obtained,

$$x_{cr0}=\left(t_D-x_D\right)\frac{\phi(1-S_{or})C_0}{\left(\sigma_{cr,\max}-\sigma_{cr,\text{initial}}\right)}-\frac{1}{\lambda L}\ \text{…….……...… (B.13a)}$$

$$t_{cr0}=\left(t_D-x_D\right)\left(\frac{\phi(1-S_{or})C_0+\left(\sigma_{cr,\max}-\sigma_{cr,\text{initial}}\right)}{\left(\sigma_{cr,\max}-\sigma_{cr,\text{initial}}\right)}\right)-\frac{1}{\lambda L}\ \text{…..……..……..… (B.13b)}$$

Finally, the retained and suspended fines concentration in zone III and Zone IV are obtained, respectively.

Zone III:

$$\begin{cases}\sigma_{FP}=\left(\sigma_{cr,\max}-\sigma_{cr,initial}\right)\exp\left(-\lambda L\left(x_D-\left(t_D-x_D\right)\dfrac{\phi(1-S_{or})C_0}{\left(\sigma_{cr,\max}-\sigma_{cr,\text{initial}}\right)}+\dfrac{1}{\lambda L}\right)\right)+\sigma_{cr,initial}\\ C_{FP}=C_0\exp\left(-\lambda L\left(x_D-\left(t_D-x_D\right)\dfrac{\phi(1-S_{or})C_0}{\left(\sigma_{cr,\max}-\sigma_{cr,\text{initial}}\right)}+\dfrac{1}{\lambda L}\right)\right)\end{cases}$$

(B.14)

In zone IV, the retained fines concentration keeps constant as $\sigma_{cr,\max}$, and the suspended fines concentration is equal to the injection condition, C_0. After

$t > t_{cr}(x_D = 1)$, all of intervals along the permeable medium have reached the maximum retention state of fine particles, and there is no room for particles attachment.

$$\text{Zone IV: } \begin{cases} \sigma_{FP} = \sigma_{cr,\max} \\ C_{FP} = C_0 \end{cases} \quad \text{..... (B.15)}$$

$$t_{cr}(x_D = 1) = \frac{\phi(1-S_{or})C_0 + \left(\sigma_{cr,\max} - \sigma_{cr,\text{initial}}\right)}{\phi(1-S_{or})C_0} x_D\Big|_{x_D=1} + \frac{\left(\sigma_{cr,\max} - \sigma_{cr,\text{initial}}\right)}{\lambda\phi L(1-S_{or})C_0} \text{ ..... (B.16)}$$

To make comparison with scenario I, initially, we pre-soaked the permeable medium with nanoparticles concentration, 0.00033, which is the same with the injection concentration at scenario I.

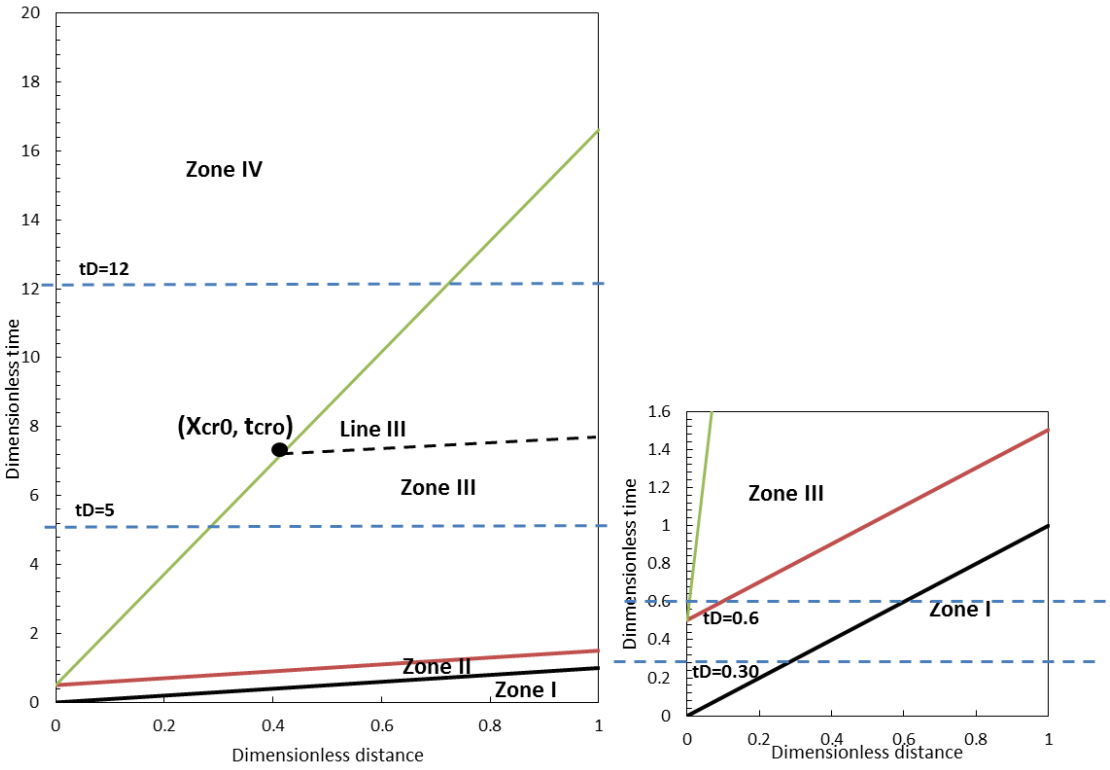


Figure B.1 Distance–time diagram or motion of particles concentration fronts in plane of x_D-t_D